

*Magnetosphere-ionosphere coupling  
currents in Jupiter's middle  
magnetosphere*

---

Thesis submitted for the degree of  
Doctor of Philosophy  
at the University of Leicester

---

Jonathan D. Nichols

Radio and Space Plasma Physics Group  
Department of Physics and Astronomy  
University of Leicester

September 2004

UMI Number: U188242

All rights reserved

INFORMATION TO ALL USERS

The quality of this reproduction is dependent upon the quality of the copy submitted.

In the unlikely event that the author did not send a complete manuscript and there are missing pages, these will be noted. Also, if material had to be removed, a note will indicate the deletion.



UMI U188242

Published by ProQuest LLC 2013. Copyright in the Dissertation held by the Author.  
Microform Edition © ProQuest LLC.

All rights reserved. This work is protected against  
unauthorized copying under Title 17, United States Code.



ProQuest LLC  
789 East Eisenhower Parkway  
P.O. Box 1346  
Ann Arbor, MI 48106-1346

## ***Abstract***

### **Magnetosphere-ionosphere coupling currents in Jupiter's middle magnetosphere**

*Jonathan Nichols*

This thesis is a theoretical study of the magnetosphere-ionosphere coupling current system in Jupiter's middle magnetosphere associated with the breakdown of corotation of iogenic plasma and the jovian main auroral oval. The study initially investigates the effects of the ionospheric Pedersen conductivity and the iogenic plasma mass outflow rate. Wide ranges of values of these parameters are inputted to the model and the results are compared for dipole and current sheet field models. It is shown that previous results, obtained using 'reasonable' spot values, are generally valid over wide ranges of the parameters. The study then investigates the effect of precipitation-induced enhancements of the Pedersen conductivity. Previous models have assumed constant conductivity, whereas it is expected to be significantly elevated by strong field-aligned currents. A model of the dependence of the Pedersen conductivity on the field-aligned current is developed and incorporated into the model. The findings help reconcile the theoretical results with observation. Specifically, the plasma is maintained closer to rigid corotation out to much further distances than theory previously predicted, the equatorial radial current exhibits a sharp rise in the inner region of the middle magnetosphere and plateaus off thereafter, in line with Galileo magnetic field data, and the field-aligned current is concentrated in a peak in the inner region, which is to where the main oval is usually mapped. Finally, the study investigates the effect of self-consistently including magnetosphere-ionosphere decoupling due to field-aligned voltages. The results show that for typical jovian conditions the effect is very small, such that the modification to the system parameters is generally two orders of magnitude below the values of the parameters themselves. The conclusion is that the assumption made in previous work, that the effect of the field-aligned voltages is small, is generally valid.

## ***Declarations***

The work undertaken during the course of this doctoral programme has led to the submission and publication of the following scientific papers:

**Cowley, S.W.H., Nichols, J.D., and Bunce E.J.:** Steady-state distributions of flow, current, and auroral precipitation in Jupiter's middle magnetosphere: Solutions for current sheet and dipole magnetic field models, *Planet. Space Sci.*, 50, 717, 2002.

**Cowley, S.W.H., Bunce, E.J., and Nichols, J.D.:** Origins of Jupiter's main oval auroral emissions, *J. Geophys. Res.*, 108 (A4), 8002, doi:10.1029/2002JA009329, 2003.

**Nichols, J.D., and Cowley, S.W.H.:** Magnetosphere-ionosphere coupling currents in Jupiter's middle magnetosphere: Dependence on the effective ionospheric Pedersen conductivity and iogenic plasma mass outflow rate, *Ann. Geophysicae*, 21, 1419, 2003.

**Nichols, J.D., and Cowley, S.W.H.:** Magnetosphere-ionosphere coupling currents in Jupiter's middle magnetosphere: Effect of precipitation-induced enhancements of the Pedersen conductivity, *Ann. Geophysicae*, 22, 1, 2004.

**Nichols, J.D., and Cowley, S.W.H.:** Magnetosphere-ionosphere coupling currents in Jupiter's middle magnetosphere: Effect of magnetosphere-ionosphere decoupling by field-aligned auroral voltages, *Ann. Geophysicae*, submitted, 2004.



The Italian renaissance artist Paris Bordone painted in 1558 this depiction of the mythical interaction of Jupiter, the king of the Roman gods, and one of his many mistresses Io, a river goddess. Jupiter, captivated by Io, disguised himself in a cloud and embraced her. In the background is Juno, Jupiter's wife, who was suspicious of the cloud and went to investigate. Just before she arrived Jupiter turned Io into a cow. However, Juno was not fooled and, craftily, she asked that Jupiter give her the cow as a gift. Reluctantly, Jupiter agreed. Juno immediately put Io under the watch of her hundred-eyed servant Argus. Jupiter was upset that Io was held prisoner in the shape of a cow, so he sent his son Mercury to rescue her. Mercury played his pipe and told many stories to Argus until he fell asleep, whereupon Mercury cut off Argus' head and freed Io. Juno was very upset by this and took the eyes of Argus and placed them on the tail of her favourite bird, the peacock. She then released a stinging fly to torment Io, who was still in the shape of a cow. Io fled across what is now known as the Ionian Sea and passed into the Black Sea through its narrow entrance Bosphorus ("the fording of the Ox"). Jupiter finally promised not to pursue Io any longer, and so Juno relented. She released Io from the shape of a cow, and Io eventually settled in Egypt, where, legend has it, she became the land's first queen. Millennia later, the first images of the moon Io taken by the Voyager spacecraft revealed an object that some people claim looks mysteriously like a hoofprint...

## *Acknowledgments*

If I were to thank everybody who has in some way or another helped me over the last three years, then I fear I would double the size of this already voluminous tome. Therefore, I will just say here thank you to all members of the Radio and Space Plasma Physics group at Leicester, it's been a pleasure to work (and drink) with you all.

I would like to express my great admiration and gratitude to my supervisor, Prof. Stan Cowley. Stan has the great ability to look at a faulty plot for a few seconds and then enlighten you as to what is wrong with your code (or more accurately, your physics) that has had you tearing your hair out for a week. His patience in explaining (and re-explaining) the intricacies of jovian plasma physics to my relatively sloth-like brain over the course of my PhD has been much appreciated.

Moving on to my officemates, past and present. First of all there is Em, my fellow jovian Stanling. Em has had to put up with me constantly bugging her with questions for three years and I'd like to say here that her help and advice has proved invaluable, thank you! Then we have Ade, fellow Office Bloke, drinking and verbal sparring partner, and occasional (physical) punch-bag. Although I'm sure he'd disagree, I'm not sure there is one topic that we have ever agreed on. Actually there are some, but none that I can recount here... Thanks also to Lisa, for putting up with me and my fellow Office Bloke, for being a good laugh and for showing me how to play beach volleyball. Thank you to Cat for also being a great laugh, for the games of squash (she'll win one day), and for reminding me that I am not, in fact, an expert.

I'd also like to thank all my friends who have shaped my life over my time at Leicester. Thanks to Nuss, the Geordie who spawned a new verb, for all the laughs, sorrows, and beers we've shared. The Ashfield Road crew: Scotty, for keeping my memory in his head; Tommi for introducing me to saunas and always being up for a beer (or twelve); Grant for putting up with my (lack of) washing up; and Fraz for our erstwhile very successful drinking partnership. Thanks to all at the Leicester University Karate Club, especially Sensei Rick, Steve, Matt, Rangan, Felicita and Sandip, for helping me vent my aggression at training! Thanks also to the guys at GMV Hall: Jim Shaw for our Sub-Warden Pizza and Wine (but mainly Wine) sessions; Danny for our many hours spent in The Bar, and of course Emma for being so kind as to take in and look after a destitute and homeless PhD student.

Of course I wouldn't be writing this at all if it wasn't for my family. So finally I'd like to express my sincere love and gratitude to Mére, Rogue, C, Grandma and Grandpa, AJ, and CD for all their love and support. Ta!

## ***Contents***

<b>Chapter 1:</b>	<b>Solar-planetary physics</b>	<b>1</b>
1.1	Introduction	1
1.2	The sun and solar wind	2
1.3	Solar and interplanetary magnetic fields	4
1.4	Planetary magnetospheres	8
1.4.1	Structure	8
1.4.2	Dynamics	9
<b>Chapter 2:</b>	<b>The structure and dynamics of the jovian magnetosphere</b>	<b>12</b>
2.1	Introduction	12
2.2	Discovery and exploration	13
2.3	The structure of Jupiter's magnetic field	15
2.3.1	Internal planetary field and size of the magnetosphere	15
2.3.2	Inner magnetosphere	16
2.3.3	Middle magnetosphere	17
2.3.4	Dayside outer magnetosphere	18
2.3.5	Magnetic tail	18
2.3.6	Field line bending	19
2.4	Plasma populations in the jovian magnetosphere	20
2.4.1	Sources of plasma mass	20
2.4.2	The Io plasma torus	21
2.4.3	Hot plasma population	23
2.4.4	Equatorial plasma flow	24
2.5	Jovian aurorae	26

<b>Chapter 3:</b>	<b>Magnetosphere-ionosphere coupling in Jupiter's middle magnetosphere</b>	<b>30</b>
3.1	Introduction	30
3.2	Physical background	32
3.3	Theory of the jovian M-I coupling system	33
3.3.1	Field description and magnetosphere-ionosphere mapping	34
3.3.2	Magnetosphere-ionosphere coupling current system	35
3.3.3	Parallel voltage, acceleration region height, and precipitated electron energy flux	39
3.3.4	Steady state angular velocity profile and field-aligned currents	41
3.3.5	Results of Hill (1979, 2001) and Pontius (1997)	43
3.3.6	Results of Cowley and Bunce (2001b) and Cowley, Nichols and Bunce (2002)	45
<b>Chapter 4</b>	<b>Magnetosphere-ionosphere coupling currents in Jupiter's middle magnetosphere: Dependence on the effective ionospheric Pedersen conductivity and iogenic plasma mass outflow rate</b>	<b>55</b>
4.1	Introduction	55
4.2	Approximate forms for small and large distances	56
4.3	Plasma angular velocity and coupling current system for a dipole magnetic field model	58
4.3.1	Normalised solution	59
4.3.2	Un-normalised current dependence on the system parameters	66
4.4	Plasma angular velocity and coupling current system for a current sheet magnetic model	70
4.4.1	Current sheet field model	70
4.4.2	Approximate normalised solution for a power law equatorial field	72

4.4.3	Un-normalised numerical and approximate analytic solutions for the current sheet model	79
4.5	Comparison of the system behaviour for the dipole and current sheet field models	83
4.6	Summary	88
<b>Chapter 5</b>	<b>Magnetosphere-ionosphere coupling currents in Jupiter's middle magnetosphere: Effect of precipitation-induced enhancements of the ionospheric Pedersen conductivity</b>	<b>91</b>
5.1	Introduction	91
5.2	Magnetic field model	93
5.3	Dependence of the Pedersen conductivity on the field-aligned current	94
5.4	Solutions for near-linear variations of the conductivity	99
5.4.1	Method of obtaining solutions	99
5.4.2	Inner region approximations	100
5.4.3	Results for a near-linear conductivity model	102
5.4.4	Outer region approximations	107
5.4.5	Solution dependence on $\dot{M}$	108
5.4.6	Results for a more realistic conductivity model	109
5.5	Solutions appropriate to jovian conditions	111
5.5.1	Observed radial current profile	112
5.5.2	Comparison with constant conductivity results	113
5.5.3	Empirical conductivity model	114
5.5.4	Results using the empirical conductivity model	115
5.6	Summary	118
<b>Chapter 6</b>	<b>Magnetosphere-ionosphere coupling currents in Jupiter's middle magnetosphere: Effect of magnetosphere-ionosphere decoupling by field-aligned auroral voltages</b>	<b>122</b>
6.1	Introduction	122
6.2	Governing equations	123

## *Contents*

---

6.2.1	Magnetosphere-ionosphere decoupling by field-aligned voltages	123
6.2.2	Current circuit equations	125
6.2.3	Conservation of angular momentum (the Hill-Pontius equation)	127
6.2.4	Governing equation	128
6.2.5	Series solution of the governing equation	129
6.2.6	Inner region approximations	132
6.3	Results	136
6.4	Summary and conclusion	142
<b>Chapter 7</b>	<b>Summary and future work</b>	<b>144</b>
7.1	Introduction	144
7.2	Dependence on the Pedersen conductivity and the mass outflow rate	145
7.3	Effect of precipitation-induced enhancements of the Pedersen conductivity	146
7.4	Effect of magnetosphere-ionosphere decoupling by field-aligned auroral voltages	147
7.5	Future work	147
<b>References</b>		<b>150</b>

# ***Chapter 1***

## ***Solar-Planetary Physics***

### ***1.1. Introduction***

The work described in this thesis is a theoretical study of the large-scale current system which flows in the jovian plasma environment and is associated with the transfer of angular momentum from the planet's atmosphere and ionosphere to the equatorial magnetospheric plasma. The current system is a direct consequence of the existence of the volcanic moon Io, which orbits deep within the jovian magnetosphere, where it liberates of the order of one tonne per second of sulphur and oxygen plasma. This plasma becomes centrifugally unstable as it is accelerated to match the angular velocity of the rapidly rotating planet, and diffuses radially outwards. As the plasma moves outwards, its angular velocity drops, as required by conservation of angular momentum. The current system discussed in this thesis is then a result of the atmosphere's attempt to maintain this plasma in rotation at the same angular velocity as the planet. A key feature of the system is the production of strong field-aligned currents (FACs) flowing between the magnetosphere and the ionosphere, which are suggested to be associated with the jovian 'main oval' aurorae. The study of this current system helps us to understand the processes occurring in Jupiter's magnetosphere and their relation to the formation of phenomena such as the jovian aurorae.

The basic physics of the Sun, solar wind, and interplanetary magnetic field, and their interactions with magnetised planets, as appropriate to Jupiter, are introduced in this chapter. The second chapter then goes on to describe in detail the present understanding of the structure and dynamics of the jovian magnetosphere. Chapter 3 describes the physics underlying the magnetosphere-ionosphere coupling current system resulting from the breakdown of corotation of iogenic plasma, which is associated with the formation of the jovian main auroral oval. The dependence of the current system on the jovian magnetic

field model employed is discussed. A detailed theoretical study of the dependence of the system on the iogenic plasma mass outflow rate and jovian ionospheric Pedersen conductivity is carried out in Chapter 4, whilst Chapter 5 goes on to modify the theory to take into account the effect of precipitation-induced Pedersen conductivity enhancements. It is found that this modification helps explain some discrepancies between theory and observation. Chapter 6 completes the analysis by self-consistently considering the effect of the resulting field-aligned voltage on the system. The conclusions of the study and suggestions for further work finally follow in Chapter 7.

## 1.2. *The Sun and solar wind*

Astronomers class the Sun as a fairly mundane star of spectral type G2V. It is, however, unique in its proximity to the Earth and thus of fundamental importance, so it seems therefore natural that we should study the Sun and its interaction with the bodies which orbit it. The Sun is essentially a massive sphere of hot gas, composed mainly of hydrogen (~90% by mass), helium (~10%) and ‘other species’ (~0.1%, e.g. C, N, O in roughly the same proportion as found at the Earth), and is held together under the action of its own gravitational pull. Table 1.1 gives various key properties of the Sun, and in order to put these values into context, some comparisons with those of the Earth.

A schematic diagram of the Sun is shown in Fig. 1, depicting some of its main features, including interior differentiation and surface phenomena such as prominences and sunspots. The mass of the Sun is great enough that the energy released during its gravitational accretion raised the temperature of the centre, or *core*, to a level which, combined with the monumental pressure in this region, allowed thermonuclear reactions to commence. It is these nuclear reactions which take place in the Sun’s core, and mainly convert hydrogen to helium with the release of the associated nuclear binding energy, that account for the high temperature of the Sun. The pressure and temperature in the core are estimated to be  $\sim 340 \times 10^{11}$  Pa and  $\sim 15 \times 10^6$  K respectively. The energy generated by the nuclear reactions is transported to the surface of the Sun by two processes. In the inner regions the energy is transmitted by radiation (the *radiative zone*), while in the outer regions the gas is convectively unstable and the dominant energy transport mechanism is via convection cells

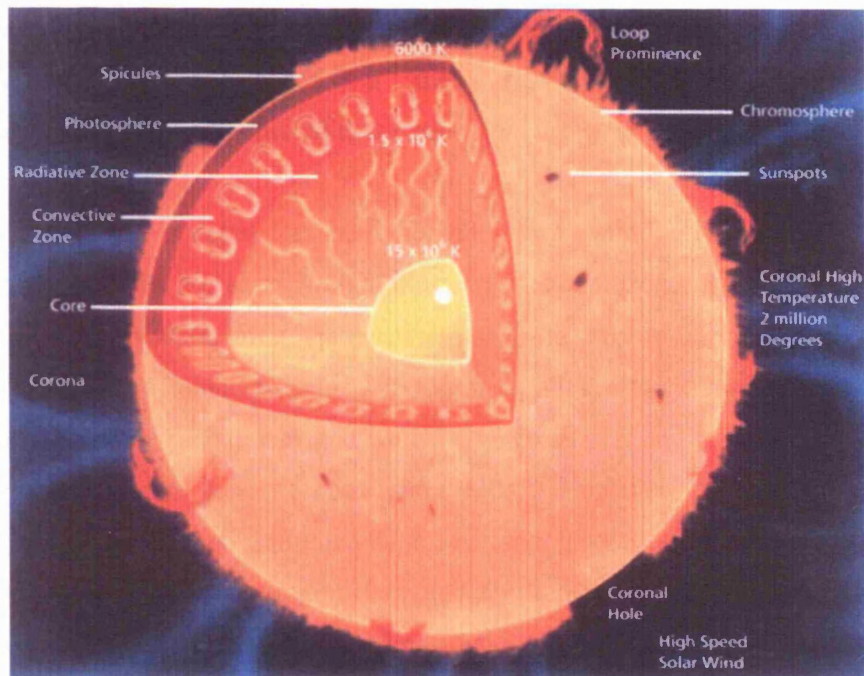


Figure 1.1. Schematic of the Sun's interior and atmosphere. From Lang (2001).

Property	Value	Value normalised to the Earth
Age	$4.5 \times 10^9$ yr	1
Mass	$1.99 \times 10^{30}$ kg	330,000
Radius	$6.96 \times 10^8$ m	109
Mean density	$1.4 \times 10^3$ kg m <sup>-3</sup>	0.25
Mean distance from Earth (1 AU)	$1.5 \times 10^{11}$ m	N/A
Surface gravity	$274$ m s <sup>-2</sup>	28
Escape velocity at surface	$6.18 \times 10^5$ m s <sup>-1</sup>	55
Luminosity	$3.86 \times 10^{26}$ W	N/A
Mass loss rate	$10^9$ kg s <sup>-1</sup>	N/A
Effective blackbody temperature	5785 K	23

Table 1.1. Key properties of the Sun and comparison with the Earth.

(the *convection zone*). The interior of the Sun is extremely opaque, such that the radiation undergoes many scatterings before it finally reaches the Sun's surface, typically  $\sim 10$  million years after it was created in the core.

The Sun's atmosphere is defined as the region which we can directly observe. It is divided into four regions. With increasing height these are: the *photosphere*, the base of which lies at the top of the convection zone; the *chromosphere*; the *transition region* and the *corona*. The photosphere, at a temperature of 5800 K, is a 500 km thick region from which the majority of the visible radiation which we observe emanates, and is covered in a granular pattern representing the tops of convection cells. However, the photosphere is not completely uniform. A visible light image reveals regions, called *sunspots*, that appear much darker than the surrounding surface and are cooler, having temperatures of order 4100 K. Sunspots have strong associated magnetic fields of strength 0.3 T, compared with a photospheric background of  $\sim 0.1$  mT, and their number is observed to vary regularly over a period of 11 years. This is called the *solar cycle*, discussed below. Above the photosphere lies the chromosphere, which extends for  $\sim 2000$  km. The chromosphere is characterised by a slow decrease in temperature to 4200 K, followed by a slow increase again out to 2000 km, where the temperature then rapidly increases to  $\sim 10^6$  K over a few hundred kilometres known as the transition region. The source of this large temperature rise is uncertain, but it is thought to be associated with the dissipation of the energy in the Sun's magnetic field.

In order to maintain pressure balance, the enormous temperature rise over the transition region is accompanied by a corresponding drop in plasma density, such that at the base of the corona, the temperature is  $\sim 2 \times 10^6$  K and the hydrogen ion density is  $\sim 10^9$  cm<sup>-3</sup>. If one now assumes the Sun's atmosphere to be in hydrostatic equilibrium, then application of the equations of mass continuity and momentum (which in hydrostatic equilibrium is simply the static force balance equation), we find that the pressure then falls off to approach an asymptotic value of  $\sim 10^{-5}$  N m<sup>-2</sup>. Now, the region of space in which the Sun's influence is dominant is called the *heliosphere*, and this is bound on the outside at an estimated distance of 100 – 150 AU (where 1 AU =  $1.5 \times 10^{11}$  m) by the *local interstellar medium*, or *LISM*. If the gas pressure of the LISM were greater than the Sun's asymptotic atmosphere pressure of  $\sim 10^{-5}$  N m<sup>-2</sup> then the Sun's atmosphere could be contained by the LISM in hydrostatic equilibrium. However, estimates put the pressure in the LISM to be of order  $10^{-13}$  N m<sup>-2</sup>,

which is many orders of magnitude less than the Sun's limiting pressure, and as such hydrostatic equilibrium is not possible. The result is that coronal plasma is driven at supersonic speeds into interplanetary space to form the *solar wind*, eventually interacting with the LISM at the boundary of the heliosphere, called the *heliopause*.

The effect of the solar wind can be seen in cometary tails, indeed this was how the existence of the solar wind was first postulated. Hoffmeister (1943) had noted that the tails of comets do not lie in a radial direction away from the Sun, but lag by about  $5^\circ$ , and this was correctly interpreted by Biermann (1951) as being a result of the interaction between the cometary ions and a solar wind. The first mathematical formulation to describe the solar wind was provided by Parker (1958). The coronal plasma is accelerated radially away from the Sun over a distance of  $\sim 5$  solar radii, after which the flow speed remains approximately constant at  $\sim 450 \text{ km s}^{-1}$  for 'streamer belt' plasma emitted from low latitudes (i.e. regions associated with closed field lines), and  $\sim 700 - 800 \text{ km s}^{-1}$  for plasma emitted from higher latitude *coronal hole* regions (associated with open field lines), until it reaches the heliopause. Consequently as the plasma expands outwards, the density and temperature drop, inversely as the distance squared in the case of the density due to mass conservation, while the temperature drop is determined by the adiabatic equation  $pV^\gamma = \text{const}$  coupled with the ideal gas equation  $p = nkT$ , where for a given plasma element  $p$  is its pressure,  $V$  is its volume,  $\gamma$  is the ratio of its specific heats,  $n$  is its particle number density,  $T$  is its temperature and  $k$  is Boltzmann's constant. However, because of heat conduction and dissipation the fall off is actually somewhat less than would be predicted from this equation. Table 1.2 summarises typical observed values of some key properties of the solar wind at the orbits of Earth and Jupiter.

### 1.3. Solar and interplanetary magnetic fields

To a first approximation, the Sun's magnetic field is dipolar and corotates with the Sun once every 27 days. This approximation is reasonably accurate during periods known as *solar minima*, however we find the Sun's magnetic field changes vastly over a period of 11 years, called the *solar cycle*. The solar cycle is an effect caused by the differential rotation of the Sun. That is, the equator moves with a higher angular velocity than the poles. This

Property	Typical Value at Earth's orbit (1 AU)	Typical Value at Jupiter's orbit (5.2 AU)
Flow speed $v_{sw} / \text{km s}^{-1}$	450	450
Number density $n_{sw} / \text{cm}^{-3}$	7	$\sim 0.26$
Temperature $T_{sw} / \text{K}$	$1.5 \times 10^5$	$1 \times 10^5$
Magnetic field magnitude $ B_{sw}  / \text{nT}$	7	1

**Table 1.2** Some key solar wind parameters at the orbits of the Earth and Jupiter. From Kivelson and Russell (1995) and Huddleston et al. (1998).

has the effect of “winding up” the Sun’s magnetic field, such that the dipole field as found at solar minimum is, after five and a half years, wound into a highly disordered state. This is known as *solar maximum*. After a further five and a half years the dipolar field re-emerges with the opposite polarity and the Sun returns to solar minimum. The whole cycle, then, is actually the 22 years taken for the Sun to return to its original polarity. The solar cycle can be tracked by the number of sunspots visible on the Sun. During solar minimum the sunspot number is low and they cluster around the equator, while at solar maximum, their number is many and they occur at higher latitudes.

The Sun’s magnetic field has an important influence on the behaviour of the solar wind because the latter carries with it a remnant of the coronal magnetic field, called the *interplanetary magnetic field*, or *IMF*. It is then useful to consider how this magnetic field behaves with respect to the solar wind plasma itself. To this end we consider Ohm’s law for a plasma with conductivity  $\sigma$

$$\mathbf{E} = -\mathbf{v} \times \mathbf{B} + \frac{\mathbf{j}}{\sigma} , \quad (1.1)$$

where  $\mathbf{E}$  is the electric field,  $\mathbf{B}$  is the magnetic field,  $\mathbf{j}$  is the electric current density and  $\mathbf{v}$  is the plasma velocity. Taking the curl of this and substituting it into Faraday’s law

$$\frac{\partial \mathbf{B}}{\partial t} = -\nabla \times \mathbf{E} , \quad (1.2)$$

and using Ampère’s law (neglecting the displacement current)

$$\nabla \times \mathbf{B} = \mu_0 \mathbf{j} , \quad (1.3)$$

where  $\mu_0$  is the permeability of free space, we obtain the induction equation

$$\frac{\partial \mathbf{B}}{\partial t} = \nabla \times (\mathbf{v} \times \mathbf{B}) + \frac{1}{\mu_0 \sigma} \nabla^2 \mathbf{B} . \quad (1.4)$$

Equation (1.4) describes the motion of the magnetic field with respect to the plasma in which it is embedded. It is characterised by two terms on the right-hand side (RHS), the first being the *transport* term and the second being the *diffusive* term. If the diffusive term were set to zero (e.g. if  $\sigma \rightarrow \infty$ ) then it can be shown that the magnetic field would move exactly with the plasma, i.e. it would be *frozen-in* to the plasma (Alfvén, 1981). If, on the other hand, the transport term were set to zero then the equation reduces to that of pure diffusion. In reality both the terms are present and taking the ratio of the first to the second provides a measure of which is dominant. This ratio is termed the *magnetic Reynolds number* and is approximated by

$$R_m = \mu_0 \sigma v L \quad , \quad (1.5)$$

where  $L$  is the characteristic scale length of the plasma. If  $R_m \gg 1$  then the diffusive term is negligible and the magnetic field can be considered to be frozen-in to the plasma. If, however,  $R_m \leq 1$  then the frozen-in approximation is not valid and the magnetic field is able to diffuse through the plasma. If we now consider the conditions in the solar wind, we find that the collisional mean free path of a particle, as calculated from gas kinetic theory, is approximately 1 AU. It is valid, therefore, to consider the solar wind as a collisionless plasma with a very high conductivity and as such  $R_m \gg 1$ . Hence, the IMF and the solar wind plasma are frozen together and propagate out into the solar system together. The frozen-in approximation breaks down in regions where the scale lengths are shorter, for example near intense current sheets, and the magnetic field is then able to diffuse through the plasma, allowing phenomena such as reconnection to occur (see e.g. Cowley (1984)).

To appreciate the form of the IMF, it is useful to consider a thought experiment in which the solar rotation is neglected and the Sun's (initially dipolar) magnetic field propagates radially away with the solar wind plasma, while the feet of the magnetic field lines remain frozen to the Sun's surface. The frozen-in theorem requires that the direction of the IMF lies along the locus of all the plasma elements emitted from a given source point on the surface of the Sun. Therefore after some time the magnetic field will point radially in towards the Sun in one hemisphere, and outward from the Sun in the other, depending on the original dipole polarity, and a thin current sheet will lie in the equatorial plane. The magnitude of the radial magnetic field  $B_r$  is determined by the 'no monopoles' law

$\text{div } \mathbf{B} = 0$ , and is given by  $B_r \propto 1/r^2$ , where  $r$  is the radial distance from the Sun's magnetic axis. If we now consider the above, but with the addition of the solar rotation, the result is that, in a manner similar to the water emitted from a spinning garden sprinkler, the IMF follows an Archimedean spiral known as the Parker spiral, illustrated in Fig. 1.2a, and the azimuthal component introduced to the IMF is given by  $B_\phi \propto 1/r$ . Therefore we find that when  $r$  is small, i.e. near to the Sun,  $B_r \gg B_\phi$ , while at the Earth's orbit  $B_r \approx B_\phi$  and further out at Jupiter's orbit  $B_\phi \gg B_r$ , such that the azimuthal component dominates the IMF. The current sheet which lies between the two regions of IMF polarity is known as the *heliospheric current sheet*, or *HCS*, and is in general inclined to the ecliptic plane due to the tilt of the Sun's magnetic dipole axis with respect to its spin axis. As such, a body lying in the ecliptic plane will over time experience different regions, or *sectors*, of IMF polarity as the Sun rotates and the HCS moves back and forth across the ecliptic plane. During solar minimum, when the Sun's magnetic field is essentially dipolar, the resulting two sector structure is clear, although the HCS tends to undulate somewhat in the manner of a ballerina's skirt, as illustrated in Fig. 1.2b. However, during solar maximum, when the Sun's magnetic field is highly disordered, the IMF is similarly disordered and consists of several sectors of IMF, as well as being characterised by transient disturbances such as shocks, coronal mass ejections (CMEs) and magnetohydrodynamic (MHD) waves.

The Sun's surface is not uniform. Some areas are more active than others and these active regions generally emit plasma at a higher velocity than less active areas. For example, as discussed above the streamer belt solar wind is much slower than the coronal hole solar wind. Therefore, as the plasma propagates out into interplanetary space, the fast regions of solar wind tend to catch up the slower ones, producing alternate regions of compression and rarefaction. As the solar wind travels away from the Sun, the plasma density perturbations evolve such that between  $\sim 2 - 3$  AU shocks develop in the compressed and rarefied regions. These are known as *corotating interaction regions (CIRs)* and they are the dominant feature in the solar wind between 2 – 8 AU (Gazis, 2000). A stable coronal hole structure may cause CIRs to recur in several rotations of the Sun and these are known as recurrent CIRs. Figure 1.3 illustrates an idealised sketch of the evolution of a CIR in the inner heliosphere. In the outer heliosphere, the IMF is more azimuthally aligned, such that the CIRs tend to merge to form *merged interaction regions (MIRs)*, where the shocks form radially moving concentric ring-like structures. Both CIRs and MIRs are characterised by

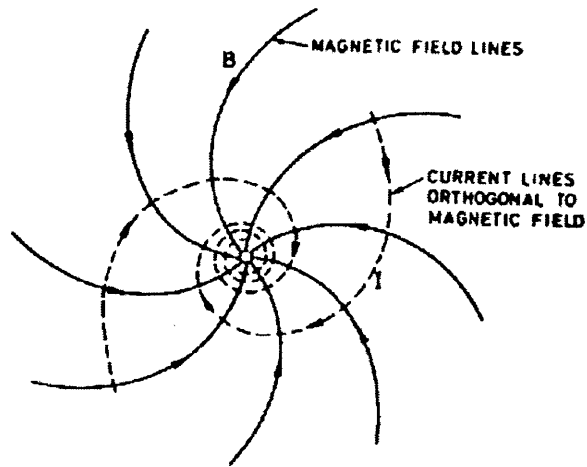


**Figure 1.2a** A sketch of the Parker spiral form of the IMF, and the spiralling electric current in the current sheet. Magnetic field lines are shown slightly above the equatorial plane, close below they have opposite polarity. From Alfvén (1981).

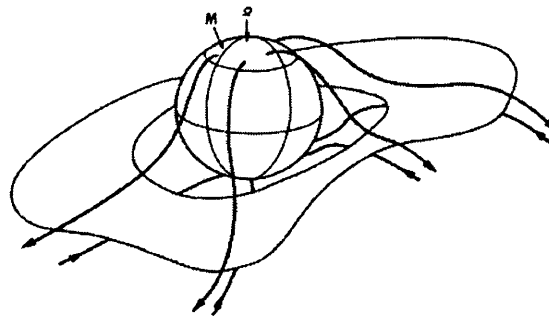


**Figure 1.2b** Current sheet in the inner heliosphere in the ballerina skirt model. The thick lines indicate the magnetic field lines. From Smith et al. (1978).

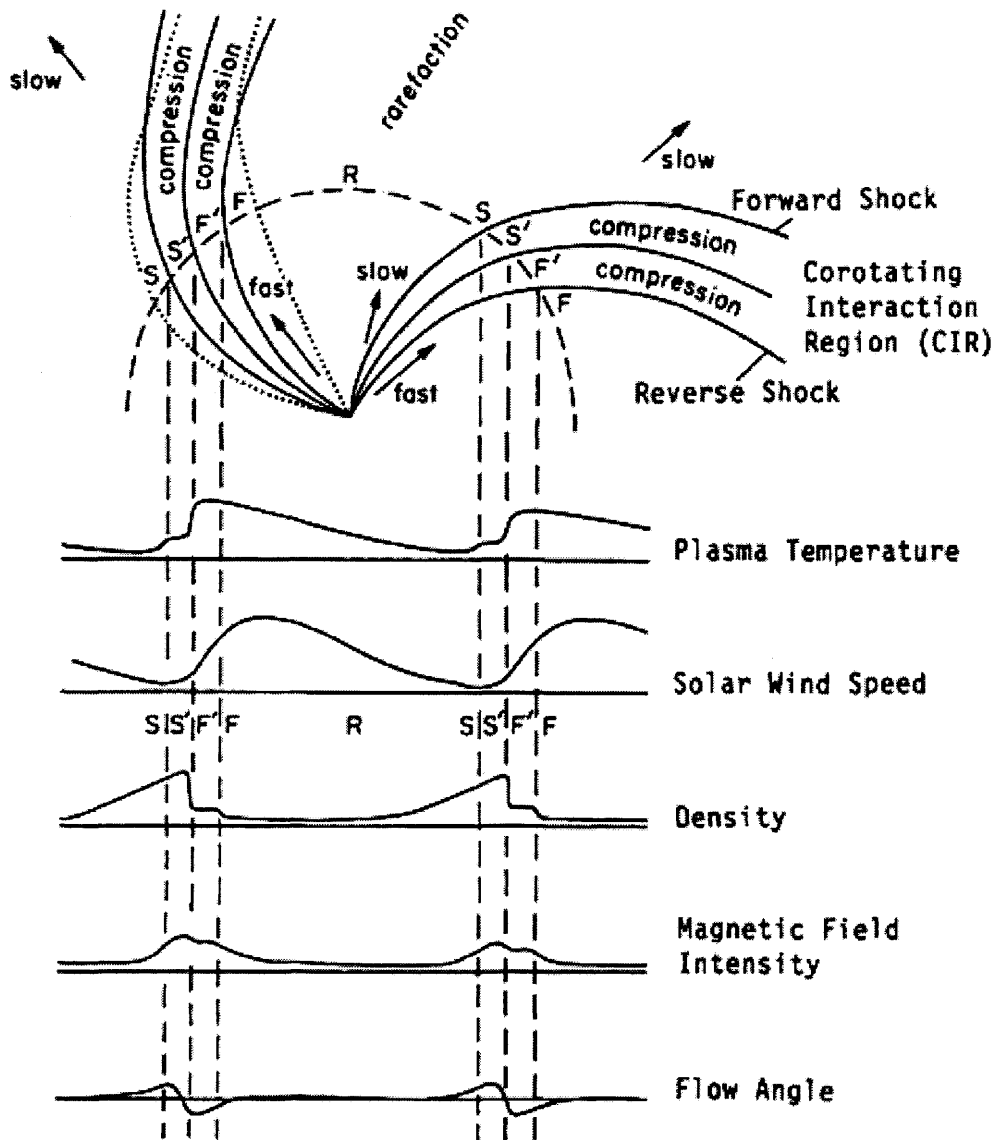


**Figure 1.3** Schematic diagram of two CIRs corotating with the Sun, along with the solar wind and magnetic field signatures associated with it at 1AU. S indicates slow plasma, S' indicates shocked slow plasma, F indicates fast plasma and F' indicates shocked fast plasma. Taken from Kunow (2001).

large increases in the solar wind velocity, pressure, temperature and IMF strength, and as such they play an important role in the modulation of the magnetospheres of the outer planets.

## 1.4. Planetary Magnetospheres

### 1.4.1 Structure

A *magnetosphere* is defined as the cavity surrounding a planet, or other body, which contains and is controlled by the body's magnetic field. Six of the planets in our solar system are known to have magnetospheres, these being Mercury, Earth, Jupiter, Saturn, Uranus and Neptune, and they exhibit very different properties from one another. Figure 1.4 shows the approximate relative sizes of the magnetospheres in our solar system, from the smallest (Mercury) to the largest (Jupiter). The key element in a magnetosphere is, of course, the planetary magnetic field, which is created by azimuthal currents flowing in the planet's core and is usually dipolar in nature. However, in some cases, e.g. Jupiter and Saturn, there also exist substantial quadrupole and octupole components as well.

To appreciate the overall form of a magnetosphere, we initially consider a dipole planetary magnetic field which contains plasma originating from, say, the planet's ionosphere. If the frozen-in theorem holds valid at all locations, the solar wind plasma (coupled to the IMF) and the planetary plasma (coupled to the planetary field) will not mix. Instead, a thin current sheet will be formed between the two which separates them, and a *closed magnetosphere* will form. The solar wind flow will compress the dayside planetary field, increasing the strength of the latter until pressure balance between the two is achieved. The boundary current sheet is called the magnetopause. In addition, since the solar wind flow is supermagnetosonic when it encounters the magnetosphere, a standing shock wave, called a bow shock, stands upstream of the dayside magnetosphere, across which the solar wind plasma is slowed, compressed and heated. The region between the bow shock and the magnetopause which contains shocked solar wind plasma is called the magnetosheath.

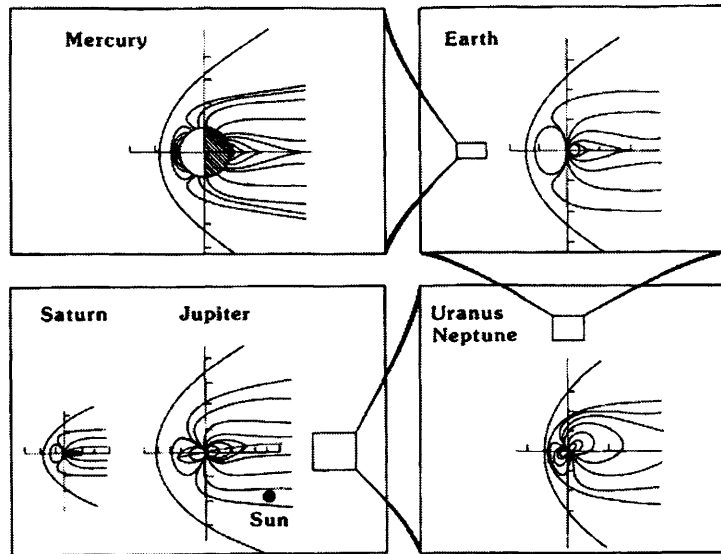


**Figure 1.4.** Relative sizes of planetary magnetospheres. From Kivelson and Russell (1995).

### 1.4.2 Dynamics

The flow of plasma within a magnetosphere is generally dependant on two driving mechanisms, due to interaction with the planet and to interaction with the solar wind. The properties of a particular magnetosphere give an indication as to which driving mechanism is dominant. If there were no other forces acting on the magnetospheric plasma, it would rotate with the same angular velocity as the planet. This flow, called corotation, is a result of angular momentum being transferred from the atmospheric neutral atoms to the plasma ions via collisions in the lower ionosphere. The torque is communicated to the magnetospheric plasma by the planetary field, such that in the steady state rigid corotation will prevail.

Interaction with the solar wind occurs at the magnetopause, where large field gradients cause the frozen-in theorem to break down, resulting in magnetic reconnection at the boundary. In this process planetary field lines connect with those in the IMF, resulting in *open* field lines, along which solar wind plasma is able to flow into the magnetosphere. Open field lines, which are frozen into the solar wind outside the magnetosphere, are pulled from the dayside to the nightside as the solar wind moves anti-sunward, forming a long magnetic tail on the nightside. In this way momentum is transferred from the solar wind to the magnetosphere. As the open field lines move down-tail they convect towards the equatorial plane, whereupon they reconnect once again and are transported back towards the planet as newly-closed field lines, and the cycle begins again. The flow due to solar wind interaction is therefore described by a twin-vortex and is known as the Dungey cycle, after J.W. Dungey, who first proposed the mechanism in 1961 (Dungey, 1961). For a particular field line the Dungey cycle takes approximately 12 hrs at the Earth, and approximately two weeks at Jupiter. An estimate of the minimum length of the magnetic tail can be made by multiplying the length of time a field line remains open (measured by radars to be  $\sim 4$  hrs for the case of the Earth and calculated by considering flux throughput to be  $\sim 5$  days at Jupiter) by the velocity of the solar wind ( $\sim 450 \text{ km s}^{-1}$ ) to give a terrestrial tail length of  $\sim 1000 R_E$  and a jovian tail of at least  $3000 R_J$  (where  $R_E$  is the Earth's radius = 6371 km and  $R_J$  is Jupiter's radius taken throughout this thesis to be 71,323 km). This calculation was first made by Dungey (1965). In comparison, a closed magnetosphere would have a magnetotail of length only approximately twice the dayside extension of the

magnetosphere (Slutz and Winkelman, 1964), and as such the existence of an extended magnetotail is taken to be evidence of dayside reconnection and the Dungey cycle.

It is possible to estimate which of these flow mechanisms, corotation or Dungey cycle, is expected to be dominant by considering the electric fields associated with each, as first considered by Brice and Ioannidis (1970). A flow of plasma with an embedded magnetic field is associated with an electric field perpendicular to both the plasma velocity vector  $\mathbf{v}$  and the magnetic field  $\mathbf{B}$ , given by  $\mathbf{E} = -\mathbf{v} \times \mathbf{B}$ . The electric field due to the Dungey cycle flow is directed from dawn to dusk in the equatorial plane at Earth, and from dusk to dawn at Jupiter, the difference in sense being due to the planets' opposite dipole polarities. The electric field produced by corotation is radially inwards at Earth and radially outwards at Jupiter, and is given by  $\mathbf{E} = -(\boldsymbol{\omega}_p \times \mathbf{r}) \times \mathbf{B}$ , where  $\boldsymbol{\omega}_p$  is the planet's angular velocity of rotation (and thus also that of the plasma if it near-rigidly corotates) and  $\mathbf{r}$  is the radial distance from the origin. A method of estimating which of these electric fields (and therefore flow mechanisms) is dominant involves calculating the position of the *stagnation point* in the magnetospheric flow, and comparing it to the size of the magnetosphere itself (see e.g. Eq. (2.1)). The combined flow in the equatorial plane is shown schematically by the dashed lines in Fig. 1.5. The stagnation point is the position where the two flows superimpose to produce zero net velocity and is taken to mark the boundary between the inner corotation dominated region and the outer solar wind driven region. It will occur (assuming the planet has a prograde rotation sense) on the dusk side, at a distance estimated by

$$\left( \frac{R_{sp}}{R_p} \right) = \left( \frac{\omega_p B_{eq} R_p}{E_o} \right)^{1/2}, \quad (1.6)$$

where  $B_{eq}$  is the planet's equatorial surface magnetic field strength,  $R_p$  is the radius of the planet, and  $E_o$  is the (assumed constant) magnitude of the dawn-dusk electric field in the equatorial plane associated with the Dungey cycle. The streamline which passes through the stagnation point (shown by the thick dashed line in Fig. 1.5) is given by the locus of all the points which have the same potential as the stagnation point, and is found to have a sub-solar distance from the planet of  $R_{sp}/2$ . Applying values appropriate to the Earth, i.e.

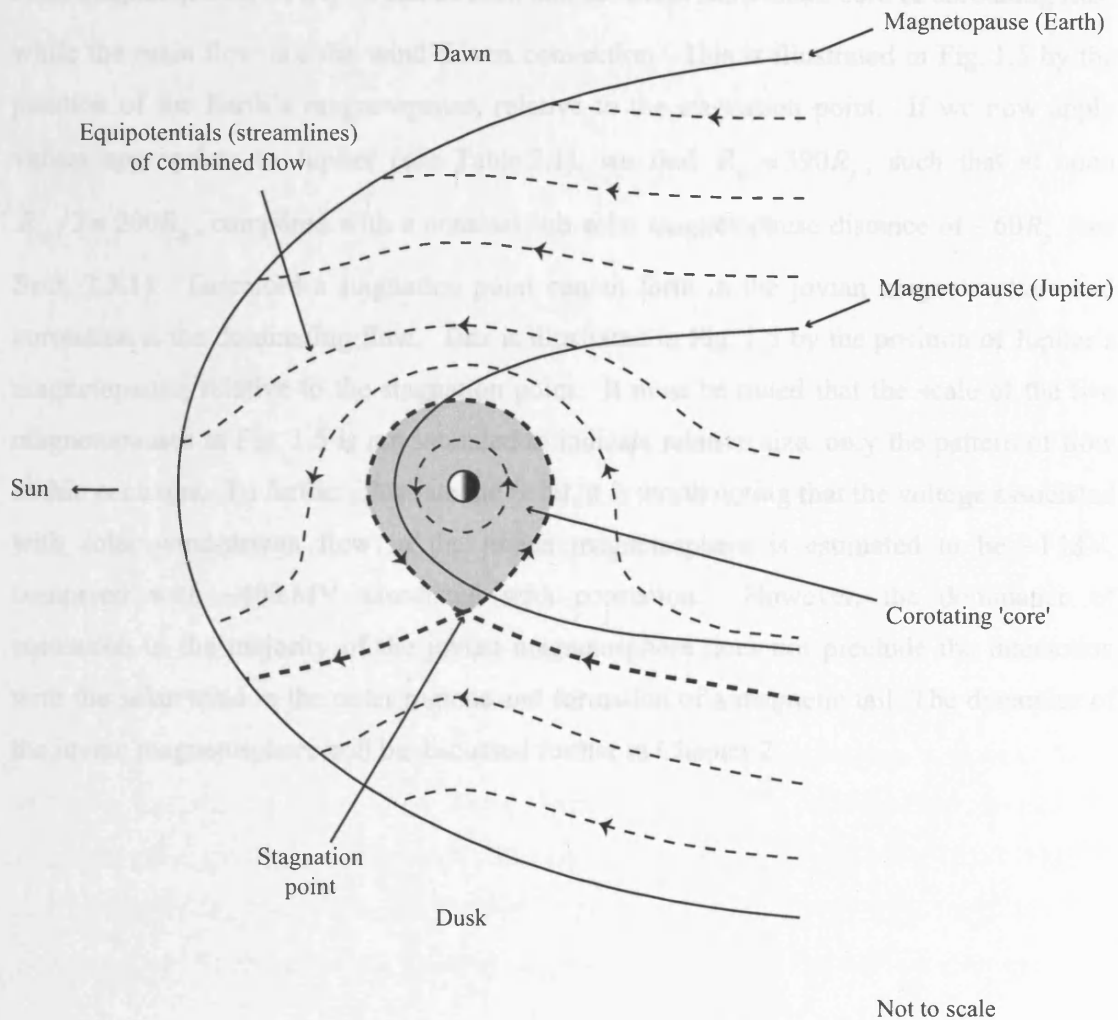


**Figure 1.5** Schematic of the combined flow in the equatorial plane resulting from the Dungey cycle and corotation. The view is from the North pole, with the Sun to the left. The dashed lines indicate equipotentials (streamlines) in the plasma, which is flowing in the direction of the arrows. The shaded area indicates the inner corotating region, while the rest is dominated by solar wind driven convection and the thick dashed line marks the separatrix, i.e. the streamline which passes through the stagnation point. The solid lines indicate magnetopauses appropriate to the jovian and terrestrial systems (labelled respectively), and indicate the pattern of flow within each. They are not intended to illustrate respective scales.

$\omega_p \approx 7 \times 10^{-5} \text{ rad s}^{-1}$ ,  $R_p \approx 6400 \text{ km}$ ,  $B_{eq} \approx 31,000 \text{ nT}$  and  $E_o \approx 2 \times 10^{-4} \text{ V m}^{-1}$ , we find that  $R_{sp} \approx 8.5R_p$ , such that at noon  $R_{sp}/2 \approx 4R_p$ . When compared with the distance to the sub-solar magnetopause,  $\sim 11R_p$ , it can be seen that the Earth has a small core of corotating flux, while the main flow is solar wind-driven convection. This is illustrated in Fig. 1.5 by the position of the Earth's magnetopause, relative to the stagnation point. If we now apply values appropriate to Jupiter (see Table 2.1), we find  $R_{sp} \approx 390R_p$ , such that at noon  $R_{sp}/2 \approx 200R_p$ , compared with a nominal sub-solar magnetopause distance of  $\sim 60R_p$  (see Sect. 2.3.1). Therefore a stagnation point cannot form in the jovian magnetosphere and corotation is the dominating flow. This is illustrated in Fig. 1.5 by the position of Jupiter's magnetopause, relative to the stagnation point. It must be noted that the scale of the two magnetopauses in Fig. 1.5 is not intended to indicate relative size, only the pattern of flow within each one. To further illustrate the point, it is worth noting that the voltage associated with solar wind-driven flow in the jovian magnetosphere is estimated to be  $\sim 1 \text{ MV}$ , compared with  $\sim 400 \text{ MV}$  associated with corotation. However, the dominance of corotation in the majority of the jovian magnetosphere does not preclude the interaction with the solar wind in the outer regions and formation of a magnetic tail. The dynamics of the jovian magnetosphere will be discussed further in Chapter 2.

## ***Chapter 2***

# ***The Structure and Dynamics of the Jovian Magnetosphere***

### ***2.1. Introduction***

In this chapter we now focus more closely on the jovian plasma environment, which is the principal topic of this thesis. Jupiter is the fifth planet from the Sun, and the largest. It is a gas giant with a diameter 11 times that of the Earth and a mass more than twice all the other planets combined. The main physical properties of Jupiter are summarised in Table 2.1, along with comparisons with the Earth. Jupiter's composition is roughly solar, i.e. it comprises mainly of hydrogen and helium. However despite its large size, Jupiter has a relatively fast rotation period of 9h 55min. This speedy rotation, combined with its metallic hydrogen core, generates a very large planetary magnetic field, which has a dipole moment of  $4.26 \times 10^4 \text{ T R}_J^{-3}$ , inclined at  $9.5^\circ$  from its spin axis towards system III longitude  $201^\circ$  (where system III longitude is a jovigraphic system defined with respect to the spin axis).

The large jovian magnetic field produces a magnetosphere, sketched in Fig. 2.1, that extends typically  $\sim 60 R_J$  on the dayside of the planet and stretches out in a very long magnetotail on the nightside. The jovian magnetotail has a length of at least  $3000 R_J$  (i.e. it stretches beyond the orbit of Saturn) and has a width of  $\sim 300 - 400 R_J$  (Ness et al., 1979c). Because the solar wind speed is supermagnetosonic in the rest frame of the planet a bow shock stands upstream of the dayside magnetopause, as at Earth, at a distance of  $\sim 75 R_J$ . The position of the magnetopause is again determined by pressure balance between the solar wind and magnetospheric plasma. The plasma in the jovian magnetosphere contains contributions of ionised hydrogen and helium and electrons from both the solar wind and the planet's ionosphere, but the dominant source of plasma is the moon Io, which orbits

Property	Value	Value normalised to the Earth
Mass	$1.9 \times 10^{27}$ kg	318
Radius $R_J$	71,323 km	11.2
Angular velocity $\Omega_J$	$1.76 \times 10^{-4}$ rad s <sup>-1</sup>	2.53
Surface equatorial field strength $B_J$	426400 nT	14.1
Mean density	$1.33 \times 10^3$ kg m <sup>-3</sup>	0.24
Mean distance from Sun	$7.78 \times 10^{11}$ m	5.2
Surface gravity	20.87 m s <sup>-2</sup>	2.12
Escape velocity at surface	$5.95 \times 10^4$ m s <sup>-1</sup>	5.33
Effective blackbody temperature	124.4 K	0.49

**Table 2.1** Some key properties of Jupiter and comparisons with the Earth.

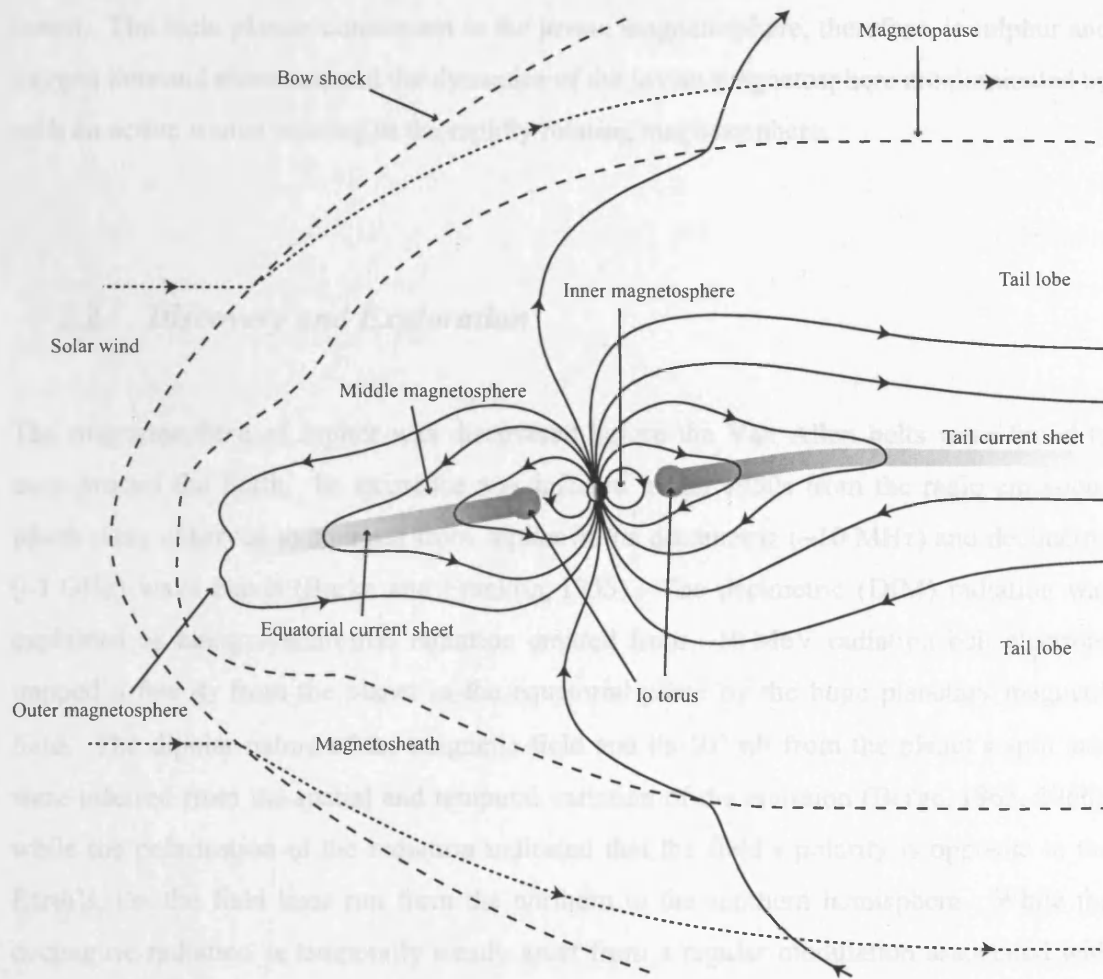


**Figure 2.1.** Sketch of the jovian magnetosphere in the noon-midnight meridian plane. The Sun is to the left and the solar wind is blowing from left to right. The solid lines are magnetic field lines, the dashed lines are the magnetopause and bow shock, and the dotted lines are solar wind streamlines. The middle magnetosphere / tail current sheet is shown by the shaded grey area.

deep within the magnetospheric cavity at  $5.9 R_J$ , where it liberates approximately 1 tonne of sulphur dioxide a second. This source rate is equivalent to the outgassing of an active comet. The main plasma constituent in the jovian magnetosphere, therefore, is sulphur and oxygen ions and electrons, and the dynamics of the jovian magnetosphere are dominated by such an active source existing in the rapidly rotating magnetosphere.

## ***2.2. Discovery and Exploration***

The magnetosphere of Jupiter was discovered before the Van Allen belts were found to exist around the Earth. Its existence was inferred in the 1950s from the radio emissions which were observed to emanate from Jupiter in the decametric ( $\sim 10$  MHz) and decimetric ( $\sim 1$  GHz) wave bands (Burke and Franklin, 1955). The decimetric (DIM) radiation was explained as being synchrotron radiation emitted from  $\sim 10$  MeV radiation belt electrons trapped a few  $R_J$  from the planet in the equatorial plane by the huge planetary magnetic field. The dipolar nature of the magnetic field and its  $10^\circ$  tilt from the planet's spin axis were inferred from the spatial and temporal variation of the emission (Berge, 1965, 1966), while the polarisation of the radiation indicated that the field's polarity is opposite to the Earth's, i.e. the field lines run from the northern to the southern hemisphere. While the decimetric radiation is temporally steady apart from a regular modulation associated with the planet's rotation (Sloanaker, 1959), the decametric (DAM) radiation is bursty, although on average is two orders of magnitude more powerful than the former. The decametric radiation is thought to be cyclotron radiation emitted by  $\sim 10$  keV electrons accelerated along the field lines into the ionosphere. The high frequency cut-off of 40 MHz for the DAM radiation then indicates a polar field strength of  $\sim 1.4 \times 10^{-3}$  T, which is approximately twenty times that of the Earth, and is remarkably large given that the jovian planetary radius is ten times the Earth's. The DAM emission bequeathed another clue as to the nature of the jovian magnetosphere when Bigg (1964) discovered that a component of this radiation was influenced by the position of the moon Io, thereby suggesting a complex interaction between moon and magnetosphere. In addition, Brown (1974), using ground-based optical observations, discovered a large cloud of neutral sodium atoms surrounding

the moon Io, and subsequent observations revealed the existence of a wider cloud, or torus, at the orbit of Io, which contained atoms and ions of sulphur and oxygen.

To date, seven spacecraft have visited the jovian system. The first to do so was Pioneer-10, which flew by in November-December 1973, and was followed shortly after by Pioneer-11 in 1974 (Smith et al., 1974, 1975, 1976). The year 1979 saw the Jupiter fly-bys of Voyagers-1 and -2 (Ness et al., 1979a,b), after which followed a gap of 13 years until the Ulysses spacecraft flew by in 1992 on its way to explore the Sun's polar regions (Balogh et al., 1992). The spacecraft Galileo was inserted into orbit in 1995, where it remained studying many aspects of the planet and its moons until the summer of 2003 when it reached the end of its working life and was de-orbited into Jupiter. The most recent Jupiter encounter at the time of writing was the Cassini millennium fly-by in December 2000 as the spacecraft was en route to the planet Saturn. Figure 2.2 shows the trajectories of the Voyager, Pioneer and Ulysses spacecraft projected onto the equatorial plane, together with the first twenty orbits of Galileo, and model magnetopause and bow shock locations based on Voyager data. As the figure indicates, all the flyby spacecraft explored the pre-noon sector on their inbound passes, and Pioneer-10 and both the Voyagers exited in the pre-dawn sector, all in the near-equatorial latitudes. In contrast, Pioneer-11 exited near noon at a northern latitude of  $\sim 33^\circ$ , and Ulysses' outbound pass took it via the dusk flank, approximately  $\sim 37^\circ$  to the south. As Galileo's mission proceeded into the Galileo Extended Mission (GEM) and the Galileo Millennium Mission (GMM), the spacecraft's orbit precessed around to cover more of the dusk region. However, at the end of the Galileo mission the spacecraft was collided with Jupiter to prevent any possible contamination of the Galilean moons, and the post-noon sector of the magnetosphere remains relatively unexplored. The Pioneer spacecraft were designed to measure the magnetic field of Jupiter and the energetic (above  $\sim 1$  MeV) particle environment (Goertz, 1976). The Voyager spacecraft had aboard instruments to measure, in addition, the full radio emission spectrum (Carr et al., 1983), the lower energy (10 - a few 100 eV and 10 - a few 100 keV) thermal plasmas (Belcher, 1983; Krimigis and Roelof, 1983), and plasma waves (Gurnett and Scarf, 1983). The Ulysses and Galileo spacecraft carried a similar set of instruments.

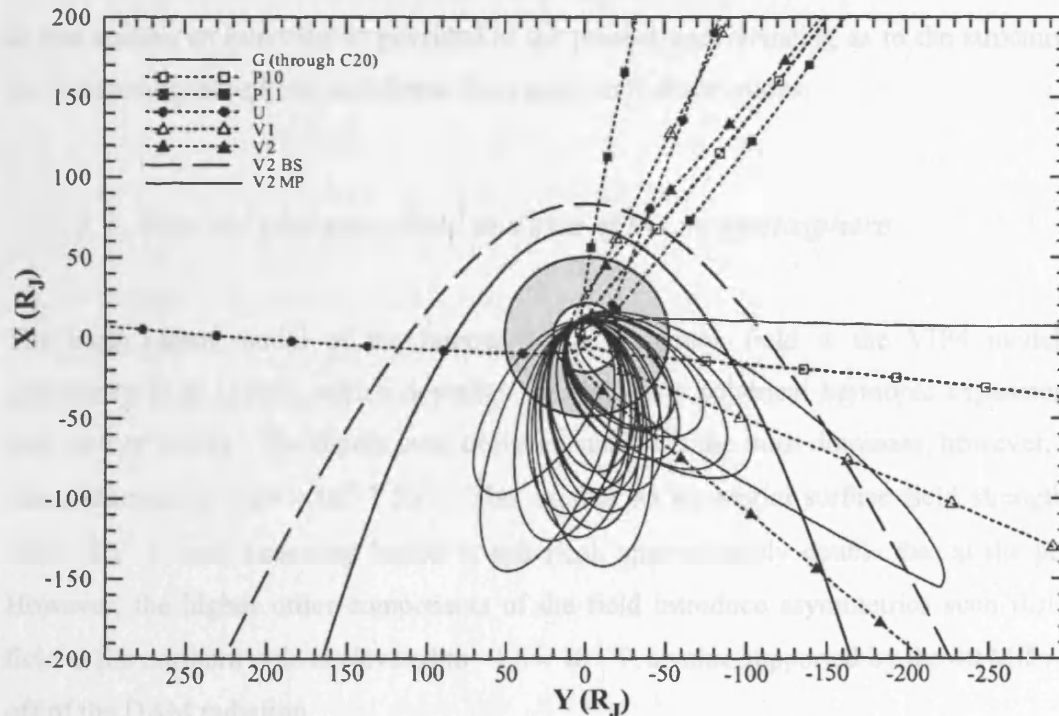


**Figure 2.2.** Trajectories of the first 20 orbits of the Galileo orbiter along with the five fly-by spacecraft relative to Jupiter, shown in Jupiter Solar Orbital coordinates. X points positive sunwards, and Y is orthogonal to X and in the plane of Jupiter's orbit. The solid line indicates the Galileo orbiter and the dashed lines indicate the fly-by spacecraft. The individual fly-by spacecraft are distinguished by the varying symbols shown in the key. A heavy dashed line depicts a model bow shock, while the heavy solid line shows the model magnetopause. Both model positions are derived from the Voyager-2 data. The region of 20-45  $R_J$ , which is the main region of the middle magnetosphere current sheet, is highlighted by the grey annulus in the centre of the plot. Taken from Bunce et al. (2002).

where  $B_0$  is the planet's equatorial average magnetic field strength,  $v$  is the solar wind bulk velocity,  $\rho$  is the solar wind mass density related to the number density  $n$  by  $\rho = (m_p + m_e)n$ , where  $m_p$  and  $m_e$  are the masses of protons and electrons respectively, and the result is normalized to the planet's radius  $R_p$ . For the V2 data

### 2.3. The structure of Jupiter's magnetic field

In this section an overview is provided of the present understanding as to the structure of the jovian magnetosphere, as inferred from spacecraft observations.

#### 2.3.1. Internal planetary field and size of the magnetosphere

The most recent model of the internal jovian magnetic field is the VIP4 model of Connerney et al. (1998), which describes the field as a spherical harmonic expansion to over twenty orders. The dipole term of the expansion is the most dominant, however, and has a moment of  $4.26 \times 10^4 \text{ T R}_J^{-3}$ . This implies an equatorial surface field strength of  $\sim 0.4 \times 10^{-3} \text{ T}$ , and, assuming Jupiter is spherical, approximately double that at the poles. However, the higher order components of the field introduce asymmetries such that the field at the northern pole is elevated to  $\sim 1.5 \times 10^{-3} \text{ T}$ , a value supported by the 40 MHz cut-off of the DAM radiation.

Given a planetary dipole moment, it is possible to make a rough estimation of the expected size of the magnetosphere by making a simple calculation based on pressure balance between the solar wind and magnetosphere. Neglecting magnetic pressure in the solar wind and gas pressure in the magnetosphere, we find that the distance to the subsolar magnetopause  $R_{mp}$  is given approximately by

$$\left( \frac{R_{mp}}{R_p} \right) = \left( \frac{B_{eq}^2}{\mu_0 \rho v^2} \right)^{1/6}, \quad (2.1)$$

where  $B_{eq}$  is the planet's equatorial surface magnetic field strength,  $v$  is the solar wind bulk velocity,  $\rho$  is the solar wind mass density related to the number density by  $\rho = n(m_e + m_p) \approx nm_p$ , where  $m_e$  and  $m_p$  are the masses of electrons and protons respectively, and the result is normalised to the planet's radius  $R_p$ . For the values

appropriate to Jupiter, as given in Table 1.2, Eq. (2.1) gives  $(R_{mp}/R_p) \approx 40$ . However, the fly-by data indicated typical sub-solar magnetopause distances of  $\sim 60 R_J$ , with variations between  $\sim 40$  and  $80 R_J$ . This inflated and ‘squashy’ magnetosphere is explained by the fact that the existence of a substantial plasma source in the jovian system (the Io torus) means that the magnetospheric plasma pressure makes a substantial contribution to the overall magnetospheric pressure and as such the assumption that it may be neglected is not strictly valid. The plasma pressure has the effect of distending the field lines outwards in the middle magnetosphere, such that the magnetic field pressure at the sub-solar magnetopause is greater than that given by a simple dipole (which is the assumption made in deriving Eq. (2.1)). The distension of the field lines is considered in more detail below.

### 2.3.2. Inner magnetosphere

A schematic of the jovian magnetosphere, as revealed by *in-situ* spacecraft observations, is shown in Fig. 2.1, which shows a cut through the noon-midnight meridian as seen from the dusk side (i.e. the Sun is to the left). Four different regions of the magnetosphere have been distinguished by the properties of the magnetic field in each (Smith et al., 1976). These are labelled in Fig. 2.1 and consist of the *inner magnetosphere*, the *middle magnetosphere*, the *outer magnetosphere* and the *magnetic tail*, and these will be discussed in turn.

The inner magnetosphere consists of the essentially undisturbed planetary field and extends to  $\sim 5 R_J$  in the equatorial plane. This is the region which holds the energetic electrons that emit the DIM radiation (Fillius, 1976). The inner magnetosphere is bound on the outside by the Io torus, which marks the beginning of the middle magnetosphere and the large azimuthal currents associated with it. Therefore the inner magnetosphere is affected by the fringing field of these azimuthal currents, which in this region produce an essentially northward field of strength  $\sim 200$  nT. However, their effect is not great as at  $5 R_J$  the equatorial planetary field is still  $\sim 3400$  nT.

### 2.3.3. Middle magnetosphere

The middle magnetosphere is the region which is central to this thesis. Its inner boundary is marked by the Io torus at  $\sim 5 R_J$  and beyond this lies a region of strong equatorial azimuthal current ( $\sim 200$  MA in total), which distends the magnetic field radially outwards in the manner shown in Fig. 2.1. This radial distension is characteristic of the middle magnetosphere, which extends to within  $\sim 15 R_J$  of the magnetopause on the dayside (such that for a nominal noon magnetopause distance of  $60 R_J$  the middle magnetosphere extends to  $45 R_J$  at noon, while extending to greater radial distances at other local times) and merges continuously with the magnetic tail on the nightside. The current sheet, which is approximately  $5 R_J$  in width, produces a perturbation field that falls off with radial distance as  $\sim \rho^{-1.5}$ , compared with the dipolar dependence of  $\rho^{-3}$ . Therefore the field is predominantly dipolar out to  $\sim 15 R_J$ , after which the current sheet perturbation becomes dominant and the field gains a strong radial component. Hence, the magnitude of north-south component of the magnetic field in the equatorial plane,  $|B_{ze}|$ , is lower than that of the planetary field alone, due to the stretched out nature of the field in this region. The magnetic field model used to represent the equatorial magnetic field in the middle magnetosphere is described in Chapter 3.

The current sheet is aligned with the magnetic equatorial plane within  $\sim 30 R_J$ , outside which two effects act to cause a departure of the sheet from the equatorial plane. The first is due to the propagation speed of information of the planet's rotation (effectively the Alfvén speed) being finite at  $\sim 40 R_J h^{-1}$ , leading to significant lags in the plane of the current sheet beyond  $\sim 30 R_J$ . Secondly, beyond  $\sim 35 R_J$  on the night side, the current sheet 'hinges' to become aligned with the tail axis, which is determined by the flow of the solar wind.

The current within the equatorial plasma sheet in the middle magnetosphere flows eastward and, to a first approximation, closes azimuthally, as illustrated in Fig. 2.3a. On the nightside this current merges continuously with the tail current associated with the Dungey cycle and which flows from dusk to dawn in the equatorial plane and closes around the magnetopause. The tail region is described in more detail below.

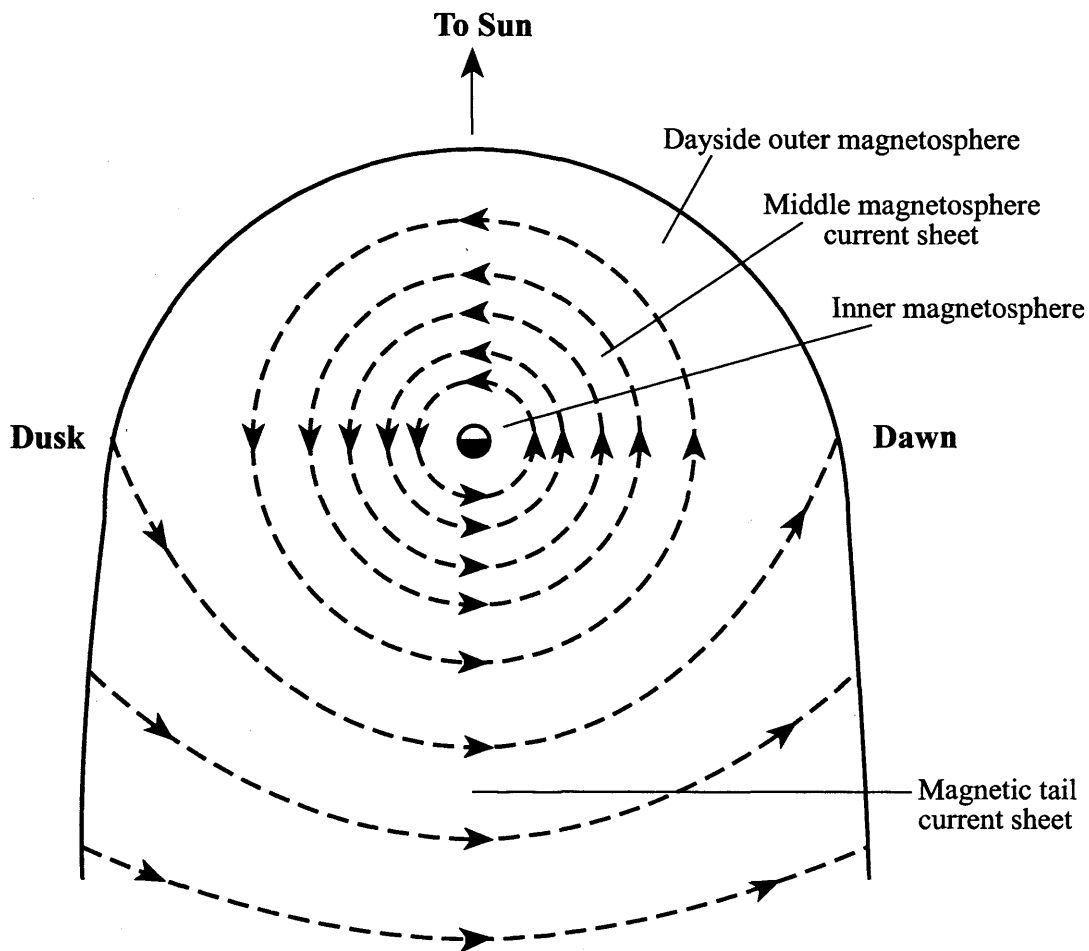


**Figure 2.3a.** Sketch of the current system in Jupiter's magnetic equatorial plane, showing the eastward-flowing current of the middle magnetosphere, which closes around the planet, and the dusk-dawn currents of the tail current sheet, which separates the tail lobes, and closes along the magnetopause. From Cowley and Bunce (2001b).

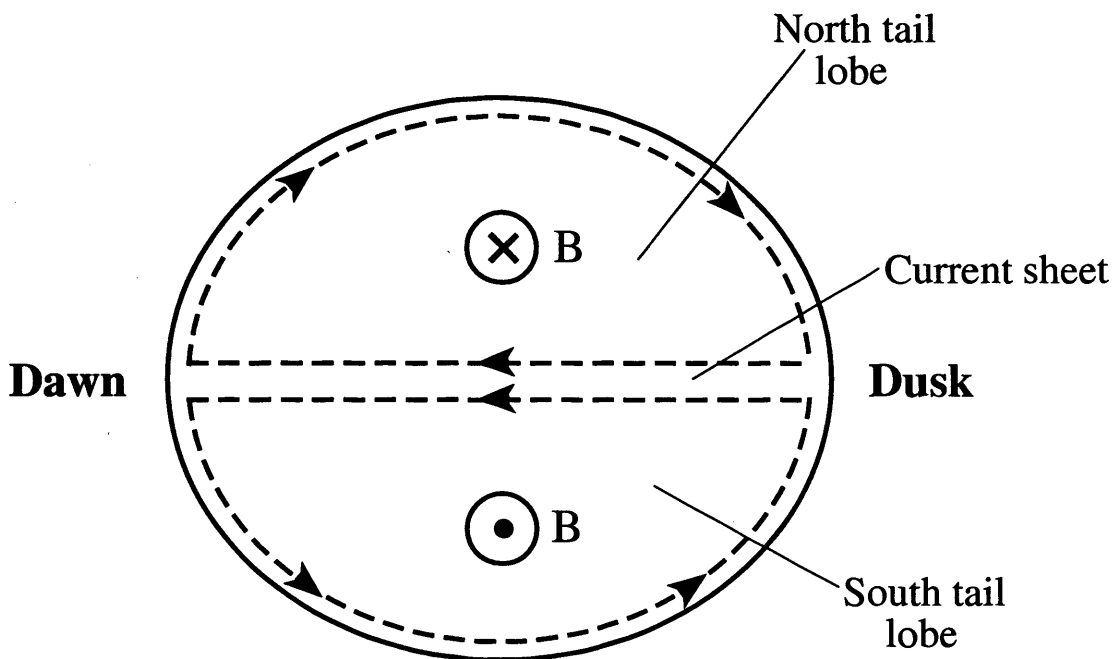


**Figure 2.3b.** Sketch of the field and current in a cross-section through the tail, looking away from the planet. The north tail lobe field points away from Jupiter (circled cross), while that of the southern lobe points towards the planet (circled dot). From Cowley and Bunce (2001b).

#### 2.3.4. Dayside outer magnetosphere

In the  $\sim 15 R_J$  between the dayside middle magnetosphere and the magnetopause lies the dayside outer magnetosphere. Here the field is somewhat disorganised but on average points to the south in the equatorial region, i.e. in the direction of the planetary field. The strength of the field, varying between  $\sim 5$  nT and  $\sim 15$  nT depending on the extension of the magnetosphere, is greater than that of the planetary dipole because of the fringing fields of the equatorial current sheet and the magnetopause. A feature which was particularly defined in the Ulysses inbound pass was the existence of a *transition region* between the middle and outer magnetosphere regions (Balogh et al., 1992; Bame et al., 1992). The equatorial field was characterised by sharp changes, indicating plasma current layers, although these were not ordered with magnetic latitude or longitude. Another feature evident in the data was ‘magnetic nulls’, which have been conjectured to be plasmoids ‘pinched off’ the middle magnetosphere plasma sheet (Belcher, 1983; Leamon et al., 1995; Southwood et al., 1995).

#### 2.3.5. Magnetic tail

As mentioned in Chapter 1, the existence of an extended magnetotail is taken to be indicative of dayside reconnection and production of open flux. The jovian magnetic tail is approximately cylindrical in shape, with a diameter of  $\sim 300 - 400 R_J$  and a length of at least  $3000 R_J$ , such that the existence of magnetopause reconnection is inferred (Ness et al., 1979c). It consists of two D-shaped tail lobes separated by an equatorial current sheet of a few  $R_J$  in thickness, which carries the dawn – dusk current associated with the Dungey cycle, which closes around the magnetopause. This is illustrated in Fig. 2.3b. The magnetic field in the tail is relatively uniform and strong, directed away from the planet in the northern lobe and towards the planet in the southern hemisphere. However, as the tail expands with increasing distance from the planet, the magnetic field falls. For example, Voyager-2 measured a field strength of  $\sim 2$  nT at a distance of  $\sim 150 R_J$  down the tail. It was pointed out by Scarf (1979) that the almost radial alignment of Jupiter and Saturn with respect to the Sun during the Voyager-2 encounter of Saturn allowed the possibility of Saturn being within Jupiter’s magnetic tail during this time. Indeed, Lepping et al. (1983)

presented evidence of the existence Jupiter's tail as far as  $9000 R_J$  downstream in the solar wind.

### *2.3.6. Field line bending*

The field lines of a dipole lie in meridional planes, i.e. lines of constant longitude with respect to the magnetic axis. The jovian field lines, however, are bent out of the meridians in the manner shown in Fig. 2.4, which is a sketch looking down on the north pole of the planet. The bending of field lines provides information as to the transfer of momentum by magnetic forces. For example, as discussed in Sect. 1.4.2, the two main sources of momentum in a magnetosphere are associated with the interaction with the solar wind and with the ionosphere. At Jupiter, the voltage associated with corotation is  $\sim 400$  MV, which is significantly greater than the  $\sim 1$  MV associated with the Dungey cycle and a stagnation point cannot form within the jovian magnetopause. Therefore, corotation is the dominant plasma flow within Jupiter's magnetosphere, as mentioned above. Having said this, the presence of a jovian magnetotail indicates dayside reconnection does occur at Jupiter, although this is confined to the outer regions of the magnetosphere. This situation is reflected in the bending of the field lines shown in Fig. 2.4. The field lines which thread through the equatorial plane in the outer regions, and which therefore map to high latitudes in the ionosphere, are bent away from noon due to the interaction with the solar wind. Lower latitude field lines, which map into the middle magnetosphere, are consistently bent into a lagging configuration at all local times due to the interaction with the ionosphere. This magnetosphere-ionosphere coupling, which is the main topic of this thesis, will be discussed in greater detail in Chapter 3. It can be seen that the field line bending associated with each mechanism is directed in the same sense on the dawn side, and is thus difficult to separate, while being in the opposite sense on the dusk side, where the two regions may be easily distinguished, such as in the Ulysses outbound pass observations (Dougherty et al., 1993).

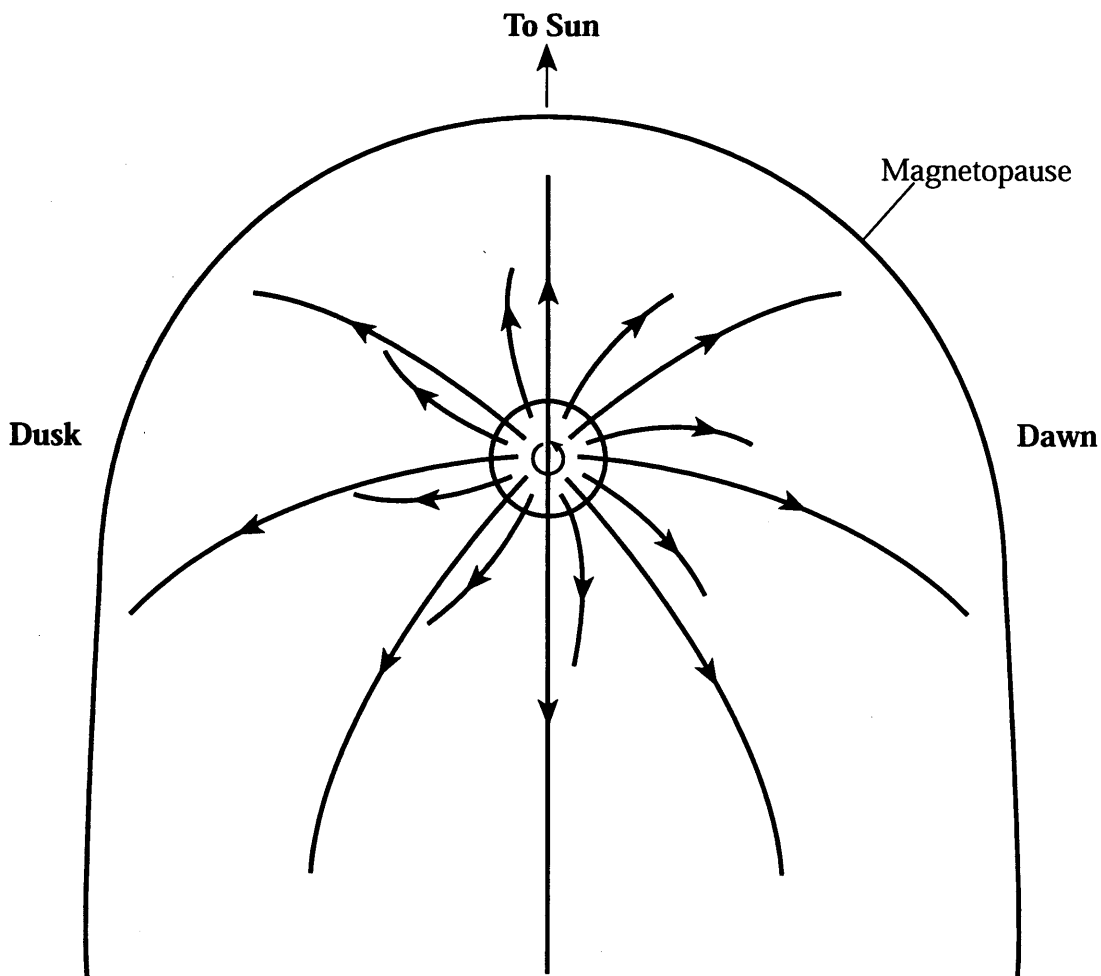


**Figure. 2.4** Sketch of field lines emanating from the northern hemisphere of Jupiter projected onto the equatorial plane, showing the bending of the field lines out of meridian planes. High-latitude field lines mapping to the outer parts of the magnetosphere are bent away from noon by the interaction with the solar wind. The current system responsible is the magnetopause-tail system. Lower-latitude field lines mapping to the middle magnetosphere current sheet are bent consistently in the clockwise sense, associated with the transfer of anticlockwise planetary angular momentum from the thermosphere/ionosphere to the magnetosphere. The current system responsible is the magnetosphere-ionosphere coupling circuit discussed in Chapter 3. From Cowley and Bunce (2001b).

## 2.4. Plasma populations in the jovian magnetosphere

### 2.4.1. Sources of plasma mass

The main sources of plasma mass in a magnetosphere are the planet's ionosphere, the solar wind, and the surfaces and atmospheres of any satellites that orbit within the magnetosphere. The dynamics of the magnetosphere are then dependent on the nature of these sources, and the nature of the processes which transfer the plasma from the sources to the sinks. Jupiter's magnetosphere contains contributions from all of these sources, to varying degrees. The solar wind and the ionosphere are both estimated to provide sources of a few  $\times 10^{28}$  ion  $s^{-1}$ , consisting of mainly hydrogen (i.e. protons and electrons in equal numbers, maintaining quasi-neutrality), such that they contribute mass sources of a few tens of  $kg s^{-1}$  (Hill et al., 1983). In addition to ionised atomic hydrogen, the ionosphere is also a minor source of molecular hydrogen ions,  $H_2^+$  and  $H_3^+$  (Hamilton et al., 1980), and the solar wind is a source of  $He^{2+}$  and traces of heavier elements such as carbon. However, these are not the major sources of plasma mass in the jovian magnetosphere. Rather, the major plasma mass component is sulphur and oxygen plasma originating from the volcanic moon Io, which orbits at a joviocentric distance of  $5.9 R_J$  (Belcher, 1983; Krimigis and Roelof, 1983). More specifically, the plasma originates principally from electron-impact ionisation of the clouds of sulphur and oxygen which surround the orbit of Io, originating from the moon's atmosphere. Estimates of the total plasma production rate within the torus lie typically within the range  $1000 - 3000 kg s^{-1}$  when both the local production near Io and the more distributed production in the co-orbiting gas clouds are included (e.g. Broadfoot et al., 1981; Brown, 1994; Bagenal, 1997; Delamere and Bagenal, 2003). In terms of ion number source rate, the production is comparable to the solar wind and the ionosphere. However, due to the fact that the mean mass of iogenic ions is  $\sim 21$  amu, compared with the  $\sim 1$  amu of hydrogen ions, the mass production rate from the Io torus is significantly greater. In addition to Io, the icy moon Europa at  $9.4 R_J$  is a source of oxygen plasma with a production rate of  $\sim 50 kg s^{-1}$  (Ip et al., 1998). However, this emission is significantly less than the former, and as such the Io torus is the dominant source of plasma mass in the jovian magnetosphere.

### 2.4.2. The Io plasma torus

The orbit of Jupiter's innermost Galilean satellite Io is enveloped in a cloud of sulphur and oxygen atoms liberated from its volcanoes as sulphur dioxide, as mentioned above. These neutral atoms, which peak in density at a few tens of  $\text{cm}^{-3}$  near the orbit of Io and fall off by roughly an order of magnitude within  $\sim 1 R_J$  on either side, orbit with a Keplerian velocity of  $\sim 17 \text{ km s}^{-1}$  (Schreier et al., 1998). As mentioned above, however, the plasma in this region roughly corotates with the planet, which at the orbit of Io implies a linear velocity of  $\sim 72 \text{ km s}^{-1}$ . The atoms in the neutral cloud are subject to electron-impact ionisation from the warm electrons in this region (see below) at a rate which is estimated to produce 1000 – 3000 kg of ions per second. As well as feeling the force of gravitation, the newly ionised particles suddenly sense the electromagnetic environment, i.e. the  $\sim 2000 \text{ nT}$  southward planetary magnetic field and the  $\sim 0.1 \text{ V m}^{-1}$  outward radial electric field associated with corotation. Hence, the new ions are suddenly accelerated to corotation velocity, and gyrate around the field lines with a speed equal to the difference between the corotation and Keplerian velocities. This energising process results in a 'warm' population with thermal energies of  $\sim 250 \text{ eV}$  for oxygen,  $\sim 500 \text{ eV}$  for sulphur and  $\sim 0.01 \text{ eV}$  for electrons. The warm ions are cooled by Coulomb collisions with electrons, which are in turn cooled by collisional excitation of the lower energy levels of the ions. The resulting photon emissions are those responsible for the optical observations of the torus.

The low energy torus plasma populations as observed by the Voyager spacecraft are described by Bagenal (1994), and the main points are summarised here. Figure 2.5 shows contours of electron density (equal to the ion charge density under quasi-neutral conditions) derived from Voyager-1 data. Two major populations may be distinguished in this plot: the warm torus and the cold torus. The most significant of these is the warm torus, which consists of the newly ionised suprathermal population ( $\sim 10\text{-}20\%$  of the total population in this region), and the associated Coulomb cooled ions mentioned above. At  $\sim 5.6 R_J$ , the inner edge of the warm torus, the warm ions and cool ions have energies of a few  $100 \text{ eV}$  and  $\sim 60 \text{ eV}$  respectively, these values increasing to  $\sim 2 \text{ keV}$  and  $\sim 300 \text{ eV}$  at  $10 R_J$ . The energy of the electrons throughout the warm torus is  $\sim 10 \text{ eV}$  (the higher electron temperatures resulting from Coulomb collisions with the warm ions), which corresponds to a velocity of  $\sim 1600 \text{ km s}^{-1}$ , hence explaining the large impact ionisation rate. Within

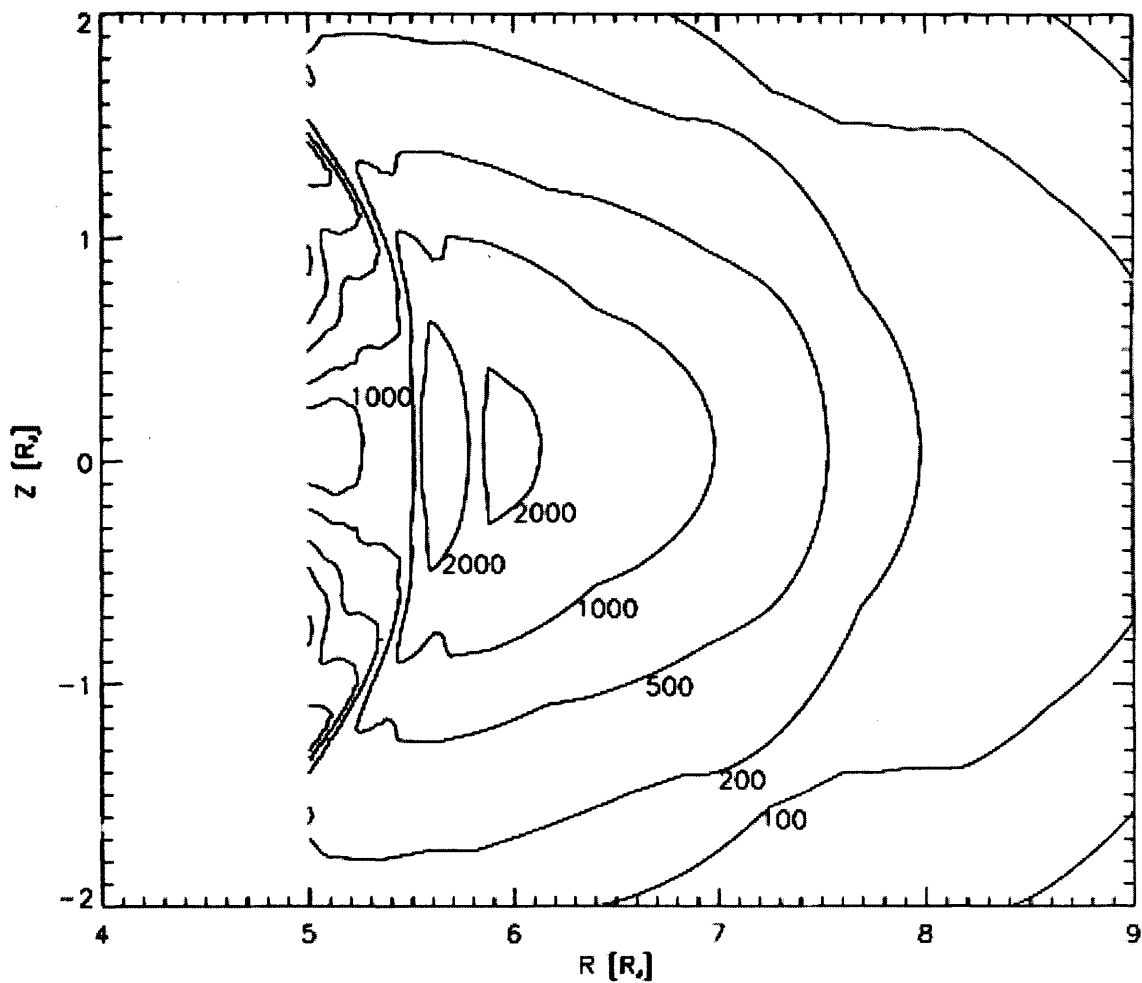


**Figure 2.5.** Contours of the electron density in the Io plasma torus in the meridian plane, determined from Voyager 1 PLS data. The vertical scale is distance from the centrifugal equator, while the horizontal axis is distance from Jupiter's spin axis, both in units of  $R_J$ . The numbers on the contours refer to electron density, equal to the ion charge density, in units of electrons  $\text{cm}^{-3}$ . Taken from Bagenal et al. (1997).

$\sim 7.5 R_J$  the ion population of the warm torus is divided equally between sulphur and oxygen; specifically  $O^+$ , and  $S^+$  and  $S^{2+}$  in approximately equal quantities. Beyond this distance the  $S^{3+}$  density increases to become comparable to those of the other sulphur ions, and the density of  $O^+$  and  $O^{2+}$  increases, possibly due to the Europa source. The second plasma population is the cold torus, which exists at radial distances inside  $\sim 5.6 R_J$ , close to the equatorial plane. In this region the ion population consists of slightly more  $S^+$  than  $O^+$ , with energies of just a few eV.

The data source for Fig. 2.5 was Voyager-1, which, of course, provided observations along the path of the spacecraft only. The two dimensional contours in Fig. 2.5 were derived by considering force balance on the plasma along the field lines. The forces acting are the plasma pressure force, the magnetic mirror force, the centrifugal force, the gravitational force, and a field-aligned electric force required to maintain quasi-neutrality at all locations. The most significant effect is that the plasma is confined to the equatorial plane by the centrifugal force, but this compression is balanced by the plasma pressure force. As such, the warm torus has a density scale height from the equatorial plane of  $\sim 1 R_J$ , while the scale height for the cold torus is only  $\sim 0.3 R_J$  due to the low temperature.

The centrifugal action on the plasma is the dominant radial force. Therefore flux tubes which have been newly loaded with iogenic plasma become centrifugally unstable and diffuse radially away from the planet, although at the feet of the field lines in the ionosphere this movement is resisted by ion-neutral collisions. The outwardly moving flux tubes are then replaced by low-density inwardly-moving flux tubes in a process known as flux tube interchange. Magnetic anomalies in the near-torus region are taken to be indicative of such interchange motions (Kivelson et al., 1997; Thorne et al., 1997). The exact mechanism by which plasma is removed from flux tubes at large distances is, at present, unknown, but it is conjectured to involve the 'pinching off' of plasmoids from the corotating flow on the dayside and in the dusk flank. This process, known as the Vasyliunas-cycle, is described in more detail below, and may be the explanation for sporadic enhancements of cool plasma in the outer magnetosphere, correlated with magnetic nulls (Southwood et al., 1993). This picture of rapid outward transport explains the cross-field structure of the warm plasma torus. The cold plasma torus structure is

explained by a weak inward diffusion, possibly powered by ionospheric interaction with neutral atmosphere wind systems, such that the plasma has time to cool radiatively, and collapse to the equator due to the reduced plasma pressure.

The middle magnetosphere current sheet is populated by warm plasma that has diffused out of the torus. However, due to the expansion of the flux tubes, the density decreases from its maximum of  $\sim 3000 \text{ cm}^{-3}$  at the inner edge of the Io torus to  $\sim 70 \text{ cm}^{-3}$  at  $\sim 10 R_J$  and further to  $\sim 0.1 \text{ cm}^{-3}$  at a few tens of  $R_J$  (Scudder et al., 1981). In addition, the average energy of the ions increases with distance, as the fraction of suprathermal particles increases.

### 2.4.3. *Hot plasma population*

The above discussion of flux tube interchange, whereby mass-loaded flux tubes diffuse outwards, while mass-reduced tubes move inwards to replace them implies a low-density plasma population exists, which is associated with the inward-moving flux tubes. This plasma would be heated as it is compressed during inward diffusion. Such a hot, low density population of protons and heavy (mainly sulphur and oxygen) ions in equal numbers has been observed by the Voyager (Mauk et al., 1996), Ulysses (Lanzerotti et al., 1993) and Galileo spacecraft (Mauk et al., 1999). The latter observed sporadic localised inward injections of this hot plasma in the current sheet between  $\sim 10$  and  $\sim 30 R_J$ , which have many features in common with substorms at the Earth, but are distributed uniformly in local time, rather than being confined to the nightside. This inward transport, and the associated heating and compression of the hot plasma is powered by the outward ‘falling’ of the warm torus plasma, and is a mechanism which acts to suppress the latter, albeit not very effectively.

According to the Voyager measurements, the density of the hot population is much lower than the warm torus plasma, being  $\sim 10^{-2} \text{ cm}^{-3}$  to  $\sim 10^{-3} \text{ cm}^{-3}$  in the outer magnetosphere, rising to  $\sim 1 \text{ cm}^{-3}$  at the inner edge of the warm torus, and decreasing within. The energy of the hot ions follows a similar trend, the average being a few tens of keV in the outer magnetosphere (with a non-Maxwellian high energy tail extending beyond a MeV), increasing to  $\sim 2 \text{ MeV}$  at  $\sim 7 R_J$ , and falling to  $\sim 100 \text{ keV}$  at the inner edge of the warm torus.

Electrons are also present with similar energies, but much lower densities. Despite the low density of the hot plasma, its high temperature means this population makes the dominant contribution to the plasma pressure within the magnetosphere (Caudal, 1986). The only exception to this is in the inner region of the warm torus, where the falling temperature of the hot plasma and the high density of the warm torus plasma mean the pressures of the two are comparable. It is this hot plasma, which diffuses inwards from the torus due to fluctuating electric fields caused by winds in the thermosphere, that constitutes the inner magnetosphere radiation belts.

The hot plasma population is the principal cause of the distension of the middle magnetosphere field lines. In this region the hot plasma has a plasma pressure comparable to that of the magnetic field, resulting in the inflation of the field lines into the current sheet configuration. The plasma pressure gradient is then balanced by the  $\mathbf{j} \times \mathbf{B}$  force associated with the azimuthal current sheet and the distended field lines. In actuality, this Lorentz force also balances the centrifugal force and the additional (albeit lesser) plasma pressure of the warm torus plasma, such that the hot plasma pressure gradient makes a  $\sim 2/3$  contribution to the inflation and the centrifugal force and warm plasma pressure make the other  $\sim 1/3$ . The hot plasma pressure is greater than the field pressure outside  $\sim 10 R_J$ , inside which the rapidly increasing planetary field strength means the magnetic field pressure assumes dominance, and the field becomes more dipolar.

#### 2.4.4. *Equatorial plasma flow*

Observational information of plasma angular velocity in the equatorial plane is relatively sparse. However, thermal plasma observations during the pre-noon inbound passes of Voyagers-1 and -2 indicate near rigid corotation in the inner part of the magnetosphere (except locally near Io's orbit), with  $\omega/\Omega_J \approx 0.8$  between 10 and 20  $R_J$ , falling to  $\sim 0.5$  at  $\sim 40 R_J$  (Belcher, 1983; Sands and McNutt, 1988). At larger distances of  $\sim 30$ -50  $R_J$  on the Voyager-2 inbound pass, values of  $\omega/\Omega_J \approx 0.5$ -0.6 have also been derived from energetic ion anisotropies (Kane et al., 1995). Similarly, at  $\sim 50$ -70  $R_J$  on the pre-noon inbound Ulysses pass, values of  $\omega/\Omega_J \approx 0.2$  have been reported from thermal electron and energetic

ion data (Phillips et al., 1993; Laxton et al., 1997). On the post-midnight outbound pass of Voyager-2 Kane et al. (1995) report values of  $\omega/\Omega_j \approx 0.5$  at  $\sim 70 R_J$ , falling to  $\sim 0.3$  at  $\sim 120 R_J$ .

The steady state equatorial plasma flow, as envisaged by Cowley et al. (2003b), is illustrated in Fig. 2.6, which is a sketch looking from the north, with the Sun to the bottom. The flow can be considered as comprising three separate regions. In the inner region, the streamlines close azimuthally around the planet, although the confining effect of the solar wind results in a day-night asymmetry in which the corotating region extends further from the planet on the night side. In addition, the dawn to dusk electric field associated with solar wind interaction will also result in a shift of these streamlines towards dawn (Goertz and Ip, 1984), however this is not shown in the figure. Also not shown is the outward-diffusing motion of the warm torus plasma discussed above. This outward motion results in the angular velocity of the plasma falling with increasing distance, due to conservation of its angular momentum, accounting for the observations outlined above. However, this effect is resisted by ion-neutral collisions in the Pedersen layer of Jupiter's ionosphere, and a current system is set up which acts to speed the equatorial plasma back up to corotation with the planet. This magnetosphere-ionosphere coupling current system will be discussed in detail in Chapter 3. In Fig. 2.6 this sub-corotating region is labelled the 'Hill region' after T.W. Hill, who first calculated the steady state angular velocity profiles for the case of a dipole field (Hill, 1979). The Hill region comprises the main part of the middle magnetosphere.

The area surrounding the Hill region is associated with the loss of the iogenic plasma from the middle magnetosphere. The mechanism illustrated in Fig. 2.6 was first discussed by Vasyliunas (1983) and is known as the Vasyliunas-cycle. This process as illustrated by Vasyliunas (1983) is shown in Fig. 2.7. In the steady state process, outer corotating plasma, which is confined on the dayside by the solar wind, expands as it rotates round to dusk, and then pinches off via magnetic reconnection. This region of reconnection is shown in Fig. 2.6 by the long-dashed line labelled as the 'Vasyliunas-cycle tail X-line', due to the X-like shape of the field around the null point (see right hand side of Fig. 2.7), and in the left hand side of Fig. 2.7 by the line of Xs. The resulting mass-loaded plasmoid then moves off down the tail along the streamline called the 'O-type line', again due to the shape

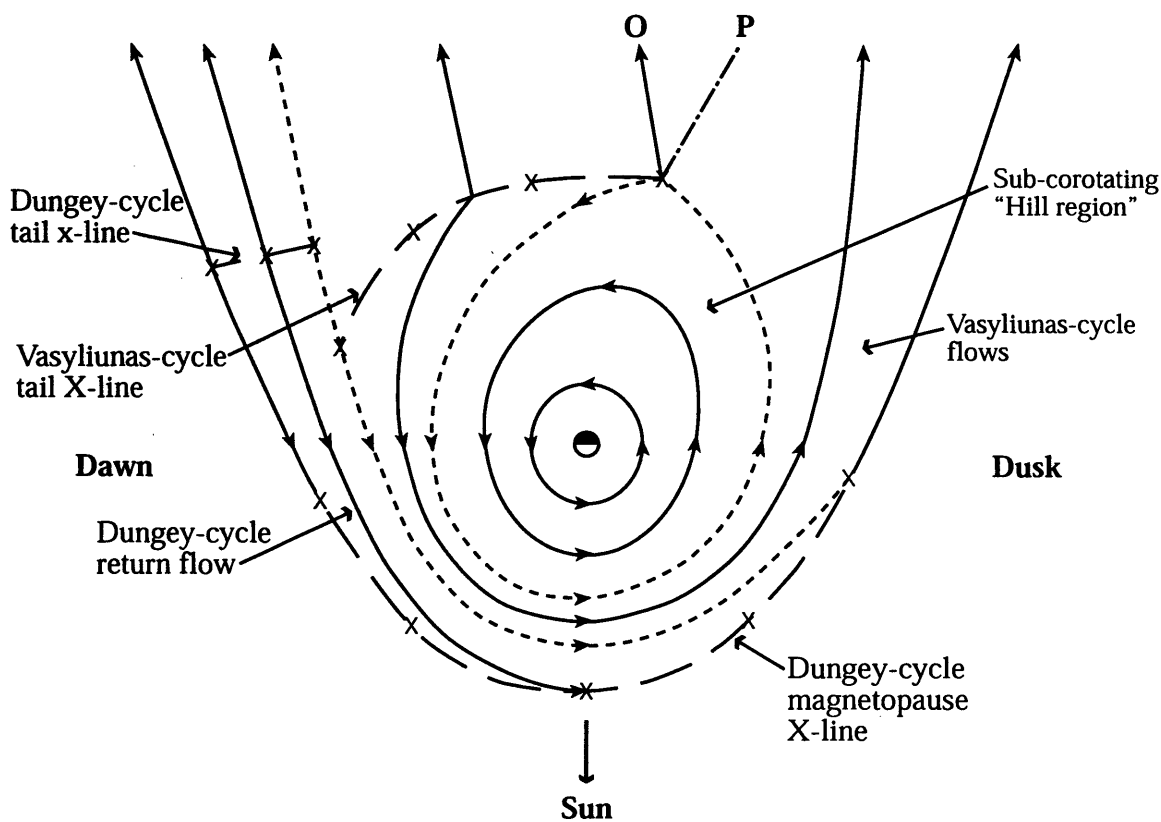


**Figure 2.6.** A sketch of the equatorial plasma flow in Jupiter's magnetosphere. The view is from the north, with the Sun to the bottom. The solid lines indicate plasma streamlines, and the short-dashed lines represent those streamlines which are separatrices between regimes of flow. The direction of flow is indicated by the arrows. The long-dashed lines with Xs represent regions of reconnection, associated with the Dungey-cycle or Vasyliunas-cycle as labelled. The lines labelled 'O' and 'P' indicate the paths of the centres and edges of Vasyliunas-cycle plasmoids, respectively. From Cowley et al. (2003).

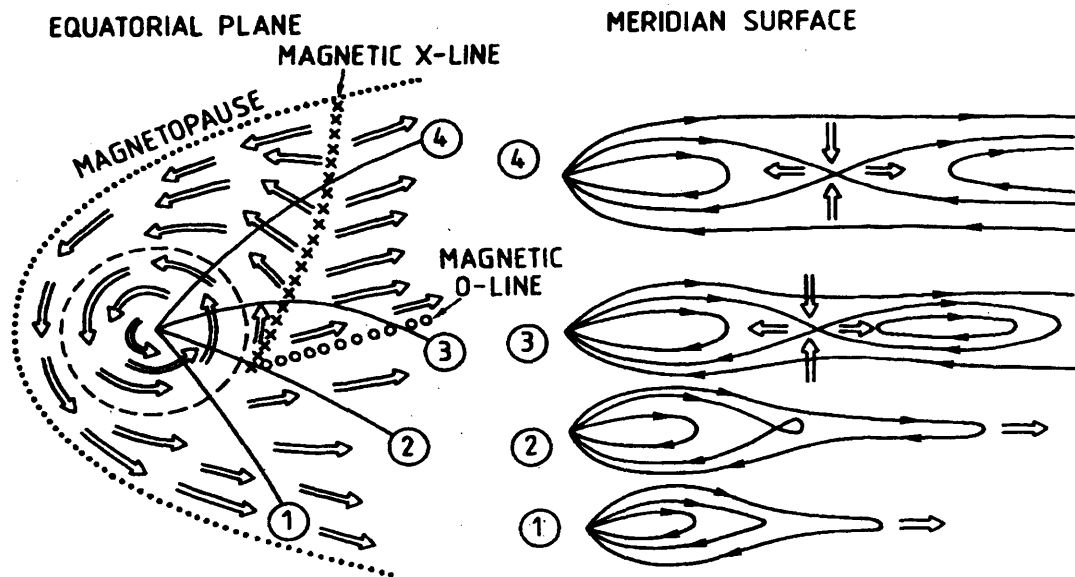


**Figure 2.7.** A qualitative sketch of plasma flow in the equatorial plane (left) and of the associated magnetic field and plasma flow in a sequence of meridian surfaces (right) as envisaged by Vasyliunas (1983). The arrows represent plasma flow and the Xs and Os represent the magnetic X- and O-lines as described in the text. From Vasyliunas (1983).

of the field surrounding the central null point, and is labelled with an 'O' in Fig. 2.6 and a line of Os in Fig. 2.7. The outer edge of the plasmoid follows the dot-dashed line marked by the 'P', which eventually meets the magnetopause at some distance down the tail. However, despite this steady-state picture, observations by Woch et al. (2002) indicate that the process may have significant time-dependency. It is anticipated that the flow in the dawn sector, sunward of the Vasyliunas-cycle tail X-line, will be faster than the inner corotating regions, due to the recent loss of mass from the field lines due to this process.

The third regime of flow is associated with the solar wind interaction, i.e. the Dungey-cycle. Reconnection occurs at the dayside magnetopause, along the long-dashed line labelled 'Dungey-cycle magnetopause X-line', under conditions of northward-directed IMF. The open field lines are then transported anti-sunward by the drag of the solar wind. Unlike the Earth, however, a significant proportion of the nightside current sheet is taken up with the Vasyliunas-cycle, such that the Dungey-cycle tail reconnection can only occur in the dawn sector, in the region labelled in Fig. 2.6 as 'Dungey-cycle tail X-line'. The newly-closed field lines then flow back sunward on the dawn flank until they reconnect again at the dayside X-line. This region of return flow, containing low plasma density, is associated with the outer magnetosphere region (Phillips et al., 1993), and the plasma pinched off in the nightside reconnection flows away from planet, along with that from Vasyliunas-cycle, in an anti-sunward 'magnetospheric wind' (Krimigis et al., 1981).

## **2.5. Jovian aurorae**

Planetary aurorae provide a means of remote sensing the dynamics occurring within a magnetosphere. The definition of aurora given by Chamberlain and Hunten (1987) is light emitted by the impact of any external energetic particles with a planet's atmosphere. Thus, for example, a region of strong upward-directed field-aligned current above a planet's ionosphere (e.g. that associated with magnetosphere-ionosphere coupling), corresponding to a large downward flux of electrons, may produce an aurora in that region. The aurorae illuminating the jovian ionosphere are the brightest in the solar system, up to a hundred times brighter than the Earth's. They were first observed directly in 1979 at UV

wavelengths by Voyager-1 (Broadfoot et al., 1979), and shortly afterwards in IR and UV by Clarke et al. (1980) using the IUE telescope in Earth orbit. Today, high resolution images from various sources are available, for example, ground-based IR telescopes (e.g. Satoh et al., 1996; Connerney et al., 1998), UV images from the Hubble Space Telescope (e.g. Clarke et al., 1998; Prangé et al., 1998) and visible wavelength images from Galileo (Ingersoll et al., 1998; Vasavada et al., 1999). An example of a UV image of Jupiter's aurora, taken in November 1998 using HST's Space Telescope Imaging Spectrograph (STIS) is shown in Fig. 2.8. Three components of emission are distinguished, as labelled. With increasing latitude these are: the 'footprints' and 'wakes' associated with the moons Europa, Ganymede and, most significantly, Io; the narrow but very intense 'main auroral oval'; and diffuse and variable polar emissions. These will be discussed in turn.

Of the aurorae linked with the magnetic footprints of the inner three Galilean moons, by far the brightest is that associated with Io. The aurora takes the form of a bright ( $\sim 1$  MR) auroral spot which is situated at the feet of the flux tube that connects to Io, followed by a 'wake', which gradually fades over an azimuthal distance of up to  $180^\circ$  downstream of the moon. It was originally thought that the auroral footprint was due to the relative motion of Io with respect to the corotational magnetic field, thus inducing a potential difference of  $\sim 500$  kV across the diameter of Io (Goldreich and Lynden-Bell, 1969), and driving field-aligned currents along the Io flux tube. However, this 'unipolar inductor' model does not explain the existence of the auroral wake. Recent theoretical ideas associate the auroral footprint and the wake with the local slowing of the equatorial plasma in the region where new plasma is being picked up by the corotational flow (Hill and Vasylunas, 2002; Delamere et al., 2003).

The second component of the aurora is the main auroral oval, which is a spatially and temporally stable auroral ring of width  $\sim 500$  km (corresponding to  $\sim 0.5^\circ$  of latitude), centred on  $\sim 15^\circ$  co-latitude. The features in the auroral oval are observed to corotate with System III longitude, suggesting a controlling process associated with the planetary magnetic field. The main auroral oval is the most significant auroral feature in terms of energy emission, with intensity exceeding  $\sim 100$  kR and in some cases peaking at a few MR at the visible and UV wavelengths (Ballester et al., 1996; Prangé et al., 1998; Vasavada et al., 1999), which, assuming a 20% conversion efficiency, implies precipitating particle

energy inputs from a few tens to a few hundred  $mW m^{-2}$ . Recent magnetic mapping studies have consistently shown that the main oval encompasses gap to the middle magnetosphere at

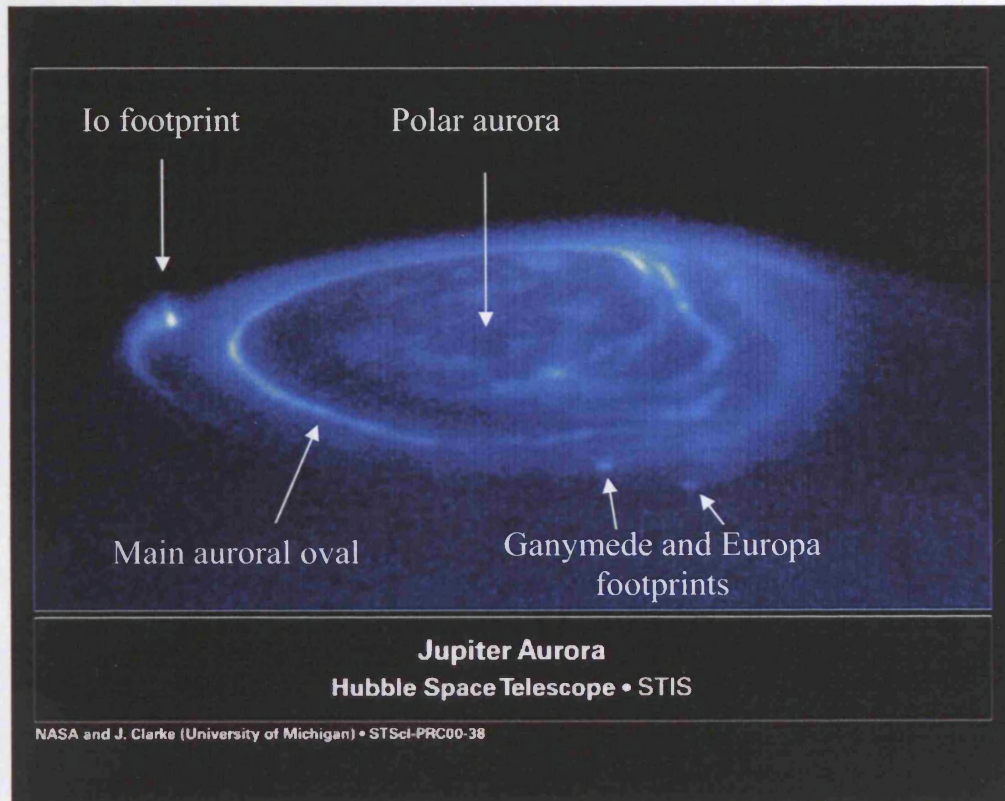


**Figure 2.8.** HST STIS image of Jupiter's northern UV aurora, taken in November 1998. The three main components of the aurora are labelled, i.e. the satellite footprints, the main oval and the polar emissions. The colour scale is logarithmic, to enhance fainter emissions next to bright ones. Dusk is to the right, dawn to the left, and sunwards (or more accurately Earthwards) is out of the plane of the photo. Taken from Clarke et al. (2004).

additional 'active region' towards noon. Crowley et al. (2005b) have interpreted the polar aurora by considering the equatorial flow shown in Fig. 2.6. A weak, but fast, poleward flow is associated with the dawn side and the fast, mass-reduced flux tubes on the dusk side. The fast, poleward upward-directed field aligned currents will be stronger on the dusk side (corresponding to the 'bright' area of the auroral Yin-Yang structure) and weaker, perhaps even reversed, on the dawn side. At the highest latitudes one has the region associated with the 'Dungey-cycle' and open field lines, where the flow is expected to be anti-sunward and slow, at  $\sim 10^4$  m/s or less. This region is skewed to the dawn side by the perturbation of the Vasyliunas-

energy inputs from a few tens to a few hundred  $\text{mW m}^{-2}$ . Recent magnetic mapping studies have consistently shown that the main oval emissions map to the middle magnetosphere at distances of a few tens of  $R_J$  (Clarke et al., 1998; Prange et al., 1998) and thus the main oval has been associated with the magnetosphere-ionosphere coupling current system driven by the breakdown of corotation of iogenic plasma in this region (Bunce and Cowley, 2001; Hill, 2001; Khurana, 2001; Southwood and Kivelson, 2001). The work presented in this thesis provides a detailed theoretical investigation as to the effect of model input parameters on this current system.

The third auroral component is the high latitude diffuse emission, also called the polar cap emission, although this is not necessarily to be confused with the Earth's polar cap, which is defined as the region in the ionosphere threaded by open field lines. Polar emissions at Jupiter simply means anything poleward of the main auroral oval. These aurorae are therefore magnetically linked to the outer magnetosphere and solar wind. The polar aurora are highly variable, exhibiting transient features, such as 'flares', which are bright (up to  $\sim 10$  MR) spots that appear over timescales of tens of seconds and decay within few minutes. The overall structure of the polar aurora, however, seems to be a 'Yin-Yang' shape of bright emission on the dusk side and a dark region on the dawn side, with an additional 'active region' towards noon. Cowley et al. (2003b) have interpreted the polar aurora by considering the equatorial flow shown in Fig. 2.6. A sketch of the flow pattern shown in Fig. 2.6, mapped along the magnetic field lines into the northern ionosphere is shown in Fig. 2.9. The format of the figure is similar to that of Fig. 2.6, the differences being the inclusion of regions of field-aligned current and the hatched area of open field lines. The outer part of the diagram represents the sub-corotational 'Hill region', and the upward-directed field-aligned current associated with it. This is the current linked to the main auroral oval, and will be discussed in Chapter 3. Poleward of the main oval lie the two regions associated with the Vasyliunas cycle; the slow, mass loaded flux tubes on the dusk side and the fast, mass-reduced flux tubes on the dawn side. The corresponding upward-directed field aligned currents will be stronger on the dusk side (corresponding to the 'bright' area of the auroral Yin-Yang structure) and weaker, perhaps even reversed, on the dawn side. At the highest latitude one has the region associated with the Dungey-cycle and open field lines, where the flow is expected to be anti-sunward and slow at  $\sim 100 \text{ m s}^{-1}$  or less. This region is skewed to the dawn side by the predominance of the Vasyliunas-

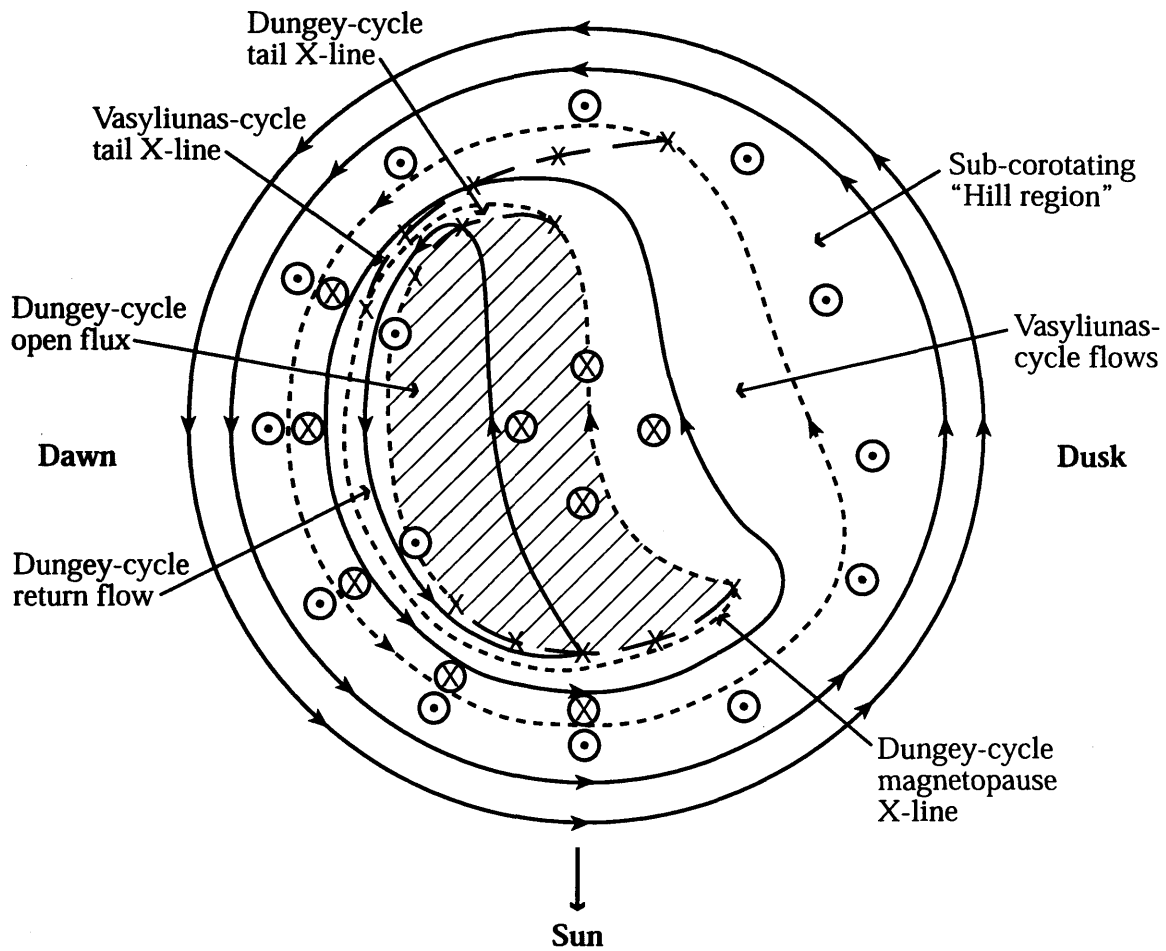


**Figure 2.9.** A sketch of the plasma flow in Jupiter's northern ionosphere, in a similar format to Fig. 2.6, where the Sun is to the bottom. The hatched region indicates open field lines. The dotted circles represent regions of upward field-aligned current and crossed circles represent regions of downward current. From Cowley et al. (2003).

cycle on the dusk flank, and is associated with the aurorally 'dark' region of the Yin-Yang structure. Finally one has the active region associated with the Dungey-cycle magnetopause X-line, where reconnection of the jovian field with the IMF represents the 'starting point' of the Dungey cycle, in a process corresponding with flux transfer events at the Earth.

In summary, therefore, the magnetosphere of Jupiter is a complex and dynamic entity, very different to the Earth's plasma environment. However, many important clues as to the nature of the processes occurring within may be obtained from the planet's aurorae. A particularly striking example is the main auroral oval, which is directly related to the dynamics of middle magnetosphere current sheet plasma and the interaction of this material with the planet. It is to this magnetosphere-ionosphere coupling system which we now turn in Chapter 3.

## ***Chapter 3***

# ***Magnetosphere – Ionosphere Coupling in Jupiter’s Middle Magnetosphere***

### ***3.1. Introduction***

The purpose of this chapter is two-fold. First, it will provide an introduction to the basic theory on which the analysis presented in later chapters is based, and second it will review the history of theoretical ideas concerning magnetosphere-ionosphere coupling at Jupiter.

Interest in the magnetosphere-ionosphere coupling currents that flow in Jupiter’s middle magnetosphere has been enhanced considerably in recent years by the suggestion by a number of authors that they are directly associated with the jovian ‘main oval’ aurorae described in Chapter 2 (Cowley and Bunce, 2001b; Hill, 2001; Khurana, 2001; Southwood and Kivelson, 2001). The implication follows that the dynamics of this region may be sensed remotely by ground- and space-based auroral observations covering a wide range of wavelengths (e.g. Satoh et al., 1996; Clarke et al., 1998; Prangé et al., 1998; Vasavada et al., 1999; Pallier and Prangé, 2001; Grodent et al., 2003). However, since Jupiter’s aurora was first observed by the Voyager spacecraft, a number of different hypotheses for the formation of the main auroral oval have been mooted. Thorne (1983) discussed wave-driven pitch angle diffusion of hot magnetospheric plasma as a mechanism by which the main oval could be produced. However, although wave amplitudes may be high enough in the jovian magnetosphere to maintain pitch angle diffusion near the strong diffusion rate, hence producing a full loss cone, estimates of the resulting energy flux of precipitating particles are found typically to be  $\sim 0.1\text{-}1 \text{ mW m}^{-2}$ , thus falling short of those required to produce main oval emissions by two to three orders of magnitude. This was confirmed by

Tsurutani et al. (1997), who examined Ulysses data and found that the energy fluxes due to wave-driven diffusion are too low to power the main auroral oval by orders of magnitude.

A suggestion that the jovian aurorae are linked to magnetosphere-ionosphere coupling and associated field-aligned current systems was first made by Kennel and Coroniti (1975), who discussed the coupling of angular momentum between magnetosphere and ionosphere in a solar wind-like radial outflow model. Another idea was put forward by Isbell et al. (1984) that the aurorae could be formed by field-aligned currents arising from the interaction between the solar wind and a rapidly rotating planet, associated with the twisting of open flux tubes in the tail. However, such a mechanism would result in emissions located at the boundary of and within the region of open field lines, whereas the main oval is magnetically linked to the middle magnetosphere. The first paper to discuss a possible auroral link with outwardly diffusing iogenic plasma was by Eviatar and Siscoe (1980), while the following year Barbosa et al. (1981) linked the jovian aurorae to field-aligned currents and associated field-aligned electron acceleration in the middle magnetosphere. A similar link was suggested by Dougherty et al. (1993) and Gérard et al. (1994) between the UV aurorae and the field-aligned current sheets observed at distances of  $\sim 15\text{-}20 R_J$  during the Ulysses outbound pass (Dougherty et al., 1993; Cowley et al., 1996).

It was V.M. Vasyliunas who, in open discussion at the Magnetospheres of the Outer Planets Meeting in Paris, August 1999, first explicitly suggested that the main auroral oval is associated with the breakdown of corotation of iogenic plasma in the middle magnetosphere current sheet. The current system associated with corotation breakdown had been discussed earlier by Hill (1979) and Vasyliunas (1983), although the currents themselves had not been explicitly calculated and related to the aurora at that time. There then followed a number of papers which discussed the formation of the main oval in terms of this magnetosphere-ionosphere coupling current system (Cowley and Bunce, 2001b; Hill, 2001; Khurana, 2001; Southwood and Kivelson, 2001). Before discussing the basic theory of the magnetosphere-ionosphere coupling system, the next section presents a discussion of the physical background.

### **3.2. Physical background**

An outline of the physics of the middle magnetosphere region is shown in Fig. 3.1, forming a background to the analysis and results which follow in this and later chapters. As discussed in Chapter 2, by far the most important plasma component in the middle magnetosphere originates from the atmosphere of the moon Io. Sulphur and oxygen ions and electrons that are produced from the neutral gas clouds that co-orbit with Io are picked up by the plasma flow, forming a dense near-corotating plasma torus in the vicinity of Io’s orbit. A significant fraction of the plasma ions that are produced in the torus undergo charge-exchange reactions with the neutral gas, and escape from the system as fast neutral particles (e.g. Pontius and Hill, 1982). The remainder flow outward under the action of the centrifugal force through flux tube interchange motions, to form a vast spinning equatorial plasma disc, shown dotted in Fig. 3.1. Estimates of the total plasma production rate within the torus lie typically within the range  $1000 - 3000 \text{ kg s}^{-1}$  when both the local production near Io and the more distributed production in the co-orbiting gas clouds are included (see Chapter 2). Of this total, perhaps one third to one half emerges into the plasma outflow in the equatorial plasma disc. Khurana and Kivelson (1993) derived a lower limit on the outward mass transport rate through the disc of  $\sim 500 \text{ kg s}^{-1}$  from consideration of the magnetic torque exerted on the plasma, as first discussed by Vasyliunas (1983). In addition, Hill (1980) estimated an outward mass transport rate of  $\sim 2000 \text{ kg s}^{-1}$  based on Voyager angular velocity profiles, though this estimate also requires knowledge of the height-integrated jovian ionospheric Pedersen conductivity, taken to be  $\sim 0.05 \text{ mho}$ . Overall, it seems reasonable to suppose that the outward transport rate of plasma through the disc is typically  $\sim 1000 \text{ kg s}^{-1}$ , with variations of perhaps a factor of  $\sim 2$  on either side. The flux tubes threading this disc constitute the jovian middle magnetosphere, which stretches typically over many tens of  $R_J$  from the vicinity of Io’s orbit to the vicinity of the magnetopause, depending on local time and the degree of extension of the magnetosphere, determined by solar wind conditions. The field lines in this region are characteristically distended radially outward from the planet, as shown in the figure, due to azimuthal currents flowing in the equatorial plasma associated with radial stress balance. The iogenic plasma is eventually lost from the outer regions of the disc by processes which are at present not well determined, but may involve plasmoid formation and outflow in the dusk sector of the magnetic tail (Vasyliunas, 1983).

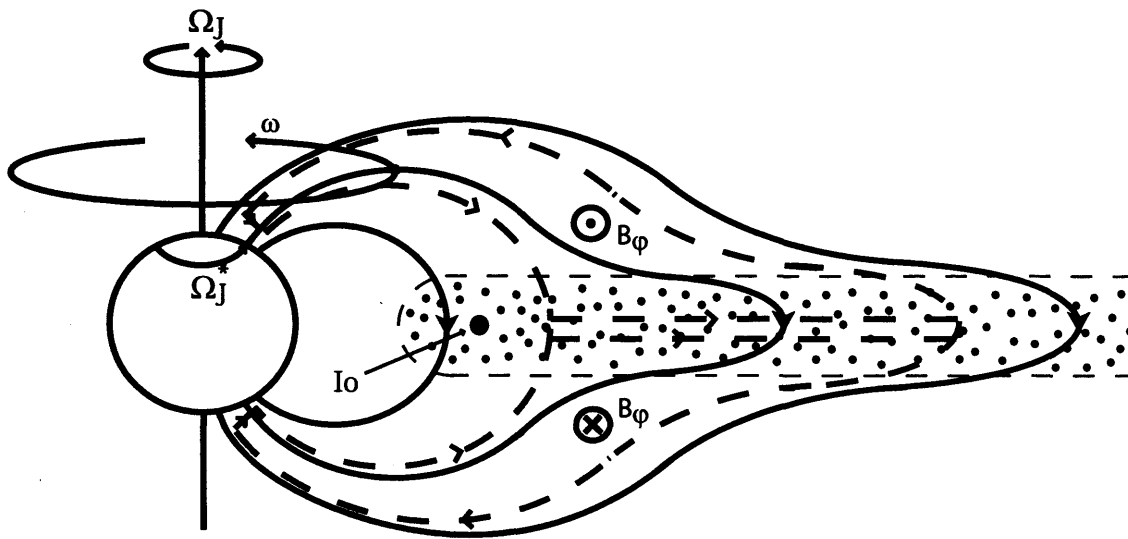


**Figure 3.1.** Sketch of a meridian cross-section through Jupiter's inner and middle magnetosphere, showing the principal physical features involved. The arrowed solid lines indicate magnetic field lines, the arrowed dashed lines the magnetosphere-ionosphere coupling current system, and the dotted region the rotating disc of out-flowing iogenic plasma. From Cowley and Bunce (2001).

As the iogenic plasma diffuses outward from the torus its angular velocity will drop below near-rigid corotation with the planet, inversely as the square of the distance if no torques act. However, when the angular velocity of the plasma and frozen-in field lines ( $\omega$  in Fig. 3.1) falls below that of the planet ( $\Omega_J$ ), or more specifically below that of the neutral upper atmosphere in the ionospheric Pedersen layer ( $\Omega^*_J$ ), ion-neutral collisions in the Pedersen layer provide a torque on the feet of the field lines which tends to spin the plasma back up towards rigid corotation. The torque is communicated to the equatorial plasma by bending of the magnetic field lines out of meridian planes, associated with the azimuthal field components  $B_\phi$  shown in Fig. 3.1, which reverse sense across the equator. The associated electric current system is shown by the dashed lines in the figure. It consists of an outward-flowing radial current in the equatorial plane associated with the reversal in the azimuthal field, which is connected to equatorward-directed Pedersen currents in both hemispheres by field-aligned currents which flow outward from the ionosphere to the magnetosphere in the inner part of the system, and return from the magnetosphere to the ionosphere in the outer part (Hill, 1979; Vasyliunas, 1983). It is with the upward-directed field-aligned currents in this system, carried by downward-precipitating magnetospheric electrons, that the ‘main oval’ auroras have been suggested to be associated. The torque associated with the  $\mathbf{j} \times \mathbf{B}$  force of the Pedersen current balances the frictional torque on the ionospheric plasma due to ion-neutral collisions, while the equal and opposite torque on the equatorial plasma tends to spin the plasma up towards rigid corotation with the planet. In the steady state, the plasma angular velocity will still generally fall with increasing distance, but at a rate which is less than the inverse square dependence expected from conservation of angular momentum. The basic theory used to describe this system is described in the following section.

### ***3.3. Theory of the jovian M-I coupling system***

This section will develop the theory of magnetosphere-ionosphere coupling at Jupiter, and will review earlier theoretical ideas concerning the system. We will start by discussing how the magnetic field is treated in the theory, and its implications for mapping between the ionosphere and magnetosphere. We will then go on to describe the current system and

follow with a derivation of the equation governing the plasma angular velocity in the equatorial plane, known as the Hill-Pontius equation. We will then briefly discuss work on this system presented by previous authors.

### 3.3.1. Field description and magnetosphere-ionosphere mapping

We first assume for simplicity that the magnetic field is axisymmetric, such that the poloidal components can be specified in cylindrical polar coordinates by a flux function  $F(\rho, z)$  related to the field components by  $\mathbf{B} = (1/\rho)\nabla F \times \hat{\boldsymbol{\phi}}$ , such that

$$B_\rho = -\frac{1}{\rho} \frac{\partial F}{\partial z} \quad \text{and} \quad B_z = \frac{1}{\rho} \frac{\partial F}{\partial \rho} \quad , \quad (3.1a,b)$$

where  $\rho$  is the perpendicular distance from the magnetic axis,  $z$  is distance along this axis from the magnetic equator, and  $\varphi$  is the azimuthal angle. As discussed in Chapter 2, modest day-night asymmetries are known to be present in the middle magnetosphere beyond  $\sim 15 R_J$ , but the essential properties of the dynamics will be adequately represented by an axisymmetric model, thereby introducing significant simplification. In this case it can be seen that  $(\mathbf{B} \cdot \nabla F) = 0$ , such that  $F = \text{constant}$  defines a flux shell. Therefore magnetic mapping between the equatorial plane (subscript ‘e’) and the ionosphere (subscript ‘i’), as required here, is simply achieved by writing

$$F_e(\rho_e) = F_i(\theta_i) \quad . \quad (3.2)$$

where  $\theta_i$  the magnetic co-latitude. The specific details of the current sheet magnetic field model and its associated flux function used in the analyses which follow is deferred until Section 3.3.6. Neglecting non-dipole planetary fields and the small perturbations due to magnetospheric currents, the flux function in the ionosphere is

$$F_i = B_J \rho_i^2 = B_J R_J^2 \sin^2 \theta_i \quad , \quad (3.3)$$

where  $B_J$  the dipole equatorial magnetic field strength at Jupiter’s surface (taken to be  $4.28 \times 10^5$  nT in conformity with the VIP 4 internal field model of Connerney et al. (1998)). The absolute value of  $F$  has been fixed by taking  $F = 0$  on the magnetic axis. The flux function in the equatorial plane is related to the north-south field  $B_{ze}(\rho_e)$  threading the current sheet by

$$B_{ze} = \frac{1}{\rho_e} \frac{dF_e}{d\rho_e} . \quad (3.4)$$

For the dipole field we have

$$B_{ze \text{ dip}} = -B_J \left( \frac{R_J}{\rho_e} \right)^3 \quad \text{and} \quad F_{e \text{ dip}} = \frac{B_J R_J^3}{\rho_e} , \quad (3.5a,b)$$

such that mapping between the equatorial plane and the ionosphere is given by

$$\sin \theta_i = \frac{\rho_i}{R_J} = \sqrt{\frac{R_J}{\rho_e}} . \quad (3.6)$$

Corresponding expressions for the current sheet fields considered in this thesis will be given later.

### 3.3.2. Magnetosphere-ionosphere coupling current system

We now consider the calculation of the field-perpendicular and field-parallel components of the magnetosphere-ionosphere coupling current system, illustrated in Fig. 3.1, for a given angular velocity profile of the equatorial plasma  $\omega(\rho_e)$ . In the following section, we will then consider how the steady state angular velocity profile is determined.

It is evident from the nature of the current sheet shown in Fig. 3.1 that continuity requires that the total equatorial current flowing in the current sheet in a given azimuthal angular

sector on a given flux shell must be equal to the height-integrated ionospheric Pedersen current flowing over the same angular sector on the same flux shell, summed over the two ionospheres. Assuming north-south symmetry, we therefore have

$$\rho_e i_p = 2\rho_i i_p \quad , \quad (3.7)$$

where  $\rho_e$  and  $\rho_i$  are (as above) the perpendicular distances of the field lines from the magnetic axis in the equatorial plane and in the ionosphere, respectively,  $i_p$  is the radial current intensity in  $\text{A m}^{-1}$  integrated across the width of the equatorial current sheet, and  $i_p$  is the height-integrated ionospheric Pedersen current intensity in each conjugate ionosphere. The latter current is determined from the ionospheric height-integrated Pedersen conductivity  $\Sigma_p$  and the electric field  $E_i$  in the rest frame of the neutral atmosphere by  $i_p = \Sigma_p E_i$ . In terms of the angular velocity of the flux shell,  $\omega$ , and the angular velocity of the neutral atmosphere averaged through the Pedersen-conducting layer,  $\Omega_j^*$ , we have

$$i_p = 2\Sigma_p B_j \rho_i (\Omega_j^* - \omega) \quad , \quad (3.8)$$

where we have taken the polar magnetic field to be near-vertical and equal to  $2B_j$  in strength (an approximation valid to within  $\sim 5\%$  in our region of interest) and  $\rho_i (\Omega_j^* - \omega)$  is the azimuthal velocity of the plasma in the neutral atmosphere rest frame (directed westward when the plasma subcorotates (i.e.  $\omega < \Omega_j^*$ ) corresponding to the direction of the currents shown in Fig. 3.1). Due to the action of the ionospheric torque, we may expect the angular velocity of the neutral atmosphere ( $\Omega_j^*$ ) to lie between that of the plasma ( $\omega$ ) and the planet ( $\Omega_j = 1.76 \times 10^{-4} \text{ rad s}^{-1}$ ) (Huang and Hill, 1989), so we may write for some  $0 < k < 1$

$$(\Omega_j - \Omega_j^*) = k(\Omega_j - \omega) \quad . \quad (3.9)$$

The value of  $k$  is not well known, but recent work with the JIM model indicates that  $k \sim 0.5$  for large current values of  $\sim 1 \mu\text{A m}^{-2}$  (see Chapter 4), while Huang and Hill (1989) calculated values  $k \sim 0.9$ . Introducing Eq. (3.9) into Eq. (3.8) we find

$$i_p = 2\Sigma_p^* B_J \Omega_J \rho_i \left(1 - \frac{\omega}{\Omega_J}\right) = 2\Sigma_p^* B_J \Omega_J \sqrt{\frac{F_i}{B_J}} \left(1 - \frac{\omega}{\Omega_J}\right), \quad (3.10)$$

where  $\Sigma_p^*$  is the 'effective' height-integrated ionospheric Pedersen conductivity, reduced from the true value by neutral atmosphere 'slippage'

$$\Sigma_p^* = (1 - k) \Sigma_p. \quad (3.11)$$

Substitution of Eq. (3.10) into Eq. (3.7) and use of Eqs. (3.2) and (3.3) then gives the equatorial radial current intensity per radian of azimuth as

$$i_\rho = \frac{4\Sigma_p^* \Omega_J F_e}{\rho_e} \left(1 - \frac{\omega}{\Omega_J}\right), \quad (3.12)$$

such that the total equatorial current, integrated in azimuth, is

$$I_\rho = 2\pi \rho_e i_\rho = 8\pi \Sigma_p^* \Omega_J F_e \left(1 - \frac{\omega}{\Omega_J}\right), \quad (3.13)$$

equal, of course, to twice the azimuth-integrated total Pedersen current

$$I_p = 2\pi \rho_i i_p = 4\pi \Sigma_p^* \Omega_J F_i \left(1 - \frac{\omega}{\Omega_J}\right) \quad (3.14)$$

flowing in each conjugate ionosphere. Given Eqs. (3.10) and (3.12) for the field-perpendicular currents, the field-parallel current density follows from the divergence of either. Differentiating the equatorial current, for example, gives  $-2j_z = \text{div}(\rho_e i_\rho)$ , where

$j_z$  is the north-south current flowing into each face of the current sheet. The field-aligned current is then obtained using the fact that  $(j_{\parallel}/B)$  is constant along a field line, to give

$$\left(\frac{j_{\parallel}}{B}\right) = \mp \frac{1}{2\rho_e B_{ze}} \frac{d}{d\rho_e} (\rho_e i_{\rho}) = \mp \frac{2}{\rho_e B_{ze}} \frac{d}{d\rho_e} [\Sigma_p^* F_e (\Omega_J - \omega)] , \quad (3.15)$$

where the upper sign of  $j_{\parallel}$  is appropriate to the northern hemisphere (and is employed throughout this thesis) and the lower sign is appropriate to the southern hemisphere. The quantity  $(j_{\parallel}/B)$  is constant along field lines between the equator and the ionosphere in the assumed absence of significant field-perpendicular currents in the intervening region. The general expression for field-aligned current density just above the ionosphere is then given by

$$j_{\parallel i} = 2B_J \left(\frac{j_{\parallel}}{B}\right) = -\frac{4B_J}{\rho_e B_{ze}} \frac{d}{d\rho_e} [\Sigma_p^* F_e (\Omega_J - \omega)] , \quad (3.16)$$

using the same approximation for the polar field as indicated above. An important assumption made in all previous studies of this system is that the effective height-integrated Pedersen conductivity  $\Sigma_p^*$  is a constant, an issue which is addressed by the analysis in Chapter 5. Making this assumption and performing the differentiation in Eq. (3.16) gives

$$j_{\parallel i} = -4B_J \Sigma_p^* \Omega_J \left( \left( \frac{F_e}{\rho_e |B_{ze}|} \right) \frac{d}{d\rho_e} \left( \frac{\omega}{\Omega_J} \right) + \left( 1 - \frac{\omega}{\Omega_J} \right) \right) , \quad (3.17)$$

where we have used Eq. (3.1b) applied to the equator and we have put  $B_{ze} = -|B_{ze}|$  since the jovian equatorial field is always directed southwards in the inner and middle magnetosphere. The northward-directed current density leaving the northern face of the equatorial current sheet on the same field line is then given by

$$j_{ze} = -\frac{|B_{ze}|}{2B_J} j_{\parallel i} , \quad (3.18)$$

where the sign is such that  $j_{ze}$  is negative (current into the sheet) for an upward (positive) field-aligned current out of the ionosphere. This calculation assumes, of course, that an oppositely directed current is also present at the southern face of the current sheet, connected to the southern ionosphere.

### 3.3.3. Parallel voltage, acceleration region height, and precipitated electron energy flux

We now briefly consider the conditions under which the field-aligned current given by Eq. (3.17) will flow. The maximum field-aligned current that can be carried by precipitating magnetospheric electrons in the absence of a field-aligned voltage is

$$j_{\parallel io} = eN \left( \frac{W_{th}}{2\pi m_e} \right)^{1/2}, \quad (3.19)$$

where  $e$  is the elementary charge,  $m_e$  the electron mass,  $N$  the magnetospheric electron number density, and  $W_{th}$  the electron thermal energy. This current corresponds to the assumption of a full downward-going loss cone and an empty upward-going loss cone. We also assume an isotropic magnetospheric electron distribution function (and the existence of weak pitch angle scattering in the magnetosphere, so that the loss cone is kept full), such that the number density  $N$  is constant along the field lines. If we take values based on Voyager results (Scudder et al., 1981), i.e.  $N = 0.01 \text{ cm}^{-3}$  and  $W_{th} = 2.5 \text{ keV}$  outside the current sheet, we find  $j_{\parallel io} \approx 0.013 \mu\text{A m}^{-2}$ . It will be seen later in this chapter that this value is comparable to those estimated for a dipole planetary field, but is an order of magnitude less than required when one employs a realistic current sheet field. Under these circumstances a substantial field-aligned voltage is required to drive the current.

The minimum field-aligned voltage  $\Phi_{\min}$  required to drive a field-aligned current greater than  $j_{\parallel io}$  is calculated from the kinetic theory of Knight (1973), who showed that

$$e\Phi_{\min} = W_{th} \left[ \left( \frac{j_{\parallel i}}{j_{\parallel io}} \right) - 1 \right] \approx W_{th} \left( \frac{j_{\parallel i}}{j_{\parallel io}} \right), \quad (3.20)$$

a result which is valid in the case where the acceleration region lies at large distances ( $\gg R_J$ ) along the field lines above the ionosphere. The approximation in Eq. (3.20) is valid when  $j_{\parallel i} \gg j_{\parallel io}$ . If the current densities required are more than an order of magnitude larger than  $j_{\parallel io}$  and  $W_{th}$  is of order a few keV, then we infer that the voltages required will be of order several tens of kV. Second, the minimum distance of the ‘top’ of the voltage drop, determined by the requirement that a large enough flux of magnetospheric electrons is present to form the current, is given by

$$\left( \frac{r_{\min}}{R_J} \right) \approx \left( \frac{j_{\parallel i}}{j_{\parallel io}} \right)^{1/3}. \quad (3.21)$$

Here we have assumed as a sufficient approximation that the field strength falls as the cube of the distance along the polar field lines. We now consider the energy flux of the precipitating electrons and the intensity of the resulting aurorae. The maximum precipitated electron energy flux for zero field-aligned voltage, i.e. when the field-aligned current is given by Eq. (3.19), is

$$E_{fo} = 2NW_{th} \left( \frac{W_{th}}{2\pi m_e} \right)^{1/2}. \quad (3.22)$$

For the above electron parameters we find  $E_{fo} \approx 0.07 \text{ mW m}^{-2}$ , which is negligible with respect to the jovian main oval aurorae. Assuming a 20% conversion efficiency of precipitating electron energy into  $\sim 10 \text{ eV}$  UV photons yields estimates of the precipitated electron energy flux of  $\sim 10\text{-}100 \text{ mW m}^{-2}$  for typical main oval UV auroral luminosities of  $\sim 100 \text{ kR}$  to  $\sim 1 \text{ MR}$ . An energy flux of  $\sim 0.1 \text{ mW m}^{-2}$  will result in an auroral intensity of only  $\sim 1 \text{ kR}$ . However, with the inclusion of a field-aligned voltage, and in the same approximation as Eq. (3.20), the energy flux becomes

$$E_f = \frac{E_{f0}}{2} \left[ \left( \frac{j_{||i}}{j_{||io}} \right)^2 + 1 \right] \approx \frac{E_{f0}}{2} \left( \frac{j_{||i}}{j_{||io}} \right)^2, \quad (3.23)$$

a result due to Lundin and Sandahl (1978). The energy flux is thus amplified by the factor  $(j_{||i}/j_{||io})^2 \sim 100-1000$ , which yields values of  $\sim 10-100 \text{ mW m}^{-2}$ , consistent with the observed UV auroral intensities.

It must be noted, however, that this aspect of the theory introduces an element of non-consistency into the calculations. This is because the currents are calculated above assuming that the magnetospheric flow and electric field are mapped along equipotential field lines into the ionosphere. However, a field-aligned voltage will modify the mapping of magnetospheric flow, and hence the current. This is an issue which is addressed in the analysis in Chapter 6.

#### 3.3.4. Steady state angular velocity profile and field-aligned currents

We now outline a derivation of the equation governing the radial variation of the steady-state angular velocity of iogenic plasma as it moves outward through the current sheet from the Io plasma torus. The derivation is equivalent to that given originally by Hill (1979) and Pontius (1997), though here we focus on the equatorial plasma rather than the ionosphere. In the steady state the electromagnetic torque on the equatorial plasma in a given flux tube is equal and opposite to the electromagnetic torque on the ionospheric plasma in the same flux tube (which balances the torque of the neutral atmosphere due to ion-neutral collisions), as already guaranteed by Eq. (3.7). The equilibrium conditions can thus be derived by consideration of the conditions at either end of the flux tube.

The angular momentum  $L$  of a body of mass  $M$  relative to some reference point O is equal to the cross product of the body’s position vector  $r$  relative to O and its linear momentum  $p$ . If the body is travelling in a circular orbit around O with angular velocity  $\omega$  its angular momentum is then given by  $L = r \times p = M\omega r^2$ . Newton’s second law then states that the rate of change of the body’s angular momentum is equal to any external torque  $T$  acting

thereon, as given by  $dL/dt = d(M\omega r^2)/dt = T$ . We assume a fixed plasma source of  $\dot{M}$  kg s<sup>-1</sup> located at a particular radial distance in the equatorial plane, from which the plasma flows outward by radial diffusion across the flux shells in a thin azimuthally symmetric equatorial disc. If the angular velocity of the plasma at a radial distance  $\rho_e$  is  $\omega(\rho_e)$ , the angular momentum per unit mass is  $\rho_e^2\omega(\rho_e)$ . The outward-directed flux of angular momentum at this radial distance is thus  $\dot{M}\rho_e^2\omega(\rho_e)$ . From Newton's second law the difference between the flux of angular momentum at  $\rho_e$  and that at  $\rho_e + d\rho_e$  is equal to the electromagnetic torque  $dT_z$  acting on the plasma in the annular disc between  $\rho_e$  and  $\rho_e + d\rho_e$ . We thus have

$$\frac{d}{d\rho_e}(\dot{M}\rho_e^2\omega(\rho_e)) = \frac{dT_z}{d\rho_e} . \quad (3.24)$$

The torque per unit volume about Jupiter's centre acting on the plasma is  $\mathbf{r} \times (\mathbf{j} \times \mathbf{B})$ , where  $\mathbf{r}$  is the jovicentric position vector of the plasma element,  $\mathbf{j}$  the current density, and  $\mathbf{B}$  the magnetic field. Integrating this over the annulus between  $\rho_e$  and  $\rho_e + d\rho_e$  then gives the z-component of the torque acting on this annulus as

$$dT_z = 2\pi\rho_e^2 i_\rho |B_{ze}| d\rho_e , \quad (3.25)$$

so that substitution into Eq. (3.24) gives

$$\frac{d}{d\rho_e}(\rho_e^2\omega(\rho_e)) = \frac{2\pi\rho_e^2 i_\rho |B_{ze}|}{\dot{M}} . \quad (3.26)$$

Expansion of the LHS and substitution of Eq. (3.12) gives

$$\frac{\rho_e}{2} \frac{d}{d\rho_e} \left( \frac{\omega}{\Omega_J} \right) + \left( \frac{\omega}{\Omega_J} \right) = \frac{4\pi\Sigma_P^* F_e |B_{ze}|}{\dot{M}} \left( 1 - \frac{\omega}{\Omega_J} \right) , \quad (3.27)$$

which is the differential equation that must be solved, with the use of a suitable boundary condition, for the equatorial angular velocity profile of the plasma. We then note that if the angular velocity profile obeys this equation, its derivative may be substituted directly into Eq. (3.17) to yield the potentially more convenient form for the ionospheric field-aligned current

$$j_{\parallel} = 4\Sigma_p^* \Omega_J B_J \left[ \left( \frac{2F_e}{\rho_e^2 |B_{ze}|} \right) \left( \left( \frac{\omega}{\Omega_J} \right) - \frac{4\pi\Sigma_p^* F_e |B_{ze}|}{\dot{M}} \left( 1 - \frac{\omega}{\Omega_J} \right) \right) - \left( 1 - \frac{\omega}{\Omega_J} \right) \right]. \quad (3.28)$$

Equation (3.27) is termed the Hill-Pontius equation after T.W. Hill and D.H. Pontius, Jr, who first derived and employed this result. That is, Hill (1979) was the first to calculate the steady-state plasma angular velocity profile of the jovian magnetosphere-ionosphere coupling system in this manner, assuming a dipole poloidal planetary magnetic field. Pontius (1997) later generalised his analysis to include a general poloidal magnetic field. It is easy to show that Eq. (3.27) is equivalent to the corresponding equations given by Hill (1979, 2001) (his Eqs. (20) and (A.11), respectively) and Pontius (1997) (his Eq. (5)), once the polar field approximation used here ( $B_i = 2B_J$ ) is applied. A brief discussion of the results of Hill (1979) and Pontius (1997) follow in the next section.

### 3.3.5. Results of Hill (1979, 2001) and Pontius (1997)

Hill (1979) solved his equivalent of Eq. (3.27) for a dipole field using the integration factor method and, assuming the plasma corotates at the origin, derived the solution

$$\left( \frac{\omega}{\Omega_J} \right) = \frac{1}{\rho^2} \exp \left[ -\rho_H^4 \left( 1 - \frac{1}{\rho^4} \right) \right] + \sqrt{\pi} \left( \frac{\rho_H}{\rho} \right)^2 \exp \left[ \left( \frac{\rho_H}{\rho} \right)^4 \right] \left[ \operatorname{erf} \left[ \left( \frac{\rho_H}{\rho} \right)^2 \right] - \operatorname{erf} \left[ (\rho_H)^2 \right] \right], \quad (3.29)$$

where  $\rho$  is radial distance from the magnetic axis in units of  $R_J$ , and  $\rho_H$  is the characteristic distance over which corotation breaks down, given by

$$\rho_H = \left( \frac{2\pi\Sigma_p^* B_J^2 R_J^2}{\dot{M}} \right)^{1/4} \quad (3.30)$$

The scaling parameter  $\rho_H$  is dependent on the ratio  $(\Sigma_p^*/\dot{M})$ , while neither  $\Sigma_p^*$  or  $\dot{M}$  were known to great accuracy in 1979. Hill (1979) plotted the solution for  $\rho_H = 64 R_J$ , which represented the existing estimates of  $\Sigma_p^* = 0.05$  mho and  $\dot{M} = 10^{28}$  amu s<sup>-1</sup> for these parameters at the time (note that  $10^{28}$  amu s<sup>-1</sup> corresponds to  $\sim 17$  kg s<sup>-1</sup>). Later, in the light of Voyager results, Hill (2001) revised this estimate to  $\rho_H = 30R_J$  for “plausible” values of  $\Sigma_p^* \sim 0.3$  mho and  $\dot{M} \sim 2000$  kg s<sup>-1</sup>. The solution for  $\rho_H = 30R_J$  is shown in Fig. 3.2. It should be noted that Hill (1979, 2001) considered the Pedersen conductivity for both hemispheres in parallel, such that his conductivity values were double those given above, while his equivalent of Eq. (3.30) did not have the factor of two in the numerator. Hill (1979) also pointed out that at large distances the solution asymptotes to the limit whereby the ionospheric torque goes to zero and the flow is governed by conservation of angular momentum alone. The plasma angular velocity is then given by

$$\left( \frac{\omega}{\Omega_J} \right) = \sqrt{\pi} \left( \frac{\rho_H}{\rho} \right)^2, \quad (3.31)$$

i.e. the velocity falls off with the inverse square of the distance as expected. Hill (1979) did not specifically calculate the currents flowing in the system at this time, an omission which he later corrected in Hill (2001). The field-aligned current density profile derived by Hill (2001) is shown in Fig. 3.3. It can be seen that the current flows upward (i.e. is positive) at lower latitudes, and reverses to downward (negative) near the pole. In this way the dipole field guarantees current closure and charge continuity. The current in the figure is normalised to the quantity  $j_o = 4\Sigma_p^* B_J \Omega_J$ , such that for the value  $\Sigma_p^* = 0.3$  mho the peak upward current is  $\sim 0.03$   $\mu\text{A m}^{-2}$ . Although this result suggested the existence of a stable, continuous ring of field aligned current, the strength of the current is approximately an order of magnitude too low to agree with observations of the auroral oval, as discussed in Section 3.3.3. In addition the location of the peak magnitude of the field-aligned current,  $\sim 10^\circ$ , differs significantly from the observed main oval latitude of  $\sim 15^\circ$ .

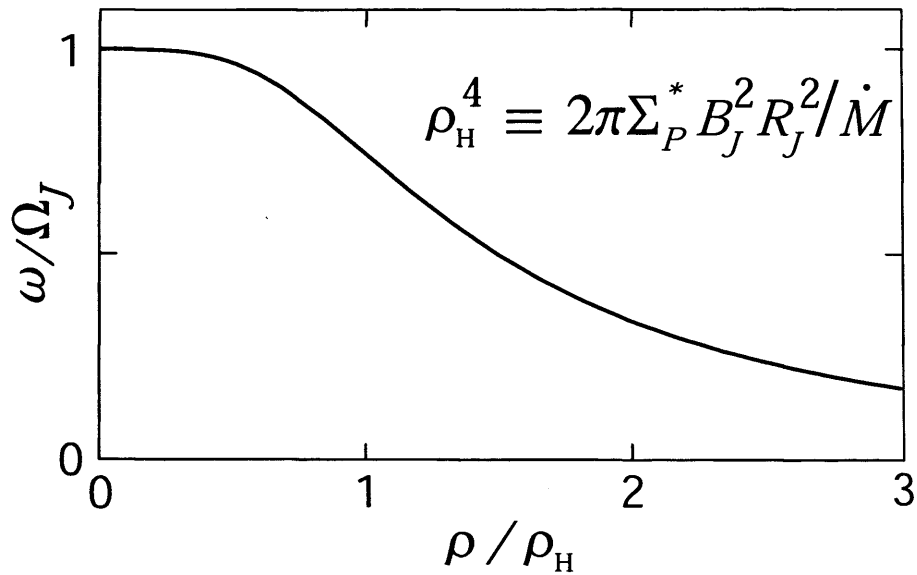


**Figure 3.2.** Hill’s solution for the equatorial angular velocity profile of current sheet plasma normalised to Jupiter’s angular velocity and plotted against equatorial radial distance  $\rho$  normalised to the Hill scaling distance  $\rho_H = 30R_J$  as defined in the figure and Eq. (3.30). From Hill (2001).

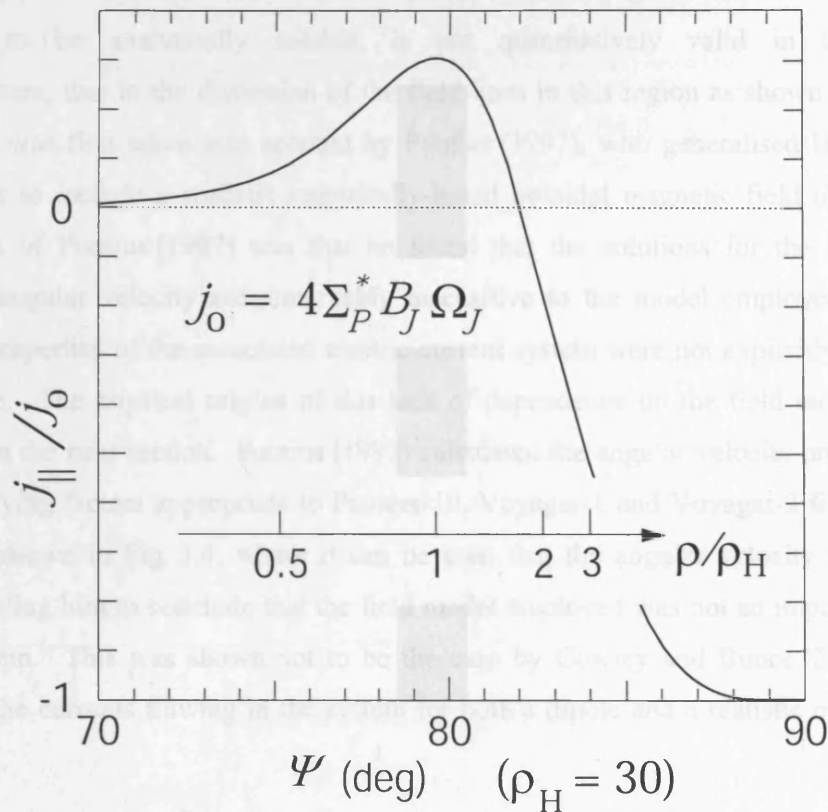


**Figure 3.3.** Ionospheric field-aligned current calculated from Hill’s solution for  $\rho_H = 30R_J$  (shown in Fig. 3.2), normalised to  $j_0$  defined in the figure and plotted against normalised equatorial radial distance (inset horizontal scale) and ionospheric latitude (bottom horizontal scale). From Hill (2001).

The assumption that the planetary field is dipolar, while having the virtue of allowing the equations to be analytically soluble, is not quantitatively valid in the middle magnetosphere, due to the distension of the field lines in this region as shown in Fig. 3.1. This effect was first taken into account by Pontius (1997), who generalised Hill’s (1979) calculations to include a realistic empirically-based poloidal magnetic field model. The main result of Pontius (1997) was that he found that the solutions for the steady-state equatorial angular velocity are remarkably insensitive to the model employed, although again the properties of the associated electric current system were not explicitly calculated at that time. The physical origins of this lack of dependence on the field model will be discussed in the next section. Pontius (1997) calculated the angular velocity profiles using field modifying factors appropriate to Pioneer-10, Voyager-1 and Voyager-2 field models. These are shown in Fig. 3.4, where it can be seen that the angular velocity profiles are similar, leading him to conclude that the field model employed was not an important factor in the system. This was shown not to be the case by Cowley and Bunce (2001b), who compared the currents flowing in the system for both a dipole and a realistic current sheet field model.

### 3.3.6. Results of Cowley and Bunce (2001b) and Cowley, Nichols, and Bunce (2002)

Cowley and Bunce (2001b) calculated the currents flowing in the magnetosphere-ionosphere coupling current system using a realistic empirical current sheet field model and an empirical model of the equatorial plasma angular velocity, and compared the results with those for the dipole field model. The empirical field model is of the north-south component of the magnetic field in the equatorial plane,  $B_{ze}$ . Within a certain distance  $\rho_e^*$  the equatorial field was taken to be given by the dipole field plus the field of the Connerney et al. (1981) current sheet model (the CAN model). That is,

$$B_{ze}(\rho_e) = -\frac{B_J R_J^3}{\rho_e^3} + B_{CAN_z}(\rho_e) \quad , \quad (3.32a)$$

where

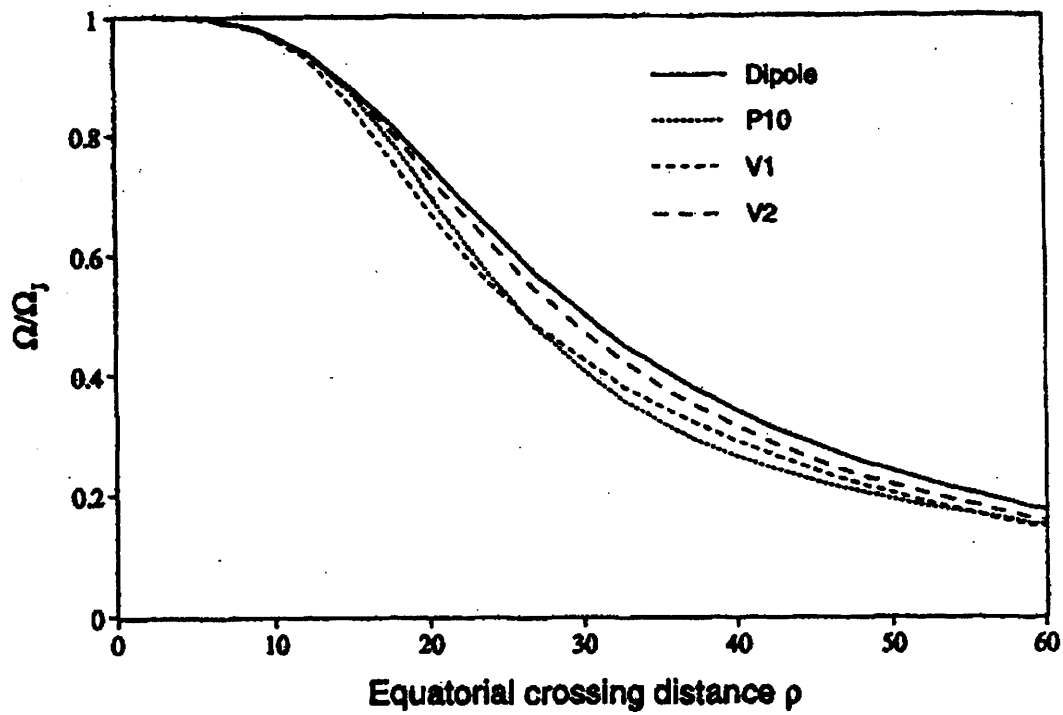


Figure 3.4. Pontius' (1997) solutions of his generalised Hill (1979) equation for the equatorial plasma angular velocity, using a dipole field and axisymmetric poloidal fields based on data from Pioneer-10, Voyager-1 and Voyager-2. From Pontius (1997).

$$B_{\text{CAN}_z}(\rho_e) = \frac{\mu_0 I_0}{2} \left\{ \begin{array}{l} \log \left[ \frac{\sqrt{\rho_e^2 + D^2} + D}{\sqrt{\rho_e^2 + D^2} - D} \right] + \frac{R_0^2 D}{2(\rho_e^2 + D^2)^{3/2}} \\ -\log \left[ \frac{\sqrt{R_1^2 + D^2} + D}{\sqrt{R_1^2 + D^2} - D} \right] - \frac{\rho_e^2 D}{2(R_1^2 + D^2)^{3/2}} \end{array} \right\}. \quad (3.32b)$$

Equation (3.32b) is the approximate form of the CAN model field derived by Edwards et al. (2001), and is accurate (relative to the CAN model) to within ~1% in the region of interest. The CAN model was derived by Connerney et al. (1981) from Voyager and Pioneer data and is valid for distances within ~30  $R_J$ . The model parameters used are the ‘Voyager-1/Pioneer-10’ set given by Connerney et al. (1981), i.e. a current half-thickness  $D = 2.5 R_J$ , inner and outer radii of the annular current sheet  $R_0 = 5 R_J$  and  $R_1 = 50 R_J$ , respectively, and a current intensity parameter  $(\mu_0 I_0/2) = 225$  nT. Beyond  $\rho_e^*$  the model employed is Khurana and Kivelson’s (1993) empirical fit to Voyager-1 outbound data (the ‘KK’ model), given by the power law

$$B_{ze}(\rho_e) = -B_0 \left( \frac{R_J}{\rho_e} \right)^m, \quad (3.33)$$

where  $B_0 = 5.4 \times 10^4$  nT and  $m = 2.71$ . This expression is applicable over the radial range ~20-100  $R_J$ , thus overlapping the CAN model in the range ~20-30  $R_J$ . Here we switch from one model to the other at the radial distance  $\rho_e^*$  where the two model curves intersect, such that  $B_{ze}$  is continuous. We find that the intersection occurs at  $\rho_e^* = 21.78 R_J$ , which thus lies in the region of overlap of their respective regimes of validity. The behaviour of the model field is indicated by the solid line in Fig. 3.5a, where the modulus of  $B_{ze}$  is plotted in log-log format against equatorial radial distance  $\rho_e$  over the range from 5  $R_J$  (the inner edge of the CAN current sheet) to 100  $R_J$  (the outer limit of validity of the KK model). The actual values are, of course, negative. The dashed line in Fig. 3.5a shows the modulus of the dipole value for comparison. It can be seen that the current sheet field is less than the dipole field by factors of 2-3 in the middle magnetosphere region, due to the outward distension of the field lines in this region caused by the equatorial currents. For

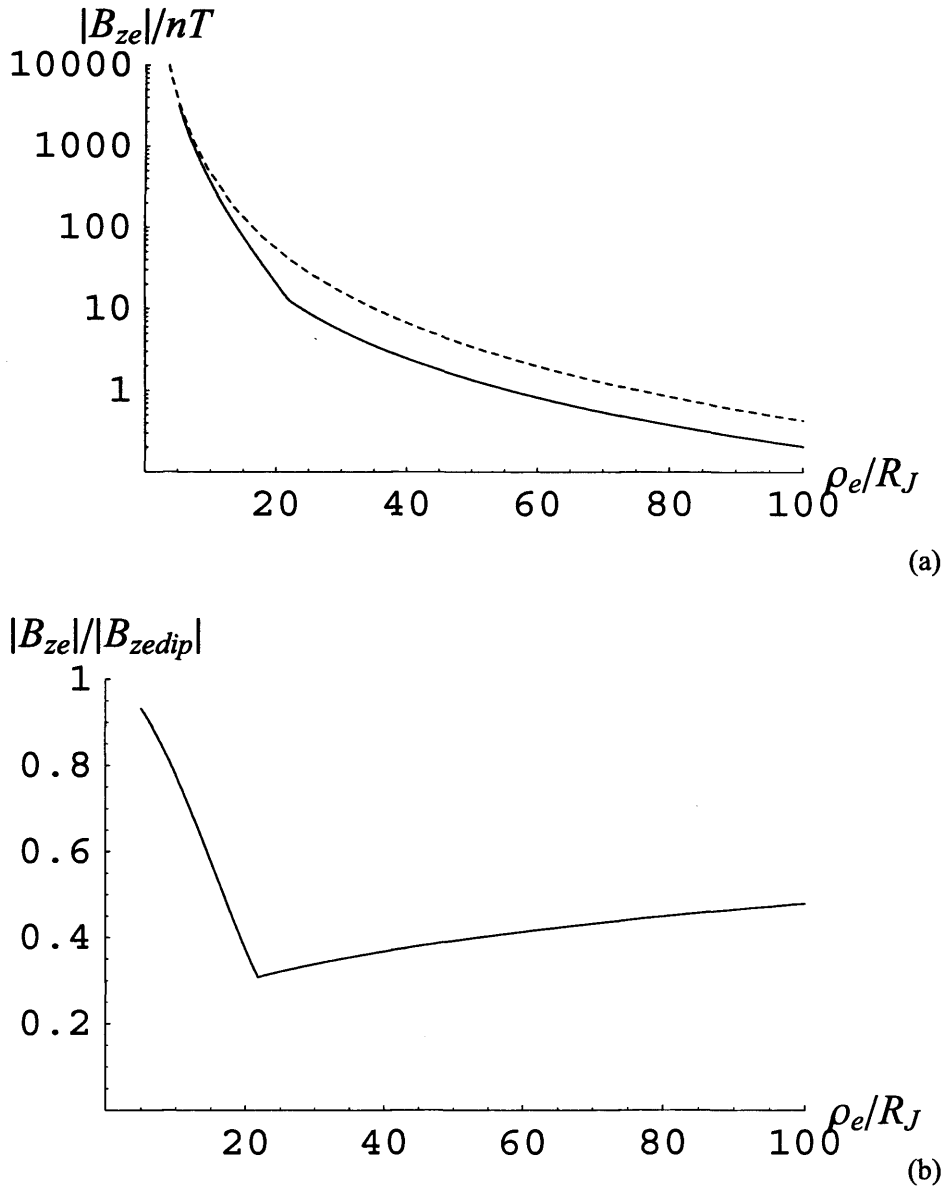


**Figure 3.5.** Plots showing relevant parameters of the current sheet field model employed in Cowley and Bunce (2001b), Cowley et al. (2002, 2003a) and in Chapter 4 of this thesis. All parameters are plotted versus jovicentric radial distance  $\rho_e$ . Plot (a) is a log-linear plot of the modulus of the north-south equatorial magnetic field  $|B_{ze}|$  threading the current sheet (solid line), where we note that the field is actually negative (i.e. points south). The kink in the curve at  $21.78 R_J$  marks the point where we switch from the CAN to the KK model. The dashed line shows the dipole value. Plot (b) shows the ratio of these fields  $(B_{ze}/B_{ze \text{ dip}})$ .

convenience of later discussion, Fig. 3.5b explicitly shows the ratio of the two fields ( $B_{ze}/B_{ze \text{ dip}}$ ). It can be seen that the ratio of the two fields declines rapidly from near unity at  $\sim 5 R_J$  to a minimum of  $\sim 0.3$  at  $\rho_e^*$ , and then slowly increases once more to  $\sim 0.5$  at  $100 R_J$ .

With this model for  $B_{ze}$ , the equatorial flux function  $F_e$  can be determined from Eq. (3.1b).

For  $\rho_e < \rho_e^*$  this is given by

$$F_e(\rho_e) = -\frac{B_J R_J^3}{\rho_e} + F_{e\text{CAN}}(\rho_e) , \quad (3.34a)$$

where

$$F_{e\text{CAN}}(\rho_e) = \frac{\mu_0 I_0}{2} \left\{ \begin{array}{l} D\sqrt{\rho_e^2 + D^2} + \frac{\rho_e^2}{2} \log \left[ \frac{\sqrt{\rho_e^2 + D^2} + D}{\sqrt{\rho_e^2 + D^2} - D} \right] - \frac{R_0^2 D}{2\sqrt{\rho_e^2 + D^2}} - D^2 \\ -\frac{\rho_e^2}{2} \log \left[ \frac{\sqrt{R_1^2 + D^2} + D}{\sqrt{R_1^2 + D^2} - D} \right] - \frac{\rho_e^4 D}{8(R_1^2 + D^2)^{3/2}} \end{array} \right\} . \quad (3.34b)$$

Equation (3.34b) has been obtained from the expression for the vector potential of the CAN current sheet given by Edwards et al. (2001), and also represents the model function to better than  $\sim 1\%$  in the region of interest. It is noted that Eqs. (3.32b) and (3.34b) obey Eq. (3.1b) exactly. For  $\rho_e \geq \rho_e^*$  integration of Eq. (3.1b) gives

$$F_e(\rho_e) = F_e(\rho_e^*) + \int_{\rho_e^*}^{\rho_e} d\rho_e' \rho_e' B_{ze}(\rho_e') = F_e(\rho_e^*) + \frac{B_0 R_J^2}{(m-2)} \left[ \left( \frac{R_J}{\rho_e} \right)^{m-2} - \left( \frac{R_J}{\rho_e^*} \right)^{m-2} \right] , \quad (3.35a)$$

where  $F_e(\rho_e^*)$ , equal to  $3.70 \times 10^4 \text{ nT R}_J^2$  for the parameter set employed here, is obtained from Eq. (3.34) and where Eq. (3.33) was introduced into the integral. Combining the constant terms, we can therefore write for  $\rho_e \geq \rho_e^*$

$$F_e(\rho_e) = F_\infty + \frac{B_0 R_J^2}{(m-2)} \left( \frac{R_J}{\rho_e} \right)^{m-2}, \quad (3.35b)$$

where  $F_\infty$ , the value of  $F_e$  at infinity according to our model, is equal to  $2.85 \times 10^4 \text{ nT R}_J^2$ . The flux function given by Eqs. (3.34) and (3.35) is plotted versus  $\rho_e$  by the solid line in Fig. 3.6a. The dashed line shows the corresponding dipole value given by the first term in Eq. (3.34a). It can be seen that the current sheet value exceeds the dipole value in the middle magnetosphere by factors typically of  $\sim 5$ , increasing with increasing distance. It can also be seen that the value at the outer limit of the region considered here,  $100 R_J$ , still has a significantly large value of  $3.14 \times 10^4 \text{ nT R}_J^2$ , as does indeed the value at infinity ( $2.85 \times 10^4 \text{ nT R}_J^2$ ). It will be recalled from Section 3.3.1 that the value of  $F_e$  relates directly to the field line mapping to the ionosphere, given by Eq. (3.6). This is shown explicitly in Fig. 3.6b, where we plot ionospheric co-latitude  $\theta_i$  versus equatorial radial distance  $\rho_e$ , for the current sheet model (solid line) and dipole (dashed line). It can be seen that the field line from  $100 R_J$  maps to a co-latitude of  $15.7^\circ$  in the current sheet model, while mapping to  $5.7^\circ$  co-latitude for the dipole, significantly closer to the pole. The implication for the current sheet is that field lines with smaller values of  $F_e$  which map to higher latitudes do not close within the middle magnetosphere, but instead correspond to the field lines of the outer magnetosphere and tail, including the open flux in the tail lobes. For example, the field line from infinity only maps to  $15.0^\circ$  co-latitude for the current sheet field, and of course  $0^\circ$  (i.e. the magnetic pole) for the dipole. For convenience of later discussion we show in Fig. 3.7a the ratio  $(F_e/F_{e \text{ dip}})^{1/2}$  versus  $\rho_e$ , which is equal (from Eq. (3.3)) to the ratio of the corresponding ionospheric mappings  $(\rho_i/\rho_{i \text{ dip}})$ . It can be seen that the value increases monotonically from near unity at  $\sim 5 R_J$  to reach nearly  $\sim 3$  at  $100 R_J$ . Two further field parameters are plotted, which will be discussed later. The first is

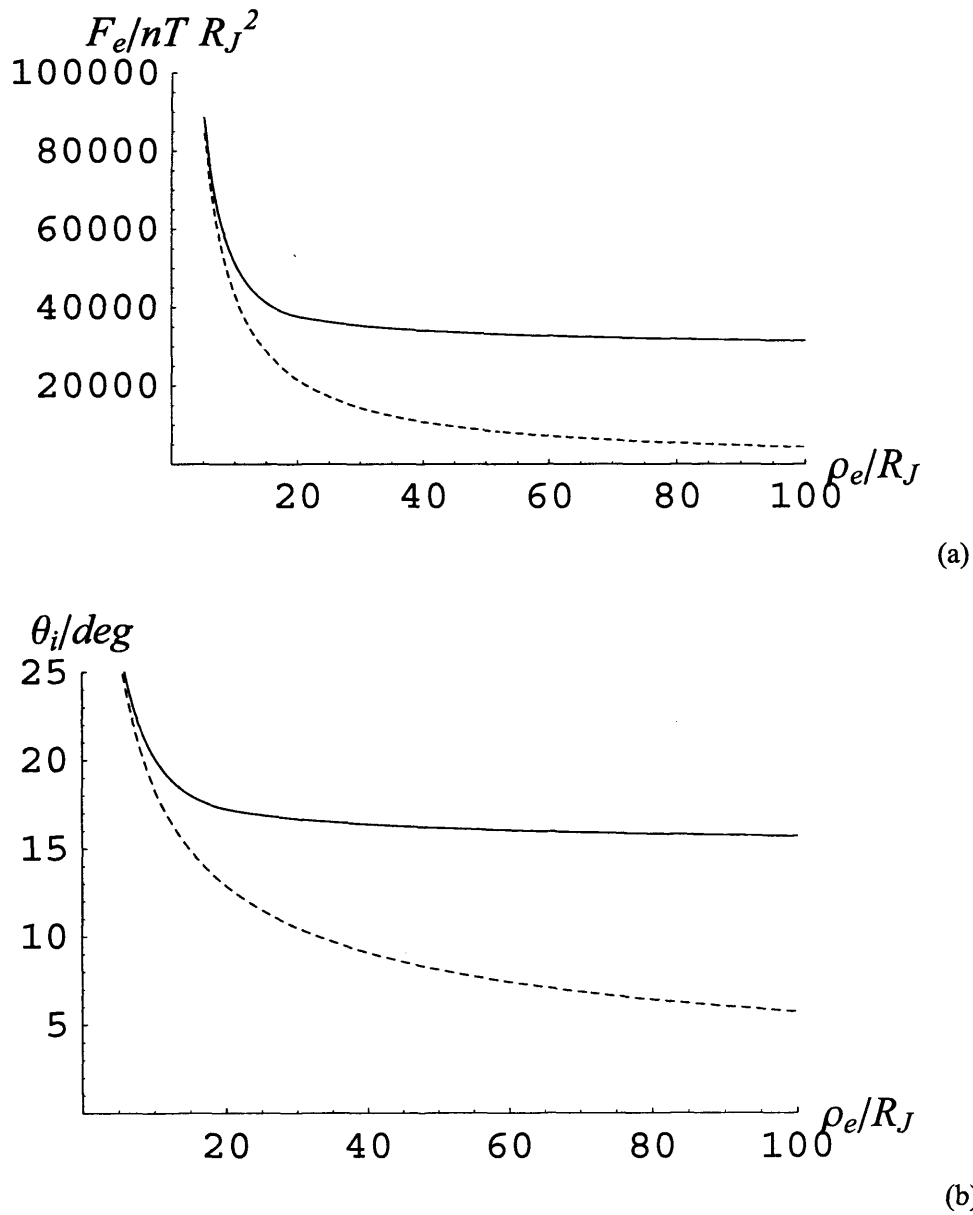


**Figure 3.6.** Plot (a) shows the equatorial flux function  $F_e$  of the current sheet magnetic field model (solid line), and the dipole value (dashed line). Plot (b) shows the mapping from the equatorial plane to the ionosphere, i.e. ionospheric co-latitude  $\theta_i$  versus equatorial radial distance  $\rho_e$ , for the current sheet model (solid line) and the dipole (dashed line).

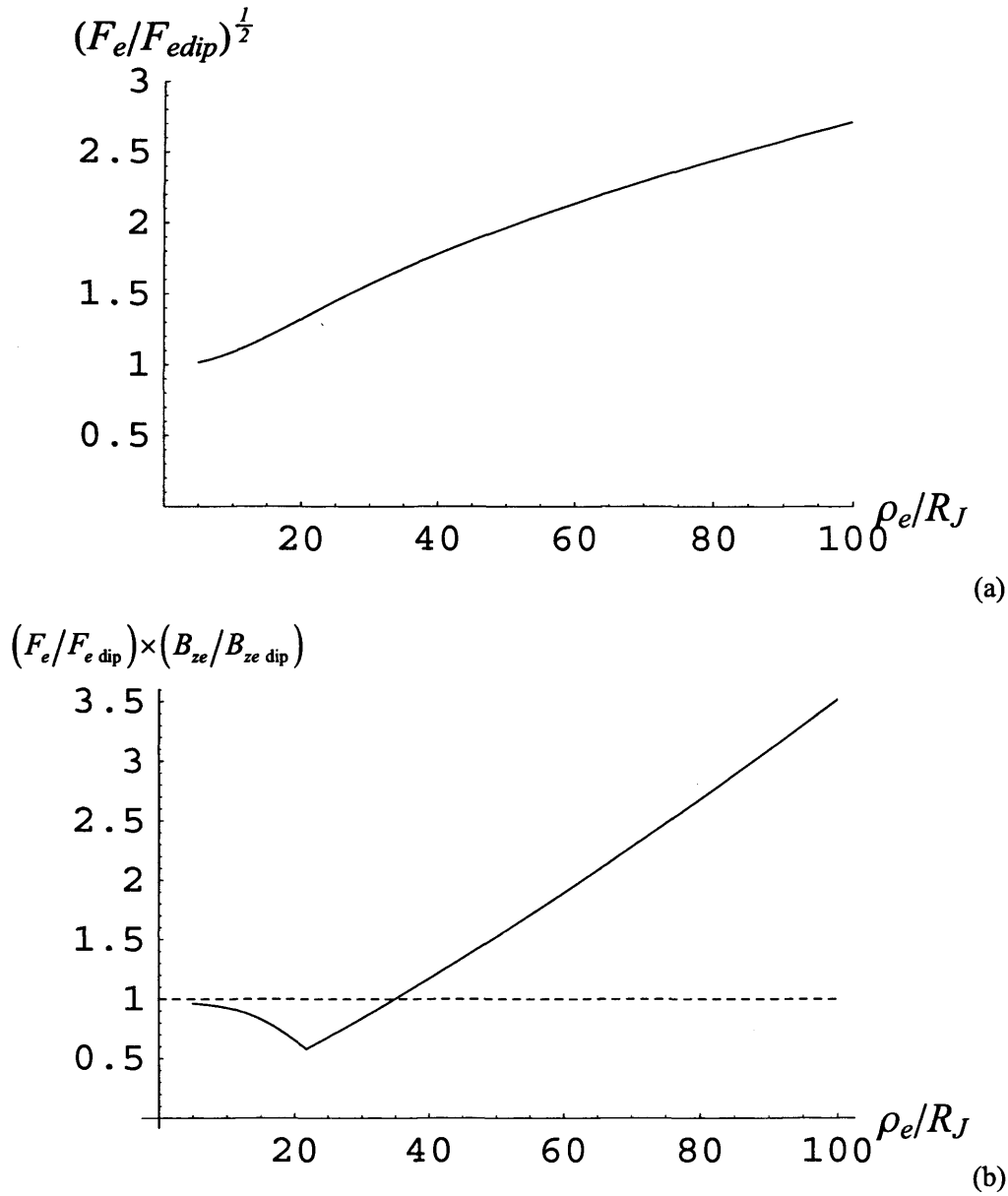


**Figure 3.7.** Plot (a) shows the square root of the ratio of the equatorial flux functions  $(F_e/F_{e \text{ dip}})^{1/2}$ . This function is equal to the ratio of the perpendicular distances from the dipole axis of the field lines when mapped into the ionosphere ( $\rho_i/\rho_{i \text{ dip}}$ ). Plot (b) shows the product of the ratios  $(F_e/F_{e \text{ dip}}) \times (B_{ze}/B_{ze \text{ dip}})$ , a quantity relevant to the form of the steady-state angular velocity profile of the plasma.

the field parameter product  $F_e |B_{ze}|$ , which appears on the right hand side of the Hill-Pontius equation Eq. (3.27). In Fig. 3.7b we show this product relative to the dipole, i.e.  $(F_e/F_{e \text{ dip}}) \times (B_{ze}/B_{ze \text{ dip}})$ , plotted versus  $\rho_e$ . As we have seen in Figs. 3.5b and 3.6b, the factor  $(B_{ze}/B_{ze \text{ dip}})$  is always less than unity, while  $(F_e/F_{e \text{ dip}})$  is always greater than unity. The deviation of these two factors from unity will therefore cancel in the product and, as can be seen in Fig. 3.7b, the latter deviates from unity (the horizontal dashed line) by less than a factor of 2 over the radial range out to  $\sim 60 R_J$ , and does not become very large beyond. The second compound field parameter is  $(F_e/\rho_e^2 |B_{ze}|) = (F_e/F_{e \text{ dip}}) / (B_{ze}/B_{ze \text{ dip}})$ , which occurs in the first (dominant) term in Eq. (3.28) for the field-aligned current. Here the above field factors combine to make a quotient which is large, as shown in Fig. 3.8. The value increases monotonically from near unity (again shown by the horizontal dotted line) at  $\sim 5 R_J$ , to reach 15.3 at  $100 R_J$ . The physical origins of the forms of these field parameters, and their implications for the current system, will be discussed below.

In contrast to the works of Hill (1979, 2001) and Pontius (1997), Cowley and Bunce (2001b) did not solve the Hill-Pontius equation to obtain an equatorial plasma angular velocity profile. They used instead an empirical representation of the plasma equatorial angular velocity observations that are outlined in Section 2.4.4. Overall, spacecraft observations indicate the plasma angular velocity is close to corotation within  $\sim 10\text{-}20 R_J$ , and then falls to  $\omega/\Omega_J \approx 0.5$  at  $\sim 50 R_J$ , and even smaller values at larger distances (should the current sheet extend beyond that distance in a particular local time sector). They therefore adopted the empirical form

$$\left( \frac{\omega}{\Omega_J} \right) = \frac{1}{\left( 1 + (\rho_e/\rho_{e0})^n \right)}, \quad (3.36)$$

where  $\rho_{e0} = 50 R_J$ . Thus for all positive  $n$   $\omega/\Omega_J \rightarrow 1$  as  $\rho_e \rightarrow 0$ ,  $\omega/\Omega_J = 0.5$  at  $\rho_e = \rho_{e0} = 50 R_J$ , and  $\omega/\Omega_J \rightarrow 0$  as  $\rho_e \rightarrow \infty$ . However, as  $n$  increases, so does the sharpness of the decrease in the angular velocity about  $\rho_{e0}$ . This is shown in Fig. 3.9, where  $\omega/\Omega_J$  is plotted against  $\rho_e$  in the range  $0\text{-}100 R_J$  for  $n = 2, 4$  and  $6$ . It was noted by

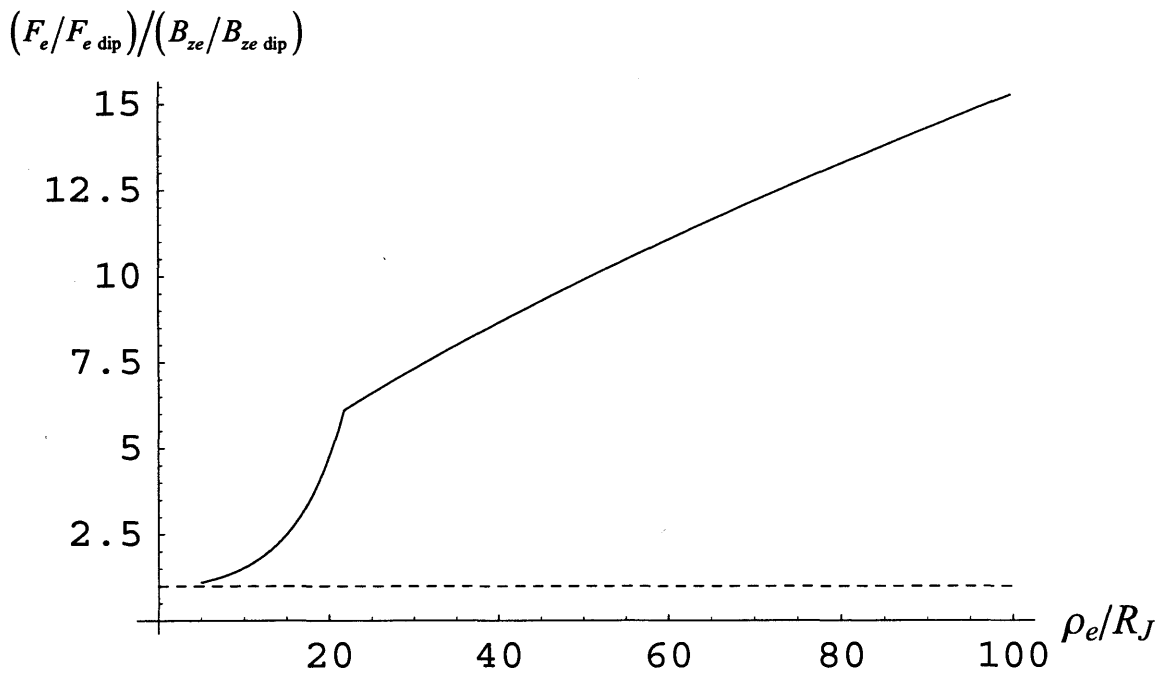


**Figure 3.8.** Plot showing the quotient of the ratios  $(F_e/F_{e \text{ dip}})/(B_{ze}/B_{ze \text{ dip}})$ , a quantity which determines the magnitude of the field-aligned current density. The horizontal dashed line indicates the value of unity.

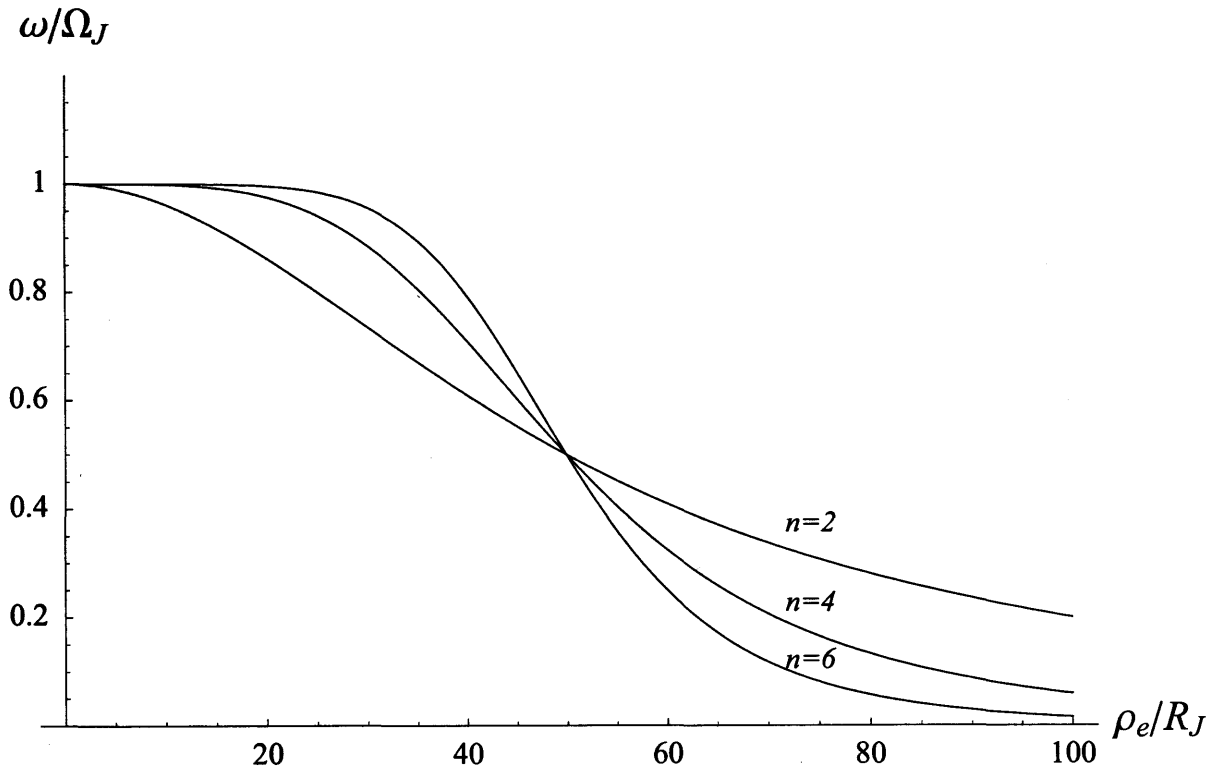
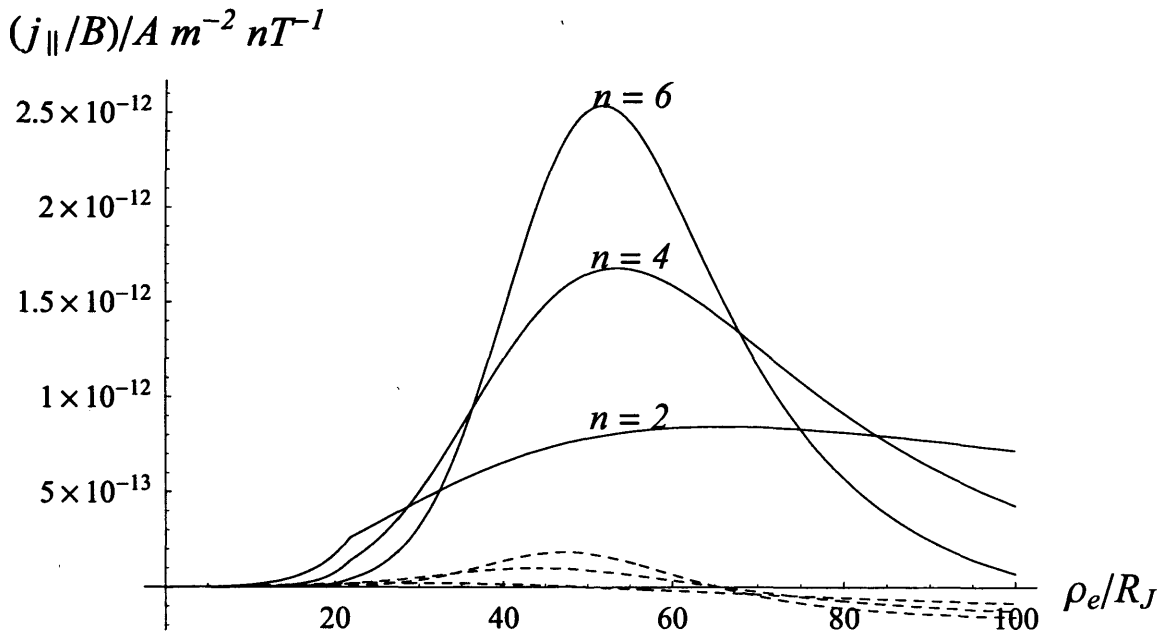


**Figure 3.9.** The empirical equatorial plasma angular velocity profiles considered by Cowley and Bunce (2001b). Plot is  $\omega/\Omega_J$  against jovicentric radial distance  $\rho_e$ . From Cowley and Bunce (2001b).

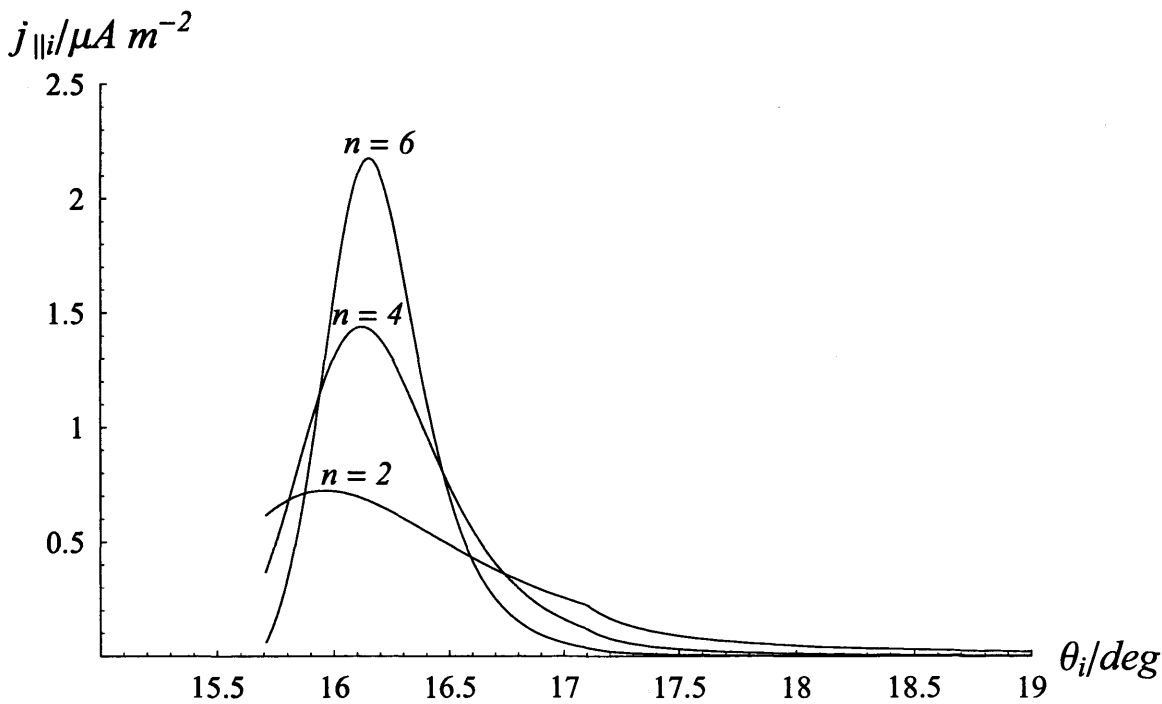
Cowley and Bunce (2001b) that, although they considered profiles with higher values of  $n$ , the  $n = 2$  profile has the weakest gradient, and thus was considered the most realistic in terms of observations. In addition, this profile has the virtue of having  $\omega/\Omega_j \propto \rho_e^{-2}$  at large distances, in conformity with the ideas discussed above on conservation of angular momentum at large distances.

Cowley and Bunce (2001b) calculated the field-aligned currents flowing in the system using these empirical models and compared the result to the case for the dipole. Their main results can be seen in Figs. 3.10 and 3.11. The field-aligned current into the northern face of the current sheet (or more specifically,  $(j_{\parallel}/B)$ ) is shown plotted against  $\rho_e$  for the current sheet field model (solid line) and the dipole (dashed line) in Fig. 3.10a. The field-aligned current in the ionosphere, i.e. at the feet of the field lines, is plotted versus dipole co-latitude for the current sheet model in Fig. 3.10b. The field-aligned voltage required by the Knight (1973) theory to drive the currents flowing in Figs. 3.10a and 3.10b is shown, plotted versus dipole co-latitude in Fig. 3.11a, assuming the values of  $N$  and  $W_{th}$  mentioned above, i.e.  $N = 0.01 \text{ cm}^{-3}$  and  $W_{th} = 2.5 \text{ keV}$ . Finally, the energy flux into the ionosphere from precipitating electrons is shown in Fig. 3.11b. It can be seen that the upward-directed field-aligned current density for the current sheet field model is typically more than an order of magnitude larger than that obtained for the dipole, and is sufficiently intense to require downward-acceleration of magnetospheric electrons through field-aligned voltages of several tens of kV, such that the precipitating electron energy flux will produce ‘main oval’ aurorae exceeding  $\sim 100 \text{ kR}$  in intensity, as observed. The origin of the field-aligned current enhancement effect lies in the differing mapping of field lines between the equatorial plane and the ionosphere in the two models, as discussed further by Cowley, Nichols, and Bunce (2002) and outlined below.

The analysis of Cowley and Bunce (2001b) was developed by Cowley, Nichols, and Bunce (2002), who, instead of calculating the field-aligned current using an empirical model for the angular velocity, took the current sheet field model used by Cowley and Bunce (2001b) and applied it to the steady state theory of Hill and Pontius to calculate the angular velocity self-consistently. They employed “reasonable” constant values of  $\Sigma_p^* = 0.25 \text{ mho}$  and  $\dot{M} = 1000 \text{ kg s}^{-1}$ , such that the characteristic distance over which the



(a)



(b)

**Figure 3.10.** Some field-aligned current parameters of the magnetosphere-ionosphere coupling current system calculated by Cowley and Bunce (2001b). Plot (a) shows  $(j_{\parallel}/B)$  plotted versus radial distance  $\rho_e$  for the current sheet model (solid lines) and dipole (dashed lines) for the values of  $n$  as indicated. Plot (b) shows the ionospheric field-aligned current  $j_{\parallel i}$  plotted versus ionospheric co-latitude  $\theta_i$ . From Cowley and Bunce (2001b).

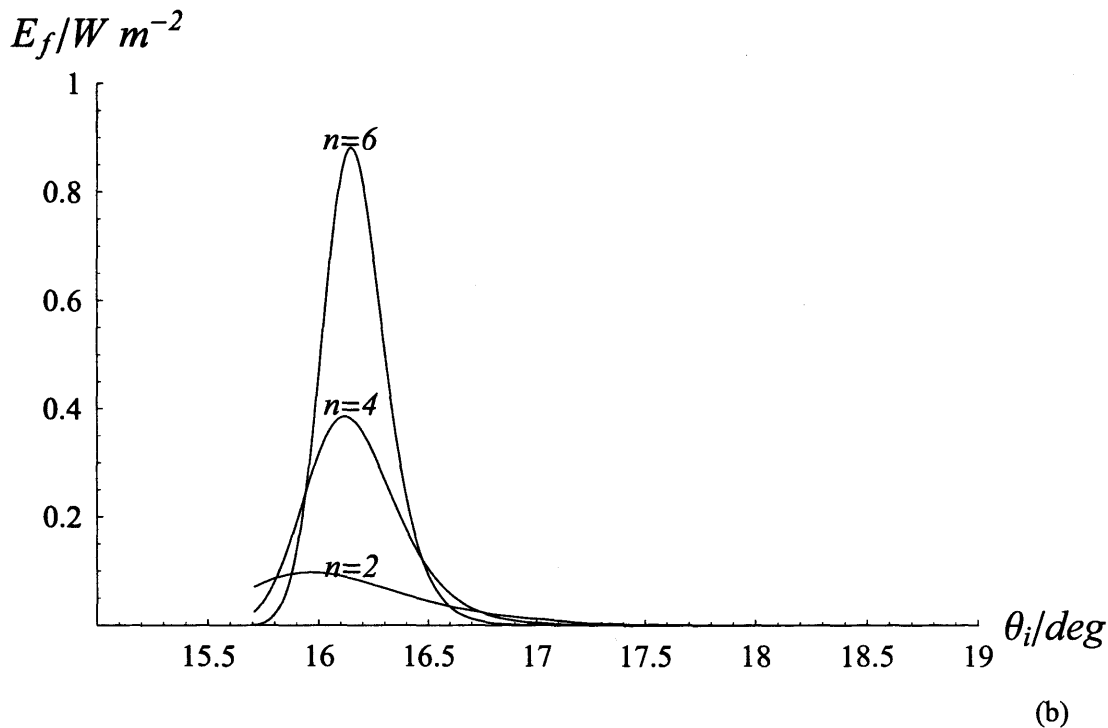
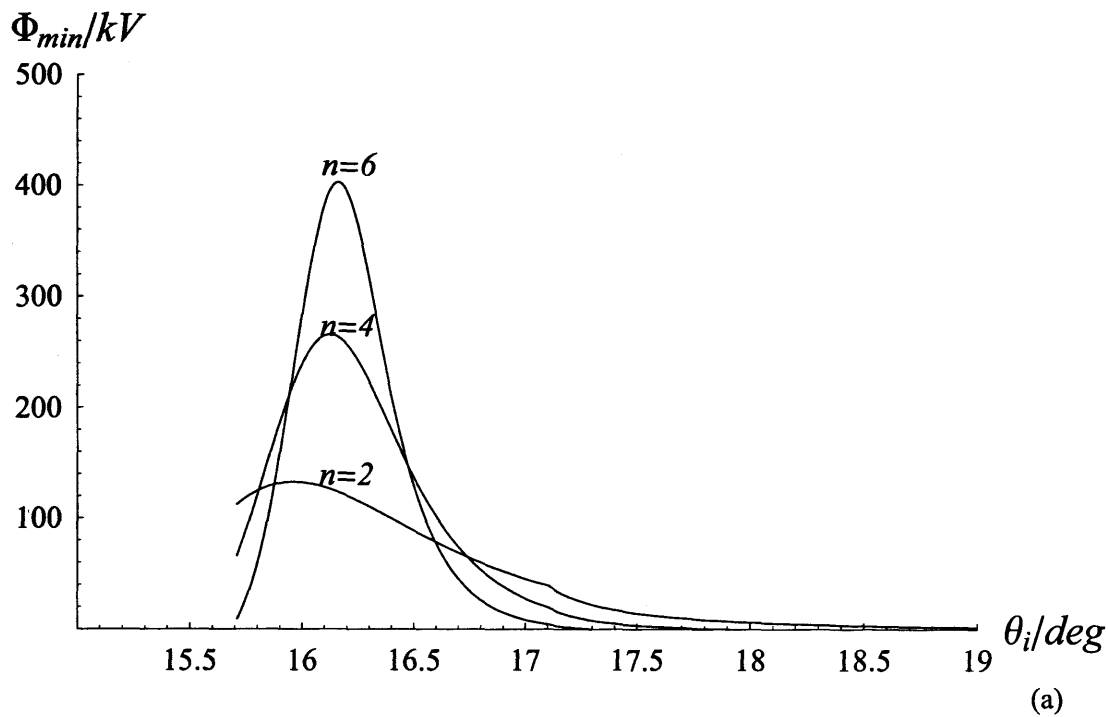


**Figure 3.11.** Plot (a) shows the field-aligned voltage  $\Phi_{min}$  required to drive the currents in Plots 3.10(a) and 3.10(b), versus ionospheric co-latitude  $\theta_i$  for the current sheet model and for the values of  $n$  as indicated. Plot (b) shows the energy flux into the ionosphere from auroral electron precipitation  $E_f$  versus ionospheric co-latitude  $\theta_i$ . From Cowley and Bunce (2001b).

plasma departs from rigid corotation (the ‘Hill distance’ given by Eq. (3.30)) is  $34.8 R_J$ . Their solution of the Hill-Pontius equation Eq. (3.27) is shown in Fig. 3.12a, where  $(\omega/\Omega_J)$  is plotted versus  $\rho_e$ . The solid line shows the solution for the current sheet field model, while for comparison the dashed line shows the result for a dipole, and the dot-dashed line shows the empirical form for the angular velocity used by Cowley and Bunce, i.e. Eq. (3.36) for  $n = 2$  shown in Fig. 3.9. It can be seen that, as found by Pontius (1997), the angular velocity profiles in the equatorial plane are similar. Numerically, the similar flow profiles are a consequence of the fact that, as shown in Fig. 3.7b, the field product  $F_e |B_{ze}|$  appearing on the RHS of Eq. (3.27) does not change greatly with the magnetic model, particularly in the region within the Hill distance, where the electromagnetic torque is significant. This term appears in the expression for the torque on the plasma, such that the larger this product, the larger the torque on the plasma, and the less rapidly will the angular velocity depart from rigid corotation with increasing distance. The situation is shown schematically in Fig. 3.13, which shows a given position at radial distance  $\rho_e$  in the equatorial plane threaded by both a current sheet and a dipole field. Clearly, the strength of the  $B_z$  field at a given distance is smaller for the current sheet field than for the dipole, thus resulting in a smaller torque on the plasma. This gives rise to the  $(B_{ze}/B_{ze \text{ dip}})$  factor in the above product. However, for a given plasma angular velocity, the equatorial current at a given radial distance is larger for the current sheet than for the dipole, hence working in the opposite direction. This arises from two factors, one physical, the other geometrical, which both come from the fact that the field lines from a given equatorial radial position map to the ionosphere at a significantly greater distance from the axis for the current sheet model than for the dipole, as pointed out in relation to Fig. 3.8. The first (physical) factor is that for a given plasma angular velocity, the actual ionospheric plasma velocity (proportional to the distance to the magnetic axis  $\rho_i$ ) will be larger for the current sheet model than for the dipole, and with it the ionospheric electric field, Pedersen current intensity, and equatorial current intensity will also be larger for the former than for the latter (Eqs. (3.7) and (3.8)). The second (geometric) factor is that the total current in a given angular sector of the ionosphere (equal to the total equatorial current in the same angular sector), is also proportional to distance from the axis, since the total current is proportional to the length of longitudinal arc in that angular sector in the ionosphere (Eq. (3.7)). Both of these effects

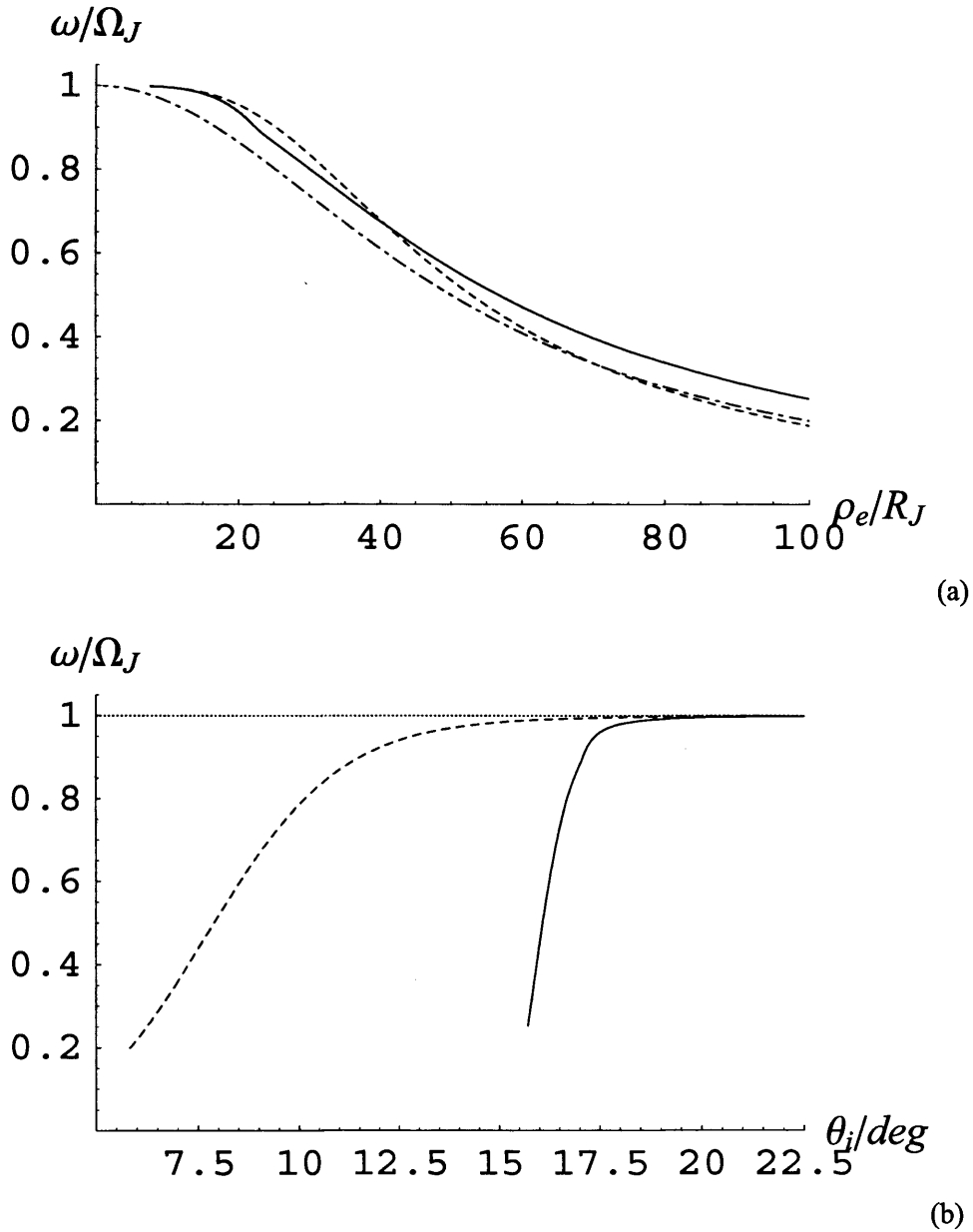


**Figure 3.12.** Plots showing the steady-state Hill-Pontius solutions for the equatorial plasma angular velocity as considered by Cowley, Nichols and Bunce (2002). Plot (a) shows  $(\omega/\Omega_J)$  versus equatorial radial distance  $\rho_e$  for the current sheet (solid line) and the dipole (dashed line) and, for comparison, the empirical model assumed by Cowley and Bunce (2001) for  $n=2$  (dot-dashed line). Plot (b) shows the current sheet and dipole angular velocity profiles mapped along the magnetic field lines into the ionosphere and plotted versus ionospheric co-latitude  $\theta_i$ . From Cowley, Nichols and Bunce (2002).

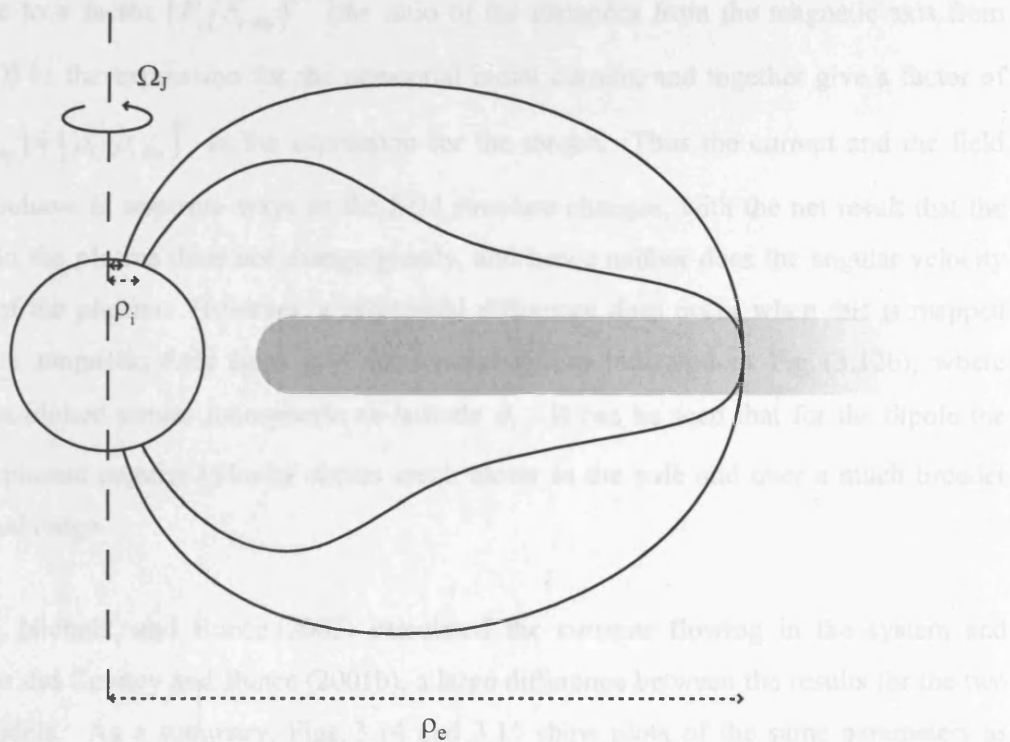


**Figure 3.13.** Schematic showing a given position  $\rho_e$  in the equatorial plane threaded by a dipole field and a distorted current sheet field. It can be seen that the decrease in the strength of the field  $|B_{ze}|$  at  $\rho_e$  associated with the current sheet field (and hence the decrease in electromagnetic torque) is offset by the fact that this field maps to the ionosphere at a larger perpendicular distance  $\rho_i$  from the magnetic axis, thereby increasing the ionospheric torque on the equatorial plasma. These factors work against each other to produce similar equatorial plasma angular velocity profiles for each model.

give rise to a factor  $(F_e/F_{e \text{ dip}})^{1/2}$  (the ratio of the distances from the magnetic axis from Eq. (3.3)) in the expression for the equatorial radial current, and together give a factor of  $(F_e/F_{e \text{ dip}}) = (\rho_i/\rho_{i \text{ dip}})^2$  in the expression for the torque. Thus the current and the field effects behave in opposite ways as the field structure changes, with the net result that the torque on the plasma does not change greatly, and hence neither does the angular velocity profile of the plasma. However, a substantial difference does occur when this is mapped along the magnetic field lines into the ionosphere, as indicated in Fig. (3.12b), where  $\omega/\Omega_j$  is plotted versus ionospheric co-latitude  $\theta_i$ . It can be seen that for the dipole the drop in plasma angular velocity occurs much closer to the pole and over a much broader latitudinal range.

Cowley, Nichols, and Bunce (2002) calculated the currents flowing in the system and found, as did Cowley and Bunce (2001b), a large difference between the results for the two field models. As a summary, Figs. 3.14 and 3.15 show plots of the same parameters as Figs. 3.10 and 3.11, with the current sheet results shown by the solid lines and the dipole results shown by the dashed lines. That is, Fig. 3.14a shows  $(j_{\parallel}/B)$  plotted versus radial distance  $\rho_e$ , Fig. 3.14b shows the ionospheric field-aligned current  $j_{\parallel i}$  plotted versus co-latitude  $\theta_i$ , Fig. 3.15a shows the field-aligned voltage  $\Phi_{\text{min}}$  required to drive the currents in Figs. 3.14a and 3.14b, and Fig. 3.15b shows the resulting energy flux  $E_f$  into the ionosphere, assuming the same values of  $N$  and  $W_{th}$  as above. It can be seen that, as found by Hill (2001), the dipole field results in a field aligned current which peaks at a few hundredths of a  $\mu\text{A m}^{-2}$  over a  $\sim 5^\circ$  range centred on  $\sim 10^\circ$  co-latitude. As discussed above, this is too weak to drive the main oval aurorae and occurs at a co-latitude  $\sim 5^\circ$  too low. On the other hand, the current sheet model results in a field-aligned current which peaks at  $\sim 0.4 \mu\text{A m}^{-2}$  over a  $\sim 2.5^\circ$  wide range centred on  $\sim 16^\circ$  co-latitude. Numerically, the larger values of the field-aligned current which occur in the current sheet model compared with the dipole model is due principally to the  $(F_e/\rho_e^2 |B_{ze}|) = (F_e/F_{e \text{ dip}})/(B_{ze}/B_{ze \text{ dip}})$  factor that appears in the dominant term in Eq. (3.28), and is plotted in Fig. 3.8. The large value of this term ensures that the field-aligned currents for a given equatorial angular velocity profile are larger for the current sheet field than for the dipole by around an order of

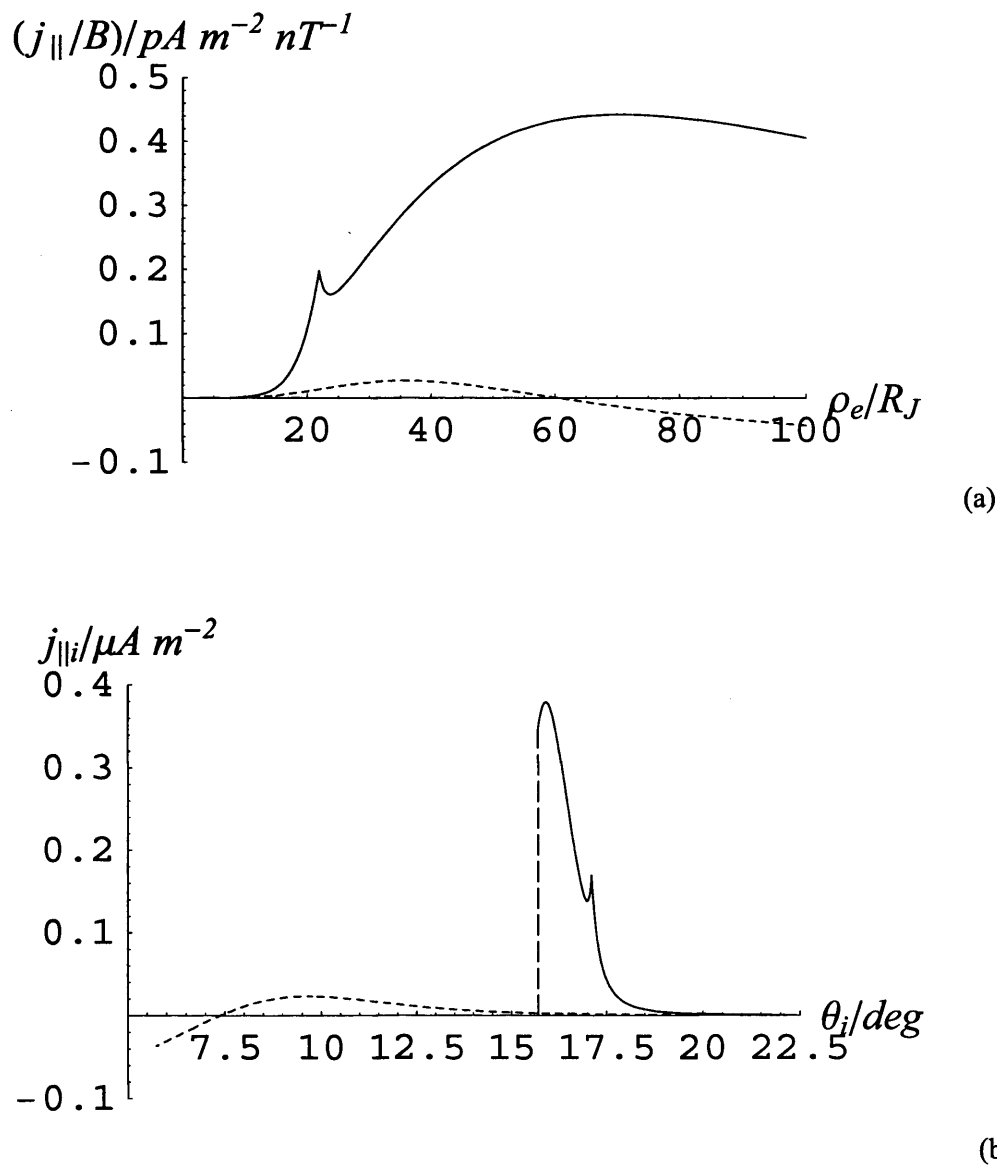
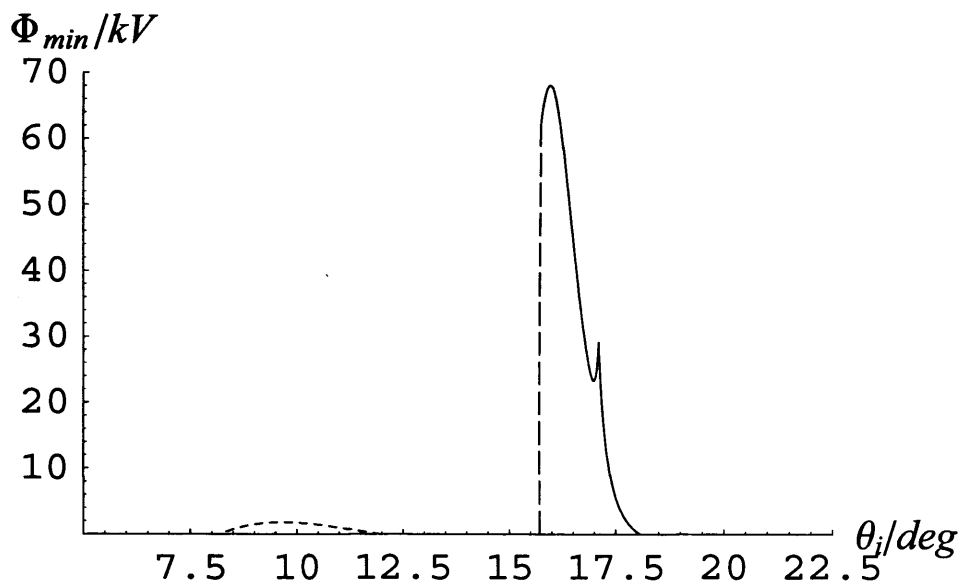
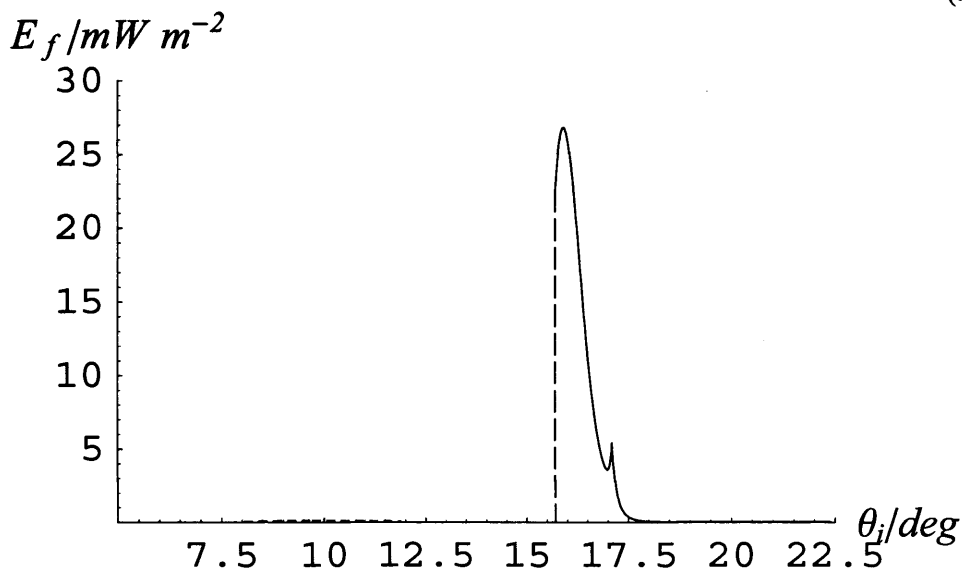


**Figure 3.14.** Some field-aligned current parameters of the magnetosphere-ionosphere coupling current system considered by Cowley, Nichols and Bunce (2002). All plots show the results for the current sheet model (solid lines) and the dipole model (dashed lines). Plot (a) shows  $(j_{\parallel}/B)$  plotted versus radial distance  $\rho_e$ . Plot (b) shows the ionospheric field-aligned current  $j_{\parallel i}$  plotted versus ionospheric co-latitude  $\theta_i$ . From Cowley, Nichols and Bunce (2002).



(a)



(b)

**Figure 3.15.** Plot (a) shows the field-aligned voltage  $\Phi_{min}$  required to drive the currents in Plots 3.14(a) and 3.14(b), versus ionospheric co-latitude  $\theta_i$ . Plot (b) shows the energy flux into the ionosphere from auroral electron precipitation  $E_f$  versus ionospheric co-latitude  $\theta_i$ . From Cowley, Nichols and Bunce (2002).

magnitude. Physically, the difference is due to two factors. The first is again that the field lines from a given equatorial radial distance map into the ionosphere at a larger distance from the magnetic axis for the current sheet than for the dipole, such that for a given equatorial plasma angular velocity the ionospheric plasma velocity, electric field, Pedersen current and Pedersen current divergence are also larger. This effect contributes a factor  $(F_e/F_{e \text{ dip}})^{1/2} \approx 2$  as can be seen in Fig. 3.7a. The second effect is simply that a given radial range in the equatorial plane maps into a much narrower latitudinal range in the ionosphere for the current sheet field than for a dipole, as a consequence of both the reduced equatorial  $B_{ze}$  field, giving a factor of  $(B_{ze \text{ dip}}/B_{ze}) \approx 2.5$  as shown in Fig. 3.5b, and the increased co-latitude of the field mapping, giving another factor of  $(F_e/F_{e \text{ dip}})^{1/2} \approx 2$ . Consequently, the latitudinal gradient of the ionospheric flow, and the divergence of the electric field and Pedersen current will be correspondingly increased by an overall factor of  $(F_e/F_{e \text{ dip}})/(B_{ze}/B_{ze \text{ dip}}) \approx 10$ . Both these effects thus work in the same direction, and lead to field-aligned current densities for the current sheet model which are an order of magnitude larger than those for the dipole model. As shown in Fig. 3.15, the consequence is that for the current sheet field model, a field-aligned voltage co-located with the field-aligned current and peaking at  $\sim 70$  kV is required to drive this current, and results in a peak energy flux of  $\sim 30 \text{ mW m}^{-2}$ , sufficient to drive a UV aurora intensity of  $\sim 300 \text{ kR}$ . This is comparable with observations of main auroral oval.

The results of Cowley, Nichols and Bunce (2002) thus showed that the field model chosen is crucial in determining the field-aligned current and auroral parameters associated with the magnetosphere-ionosphere coupling current system. However, as mentioned above their analysis as it stands is inconsistent for two reasons. The first rests in the fact that it is not expected that the Pedersen conductivity will be constant, as assumed in the above calculations. For example, Strobel and Atreya (1983) (and more recently Millward et al., 2002, see Chapter 5) estimated that significant auroral precipitation (as predicted by the above theory) would enhance the ionospheric Pedersen conductivity in this region from a background of a few tenths of a mho to  $\sim 10$  mho. This calls into question the approximation that  $\Sigma_p^*$  is constant in the above analysis, and further work to solve the equations self consistently, i.e. with a variable Pedersen conductivity built in, is required.

This is the issue addressed in Chapter 5. The first step on this road, however, is to examine the behaviour of the system as it stands over a range of values of  $\Sigma_p^*$  and  $\dot{M}$ , as neither of these quantities are at present known to great accuracy and the results of Hill (1979, 2001), Cowley and Bunce (2001b) and Cowley, Nichols and Bunce (2002) explored solutions for only a few spot values. This is the topic of the next chapter. The second inconsistency is due to the fact that the mapping between the equatorial plane and the ionosphere is carried out along equipotentials, whilst the outcome of the theory is the existence of significant field aligned voltages. The equations must therefore be solved with this effect self-consistently accounted for, and this is the topic of Chapter 6.

## ***Chapter 4***

# ***Magnetosphere-Ionosphere Coupling Currents in Jupiter's Middle Magnetosphere: Dependence on the Effective Ionospheric Pedersen Conductivity and Iogenic Plasma Mass Outflow Rate***

### ***4.1. Introduction***

As discussed in Chapter 3, the solutions for the plasma angular velocity and the current depend on two system parameters, the ‘effective’ value of the height-integrated ionospheric Pedersen conductivity, and the plasma mass outflow rate from the Io torus. Neither of these parameters is well determined at present, with estimates of the conductivity ranging from  $\sim 0.1$  to  $\sim 10$  mho, and estimates of the mass outflow rate from  $\sim 500$  to  $\sim 2000$   $\text{kg s}^{-1}$ . The purpose of this chapter is to examine how the solutions for the plasma angular velocity and coupling currents depend on these two system parameters for both dipole and current sheet field models. Some results for the dipole model have been presented previously by Hill (2001), as discussed in Chapter 3, who gave formulae for the magnitude and position of the extrema in both the total field-perpendicular current and in the field-aligned current. For the current sheet field model, however, only a few numerical solutions using ‘reasonable’ spot values of the system parameters have been previously published (Cowley and Bunce, 2001b; Cowley, Nichols and Bunce 2002; and Cowley, Bunce and Nichols, 2003; see Chapter 3). In this chapter we first introduce some simple analytic forms that are valid at small and large distances and which show how the solutions depend on the system parameters in these limits. We then provide a complete solution for the

dipole field, and go on to provide an approximate analytic solution for the current sheet model in which the equatorial field is taken to vary with distance as a power law. We compare this analytic solution both with numerically computed results, and with corresponding results for the dipole field. The work presented here thus provides detailed information on how the coupling current system depends on the two system parameters over a substantial range of values, here taken to be constant quantities in a given solution. This knowledge provides valuable background for the more complex studies in later chapters in which the system parameters are taken to vary in space, as may more generally be the case.

#### 4.2. Approximate forms for small and large distances

Before describing the full solutions for the case of the dipole and current sheet model, it is worth noting some simple approximate forms which are valid at small and large distances from the plasma source region. It is an important general property of the physically interesting solutions of the governing equations (see Chapter 3) that at small radial distances the currents depend only on  $\dot{M}$  and not on  $\Sigma_p^*$ , while at large radial distances they depend only on  $\Sigma_p^*$  and not on  $\dot{M}$ . The small- $\rho_e$  approximations follow from a series solution of the Hill-Pontius equation Eq. (3.27) for the case in which  $(\omega/\Omega_j)=1$  at  $\rho_e=0$  (such that the plasma rigidly corotates at small distances). Taking  $(\dot{M}/\Sigma_p^*)$  as the formal expansion parameter, we write

$$\frac{\omega}{\Omega_j} = \sum_{n=0}^{\infty} a_n \left( \frac{\dot{M}}{\Sigma_p^*} \right)^n, \quad (4.1)$$

and substituting into Eq. (3.27) and equating coefficients of powers of  $(\dot{M}/\Sigma_p^*)$  we find that  $a_0=1$ , and that for  $n \geq 1$  the  $a_n$  are determined by the recurrence relation

$$a_{n+1} = -\frac{1}{8\pi\rho_e F_e |B_{ze}|} \frac{d}{d\rho_e} (\rho_e^2 a_n). \quad (4.2)$$

Thus the leading term describing the breakdown of rigid corotation in the inner region, which we take as our small- $\rho_e$  ('S') approximation, is

$$\left(\frac{\omega}{\Omega_J}\right)_S = 1 - \frac{\dot{M}}{4\pi\Sigma_p^*F_e|B_{ze}|} \quad (4.3)$$

as given previously (but not derived in this manner) by Cowley, Bunce and Nichols (2003). We note that the departure from rigid corotation is proportional to  $\dot{M}$  and inversely proportional to  $\Sigma_p^*$ . When substituted into Eqs. (3.10), (3.12)-(3.15) and (3.17) to find the corresponding approximations for the currents, we find that the currents on a given field line depend only on  $\dot{M}$  and not on  $\Sigma_p^*$

$$i_{pS} = \frac{\dot{M}\Omega_J}{2\pi\rho_i|B_{ze}|}, \quad I_{pS} = \frac{\dot{M}\Omega_J}{|B_{ze}|}, \quad (4.4a,b)$$

$$i_{\rho S} = \frac{\dot{M}\Omega_J}{\pi\rho_e|B_{ze}|}, \quad I_{\rho S} = \frac{2\dot{M}\Omega_J}{|B_{ze}|}, \quad (4.4c,d)$$

$$\left(\frac{j_{\parallel}}{B}\right)_S = -\frac{\dot{M}\Omega_J}{2\pi\rho_e|B_{ze}|^3} \frac{d|B_{ze}|}{d\rho_e}, \quad \text{and} \quad j_{\parallel S} = -\frac{\dot{M}\Omega_J B_J}{\pi\rho_e|B_{ze}|^3} \frac{d|B_{ze}|}{d\rho_e}. \quad (4.4e,f)$$

While the currents are formally proportional to  $\Sigma_p^*$ , the departure of the plasma from rigid corotation in this regime, and hence the electric field in the ionosphere, is inversely proportional to  $\Sigma_p^*$ , so these dependencies cancel, leaving the currents proportional only to  $\dot{M}$ . These expressions can also be derived directly by substituting  $\omega = \Omega_J$  into the left side of Eq. (3.26) and the substituting into the equations for the currents, Eqs. (3.10), (3.12)-(3.15) and (3.17), i.e. they are just the currents required to maintain near-rigid corotation in the inner region.

The large- $\rho_e$  ('L') approximations are simply obtained by putting  $(\omega/\Omega_J)_L = 0$  into Eqs. (3.10), (3.12)-(3.15) and (3.17) and assuming that  $\rho_e$  is large, to find

$$i_{pL} = 2\Sigma_p^* B_J \Omega_j \rho_i , \quad I_{pL} = 4\pi\Sigma_p^* B_J \Omega_j \rho_i^2 , \quad (4.5a,b)$$

$$i_{\rho L} = \frac{4\Sigma_p^* \Omega_j F_e}{\rho_e} , \quad I_{\rho L} = 8\pi\Sigma_p^* \Omega_j F_e , \quad (4.5c,d)$$

$$\left(\frac{j_{\parallel}}{B}\right)_L = -2\Sigma_p^* \Omega_j , \quad \text{and} \quad j_{\parallel i L} = -4\Sigma_p^* B_J \Omega_j . \quad (4.5e,f)$$

which thus depend only on  $\Sigma_p^*$  and not on  $\dot{M}$ . This follows from the fact that in this approximation the angular velocity is specified as being zero in the inertial frame, so the currents depend only on  $\Sigma_p^*$  and no reference is made to  $\dot{M}$ . A higher order form for large- $\rho_e$  can also be derived (subscript 'L'), in which the non-zero plasma angular velocity falls with distance as  $\rho_e^{-2}$  due to negligible ionospheric torque on the equatorial plasma at large distances. This will be discussed in more detail later.

### 4.3. Plasma angular velocity and coupling current system for a dipole magnetic field model

Following the earlier work of Hill (1979, 2001), Cowley and Bunce (2001b) and Cowley, Nichols and Bunce (2002) described in the previous chapter, in this section we provide a complete analytic solution for the case where the poloidal field is taken to be the planetary dipole alone. The results include a normalised solution which shows how the angular velocity and each current component vary in amplitude and spatial scales with the system parameters. We also discuss the behaviour of the un-normalised quantities, which more readily show the behaviour at small and large distances described in the above section. These results form a useful introduction to, and point of comparison with, the results for the current sheet field to be presented in the Section 4.4.

### 4.3.1. Normalised solution

Introducing Eq. (3.5) into Eq. (3.27), the Hill-Pontius equation for the dipole field is

$$\frac{\rho_e}{2} \frac{d}{d\rho_e} \left( \frac{\omega}{\Omega_J} \right) + \left( \frac{\omega}{\Omega_J} \right) = 2 \left( \frac{R_{De}}{\rho_e} \right)^4 \left( 1 - \frac{\omega}{\Omega_J} \right), \quad (4.6)$$

where  $R_{De}$  is our notation for the equatorial ‘Hill distance’ ( $\equiv \rho_H$ ) for the dipole field (subscript ‘D’), given by

$$\frac{R_{De}}{R_J} = \left( \frac{2\pi\Sigma_p^* B_J^2 R_J^2}{\dot{M}} \right)^{1/4}. \quad (4.7)$$

From Eq. (4.6) it can be seen that the angular velocity in this case is a function only of  $(\rho_e/R_{De})$ , so that the solutions scale with distance as  $R_{De}$  and hence with the system parameters as  $(\Sigma_p^*/\dot{M})^{1/4}$ . As outlined below,  $R_{De}$  varies between  $\sim 30$  and  $\sim 90 R_J$  over the range of parameters mentioned in the introduction, thus being comparable to the radial scale of the jovian middle magnetosphere (which extends to distances between  $\sim 40$  and  $\sim 100 R_J$ , depending on local time and the state of the magnetosphere). As discussed in Chapter 3, the general analytic solution of Eq. (4.6) can be obtained by the integration factor method

$$\left( \frac{\omega}{\Omega_J} \right) = \sqrt{\pi} \left( \frac{R_{De}}{\rho_e} \right)^2 \exp \left[ \left( \frac{R_{De}}{\rho_e} \right)^4 \right] \left[ \operatorname{erfc} \left[ \left( \frac{R_{De}}{\rho_e} \right)^2 \right] + K \right], \quad (4.8)$$

where  $\operatorname{erfc}(z)$  is the complementary error function (related to the error function  $\operatorname{erf}(z)$  by  $\operatorname{erfc}(z) = 1 - \operatorname{erf}(z)$ ), and  $K$  is a constant of integration. All solutions diverge at the origin except the solution with  $K = 0$ . This special solution rigidly corotates (i.e.  $(\omega/\Omega_J) = 1$ ) when  $(\rho_e/R_{De})$  goes to zero, and is the solution derived previously by Hill (1979, 2001), but where we use the ionospheric approximation  $B_i \approx 2B_J$ .

Mapping to the ionosphere is accomplished using Eq. (3.6). We introduce an ionospheric counterpart of the ‘Hill distance’ given by

$$R_{Di} = \sqrt{\frac{R_J}{R_{De}}} R_J = \left( \frac{\dot{M}}{2\pi \Sigma_p^* B_J^2 R_J^2} \right)^{1/8} R_J, \quad (4.9)$$

such that the angular velocity mapped to the ionosphere is a function only of  $(\rho_i/R_{Di})$ , where

$$\left( \frac{\rho_i}{R_{Di}} \right) = \sqrt{\frac{R_{De}}{\rho_e}}. \quad (4.10)$$

Solutions mapped to the ionosphere thus scale with distance from the magnetic axis as  $R_{Di}$ , and hence with the system parameters as  $(\dot{M}/\Sigma_p^*)^{1/8}$ . The value of  $R_{Di}$  varies only between  $\sim 0.1$  and  $\sim 0.2 R_J$  over the range of parameters mentioned above.

The solid lines in Figs. 4.1a and 4.1b show the normalised angular velocity solution with  $K=0$  plotted versus  $(\rho_e/R_{De})$  in the equatorial plane, and versus  $(\rho_i/R_{Di})$  in the ionosphere, respectively. It can be seen in Fig. 4.1a that near-rigid corotation is maintained to  $(\rho_e/R_{De}) \approx 0.5$ , beyond which  $(\omega/\Omega_J)$  decreases rapidly, reaching  $\sim 0.758$  when  $(\rho_e/R_{De})=1$  and  $0.5$  when  $(\rho_e/R_{De}) \approx 1.52$ . At large distances  $(\omega/\Omega_J)$  falls approximately as the inverse square of the distance due to the ineffective nature of the ionospheric torque, the effective exponent  $m$  describing the rate of decrease,  $\omega \propto \rho_e^{-m}$ , falling below  $-1.9$  for  $(\rho_e/R_{De}) \geq 4.682$ . We also note that solutions started with non-zero  $K$  within  $(\rho_e/R_{De}) \leq 0.5$  converge very rapidly onto this solution at larger distances, such that the solutions are only weakly dependent on the choice of boundary condition in this case (Cowley, Bunce and Nichols., 2003). In Fig. 4.1b the angular velocity rises from zero at the pole to near-rigid corotation beyond  $(\rho_i/R_{Di}) \approx 1.5$ .

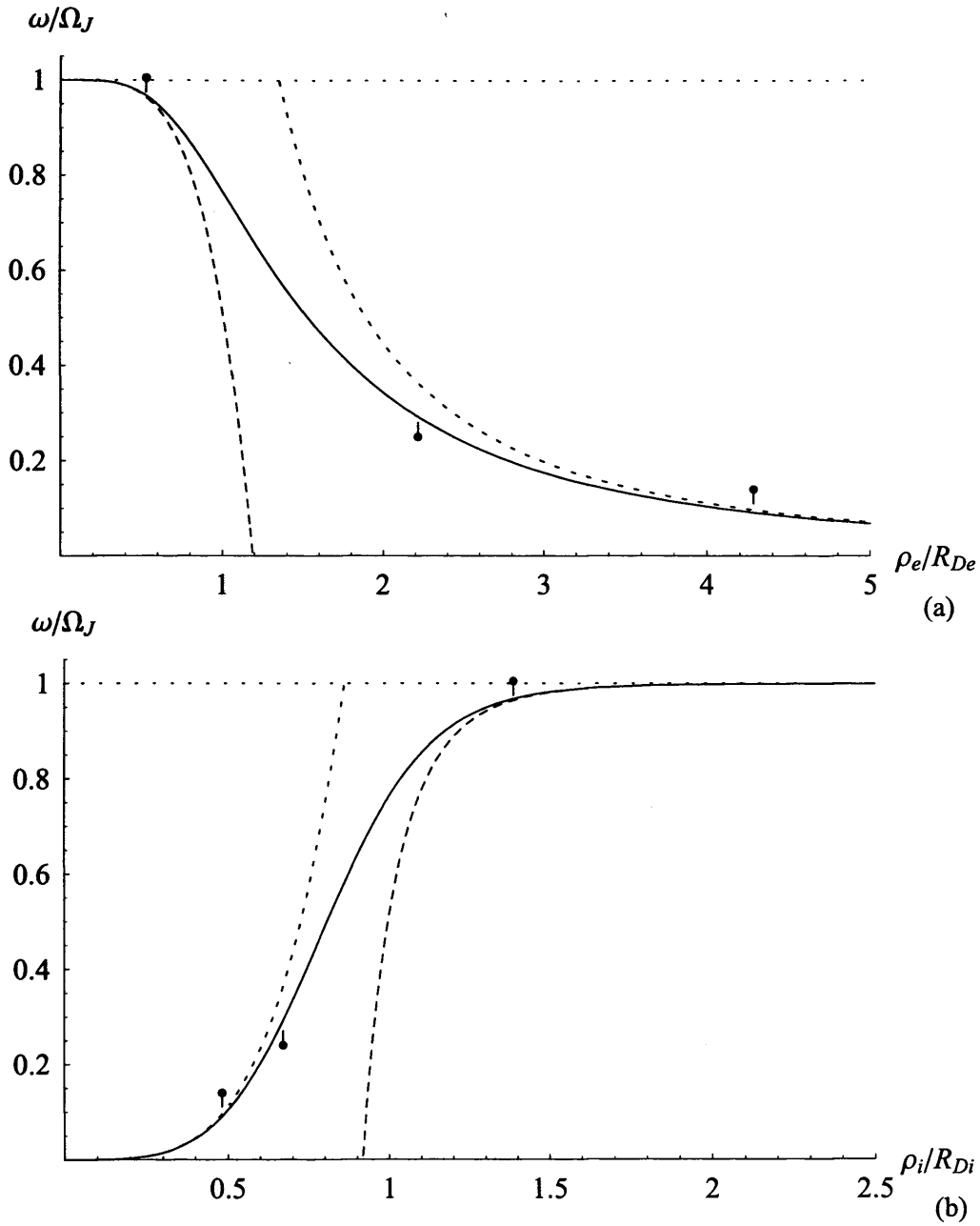


**Figure 4.1.** Plots of the steady state plasma angular velocity profile for a dipole magnetic field, shown (a) versus normalised equatorial radial distance ( $\rho_e/R_{De}$ ), and (b) versus normalised distance from the magnetic axis ( $\rho_i/R_{Di}$ ) in the ionosphere. The solid line in each case shows the full solution obtained from Eq. (4.8) with  $K = 0$ , such that the plasma rigidly corotates at small radial distances. The long-dashed lines show the small  $\rho_e$  form given by Eq. (4.11), while the large  $\rho_e$  form is just  $(\omega/\Omega_J)_L = 0$ . The downward-pointing tick-marks indicate the limits of validity of both the small and large  $\rho_e$  approximations as defined by Eq. (4.12). The short-dashed lines show the higher-order large  $\rho_e$  form given by Eq. (4.13), whose limit of validity defined by Eq. (4.14) is indicated by the upward-pointing tick-mark. The horizontal dotted lines indicate the condition for rigid corotation,  $(\omega/\Omega_J) = 1$ .

The dashed lines in Fig. 4.1 show the approximate forms mentioned in the above section, with the tick-marks indicating their regimes of validity. The long-dashed lines show the small- $\rho_e$  ('S') approximation given by Eq. (4.3), which in normalised form becomes

$$\left(\frac{\omega}{\Omega_J}\right)_S = 1 - \frac{1}{2} \left(\frac{\rho_e}{R_{De}}\right)^4 = 1 - \frac{1}{2} \left(\frac{R_{Di}}{\rho_i}\right)^8. \quad (4.11)$$

(We note that the series generated by Eq. (4.1) is the same as that obtained by asymptotic expansion of the error function in Eq. (4.8) for large argument.) The approximate form falls away from rigid corotation more quickly than the full solution, and reaches zero, equal to the large- $\rho_e$  ('L') approximation  $(\omega/\Omega_J)_L = 0$ , at  $(\rho_e/R_{De}) = \sqrt[4]{2} \approx 1.189$ . We define the limits of validity of these approximations as being the points where

$$\left(1 - (\omega/\Omega_J)_{S,L}\right) = 1.1 \left(1 - (\omega/\Omega_J)\right), \quad (4.12)$$

such that the departure from rigid corotation given by the approximate form exceeds that of the full solution by 10% of the latter. At these points the forms for the field-perpendicular currents thus also exceed those of the full solution by 10%. The outer limit of validity of the small  $\rho_e$  form then lies at  $(\rho_{eS}/R_{De}) \approx 0.516$  where  $(1 - (\omega/\Omega_J)) \approx 0.032$ , while the inner limit of validity of the large  $\rho_e$  form lies at  $(\rho_{eL}/R_{De}) \approx 4.284$ , where (since  $(\omega/\Omega_J)_L = 0$ )  $(\omega/\Omega_J) \approx 0.091$ . These limiting positions are shown by the downward-pointing tick-marks in Fig. 4.1.

The short-dashed lines in Fig. 4.1 show the higher-order large- $\rho_e$  form ('L'), in which the plasma angular velocity falls with distance as  $\rho_e^{-2}$  due to negligible ionospheric torque. Noting that both the exponential and the error function go to unity in Eq. (4.8) as  $\rho_e \rightarrow \infty$ , we find with Hill (1979) that for  $K = 0$

$$\left(\frac{\omega}{\Omega_J}\right)_{L'} = \sqrt{\pi} \left(\frac{R_{De}}{\rho_e}\right)^2. \quad (4.13)$$

The limit of validity of this approximation is similarly defined as the point where

$$\left(1 - (\omega/\Omega_J)_{L'}\right) = 0.9 \left(1 - (\omega/\Omega_J)\right) , \quad (4.14)$$

such that the departure from rigid corotation given by the approximation is less than that of the full solution by 10% of the latter, and similarly for the field-perpendicular currents. With this condition the inner limit of validity lies at  $(\rho_{eL'}/R_{De}) \approx 2.209$ , where  $(\omega/\Omega_J) \approx 0.292$ , and is marked by the upward-pointing tick-marks in Fig. 4.1.

The normalised solutions for the current components then follow from Eqs. (3.10), (3.12)-(3.15) and (3.17), giving

$$\frac{i_P}{i_{PD}} = 2 \left( \frac{\rho_i}{R_{Di}} \right) \left( 1 - \frac{\omega}{\Omega_J} \right) \quad \text{where} \quad i_{PD} = \left( \frac{\Sigma_P^* \dot{M}}{2\pi} \right)^{1/8} (B_J R_J)^{3/4} \Omega_J , \quad (4.15a)$$

$$\frac{I_P}{I_{PD}} = 4\pi \left( \frac{\rho_i}{R_{Di}} \right)^2 \left( 1 - \frac{\omega}{\Omega_J} \right) \quad \text{where} \quad I_{PD} = \left( \frac{\Sigma_P^* \dot{M}}{2\pi} \right)^{1/4} (B_J R_J^3)^{1/2} \Omega_J , \quad (4.15b)$$

$$\frac{i_\rho}{i_{\rho D}} = 4 \left( \frac{R_{De}}{\rho_e} \right)^2 \left( 1 - \frac{\omega}{\Omega_J} \right) \quad \text{where} \quad i_{\rho D} = \left( \frac{\Sigma_P^* \dot{M}}{2\pi} \right)^{1/2} \Omega_J , \quad (4.15c)$$

$$\frac{I_\rho}{I_{\rho D}} = 8\pi \left( \frac{R_{De}}{\rho_e} \right) \left( 1 - \frac{\omega}{\Omega_J} \right) \quad \text{where} \quad I_{\rho D} = \left( \frac{\Sigma_P^* \dot{M}}{2\pi} \right)^{1/4} (B_J R_J^3)^{1/2} \Omega_J , \quad (4.15d)$$

$$\frac{(j_{\parallel}/B)}{(j_{\parallel}/B)_D} = 2 \left[ 2 \left( \frac{\omega}{\Omega_J} \right) - \left( 1 + 4 \left( \frac{R_{De}}{\rho_e} \right)^4 \right) \left( 1 - \frac{\omega}{\Omega_J} \right) \right] \quad \text{where} \quad (j_{\parallel}/B)_D = \Sigma_P^* \Omega_J , \quad (4.15e)$$

$$\frac{j_{\parallel i}}{j_{\parallel i D}} = 2 \left[ 2 \left( \frac{\omega}{\Omega_J} \right) - \left( 1 + 4 \left( \frac{\rho_i}{R_{Di}} \right)^8 \right) \left( 1 - \frac{\omega}{\Omega_J} \right) \right] \quad \text{where} \quad j_{\parallel i D} = 2 \Sigma_P^* B_J \Omega_J . \quad (4.15f)$$

We note that Eqs. (4.15b) and (4.15d) are equivalent to Hill's (2001) Eq. (A13), while Eqs. (4.15e) and (4.15f) are the same as Hill's Eq. (A12). These normalised forms are plotted as solid lines in Figs. 4.2-4.4 versus either  $(\rho_e/R_{De})$  or  $(\rho_i/R_{Di})$  as appropriate. The values and positions of principal features are also tabulated in Table 4.1 in normalised units.

The dashed lines and tick-marks in Figs. 4.2-4.4 then show approximate forms in the same format as Fig. 4.1 for the angular velocity. Specifically, for small- $\rho_e$  the long-dashed lines show the currents obtained by introducing Eq. (4.11) (the 'S' approximation) into Eq. (4.15) to give

$$\left(\frac{i_p}{j_{PD}}\right)_S = \left(\frac{R_{Di}}{\rho_i}\right)^7, \quad \left(\frac{I_p}{I_{PD}}\right)_S = 2\pi \left(\frac{R_{Di}}{\rho_i}\right)^6, \quad (4.16a,b)$$

$$\left(\frac{i_\rho}{j_{\rho D}}\right)_S = 2 \left(\frac{\rho_e}{R_{De}}\right)^2, \quad \left(\frac{I_\rho}{I_{\rho D}}\right)_S = 4\pi \left(\frac{\rho_e}{R_{De}}\right)^3, \quad (4.16c,d)$$

$$\left(\frac{(j_{\parallel}/B)}{(j_{\parallel}/B)_D}\right)_S = 3 \left(\frac{\rho_e}{R_{De}}\right)^4, \quad \text{and} \quad \left(\frac{j_{\parallel i}}{j_{\parallel i D}}\right)_S = 3 \left(\frac{R_{Di}}{\rho_i}\right)^8. \quad (4.16e,f)$$

where we note that to quote the small- $\rho_e$  approximation to the field-aligned current correctly to  $(\rho_e/R_{De})^4$  in (4.16e) one must actually employ the small- $\rho_e$  approximation for the angular velocity to third order (given for the dipole by Eq. (6.35) with  $\varepsilon = 0$ ), due to the  $(R_{De}/\rho_e)^4$  term in Eq. (4.15e). This similarly applies for the ionospheric field-aligned current in Eq. (4.16f). The expressions for the currents in Eq. (4.16) are the same as Eq. (4.4) for a dipole field, when expressed in normalised form. This 'S' approximation is drawn to the point where  $(\omega/\Omega)_S$  falls to zero. Beyond this we draw the currents obtained by introducing  $(\omega/\Omega)_L = 0$  into Eq. (4.15) (the 'L' approximation) and assuming that  $\rho_e$  is large, to give

Feature	$\left(\frac{\rho_e}{R_{De}}\right)$	$\left(\frac{\rho_i}{R_{Di}}\right)$	$\left(\frac{\omega}{\Omega_j}\right)$
Maximum upward field-aligned current density $((j_{\parallel}/B)/(j_{\parallel}/B)_D)_{max} = (j_{\parallel i}/j_{\parallel iD})_{max} \approx 0.6111$	1.0203	0.9900	0.7467
Maximum sheet-integrated equatorial radial current $(i_{\rho}/i_{\rho D})_{max} \approx 0.9809$	1.1034	0.9520	0.7014
Plasma angular velocity falls to $\left(\frac{\omega}{\Omega_j}\right) = 0.5$	1.5201	0.8111	0.5
Maximum azimuth-integrated total current $(I_{\rho}/I_{\rho D})_{max} = 2(I_P/I_{PD})_{max} \approx 8.404$ Field-aligned current passes through zero	1.7409	0.7579	0.4178
Maximum height-integrated ionospheric Pedersen current $(i_P/i_{PD})_{max} \approx 0.9631$	2.5674	0.6241	0.2284
Maximum downward field-aligned current density $((j_{\parallel}/B)/(j_{\parallel}/B)_D)_{min} = (j_{\parallel i}/j_{\parallel iD})_{min} = -2$	$\infty$	0	0

**Table 4.1.** Principal features of the plasma angular velocity and coupling current system for a dipole field in normalised units.

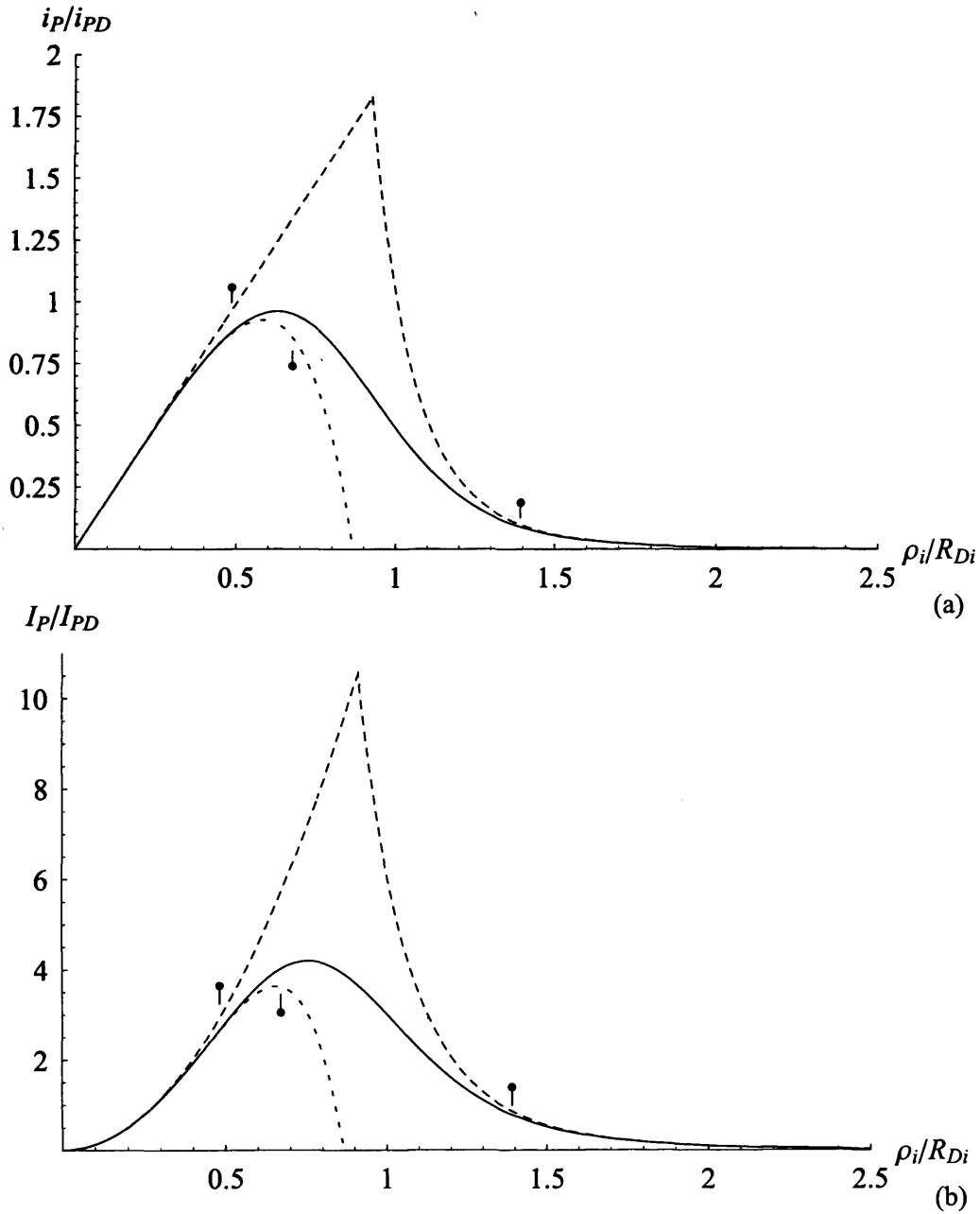


**Figure 4.2.** Plots of (a) the normalised height-integrated ionospheric Pedersen current intensity, and (b) the normalised azimuth- and height-integrated total ionospheric Pedersen current for a dipole magnetic field, plotted versus normalised distance from the magnetic axis ( $\rho_i/R_{Di}$ ) in the ionosphere. The normalization constants are given by Eqs. (4.15a) and (4.15b). The solid lines show the full solutions given by Eqs. (4.8) and (4.15a,b), while the long-dashed lines show the small- and large- $\rho_e$  forms given by Eqs. (4.16a,b) and (4.17a,b), drawn to a common boundary at  $(\rho_i/R_{Di}) = 1/\sqrt[3]{2}$ . The downward-pointing tick-marks show the limits of validity of these approximate forms as defined by Eq. (4.12) (as in Fig. 4.1). The short-dashed lines show the higher-order large- $\rho_e$  form given by Eq. (4.13), whose limit of validity defined by Eq. (4.14) is indicated by the upward-pointing tick-mark.

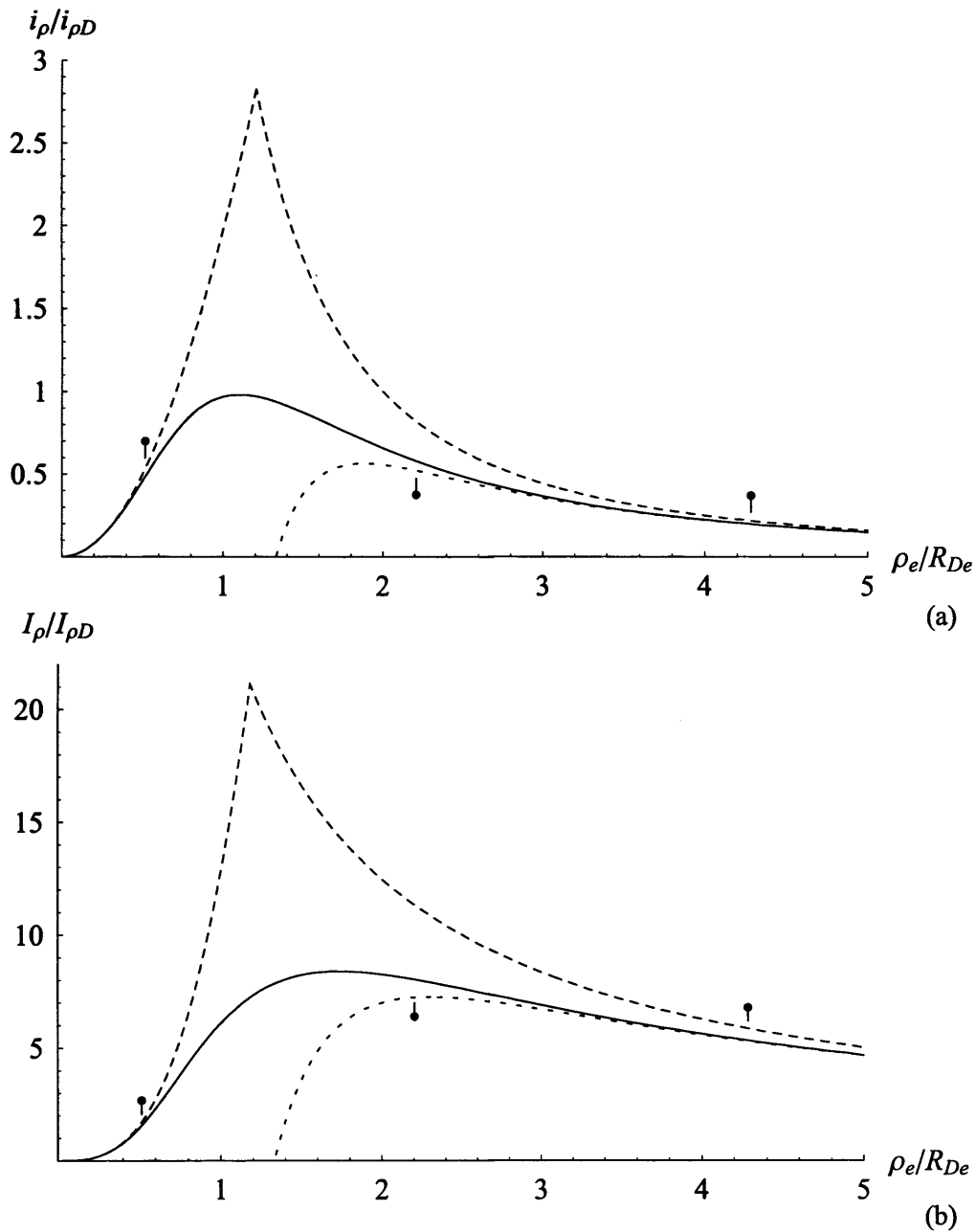


**Figure 4.3.** Plots of (a) the normalised current sheet-integrated equatorial radial current intensity, and (b) the normalised azimuth- and current sheet-integrated total equatorial radial current for a dipole magnetic field, plotted versus normalised equatorial radial distance ( $\rho_e/R_{De}$ ). The normalization constants are given by Eqs. (4.15c) and (4.15d). The solid lines show the full solutions given by Eqs. (4.8) and (4.15c,d), while the long-dashed lines show the small- and large- $\rho_e$  forms given by Eqs. (4.16c,d) and (4.17c,d), drawn to a common boundary at  $(\rho_e/R_{De}) = \sqrt{2}$ . The tick-marks are in the same format as Fig. 4.2.

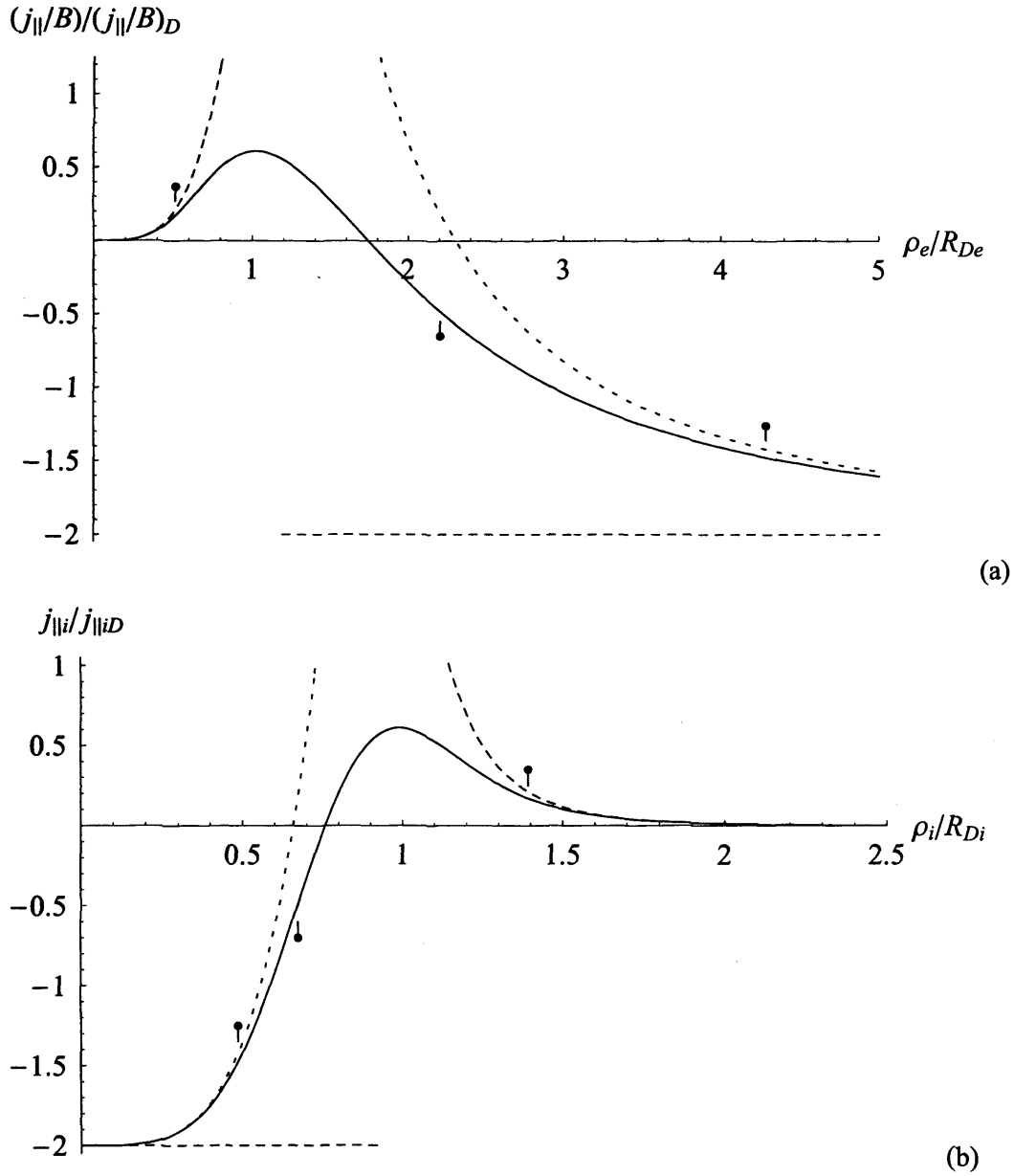


**Figure 4.4.** Plots of (a) the normalised equatorial field-aligned current density per unit magnetic field strength, plotted versus normalised equatorial radial distance ( $\rho_e/R_{De}$ ), and (b) the normalised field-aligned current density just above the ionosphere for a dipole magnetic field, plotted normalised distance from the magnetic axis ( $\rho_i/R_{Di}$ ) in the ionosphere. The normalization constants are given by Eqs. (4.15e) and (4.15f). The solid lines show the full solutions given by Eqs. (4.8) and (4.15e,f), while the long-dashed lines show the small- and large- $\rho_e$  forms given by Eqs. (4.16e,f) and (4.17e,f), drawn to a common boundary at  $(\rho_e/R_{De}) = \sqrt[4]{2}$  and  $(\rho_i/R_{Di}) = 1/\sqrt[4]{2}$  respectively. The tick-marks are in the same format as Fig. 4.2.

$$\left(\frac{i_p}{i_{pD}}\right)_L = 2\left(\frac{\rho_i}{R_{Di}}\right), \quad \left(\frac{I_p}{I_{pD}}\right)_L = 4\pi\left(\frac{\rho_i}{R_{Di}}\right)^2, \quad (4.17a,b)$$

$$\left(\frac{i_\rho}{i_{\rho D}}\right)_L = 4\left(\frac{R_{De}}{\rho_e}\right)^2, \quad \left(\frac{I_\rho}{I_{\rho D}}\right)_L = 8\pi\left(\frac{R_{De}}{\rho_e}\right), \quad (4.17,c,d)$$

$$\left(\frac{(j_{\parallel}/B)}{(j_{\parallel}/B)_D}\right)_L = -2, \quad \text{and} \quad \left(\frac{j_{\parallel i}}{j_{\parallel i D}}\right)_L = -2, \quad (4.17,e,f)$$

which are the same as Eq. (4.5) for the dipole, when expressed in normalised form. The small- $\rho_e$  form for the angular velocity falls away from rigid corotation (the horizontal dotted line) more quickly than the full solution, and goes to zero, equal to the large- $\rho_e$  form, at  $(\rho_e/R_{De}) = \sqrt[4]{2} \approx 1.189$  (or  $(\rho_i/R_{Di}) = 1/\sqrt[4]{2} \approx 0.917$  in the ionosphere). The long-dashed lines thus represent the current profiles that would be driven by an angular velocity profile given by the ‘S’ approximation to the point where  $(\omega/\Omega_j)_s$  falls to zero, with zero being taken beyond. These curves thus provide good approximations at small and large distances, but do not give an accurate description between, where, because the departure of the angular velocity from rigid corotation is always larger than for the full solution, the magnitude of the currents is also larger. The short-dashed lines then show the profiles obtained by introducing Eq. (4.13) (the ‘L’ approximation) into Eq. (4.15) to yield

$$\left(\frac{i_p}{i_{pD}}\right)_{L'} = 2\left(\frac{\rho_i}{R_{Di}}\right)\left(1 - \sqrt{\pi}\left(\frac{\rho_i}{R_{Di}}\right)^4\right) \quad \text{where} \quad \left(\frac{I_p}{I_{pD}}\right)_{L'} = 4\pi\left(\frac{\rho_i}{R_{Di}}\right)^2\left(1 - \sqrt{\pi}\left(\frac{\rho_i}{R_{Di}}\right)^4\right), \quad (4.18a,b)$$

$$\left(\frac{i_\rho}{i_{\rho D}}\right)_{L'} = 4\left(\frac{R_{De}}{\rho_e}\right)^2\left(1 - \sqrt{\pi}\left(\frac{R_{De}}{\rho_e}\right)^2\right) \quad \text{where} \quad \left(\frac{I_\rho}{I_{\rho D}}\right)_{L'} = 8\pi\left(\frac{R_{De}}{\rho_e}\right)\left(1 - \sqrt{\pi}\left(\frac{R_{De}}{\rho_e}\right)^2\right), \quad (4.18c,d)$$

$$\left(\frac{(j_{\parallel}/B)}{(j_{\parallel}/B)_D}\right)_{L'} = -2\left(1 - 3\sqrt{\pi}\left(\frac{R_{De}}{\rho_e}\right)^2\right) \quad \text{where} \quad \left(\frac{j_{\parallel i}}{j_{\parallel i D}}\right)_{L'} = -2\left(1 - 3\sqrt{\pi}\left(\frac{\rho_i}{R_{Di}}\right)^4\right), \quad (4.18e,f)$$

such that these revert to Eq. (4.17) on replacing the final bracket in each case with unity. In this approximation the departure from rigid corotation is always less than for the full solution, so the magnitude of the currents is also less.

The normalised solutions given above show how the form and amplitude of the plasma angular velocity and currents vary with the system parameters for a dipole field. Specifically, Eqs. (4.7) and (4.9) show that the solutions scale spatially in the equatorial plane and in the ionosphere as  $\rho_e \propto (\Sigma_p^* / \dot{M})^{1/4}$  and  $\rho_i \propto (\dot{M} / \Sigma_p^*)^{1/8}$ , respectively, while Eq. (4.15) shows that the amplitude of each component of the current system scales as some power of  $\Sigma_p^*$  and  $\dot{M}$  of the form

$$i \propto \Sigma_p^* \frac{(1+\gamma)}{2} \dot{M} \frac{(1-\gamma)}{2} \quad (4.19)$$

where  $\gamma$  is equal to zero for the sheet-integrated equatorial radial current,  $1/2$  for the azimuth-integrated total field-perpendicular current,  $3/4$  for the height-integrated ionospheric Pedersen current, and  $1$  for the field-aligned current density. The fact that these spatial and amplitude scales combine to produce a linear dependence of the current on  $\dot{M}$  for small  $\rho_e$ , as given by Eq. (4.4), and a linear dependence on  $\Sigma_p^*$  at large  $\rho_e$ , as given by Eq. (4.5), implies that the currents grow with a specific power of the distance in the inner region, and decline with a specific power of the distance at large distances. It is easy to show that at small distances the currents grow as

$$i_s \propto \dot{M} \rho_e^{2(1+\gamma)} \propto \frac{\dot{M}}{\rho_i^{4(1+\gamma)}} \quad (4.20)$$

while at large distances they decline as

$$i_L \propto \frac{\Sigma_p^*}{\rho_e^{2(1-\gamma)}} \propto \Sigma_p^* \rho_i^{4(1-\gamma)} \quad (4.21)$$

as may be readily verified by substituting the appropriate form for the angular velocity (i.e. the 'S' or 'L' approximations) into Eq. (4.15). Thus, in summary, the currents grow in the

inner region according to Eq. (4.20), and depart from this behaviour at an equatorial distance proportional to  $(\Sigma_p^*/\dot{M})^{1/4}$  (as shown by the ‘inner’ downward tick-marks in Figs. 4.2-4.4), where the current value depends on  $\Sigma_p^*$  and  $\dot{M}$  according to Eq. (4.19). Similarly, the currents decline in the outer region according to Eq. (4.21), starting at an equatorial distance proportional to  $(\Sigma_p^*/\dot{M})^{1/4}$  (as shown by the ‘outer’ downward tick-marks in Figs. 4.2-4.4), where the current value again depends on  $\Sigma_p^*$  and  $\dot{M}$  according to Eq. (4.19). These dependencies on  $\Sigma_p^*$  and  $\dot{M}$  may be more readily appreciated when the angular velocity and current profiles are plotted in physical, rather than normalised units, as in the following section.

#### *4.3.2. Un-normalised current dependence on the system parameters*

We now consider how the un-normalised solutions vary with the system parameters, and begin by considering the likely ranges of the latter. With regard to the conductivity, Strobel and Atreya (1983) estimated that for a jovian ionosphere produced solely by solar UV radiation, the height integrated Pedersen conductivity uncorrected for atmospheric slippage is  $\sim 0.2$  mho. They also pointed out that in the presence of intense auroral precipitation this value could rise to  $\sim 10$  mho. We noted in Chapter 3 that atmospheric slippage might reduce these to ‘effective’ values which are less by factors of two or more. Bunce and Cowley (2001) made a rough empirical determination of the effective value  $\Sigma_p^*$  based on angular velocity profiles derived from spacecraft measurements of  $B_\phi$  (see Fig. 3.1). They inferred values of  $\Sigma_p^* \sim 0.3-0.8$  mho. Here we will investigate a range from 0.1 to 10 mho. With regard to the iogenic plasma mass outflow rate  $\dot{M}$ , estimates of the total plasma production rate within the torus lie typically within the range  $1000 - 3000 \text{ kg s}^{-1}$  as discussed in Chapter 2, of which one third to one half emerges as plasma outflow in the equatorial disc. Here we will investigate a range of  $\dot{M}$  between 100 and  $10,000 \text{ kg s}^{-1}$ .

With these values we can now estimate the likely ranges of the equatorial and ionospheric ‘Hill distances’, Eqs. (4.7) and (4.9), that scale the respective spatial distributions. Numerically we find

$$\frac{R_{De}}{R_J} \approx 49.21 \left( \frac{\Sigma_p^* (\text{mho})}{\dot{M} (10^3 \text{ kg s}^{-1})} \right)^{1/4} \quad \text{and} \quad \frac{R_{Di}}{R_J} \approx 0.1426 \left( \frac{\dot{M} (10^3 \text{ kg s}^{-1})}{\Sigma_p^* (\text{mho})} \right)^{1/8}, \quad (4.22a,b)$$

such that for system parameters at the centre of the above ranges, i.e.  $\Sigma_p^* = 1$  mho and  $\dot{M} = 1000 \text{ kg s}^{-1}$ , we find  $R_{De} \approx 49.2 R_J$  and  $R_{Di} \approx 0.14 R_J$  (corresponding to a co-latitude of  $8.2^\circ$ ). If we fix  $\dot{M}$  at this value and allow  $\Sigma_p^*$  to increase from 0.1 to 10 mho, we find that  $R_{De}$  increases from 27.7 to  $87.5 R_J$ , while  $R_{Di}$  decreases from 0.19 to  $0.11 R_J$  (co-latitudes between  $11.0^\circ$  and  $6.1^\circ$ ), as indicated above. Similarly, if we fix  $\Sigma_p^*$  at 1 mho and allow  $\dot{M}$  to increase from 100 to  $10,000 \text{ kg s}^{-1}$ , we find that  $R_{De}$  and  $R_{Di}$  vary over the same ranges but in the reversed sense. Thus because  $R_{De}$  and  $R_{Di}$  depend on the system parameters only as the quarter and eighth powers, respectively, they change only by modest factors as the system parameters vary widely.

We also note here that the value of  $R_{De}$  significantly exceeds the radial distance of the Io source at  $\rho_{e \text{ Io}} \approx 6 R_J$  over the whole range of parameters considered, such that the normalized distance of the source is typically  $(\rho_{e \text{ Io}}/R_{De}) \approx 0.1 - 0.2$ . Reference to Fig. 4.1a shows that near-rigid corotation will then indeed be valid in the vicinity of Io under all conditions examined (though additional considerations apply, of course, within the plasma pick-up region itself).

Variation of the un-normalised distributions of plasma angular velocity and current with the system parameters is illustrated in Figs. 4.6-4.11, in a similar format to Figs. 4.1-4.4. The values of the physical constants employed are  $B_J = 428,000 \text{ nT}$ ,  $R_J = 71,373 \text{ km}$ , and  $\Omega_J = 1.76 \times 10^{-4} \text{ rad s}^{-1}$ . Figs. 4.6-4.8 show how the current components vary with  $\Sigma_p^*$  at fixed  $\dot{M}$ , specifically for  $\Sigma_p^* = 0.2, 1, \text{ and } 5$  mho at  $\dot{M} = 1000 \text{ kg s}^{-1}$ , while Figs. 4.9-4.11 shows how they vary with  $\dot{M}$  at fixed  $\Sigma_p^*$ , specifically for  $\dot{M} = 200, 1000, \text{ and } 5000 \text{ kg s}^{-1}$  at  $\Sigma_p^* = 1$  mho. These solutions correspond to only one set of angular velocity profiles, however, with  $(\Sigma_p^*/\dot{M}) = 2 \times 10^{-4}, 10^{-3}, \text{ and } 5 \times 10^{-3} \text{ mho s kg}^{-1}$ , and these are shown in Fig. 4.5. The corresponding ‘Hill distances’ are 33, 49, and  $74 R_J$  in the equatorial plane,

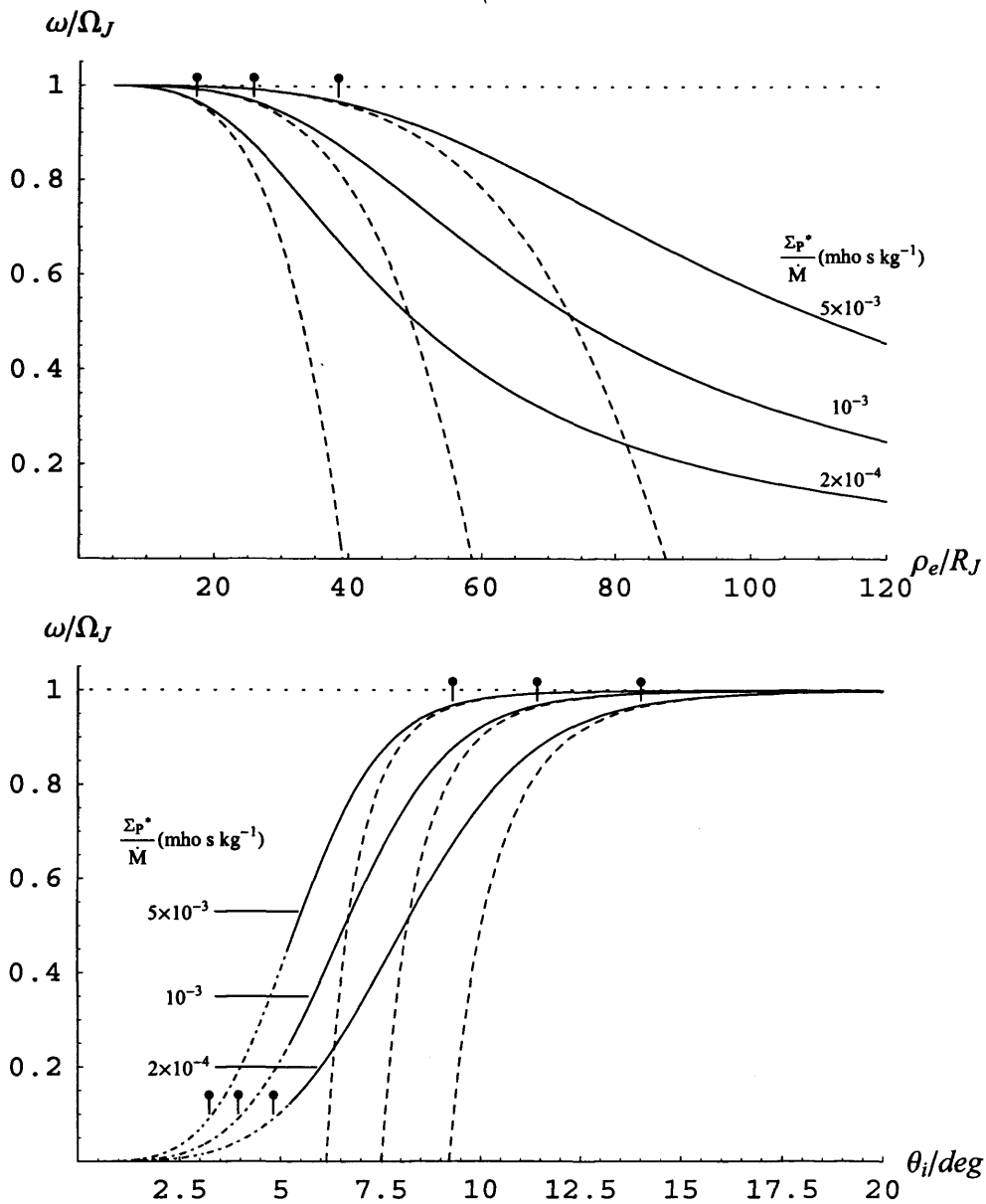


**Figure 4.5.** Plasma angular velocity profiles for a dipole field are plotted (a) versus equatorial radial distance  $\rho_e$ , and (b) versus magnetic co-latitude  $\theta_i$ . Profiles are shown in each case for  $(\Sigma_P^*/M) = 2 \times 10^{-4}, 10^{-3}$ , and  $5 \times 10^{-3}$  mho s  $\text{kg}^{-1}$ , as marked in the figure. The solid lines show the full solutions given by Eq. (4.8) with  $K = 0$ , the dashed lines the small- $\rho_e$  form given by Eq. (4.11), the large- $\rho_e$  form being just  $(\omega/\Omega_J)_L = 0$ , while the tick-marks show the limits of validity of these approximations according to the criterion given by Eq. (4.12) (the large- $\rho_e$  limits only lying within the range in plot (b)). In the ionospheric projection in (b), the full solution curves are continued towards the pole beyond the  $120 R_J$  limit taken in plot (a) (mapping to a co-latitude of  $5.24^\circ$  in the ionosphere); the curves in this regime are shown by dot-dashed lines. The horizontal dotted lines indicate the condition for rigid corotation,  $(\omega/\Omega_J) = 1$ .

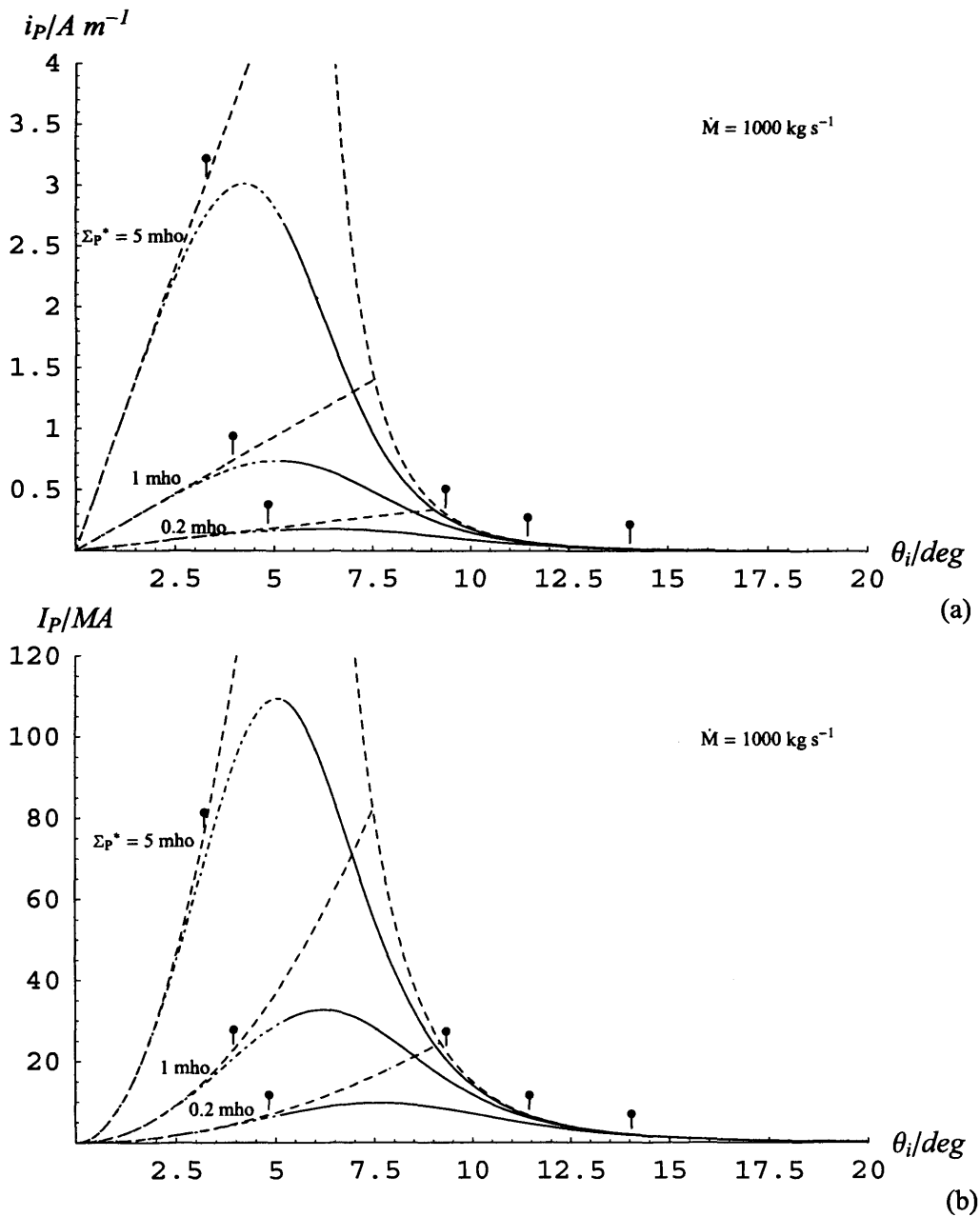


**Figure 4.6.** Set of solutions for (a) the height-integrated ionospheric Pedersen current intensity and (b) the azimuth- and height-integrated total ionospheric Pedersen current for a dipole magnetic field, plotted versus co-latitude in the ionosphere and shown in physical units. Plots are shown in each case for  $\dot{M}$  held fixed at  $1000 \text{ kg s}^{-1}$ , while  $\Sigma_p^*$  takes the values 0.2, 1, and 5 mho as marked. The format follows that in Figs. 4.2-4.4, except that the higher-order large- $\rho_e$  approximation (the short-dashed line in Figs. 4.2-4.4) is not shown to avoid clutter. Note that there is only one ‘small  $\rho_e$ ’ approximation (dashed) curve in each plot corresponding to the fixed  $\dot{M}$  value, while the three ‘large  $\rho_e$ ’ approximation curves are simply proportional to  $\Sigma_p^*$ .

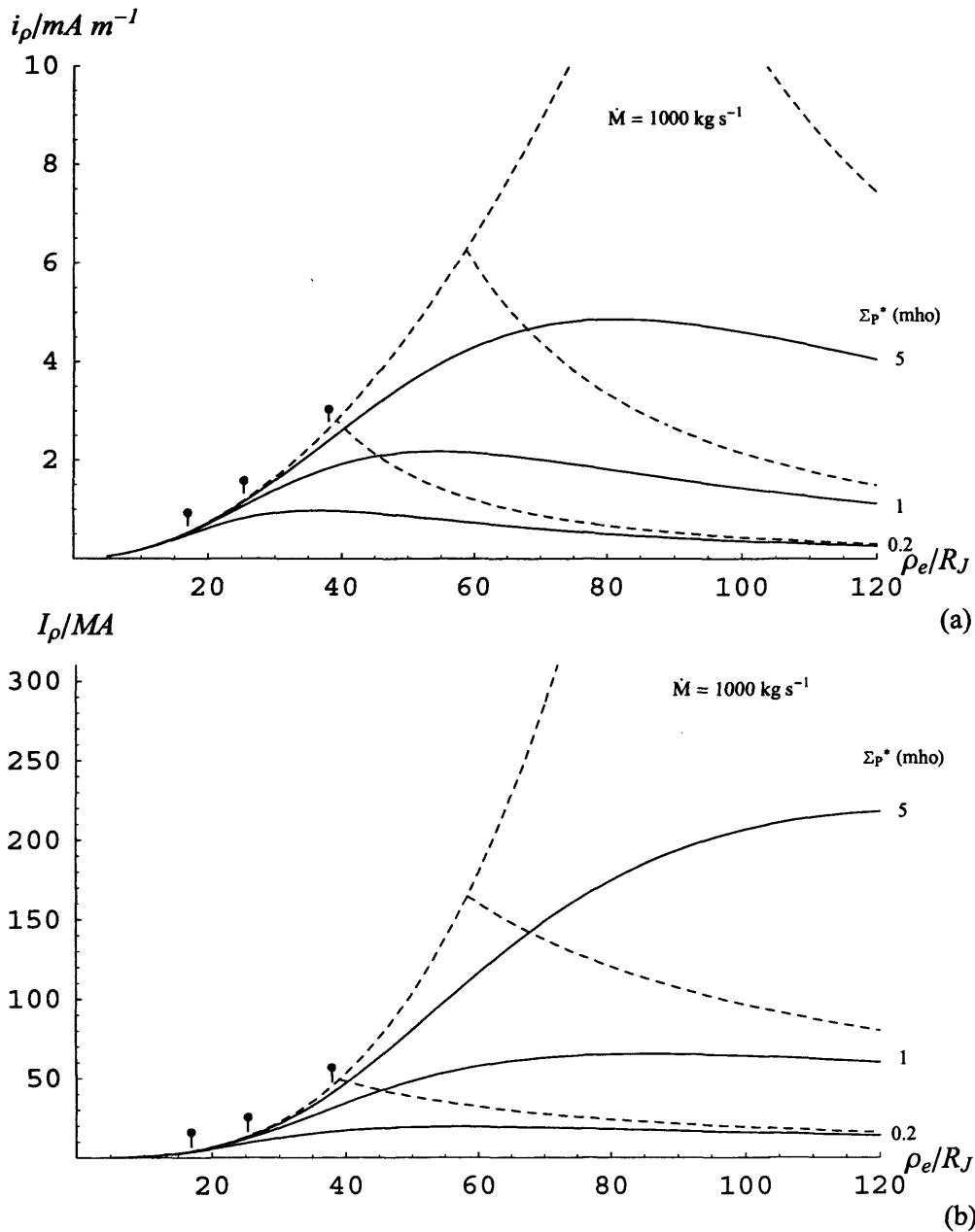


**Figure 4.7.** Set of solutions for (a) the current sheet-integrated equatorial radial current intensity and (b) the azimuth- and current sheet-integrated total equatorial radial current for a dipole magnetic field, plotted versus equatorial radial distance and shown in physical units. Plots are shown in each case for  $\dot{M}$  held fixed at  $1000 \text{ kg s}^{-1}$ , while  $\Sigma_p^*$  takes the values 0.2, 1, and 5 mho as marked. The format follows that in Fig. 4.6. Again, note that there is only one ‘small- $\rho_e$ ’ approximation (dashed) curve in each plot corresponding to the fixed  $\dot{M}$  value, while the three ‘large- $\rho_e$ ’ approximation curves are simply proportional to  $\Sigma_p^*$ .

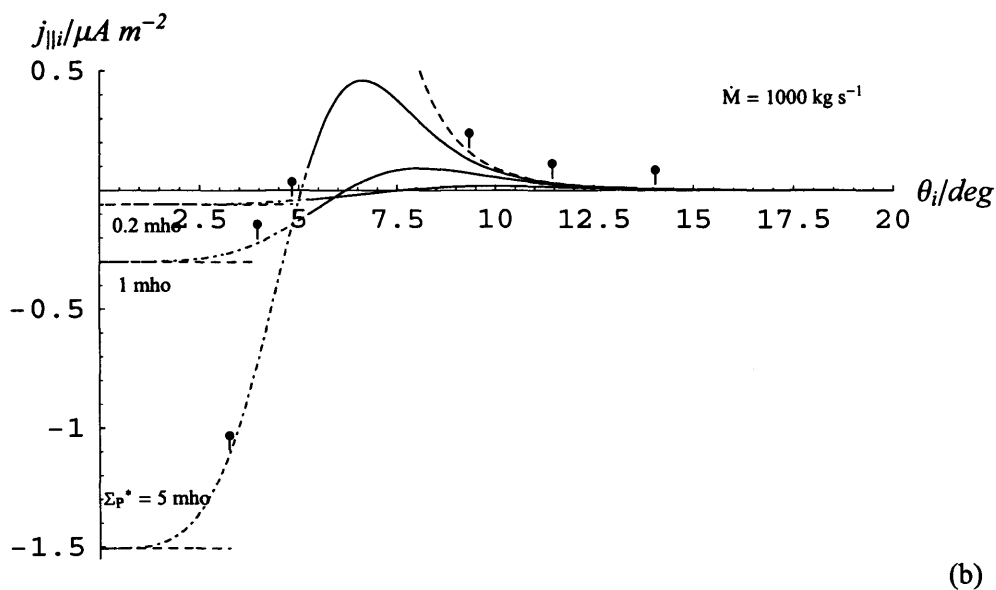
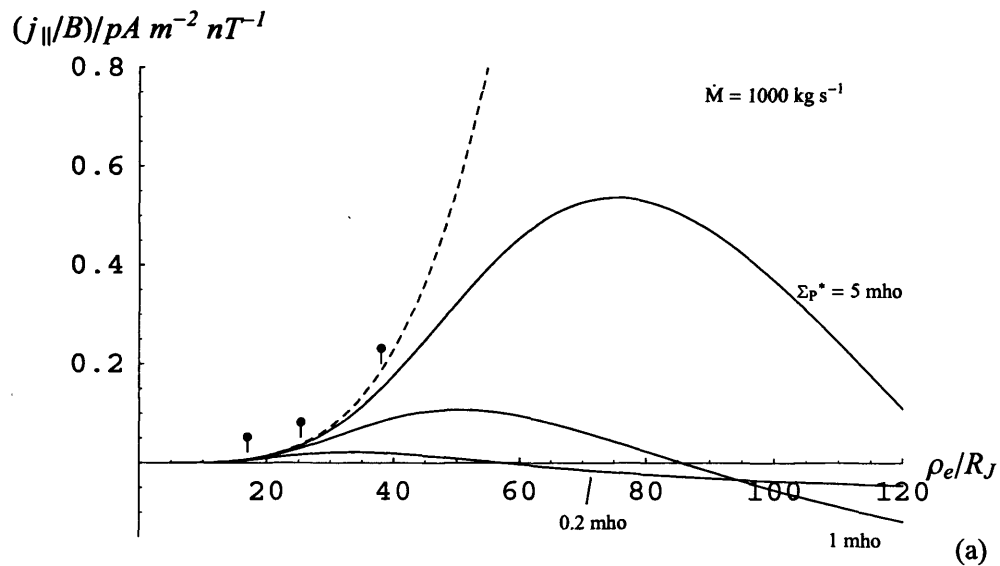


**Figure 4.8.** Set of solutions for (a) the equatorial field-aligned current density per unit magnetic field strength, plotted versus radial distance in the equatorial plane, and (b) the field-aligned current density just above the ionosphere, plotted versus co-latitude in the ionosphere, for a dipole magnetic field and shown in physical units. Plots are shown in each case for  $\dot{M}$  held fixed at  $1000 \text{ kg s}^{-1}$ , while  $\Sigma_p^*$  takes the values 0.2, 1, and 5 mho as marked. The format follows that in Figs. 4.6 and 4.7. Again, note that there is only one ‘small- $\rho_e$ ’ approximation (dashed) curve in each plot corresponding to the fixed  $\dot{M}$  value, while the three ‘large- $\rho_e$ ’ approximation curves are simply proportional to  $\Sigma_p^*$ .

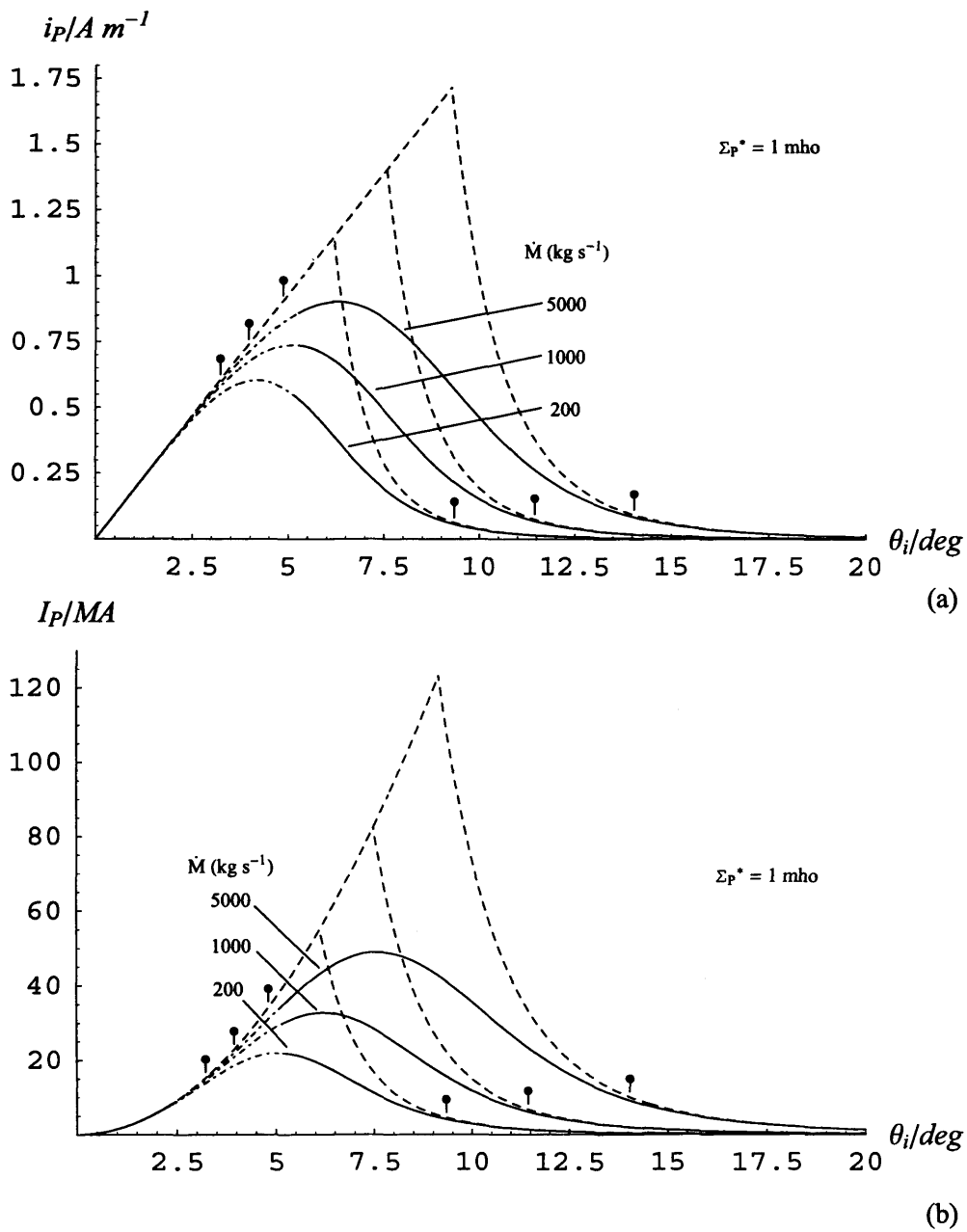


**Figure 4.9.** Set of solution curves for (a) the height-integrated ionospheric Pedersen current intensity and (b) the azimuth- and height-integrated total ionospheric Pedersen current for a dipole magnetic field shown in physical units, as in Fig. 4.6, but where  $\Sigma_p^*$  is held fixed at 1 mho, while  $\dot{M}$  takes the values 200, 1000, and 5000  $kg\ s^{-1}$ . The format is the same as Figs. 4.6-4.8. Note that in this case there is only one 'large- $\rho_e$ ' approximation (dashed) curve in each plot corresponding to the fixed  $\Sigma_p^*$  value, while the three 'small- $\rho_e$ ' approximation curves are simply proportional to  $\dot{M}$ .

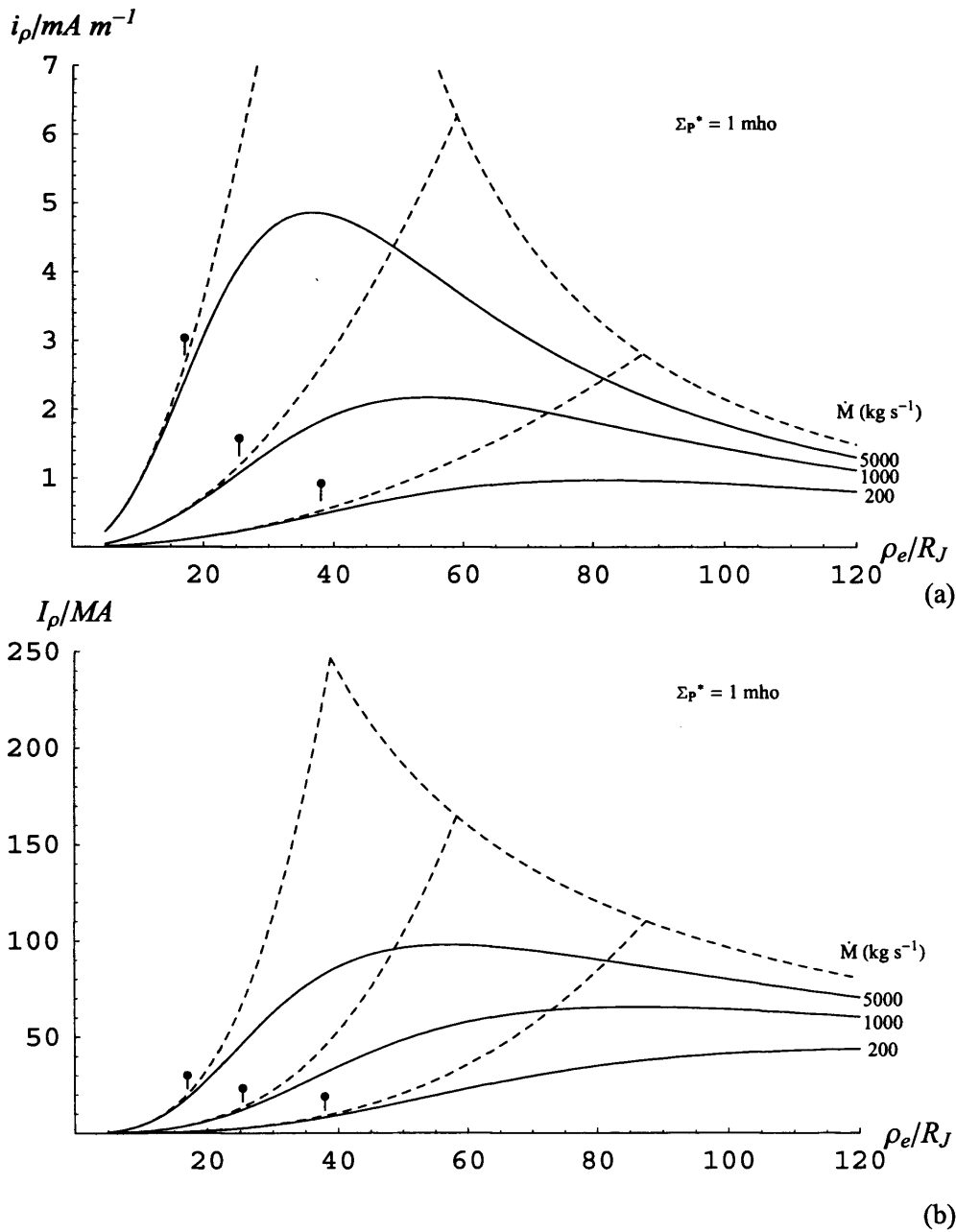


**Figure 4.10.** Set of solution curves for (a) the current sheet-integrated equatorial radial current intensity and (b) the azimuth- and current sheet-integrated total equatorial radial current for a dipole magnetic field shown in physical units, as in Fig. 4.7, but where  $\Sigma_p^*$  is held fixed at 1 mho, while  $\dot{M}$  takes the values 200, 1000, and 5000  $\text{kg s}^{-1}$ . The format is the same as Figs. 4.6-4.8. Again, note that there is only one ‘large- $\rho_e$ ’ approximation (dashed) curve in each plot corresponding to the fixed  $\Sigma_p^*$  value, while the three ‘small- $\rho_e$ ’ approximation curves are simply proportional to  $\dot{M}$ .

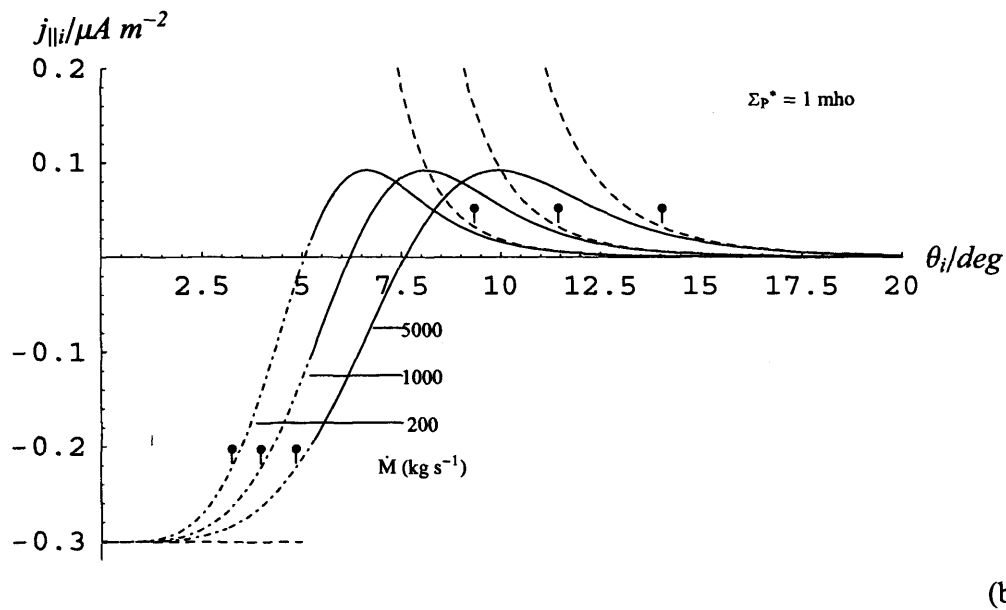
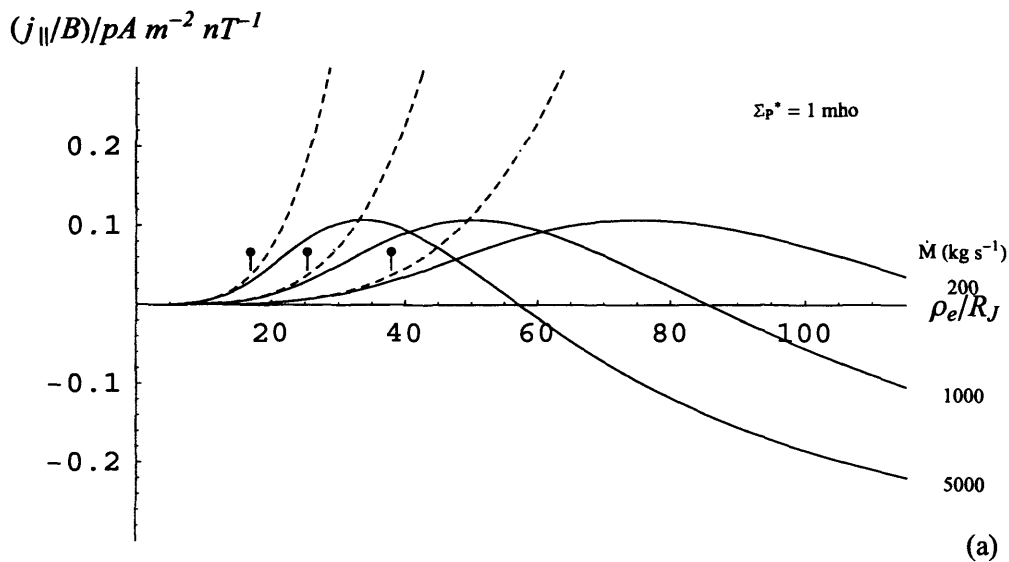


**Figure 4.11.** Set of solution curves for (a) the equatorial field-aligned current density per unit magnetic field strength, plotted versus radial distance in the equatorial plane, and (b) the field-aligned current density just above the ionosphere, plotted versus co-latitude in the ionosphere, for a dipole magnetic field and shown in physical units, as in Fig. 4.8, but where  $\Sigma_p^*$  is held fixed at 1 mho, while  $\dot{M}$  takes the values 200, 1000, and 5000  $\text{kg s}^{-1}$ . The format is the same as Figs. 4.6-4.8. Again, note that there is only one ‘large- $\rho_e$ ’ approximation (dashed) curve in each plot corresponding to the fixed  $\Sigma_p^*$  value, while the three ‘small- $\rho_e$ ’ approximation curves are simply proportional to  $\dot{M}$ .

and 0.17, 0.14 and 0.12  $R_J$  in the ionosphere. Fig. 4.5a shows  $(\omega/\Omega_j)$  versus equatorial radial distance out to 120  $R_J$ , the same distance that will be employed below for the current sheet model. The solid lines show the full solutions given by Eq. (4.8) with  $K = 0$ , while the dashed lines show the small- $\rho_e$  forms given by Eq. (4.11). The tick-marks show the outer limit of validity of the latter forms as defined by Eq. (4.12). No tick-marks associated with the large- $\rho_e$  forms are shown because none of the curves reach the  $(\omega/\Omega_j) \approx 0.091$  limit of validity within the range. To avoid clutter, the higher-order large- $\rho_e$  form Eq. (4.13) is not shown. Fig. 4.5b then shows these profiles projected to the ionosphere and plotted versus co-latitude  $\theta_i$ . In this plot we have extended the full solution curves towards the pole beyond the 120  $R_J$  limit of Fig. 4.5a, where the curves are shown dot-dashed. Overall, Fig. 4.5 demonstrates the expansion of plasma corotation to increasing distances as the ionospheric conductivity increases or, equivalently, the iogenic mass outflow rate decreases.

The behaviour of the current components are shown in Figs. 4.6-4.11, and follow expectations based on the normalised forms. For example, the plots of the equatorial radial current in Fig. 4.7b show that at fixed  $\dot{M}$  the peak current increases with increasing conductivity as  $\Sigma_p^{*1/2}$  and is located at increasing radial distances as  $\Sigma_p^{*1/4}$ , while in Fig. 4.10a we find that at fixed  $\Sigma_p^*$  the peak current also increases with increasing mass outflow rate as  $\dot{M}^{1/2}$ , but is located at decreasing radial distances as  $\dot{M}^{-1/4}$ . Corresponding statements follow for the other components. For convenience, in Table 4.2 we give the peak values and positions of the various current components in physical units, where values of  $\Sigma_p^*$  are to be substituted in mhos, and values of  $\dot{M}$  in units of 1000 kg s<sup>-1</sup>.

The behaviour of the currents outlined in Section 4.2 can be seen in Figs. 4.6-4.11 more clearly than with the normalised forms shown in Figs. 4.2-4.4. That is, in the small distance limit the currents depend only on  $\dot{M}$  and not on  $\Sigma_p^*$ , while in the large distance limit they depend only on  $\Sigma_p^*$  and not on  $\dot{M}$ . Thus in Figs. 4.6-4.8, where  $\dot{M}$  is held fixed while  $\Sigma_p^*$  is varied, only one ‘small  $\rho_e$ ’ dashed curve is shown in each plot, while the three ‘large- $\rho_e$ ’ dashed curves take values which are simply proportional to  $\Sigma_p^*$ . Similarly in Figs. 4.9-4.11 where  $\Sigma_p^*$  is held fixed while  $\dot{M}$  is varied, only one ‘large- $\rho_e$ ’ dashed

Feature	$\left(\frac{\rho_e}{R_j}\right)$	$\sin \theta_i = \left(\frac{\rho_i}{R_j}\right)$
Maximum upward field-aligned current density $(j_{\parallel}/B)_{max} \approx 0.1076 \Sigma_p^* (\text{mho}) \text{ pA m}^{-2} \text{ nT}^{-1}$ $j_{\parallel i max} \approx 0.09206 \Sigma_p^* (\text{mho}) \mu\text{A m}^{-2}$	$50.21 \left( \frac{\Sigma_p^* (\text{mho})}{\dot{M} (10^3 \text{ kg s}^{-1})} \right)^{1/4}$	$0.1411 \left( \frac{\dot{M} (10^3 \text{ kg s}^{-1})}{\Sigma_p^* (\text{mho})} \right)^{1/8}$
Maximum sheet-integrated equatorial radial current $i_{p max} \approx 2.178 (\Sigma_p^* (\text{mho}) \dot{M} (10^3 \text{ kg s}^{-1}))^{1/2} \text{ mA m}^{-1}$	$54.30 \left( \frac{\Sigma_p^* (\text{mho})}{\dot{M} (10^3 \text{ kg s}^{-1})} \right)^{1/4}$	$0.1357 \left( \frac{\dot{M} (10^3 \text{ kg s}^{-1})}{\Sigma_p^* (\text{mho})} \right)^{1/8}$
Plasma angular velocity falls to $\left(\frac{\omega}{\Omega_j}\right) = 0.5$	$74.80 \left( \frac{\Sigma_p^* (\text{mho})}{\dot{M} (10^3 \text{ kg s}^{-1})} \right)^{1/4}$	$0.1156 \left( \frac{\dot{M} (10^3 \text{ kg s}^{-1})}{\Sigma_p^* (\text{mho})} \right)^{1/8}$
Maximum azimuth-integrated total current $I_p max = 2 I_p max \approx$ $65.54 (\Sigma_p^* (\text{mho}) \dot{M} (10^3 \text{ kg s}^{-1}))^{1/4} \text{ MA}$ Field-aligned current passes through zero	$85.67 \left( \frac{\Sigma_p^* (\text{mho})}{\dot{M} (10^3 \text{ kg s}^{-1})} \right)^{1/4}$	$0.1080 \left( \frac{\dot{M} (10^3 \text{ kg s}^{-1})}{\Sigma_p^* (\text{mho})} \right)^{1/8}$
Maximum ionospheric Pedersen current $i_p max \approx 0.7381 (\Sigma_p^* (\text{mho}) \dot{M} (10^3 \text{ kg s}^{-1}))^{1/8} \text{ A m}^{-1}$	$126.34 \left( \frac{\Sigma_p^* (\text{mho})}{\dot{M} (10^3 \text{ kg s}^{-1})} \right)^{1/4}$	$0.0890 \left( \frac{\dot{M} (10^3 \text{ kg s}^{-1})}{\Sigma_p^* (\text{mho})} \right)^{1/8}$
Maximum downward field-aligned current density $(j_{\parallel}/B)_{min} \approx -0.352 \Sigma_p^* (\text{mho}) \text{ pA m}^{-2} \text{ nT}^{-1}$ $j_{\parallel i min} \approx -0.3013 \Sigma_p^* (\text{mho}) \mu\text{A m}^{-2}$	$\infty$	$0$

**Table 4.2.** Principal features of the plasma angular velocity and coupling current system for a dipole field in physical units.

curve is shown in each plot, while the three ‘small- $\rho_e$ ’ dashed curves are simply proportional to  $\dot{M}$ . This represents a particular instance of a general property of the solutions discussed by Cowley, Bunce and Nichols (2003) and in Section 4.2 above. If we expand the ‘small- $\rho_e$ ’ forms given by Eq. (4.16) we find

$$i_{pS} = \frac{\dot{M}\Omega_J}{2\pi B_J R_J} \left( \frac{R_J}{\rho_i} \right)^7, \quad I_{pS} = \frac{\dot{M}\Omega_J}{B_J} \left( \frac{R_J}{\rho_i} \right)^6, \quad (4.23a,b)$$

$$i_{\rho S} = \frac{\dot{M}\Omega_J}{\pi B_J R_J} \left( \frac{\rho_e}{R_J} \right)^2, \quad I_{\rho S} = \frac{2\dot{M}\Omega_J}{B_J} \left( \frac{\rho_e}{R_J} \right)^3, \quad (4.23c,d)$$

$$\left( \frac{j_{\parallel}}{B} \right)_S = \frac{3\dot{M}\Omega_J}{2\pi B_J^2 R_J^2} \left( \frac{\rho_e}{R_J} \right)^4, \quad \text{and} \quad j_{\parallel S} = \frac{3\dot{M}\Omega_J}{\pi B_J R_J^2} \left( \frac{R_J}{\rho_i} \right)^8, \quad (4.23e,f)$$

which thus depend only on  $\dot{M}$  as expected. We recall that the departure from rigid corotation is by only  $\sim 3.2\%$  at the point we have taken to be the outer limit of validity of this approximation, i.e.  $\rho_{eS} \approx 0.516 R_{De}$  and, while the currents in the inner region depend only on  $\dot{M}$ , the radial range over which they apply depends both on  $\Sigma_p^*$  and  $\dot{M}$ , through the dependence of  $R_{De}$  on these parameters. Thus, for example, the equatorial radial current given by Eq. (4.16c) grows in the inner region in proportion to  $\rho_e^2$  to a distance which is proportional to  $(\Sigma_p^*/\dot{M})^{1/4}$ , thus achieving a value at the limit which is proportional to  $(\Sigma_p^*\dot{M})^{1/2}$ , in agreement with the normalised form in Eq. (4.15c). Corresponding statements apply also to the other current components.

Similarly, if we expand the ‘large  $\rho_e$ ’ forms given by Eq. (4.17) we find

$$i_{pL} = 2\Sigma_p^* B_J \Omega_J \rho_i, \quad I_{pL} = 4\pi \Sigma_p^* B_J \Omega_J \rho_i^2, \quad (4.24a,b)$$

$$i_{\rho L} = 4\Sigma_p^* B_J R_J \Omega_J \left( \frac{R_J}{\rho_e} \right)^2, \quad I_{\rho L} = 8\pi \Sigma_p^* B_J R_J^2 \Omega_J \left( \frac{R_J}{\rho_e} \right), \quad (4.24c,d)$$

$$\left(\frac{j_{\parallel}}{B}\right)_L = -2\Sigma_p^* \Omega_J, \quad \text{and} \quad j_{\parallel i L} = -4\Sigma_p^* B_J \Omega_J, \quad (4.24e,f)$$

which thus depend only on  $\Sigma_p^*$ . However, the inner limit of validity of these forms (i.e.  $\rho_{e L} \approx 4.284 R_{De}$ ) again depends on both  $\Sigma_p^*$  and  $\dot{M}$  through the dependence of  $R_{De}$  on these parameters, such that the value of the current at the limit again scales as indicated by the normalised forms given above.

#### 4.4. Plasma angular velocity and coupling current system for a current sheet magnetic model

##### 4.4.1. Current sheet field model

The solution for the coupling currents for a dipole field represents an important paradigm case. Nevertheless, one major reason why the model is unrealistic in its application to Jupiter lies in the fact that the middle magnetosphere field lines are not quasi-dipolar, but are significantly distorted outwards from the planet by azimuthal currents flowing in the equatorial plasma, as shown in Fig. 3.1. Thus field lines at a given radial distance in the equatorial plane map to a significantly lower latitude in the ionosphere than in the dipole model, thereby increasing the electric field and current for a given departure of the plasma from rigid corotation. In their previous investigations outlined in Chapter 3, Cowley and Bunce (2001b) and Cowley, Nichols and Bunce (2002) employed an empirical model of the equatorial field based on Voyager magnetic data. This model will also be used here, its properties being described in Section 3.3.6. It consists of two empirical models, joined at their intersection at radial distance  $\rho_e^* \approx 21.78 R_J$ . The inner region, where  $\rho_e < \rho_e^*$ , is given by the CAN model Eq. (3.32), while for  $\rho_e > \rho_e^*$  the field is given by the KK model Eq. (3.33), which is a simple power law.

Solutions for such a current sheet field model must generally be computed numerically for specific values of the system parameters, and results have been presented to date by Cowley et al. (2002, 2003a) for a few spot values (see Chapter 3). In the next section, however, we present an approximate analytic solution which applies to the region beyond  $\rho_e^* \approx 21.78 R_J$ , where the field varies with distance as a power law, which previous work has shown to be the main current-carrying region provided  $\Sigma_p^*$  is not too low and/or  $\dot{M}$  not too high. Here we first enquire how solutions in this outer region depend on conditions inside the region, where the dipole field is dominant and the transition to the power law field takes place.

We commented previously for the dipole problem that solutions of the Hill-Pontius equation which are started at an arbitrary angular velocity well within the ‘Hill distance’ converge rapidly onto the solution which rigidly corotates at small distances, such that the behaviour at larger distances is very insensitive to the choice of initial condition. Numerical investigation shows that the solutions for the current sheet field exhibit the same property (Cowley and Bunce, 2003a). The implication for the present problem is that, provided the effective ‘Hill distance’ is larger than  $\rho_e^* \sim 20 R_J$  (i.e. provided the value of  $(\Sigma_p^*/\dot{M})$  is not too low), the solutions in the ‘power law’ region will be insensitive to conditions in the interior region. In this case, we can simply take the power law field to be valid over all distances, but apply the results only to the region outside of  $\rho_e^*$ . The validity of this statement may be judged from Figs. 4.12 and 4.13, where we show numerically computed solutions for the plasma angular velocity in the inner part of the system spanning  $\rho_e^*$ , for three values of  $(\Sigma_p^*/\dot{M})$  covering our range of interest, i.e. for  $10^{-4}$ ,  $10^{-3}$ , and  $10^{-2}$  mho s kg<sup>-1</sup>. The solid lines show numerical solutions using the full current sheet field model shown in Fig. 3.5, while the dashed lines similarly show numerical solutions using the power law field over the whole range. (The dot-dashed lines show the analytic approximation to be derived below). Both numerical solutions were initialised by imposing the near-rigid corotation approximation given by Eq. (4.3) at  $\rho_e = 5 R_J$ . The position of  $\rho_e^*$  is indicated by the tick-mark in each plot, such that both models use the same power law field at larger distances. It can be seen that the two numerical solutions converge rapidly beyond this distance, the convergence becoming increasingly rapid as  $(\Sigma_p^*/\dot{M})$

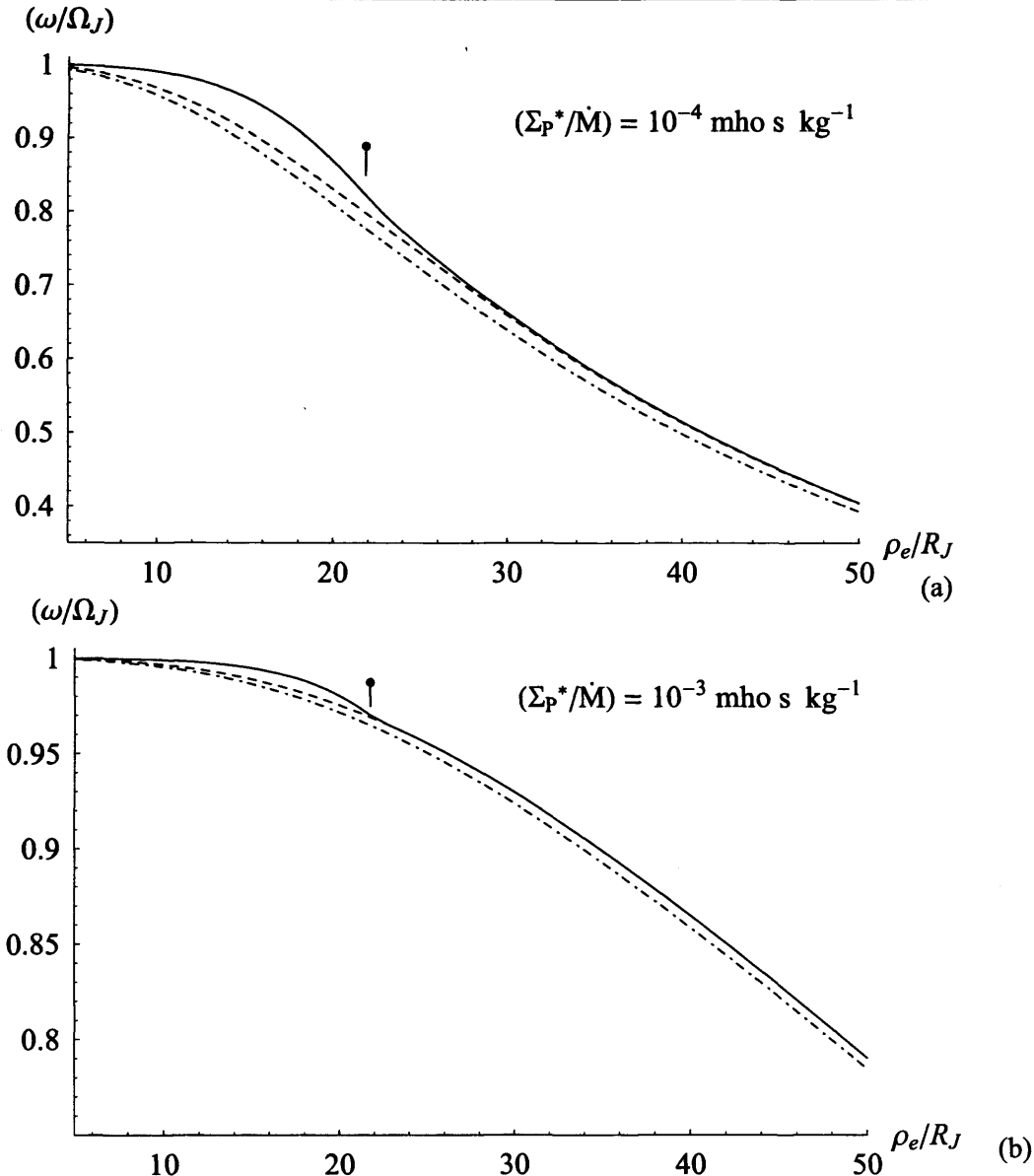


**Figure 4.12.** Plots showing plasma angular velocity profiles versus equatorial radial distance for  $(\Sigma_P^*/\dot{M})$  equal to (a)  $10^{-4}$ , and (b)  $10^{-3} \text{ mho s kg}^{-1}$ . The solid lines show the solution obtained by numerical integration of Eq. (3.27) using the full ‘current sheet’ magnetic model described in Section 3.3.6, starting from the near-rigid corotation approximation Eq. (4.3) at  $\rho_e = 5 R_J$ . The tick-marks show the point ( $\rho_e^* \approx 21.78 R_J$ ) where the magnetic field switches from the ‘CAN’ model to the power-law ‘KK’ model. The dashed lines then show the numerical solution obtained by employing the ‘KK’ power law field (given by Eqs. (3.33) and (3.35)) over the full distance range, the solutions again being initialised using the appropriate form of Eq. (4.3) at  $\rho_e = 5 R_J$ . The dot-dashed lines show the approximate analytic solution using the ‘KK’ power law field, given by Eq. (4.27) with  $K = 0$  and  $m = 2.71$ . Note that the vertical scale has been tailored to the plot in each case.

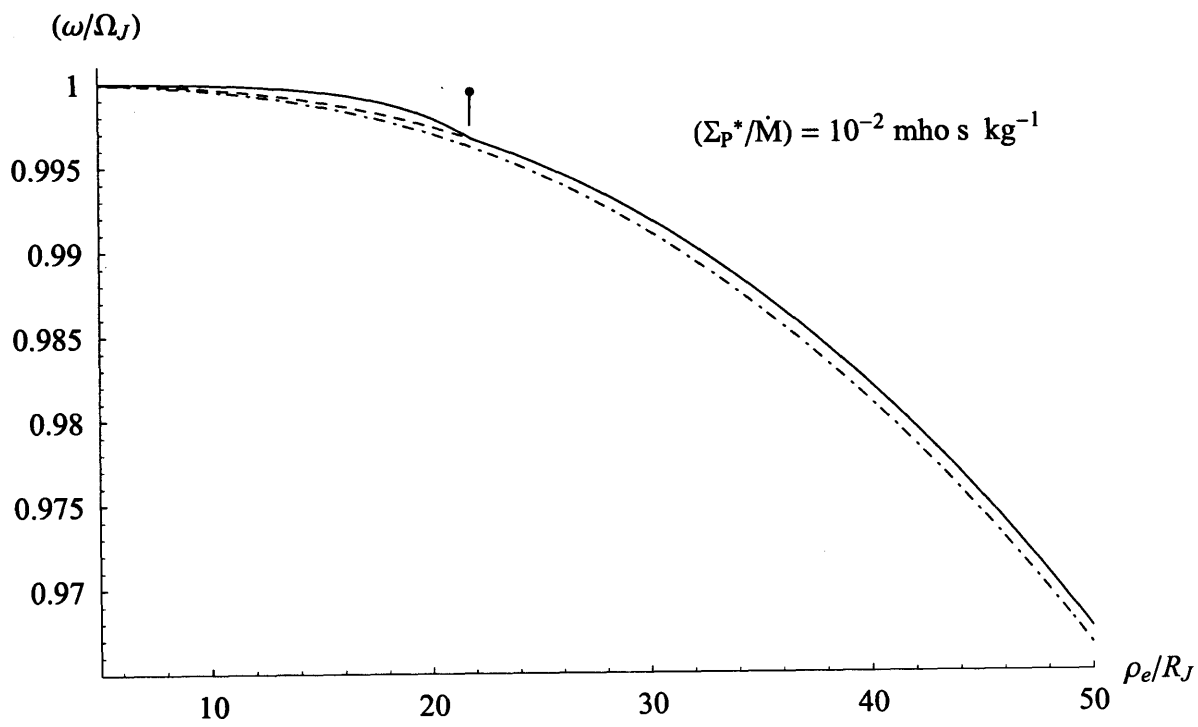


Figure 4.13. As Fig. 4.12, but with  $(\Sigma_p^*/\dot{M}) = 10^{-2} \text{ mho s kg}^{-1}$ .

increases. Thus in the parameter range of interest, the solutions in the power law field region can be approximated by taking the power law field to be valid at all distances. We note that the values of the ‘Hill distance’ corresponding to the values of  $(\Sigma_p^*/\dot{M})$  shown in the figure are 27.7, 49.2, and 87.5  $R_J$ , thus exceeding  $\rho_e^* \approx 21.78 R_J$  in each case, though only just so at the lower limit. Convergence of the two solutions is found to break down for lower values of  $(\Sigma_p^*/\dot{M}) \sim 10^{-5}$  mho s  $\text{kg}^{-1}$ , corresponding to a ‘Hill distance’ of 15.6  $R_J$ , at the limit of the parameter range considered here.

#### 4.4.2. Approximate normalised solution for a power law equatorial field

We thus consider solutions for the case in which the equatorial field is taken to be given by the power law Eq. (3.33) at all distances. We also make the further approximation that the flux function is taken to be a constant in the Hill-Pontius equation. Thus, over the region of interest, the equatorial field is taken to map in the ionosphere to a narrow range of distances from the magnetic axis, an approximation shown to be well satisfied for the empirical current sheet model, as discussed in Chapter 3. While this approximation will generally be valid for ‘current sheet’ fields, it is clearly not valid for quasi-dipolar fields. We thus note that the solutions obtained here do not reduce to the dipole case in the limit that we choose  $m = 3$  in Eq. (3.33). With this ‘current sheet’ approximation, then, the Hill-Pontius equation Eq. (3.27) becomes

$$\frac{\rho_e}{2} \frac{d}{d\rho_e} \left( \frac{\omega}{\Omega_j} \right) + \left( \frac{\omega}{\Omega_j} \right) = 2 \left( \frac{R_{CS_e}}{\rho_e} \right)^m \left( 1 - \frac{\omega}{\Omega_j} \right), \quad (4.25)$$

where  $R_{CS_e}$  is the equatorial ‘Hill distance’ for the power law current sheet field (subscript ‘CS’)

$$\frac{R_{CS_e}}{R_J} = \left( \frac{2\pi\Sigma_p^* B_o F_o}{\dot{M}} \right)^{1/m}. \quad (4.26)$$

Here we have put  $F_e = F_o$ , a constant, into Eq. (3.27), such that the field lines are taken to map in the ionosphere to a fixed distance from the magnetic axis given by  $(\rho_{io}/R_J) = \sqrt{(F_o/B_J R_J^2)}$  (Eq. (3.3)). The value of  $F_o$  could be taken e.g. to be equal to  $F_\infty$  in Eq. (3.33b) (in which case  $(\rho_{io}/R_J) \approx 0.258$ , corresponding to a co-latitude of  $\sim 14.95^\circ$ ), or to some nearby value representative of the field lines in the region of interest. Equation (4.25) is then of the same form as Eq. (4.6) for the dipole (they are identical when  $m = 4$ ), from which it is clear that the solutions are functions only of  $(\rho_e/R_{CS_e})$ , and hence scale with distance as  $R_{CS_e}$  and with the system parameters as  $(\Sigma_p^*/\dot{M})^{1/m}$ . With  $m = 2.71$ , therefore, as used throughout here, the scale length varies somewhat more rapidly with the system parameters than for the dipole, which varies as  $(\Sigma_p^*/\dot{M})^{1/4}$ . The value of  $R_{CS_e}$  varies between  $\sim 25$  and  $\sim 125 R_J$  over the range of parameters considered here, compared with  $\sim 30$  to  $\sim 90 R_J$  for the dipole.

The general solution of Eq. (4.25) can again be found by the integration factor method

$$\left(\frac{\omega}{\Omega_J}\right) = \left(\frac{4}{m}\right)^{\frac{2}{m}} \left(\frac{R_{CS_e}}{\rho_e}\right)^2 \exp\left[\frac{4}{m}\left(\frac{R_{CS_e}}{\rho_e}\right)^m\right] \left[ \Gamma\left[1 - \frac{2}{m}, \frac{4}{m}\left(\frac{R_{CS_e}}{\rho_e}\right)^m\right] + K \right], \quad (4.27)$$

where  $\Gamma(a, z)$  is the incomplete gamma function

$$\Gamma(a, z) = \int_z^\infty e^{-t} t^{a-1} dt. \quad (4.28)$$

The solutions again diverge at the origin except for the special solution with  $K = 0$ , which rigidly corotates for small  $\rho_e$ . To map the solution to the ionosphere we equate Eqs. (3.3) and (3.35b), and define an ionospheric scaling distance

$$\frac{R_{CS_i}}{R_J} = \frac{1}{2(m-2)} \left(\frac{B_o}{B_J}\right) \sqrt{\frac{B_J R_J^2}{F_\infty}} \left(\frac{\dot{M}}{2\pi \Sigma_p^* B_o F_o}\right)^{1-\frac{2}{m}}, \quad (4.29)$$

such that the angular velocity mapped to the ionosphere is a function only of

$$\left(\frac{\Delta\rho_i}{R_{CSi}}\right) = \left(\frac{R_{CSe}}{\rho_e}\right)^{m-2}, \quad (4.30)$$

where  $\Delta\rho_i = (\rho_i - \rho_{\infty})$ , and  $\rho_{\infty}$  is the distance from the magnetic axis of the field line from infinity as given above. In deriving Eq. (4.30) we have assumed that  $\Delta\rho_i$  is small compared with  $\rho_{\infty}$ , in keeping with the ‘current sheet’ approximation introduced above.

With  $\omega \sim 0.04 R_J$  over the range of system parameters discussed above, scaling as  $(\dot{M}/\Sigma_p^*)^{-(2/m)}$  (i.e. as  $(\dot{M}/\Sigma_p^*)^{0.262}$  for  $m = 2.71$ ), such that  $\Delta\rho_i$  will indeed be small compared with  $\rho_{\infty}$  (for  $(\Delta\rho_i/R_{CSi}) \sim 1$ ), for  $(\Delta\rho_i/R_{CSi}) \sim 1$ .

The solid lines in Figs. 4.14a and 4.14b show the normalised angular velocity solution given by Eq. (4.27) with  $K = 0$  and  $m = 2.71$ , plotted versus  $(\rho_e/R_{CSe})$  in the equatorial plane, and versus  $(\Delta\rho_i/R_{CSi})$  in the ionosphere, respectively. The form is similar to that for the dipole, though falling away from rigid corotation more quickly (in normalised units) in the inner region, and less quickly in the outer region. This solution is also shown in unnormalised form (with the above value of  $F_0$ ) by the dot-dashed lines in Figs. 4.12 and 4.13, where it is compared with the results of numerical integration of the full solution (solid and dashed lines as described above). It can be seen that the analytic solution forms a very close approximation to the numerical solutions for  $\rho_e > \rho_e^*$  under all conditions of interest here, a result we have confirmed by a wider comparative study not illustrated here. The dashed lines and tick marks in Fig. 4.14 show normalised approximate forms and their regimes of validity, in the same format as Fig. 4.1. Specifically, the long-dashed lines show the small- $\rho_e$  (‘S’) approximation given by Eq. (4.3)

$$\left(\frac{\omega}{\Omega_J}\right)_S = 1 - \frac{1}{2} \left(\frac{\rho_e}{R_{CSe}}\right)^m = 1 - \frac{1}{2} \left(\frac{R_{CSi}}{\Delta\rho_i}\right)^{\frac{m}{m-2}} \quad (4.31)$$

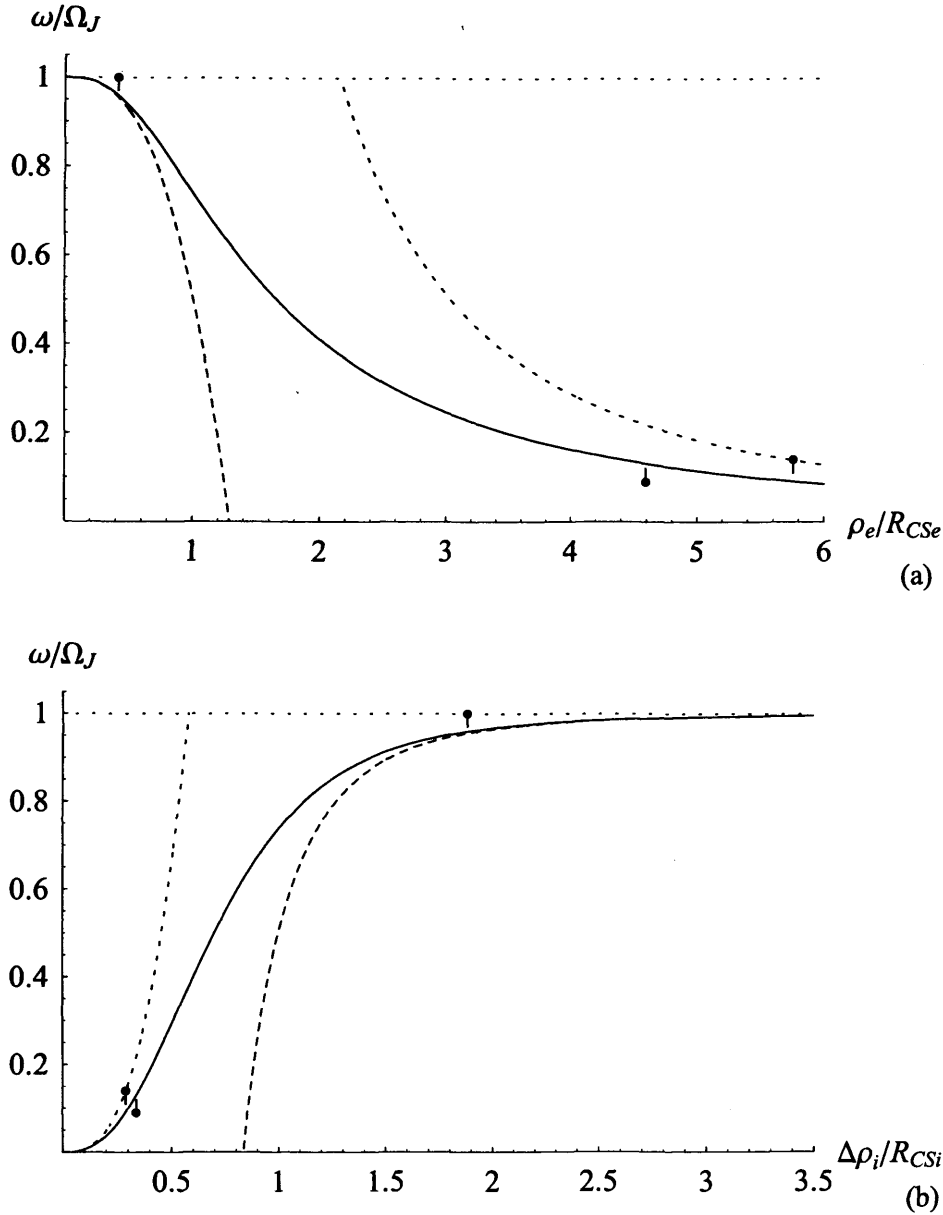


**Figure 4.14.** Plots of the steady state plasma angular velocity profile for a power law equatorial magnetic field (Eq. (3.33) with  $m=2.71$ ) and ‘current sheet’ approximate mapping to the ionosphere, shown (a) versus  $(\rho_e/R_{CSe})$  in the equatorial plane, and (b) versus  $(\Delta\rho_i/R_{CSi})$  in the ionosphere. The solid line in each case shows the full solution obtained from Eq. (4.27) with  $K=0$ , such that the plasma rigidly corotates at small radial distances. The long-dashed lines show the small- $\rho_e$  form given by Eq. (4.31), while the large- $\rho_e$  form is just  $(\omega/\Omega_J)_L = 0$ . The downward-pointing tick-marks indicate the limits of validity of both the small- and large- $\rho_e$  approximations as defined by Eq. (4.12). The short-dashed lines show the higher-order large- $\rho_e$  form given by Eq. (4.32), whose limit of validity defined by Eq. (4.14) is indicated by the upward-pointing tick-mark. The horizontal dotted line indicates the condition for rigid corotation,  $(\omega/\Omega_J)=1$ .

where we again note that the series generated by Eq. (4.1) (of which Eq. (4.31) is the leading term) is the same as that obtained by asymptotic expansion of the gamma function in Eq. (4.27) for large argument. The short-dashed lines then show the higher-order large- $\rho_e$  ('L') approximation, obtained from Eq. (4.27) as

$$\left(\frac{\omega}{\Omega_j}\right)_{L'} = \left(\frac{4}{m}\right)^{\frac{2}{m}} \Gamma\left(1 - \frac{2}{m}\right) \left(\frac{R_{CSe}}{\rho_e}\right)^2 = \alpha(m) \left(\frac{R_{CSe}}{\rho_e}\right)^2 \quad (4.32)$$

The lower-order large- $\rho_e$  ('L') approximation is again simply  $(\omega/\Omega_j)_L = 0$ . The outer limit of the small- $\rho_e$  approximation lies at  $(\rho_{es}/R_{CSe}) \approx 0.410$  where  $(1 - (\omega/\Omega_j)) \approx 0.041$ , the inner limit of the large- $\rho_e$  approximation lies at  $(\rho_{eL}/R_{CSe}) \approx 5.761$ , where  $(\omega/\Omega_j) \approx 0.091$ , while the inner limit of the higher-order large- $\rho_e$  approximation lies at  $(\rho_{eL'}/R_{CSe}) \approx 4.594$ , where  $(\omega/\Omega_j) \approx 0.131$ .

The normalised approximate solutions for the currents then follow from Eqs. (3.10), (3.12)-(3.15) and (3.17)

$$\frac{i_P}{i_{PCS}} = 2 \left(1 - \frac{\omega}{\Omega_j}\right) \quad \text{where} \quad i_{PCS} = \sqrt{\frac{F_o}{B_j R_j^2}} \Sigma_P^* B_j R_j \Omega_j, \quad (4.33a)$$

$$\frac{I_P}{I_{PCS}} = 4\pi \left(1 - \frac{\omega}{\Omega_j}\right) \quad \text{where} \quad I_{PCS} = \left(\frac{F_o}{B_j R_j^2}\right) \Sigma_P^* B_j R_j^2 \Omega_j, \quad (4.33b)$$

$$\frac{i_\rho}{i_{\rho CS}} = 4 \left(\frac{R_{CSe}}{\rho_e}\right) \left(1 - \frac{\omega}{\Omega_j}\right) \quad \text{where} \quad i_{\rho CS} = \left(\frac{F_o}{B_j R_j^2}\right) \left(\frac{\dot{M}}{2\pi \Sigma_P^* B_o F_o}\right)^{1/m} \Sigma_P^* B_j R_j \Omega_j, \quad (4.33c)$$

$$\frac{I_\rho}{I_{\rho CS}} = 8\pi \left(1 - \frac{\omega}{\Omega_j}\right) \quad \text{where} \quad I_{\rho CS} = \left(\frac{F_o}{B_j R_j^2}\right) \Sigma_P^* B_j R_j^2 \Omega_j, \quad (4.33d)$$

$$\frac{(j_{\parallel}/B)}{(j_{\parallel}/B)_{CS}} = 4 \left(\frac{\rho_e}{R_{CSe}}\right)^{m-2} \left[ \left(\frac{\omega}{\Omega_j}\right) - 2 \left(\frac{R_{CSe}}{\rho_e}\right)^m \left(1 - \frac{\omega}{\Omega_j}\right) \right]$$

$$\text{where } (j_{\parallel}/B)_{CS} = \left(\frac{B_J}{B_o}\right) \left(\frac{F_o}{B_J R_J^2}\right) \left(\frac{2\pi \Sigma_P^* B_o F_o}{M}\right)^{1-\frac{2}{m}} \Sigma_P^* \Omega_J, \quad (4.33e)$$

and

$$\frac{j_{\parallel}}{j_{\parallel CS}} = 4 \left(\frac{R_{CSi}}{\Delta \rho_i}\right) \left[ \left(\frac{\omega}{\Omega_J}\right) - 2 \left(\frac{\Delta \rho_i}{R_{CSi}}\right)^{\frac{m}{m-2}} \left(1 - \frac{\omega}{\Omega_J}\right) \right]$$

$$\text{where } j_{\parallel CS} = 2 \left(\frac{B_J}{B_o}\right) \left(\frac{F_o}{B_J R_J^2}\right) \left(\frac{2\pi \Sigma_P^* B_o F_o}{M}\right)^{1-\frac{2}{m}} \Sigma_P^* B_J \Omega_J. \quad (4.33f)$$

These forms are shown by the solid lines in Figs. 4.15-4.17, plotted versus either  $(\rho_e/R_{CSe})$  or  $(\Delta \rho_i/R_{CSi})$  as appropriate.

The dashed lines in Figs. 4.15-4.17 show approximate forms based on the 'S', 'L' and 'L'' approximations for the angular velocity, in the same format as Figs. 4.2-4.4 for the dipole. Specifically, the small- $\rho_e$  forms for the currents are obtained by introducing Eq. (4.31) into Eq. (4.33) (again including the third order term in the approximation for the FAC)

$$\left(\frac{i_p}{i_{PCS}}\right)_S = \left(\frac{R_{CSi}}{\Delta \rho_i}\right)^{\frac{m}{m-2}}, \quad \left(\frac{I_p}{I_{PCS}}\right)_S = 2\pi \left(\frac{R_{CSi}}{\Delta \rho_i}\right)^{\frac{m}{m-2}}, \quad (4.34a,b)$$

$$\left(\frac{i_p}{i_{\rho CS}}\right)_S = 2 \left(\frac{\rho_e}{R_{CSe}}\right)^{m-1}, \quad \left(\frac{I_p}{I_{\rho CS}}\right)_S = 4\pi \left(\frac{\rho_e}{R_{CSe}}\right)^m, \quad (4.34c,d)$$

$$\left(\frac{(j_{\parallel}/B)}{(j_{\parallel}/B)_{CS}}\right)_S = m \left(\frac{\rho_e}{R_{CSe}}\right)^{2(m-1)}, \quad \text{and} \quad \left(\frac{j_{\parallel}}{j_{\parallel CS}}\right)_S = m \left(\frac{R_{CSi}}{\Delta \rho_i}\right)^{\frac{2(m-1)}{m-2}}. \quad (4.34e,f)$$

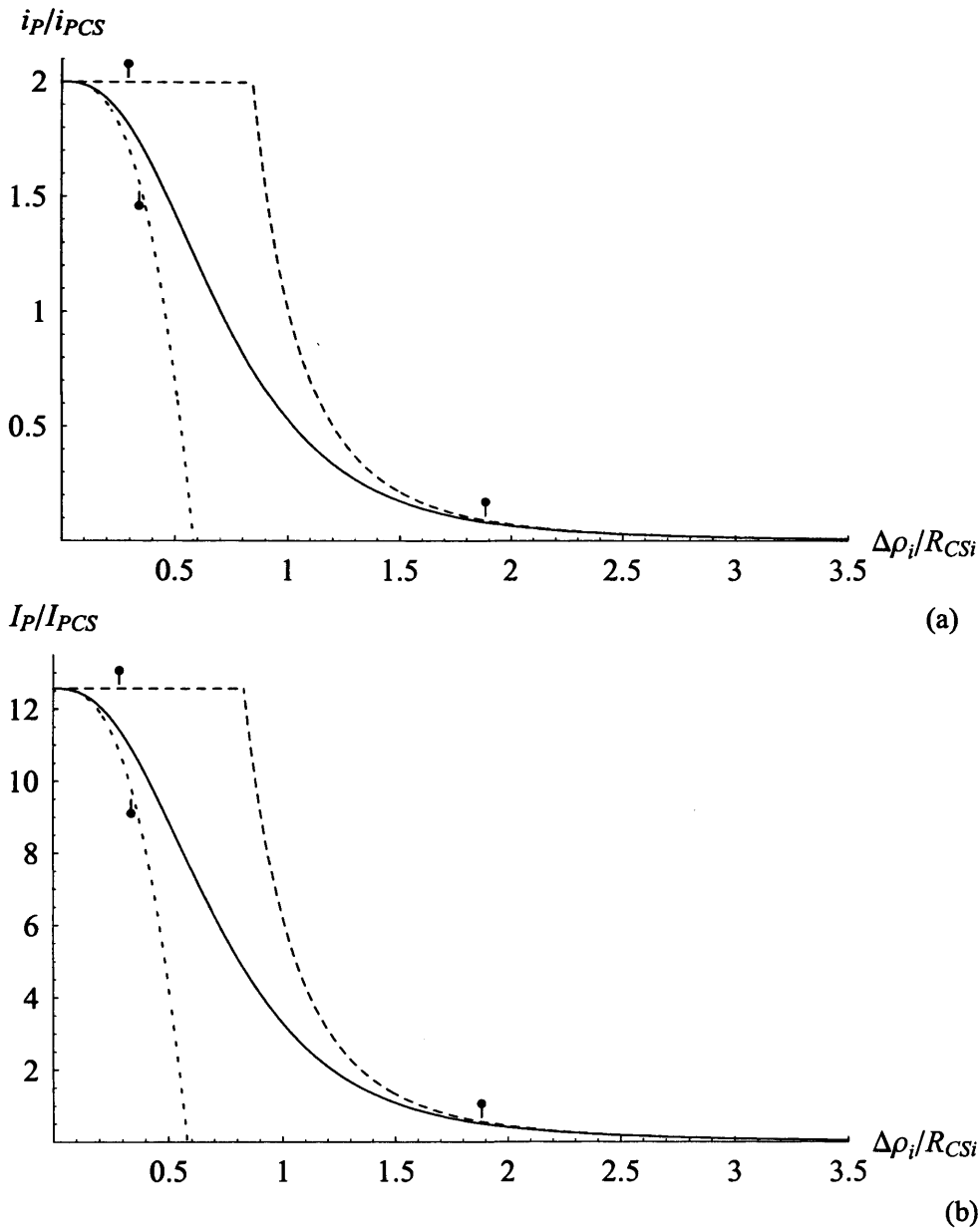


**Figure 4.15** Plots of (a) the normalised height-integrated ionospheric Pedersen current intensity, (b) the normalised azimuth- and height-integrated total ionospheric Pedersen current, plotted versus  $(\Delta\rho_i/R_{CSi})$ , for a power law equatorial magnetic field (Eq. (3.33) with  $m = 2.71$ ) and ‘current sheet’ approximate mapping to the ionosphere. The format is similar to Fig. 4.2 for the dipole. The normalization constants are given by Eqs. (4.33a) and (4.33b). The solid lines show the full solutions given by Eqs. (4.33a) and (4.33b), while the long-dashed lines show the small- and large- $\rho_e$  forms given by Eqs. (4.34a,b) and (4.35a,b), drawn to a common boundary at  $(\rho_e/R_{CSe}) = \sqrt[4]{2}$ . The downward-pointing tick-marks show the limits of validity of these approximate forms as defined by Eq. (4.12) (as in Fig. 4.1). The short-dashed lines show the higher-order large- $\rho_e$  form given by Eq. (4.36), whose limit of validity defined by Eq. (4.14) is indicated by the upward-pointing tick-mark.

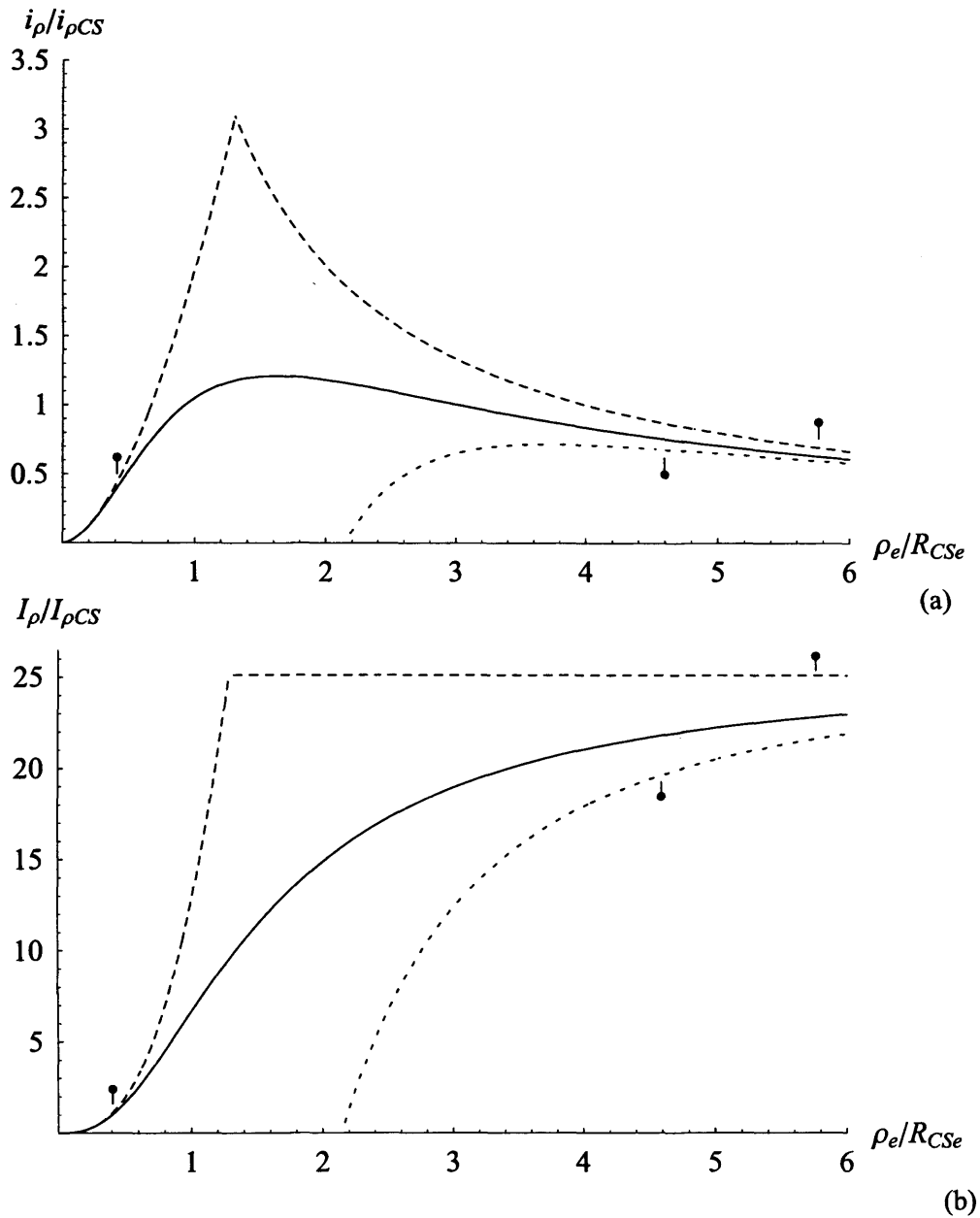


**Figure 4.16** Plots of (a) the normalised current sheet-integrated equatorial radial current intensity, and (b) the normalised azimuth- and current sheet-integrated total equatorial radial current, plotted versus  $(\rho_e/R_{CSe})$ , for a power law equatorial magnetic field (Eq. (3.33) with  $m=2.71$ ) and ‘current sheet’ approximate mapping to the ionosphere. The normalization constants are given by Eqs. (4.33c) and (4.33d). The solid lines show the full solutions given by Eqs. (4.33c) and (4.33d), while the long-dashed lines show the small- and large- $\rho_e$  forms given by Eqs. (4.34c,d) and (4.35c,d), drawn to a common boundary at  $(\rho_e/R_{CSe})=\sqrt[3]{2}$ . The short-dashed lines show the higher order large- $\rho_e$  approximation. The tick-marks are in the same format as Fig. 4.15.

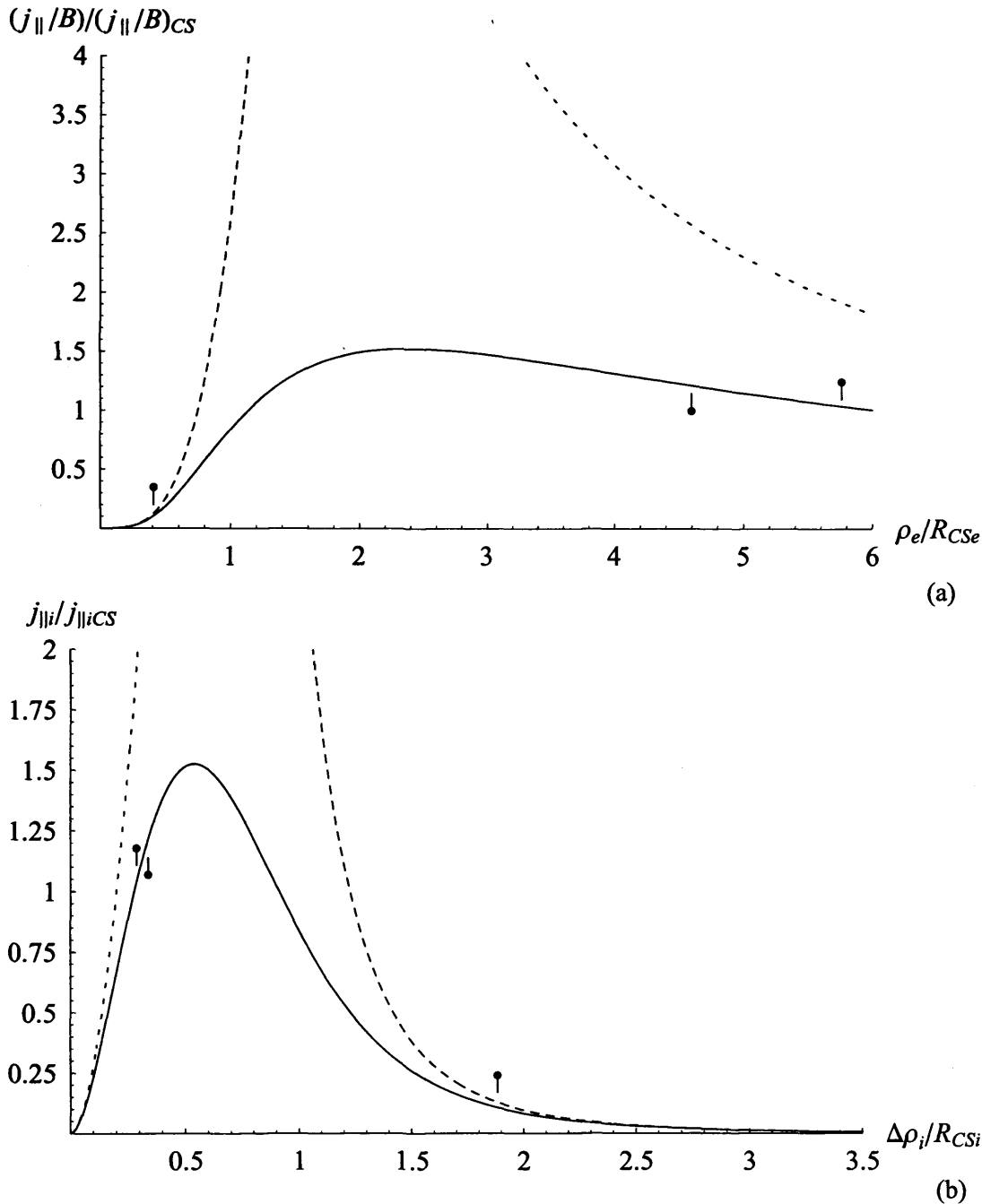


**Figure 4.17** Plots of (a) the normalised equatorial field-aligned current density per unit magnetic field strength, plotted versus normalised equatorial radial distance ( $\rho_e/R_{De}$ ), and (b) the normalised field-aligned current density just above the ionosphere, plotted versus normalised distance from the magnetic axis ( $\rho_i/R_{Di}$ ) in the ionosphere, for a power law equatorial magnetic field (Eq. (3.33) with  $m=2.71$ ) and ‘current sheet’ approximate mapping to the ionosphere. The normalization constants are given by Eqs. (4.33e) and (4.33f). The solid lines show the full solutions given by Eqs. (4.33e) and (4.33f), while the long-dashed lines show the small- $\rho_e$  form given by Eqs. (4.34e,f), and the short dashed line shows the higher-order large- $\rho_e$  approximation given by Eqs. (4.36e,f). The tic-marks are in the same format as Fig. 4.15.

The lowest-order large- $\rho_e$  forms are again given by taking  $(\omega/\Omega_j)_L = 0$ , so that Eq. (4.33) yields (again assuming that  $\rho_e$  is large)

$$\left(\frac{i_p}{i_{PCS}}\right)_L = 2, \quad \left(\frac{I_P}{I_{PCS}}\right)_L = 4\pi, \quad (4.35a,b)$$

$$\left(\frac{i_\rho}{i_{\rho CS}}\right)_L = 4\left(\frac{R_{CSe}}{\rho_e}\right), \quad \left(\frac{I_\rho}{I_{\rho CS}}\right)_L = 8\pi, \quad (4.35c,d)$$

$$\left(\frac{(j_{\parallel}/B)}{(j_{\parallel}/B)_{CS}}\right)_L = 0, \quad \text{and} \quad \left(\frac{j_{\parallel i}}{j_{\parallel i CS}}\right)_L = 0. \quad (4.35e,f)$$

Eqs.(4.34) and (4.35) are equivalent to Eqs. (4.4) and (4.5) when expanded out into un-normalised form. The higher-order large- $\rho_e$  form obtained by substituting Eq. (4.32) into Eq. (4.33), to yield

$$\left(\frac{i_p}{i_{PCS}}\right)_{L'} = 2\left(1 - \alpha(m)\left(\frac{\Delta\rho_i}{R_{CSi}}\right)^{\frac{2}{m-2}}\right), \quad \left(\frac{I_P}{I_{PCS}}\right)_{L'} = 4\pi\left(1 - \alpha(m)\left(\frac{\Delta\rho_i}{R_{CSi}}\right)^{\frac{2}{m-2}}\right), \quad (4.36a,b)$$

$$\left(\frac{i_\rho}{i_{\rho CS}}\right)_{L'} = 4\left(\frac{R_{CSe}}{\rho_e}\right)\left(1 - \alpha(m)\left(\frac{R_{CSe}}{\rho_e}\right)^2\right), \quad \left(\frac{I_\rho}{I_{\rho CS}}\right)_{L'} = 8\pi\left(1 - \alpha(m)\left(\frac{R_{CSe}}{\rho_e}\right)^2\right), \quad (4.36c,d)$$

$$\left(\frac{(j_{\parallel}/B)}{(j_{\parallel}/B)_{CS}}\right)_{L'} = 4\alpha(m)\left(\frac{R_{CSe}}{\rho_e}\right)^{4-m}, \quad \text{and} \quad \left(\frac{j_{\parallel i}}{j_{\parallel i CS}}\right)_{L'} = 4\alpha(m)\left(\frac{\Delta\rho_i}{R_{CSi}}\right)^{\frac{4-m}{m-2}}. \quad (4.36e,f)$$

Comparison with Figs. 4.2-4.4 shows similarities, but also major differences with the currents for the dipole field. The differences arise from the fact that the current sheet field lines reach the ionosphere in a narrow band at a finite co-latitude, rather than continuously approaching the pole with increasing radial distance, as for the dipole. The ionospheric Pedersen current (Eq. (4.36a)), while being proportional to the displacement of the band

from the magnetic axis  $\sqrt{F_0/B_j R_j^2}$ , then varies with co-latitude only through the variation of the plasma angular velocity. As seen in Fig. 4.15a, the Pedersen current therefore peaks at the poleward edge of the band where the angular velocity is zero, and falls monotonically with distance from the boundary as the angular velocity approaches rigid corotation (Fig. 4.14b). This implies that the azimuth-integrated total current also varies monotonically with distance, the total equatorial current (Eq. (4.36d)) thus rising with increasing equatorial distance towards  $8\pi F_0 \Sigma_p^* \Omega_j$  (strictly,  $8\pi F_\infty \Sigma_p^* \Omega_j$ ) at infinity, as seen in Fig. 4.16b. This behaviour also implies that the radial current intensity (Eq. (4.36c)) rises to a peak value with increasing distance, and then falls as  $\rho_e^{-1}$  at large distances, as seen in Fig. 4.16a. The further implication of a monotonically increasing total current is that the field-aligned current is unidirectional in this approximation, flowing consistently from the ionosphere to the equatorial current sheet, as shown in Fig. 4.17a and 4.17b. Closure of the current system must then occur outside the region described by the model. This behaviour thus mirrors the numerical results presented previously by Cowley and Bunce (2001b) and Cowley, Nichols and Bunce (2002) using the full current sheet field model illustrated in Fig. 3.5. A comparison with numerical results will be presented in the next section.

In like manner to the dipole results, the normalised solutions given above show how the form and amplitude of the plasma angular velocity and currents vary with the system parameters in the case of a power law current sheet field. Eqs. (4.26) and (4.29) show that the solutions scale spatially in the equatorial plane and in the ionosphere as  $\rho_e \propto (\Sigma_p^*/\dot{M})^{1/m}$  and  $\Delta\rho_i \propto (\dot{M}/\Sigma_p^*)^{1-2/m}$ , respectively, while Eq. (4.33) shows that the amplitude of each component of the current system scales as some power of  $\Sigma_p^*$  and  $\dot{M}$  of the same form as Eq. (4.19), but with  $\gamma$  equal to  $1-2/m$  for the equatorial radial current, 1 for the Pedersen current and azimuth-integrated total field-perpendicular current (such that these currents scale linearly with  $\Sigma_p^*$  and are independent of  $\dot{M}$ ), and  $3-4/m$  for the field-aligned current density. Since these values of  $\gamma$  are consistently higher for a given current component for the current sheet model than for the dipole (at least for  $m > 2$ , as investigated here), the implication is that the currents scale as a somewhat higher power of the conductivity for the current sheet model than for the dipole, and as a somewhat lower

power of the mass outflow rate. The corresponding behaviours at small and large distances, such that the solutions obey Eqs. (4.4) and (4.5), are

$$i_S \propto \dot{M} \rho_e^{\frac{m}{2}(1+\gamma)} \propto \frac{\dot{M}}{\Delta \rho_i^{(m(1+\gamma)/2(m-2))}} , \quad (4.37)$$

and

$$i_L \propto \frac{\Sigma_P^*}{\rho_e^{m(1-\gamma)/2}} = \Sigma_P^* \Delta \rho_i^{(m(1-\gamma)/2(m-2))} , \quad (4.38)$$

as can be verified by substituting the appropriate approximations ('S' and 'L') for the angular velocity into Eq. (4.33). Thus for example, with  $\gamma = 1 - 2/m$ , the equatorial radial current increases as  $\rho_e^{m-1}$  in the inner region and falls as  $\rho_e^{-1}$  at large distances, while the field-aligned current with  $\gamma = 3 - 4/m$  grows as  $\rho_e^{2(m-1)}$  in the equatorial plane in the inner region and approaches zero in this approximation at large distances, as indicated above (Figs. 4.17a,b). The spatial variation of the field-aligned current in the large-distance limit may then be obtained from the higher-order large-distance approximation (Eq. (4.32)), from which it is found that the current varies as  $\rho_e^{-(4-m)}$  in the equatorial plane, and as  $\Delta \rho_i^{(4-m)/(m-2)}$  in the ionosphere. A comparison of these dependencies for the dipole and power law current sheet fields will be given below in Section 4.5. Table 4.3 also summarises the amplitudes and positions of the peak currents in normalised units for the  $m = 2.71$  power law field.

#### 4.4.3. Un-normalised numerical and approximate analytic solutions for the current sheet model

We now consider how the un-normalised solutions for the current sheet field vary with the system parameters, comparing the approximate analytic results for the power law field derived above with numerical results using the full field shown in Fig. 3.5. The format of the presentation follows that for the dipole in Section 4.2.3, so that simple comparison can

Feature	$\left(\frac{\rho_e}{R_{CSe}}\right)$	$\left(\frac{\Delta\rho_i}{R_{CSI}}\right)$	$\left(\frac{\omega}{\Omega_j}\right)$
Maximum sheet-integrated equatorial radial current $(i_\rho/i_{\rho CS})_{max} \approx 1.2109$	1.6142	0.7118	0.5113
Plasma angular velocity falls to $\left(\frac{\omega}{\Omega_j}\right) = 0.5$	1.6521	0.7002	0.5
Maximum upward field-aligned current density $((j_{  }/B)/(j_{  }/B)_{CS})_{max} = (j_{  i}/j_{  iCS})_{max} \approx 1.5274$	2.3777	0.5407	0.3339
Maximum height-integrated ionospheric Pedersen current $(i_P/i_{PCS})_{max} = 2$			
Maximum azimuth-integrated total current $(I_\rho/I_{\rho CS})_{max} = 2(I_P/I_{PCS})_{max} = 8\pi \approx 25.133$	$\infty$	0	0
Field-aligned current goes to zero			

**Table 4.3.** Principal features of the plasma angular velocity and coupling current system for the power law current sheet field in normalised units, obtained (with  $m = 2.71$ ) from the approximate analytic solution of Section 4.4.

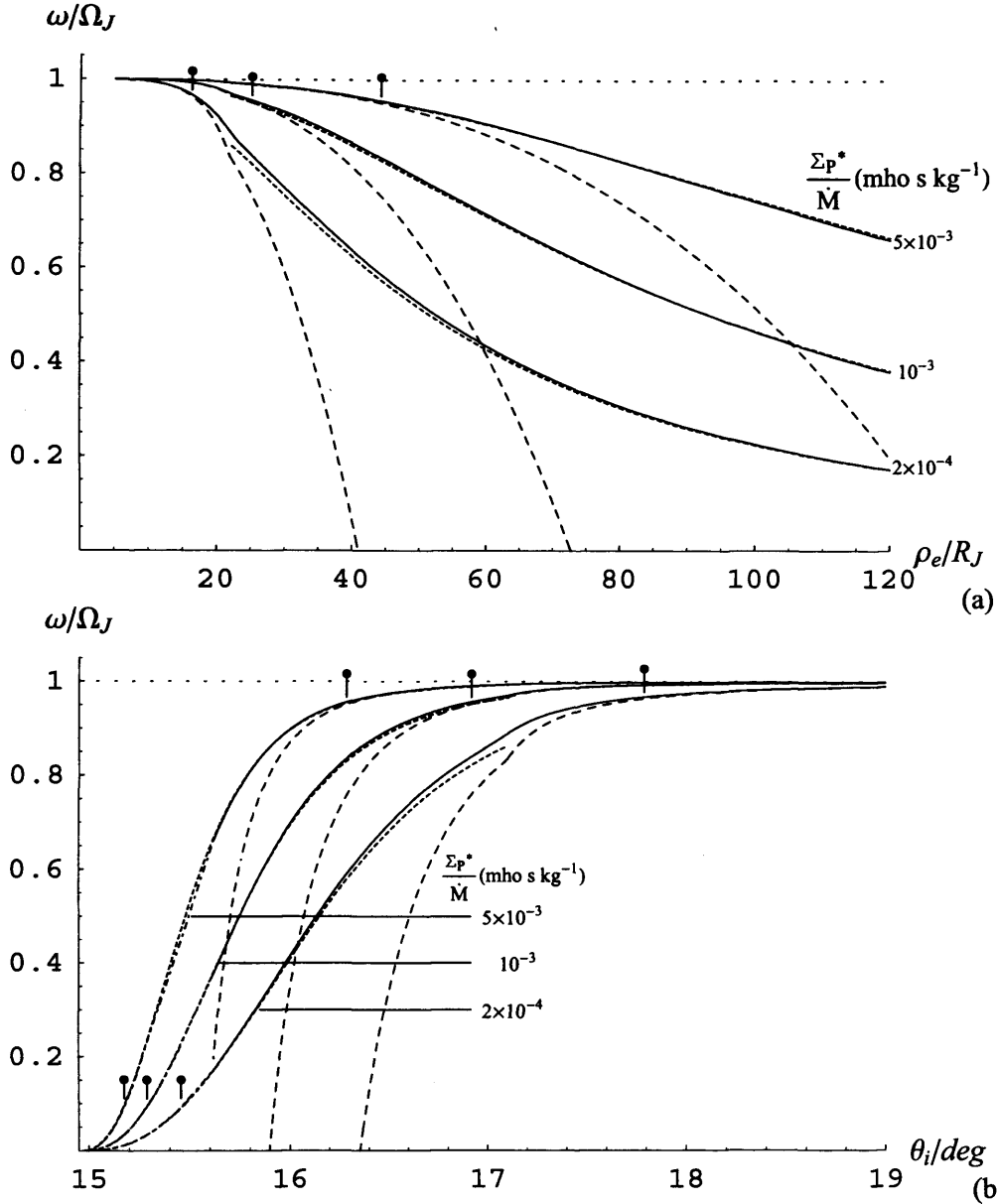


**Figure 4.18** Plasma angular velocity profiles for the current sheet magnetic field model are plotted (a) versus equatorial radial distance  $\rho_e$ , and (b) versus magnetic co-latitude  $\theta_i$ . Profiles are shown in each case for  $(\Sigma_p^*/M) = 2 \times 10^{-4}, 10^{-3}$ , and  $5 \times 10^{-3}$  mho s kg<sup>-1</sup>, as marked. The solid lines show numerically computed solutions of Eq. (3.27) using the full field model described in Section 3.3.6, starting from the near-rigid corotation value given by Eq. (4.3) at  $\rho_e = 5 R_J$ . The long-dashed lines show the small- $\rho_e$  approximation given by Eq. (4.3), the corresponding large- $\rho_e$  form being just  $(\omega/\Omega_J)_L = 0$ , while the tick-marks show the limits of validity of these approximations according to the criterion given by Eq. (4.12) (the large- $\rho_e$  limits only lying within the range in plot (b)). In the ionospheric projection in (b), the solution curves are continued beyond the  $120 R_J$  limit of plot (a) (mapping to a co-latitude of  $15.62^\circ$  in the ionosphere) towards the limiting latitude defined by the current sheet field line from infinity (mapping to  $\sim 14.95^\circ$  in the ionosphere), which lies at the left-hand edge of the plot. The angular velocity curves in this regime are shown by dot-dashed lines. The short-dashed lines in both plots show the approximate analytic solution in the power-law field region given by Eq. (4.27) with  $K=0$  and  $F_0 = F_e(\rho_e = 70 R_J) \approx 3.22 \times 10^4$  nT  $R_J^2$ . The horizontal dotted lines indicate the condition for rigid corotation,  $(\omega/\Omega_J) = 1$ .

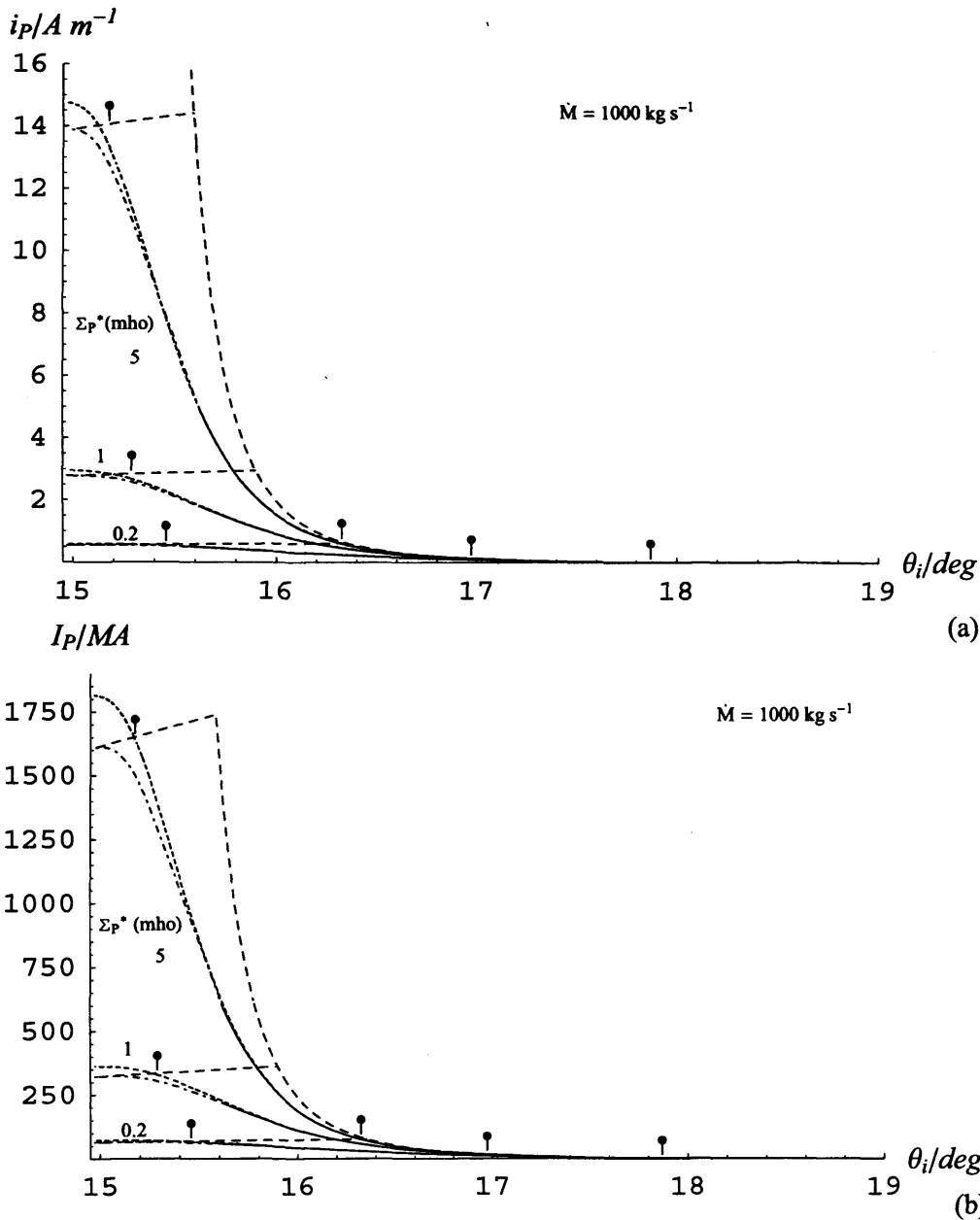


**Figure 4.19** Set of solutions for (a) the height-integrated Pedersen current intensity, and (b) the azimuth- and height-integrated total ionospheric Pedersen current for the current sheet field model, shown for  $\dot{M}$  held fixed at  $1000 \text{ kg s}^{-1}$  while  $\Sigma_p^*$  takes the values 0.2, 1, and 5 mho as marked. These are plotted versus ionospheric co-latitude. The format follows that in Fig. 4.18, such that the solid lines show values obtained by numerical integration of Eq. (3.27) using the full field model together with Eqs. (3.10) and (3.14), the long-dashed lines show the approximate forms given by Eqs. (4.4a,b) and (4.5a,b) with limits of validity indicated by the tick-marks, while the short-dashed lines show the approximate analytic solution in the power-law field region given by Eqs. (4.27) and (4.33a,b). Note that there is only one ‘small- $\rho_e$ ’ approximation (long-dashed) curve in each plot corresponding to the fixed  $\dot{M}$  value, while the three ‘large- $\rho_e$ ’ approximation curves are simply proportional to  $\Sigma_p^*$ .

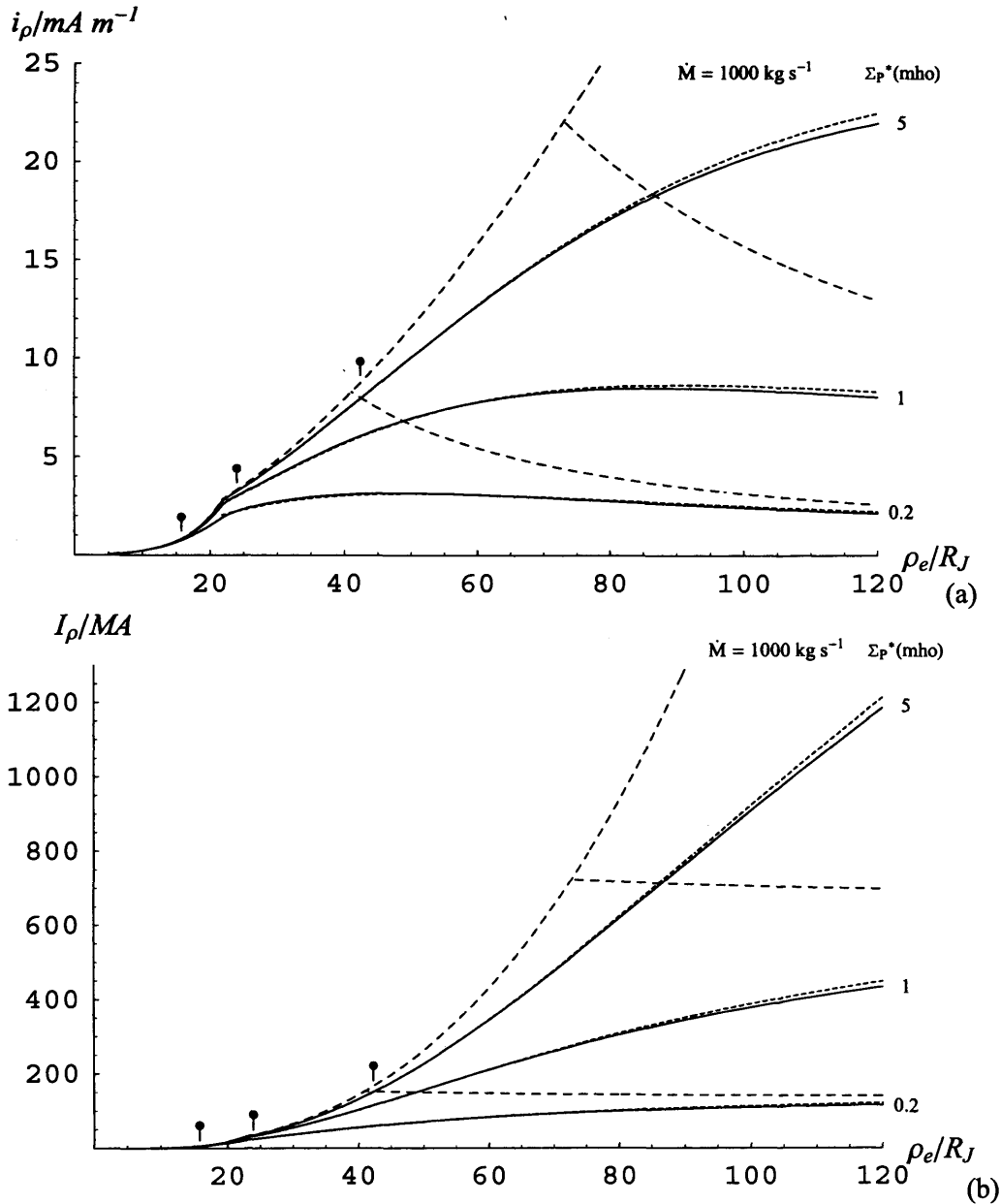


**Figure 4.20** Set of solutions for (a) the sheet-integrated equatorial radial current intensity, (b) the azimuth- and sheet-integrated total equatorial radial current for the current sheet field model, shown for  $\dot{M}$  held fixed at  $1000 \text{ kg s}^{-1}$  while  $\Sigma_p^*$  takes the values 0.2, 1, and 5 mho as marked. These are plotted versus equatorial radial distance. The format follows that in Fig. 4.18, such that the solid lines show values obtained by numerical integration of Eq. (3.27) using the full field model together with Eqs. (3.12) and (3.13), the long-dashed lines show the approximate forms given by Eqs. (4.4c,d) and (4.5c,d) with limits of validity indicated by the tick-marks, while the short-dashed lines show the approximate analytic solution in the power-law field region given by Eqs. (4.27) and (4.33c,d). Again, note that there is only one ‘small- $\rho_e$ ’ approximation (long-dashed) curve in each plot corresponding to the fixed  $\dot{M}$  value, while the three ‘large- $\rho_e$ ’ approximation curves are simply proportional to  $\Sigma_p^*$ .

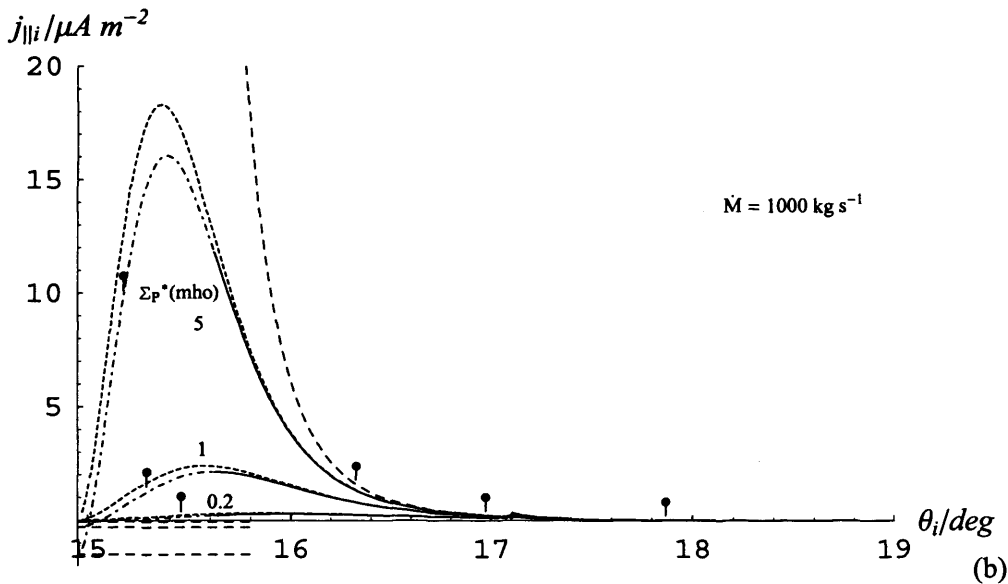
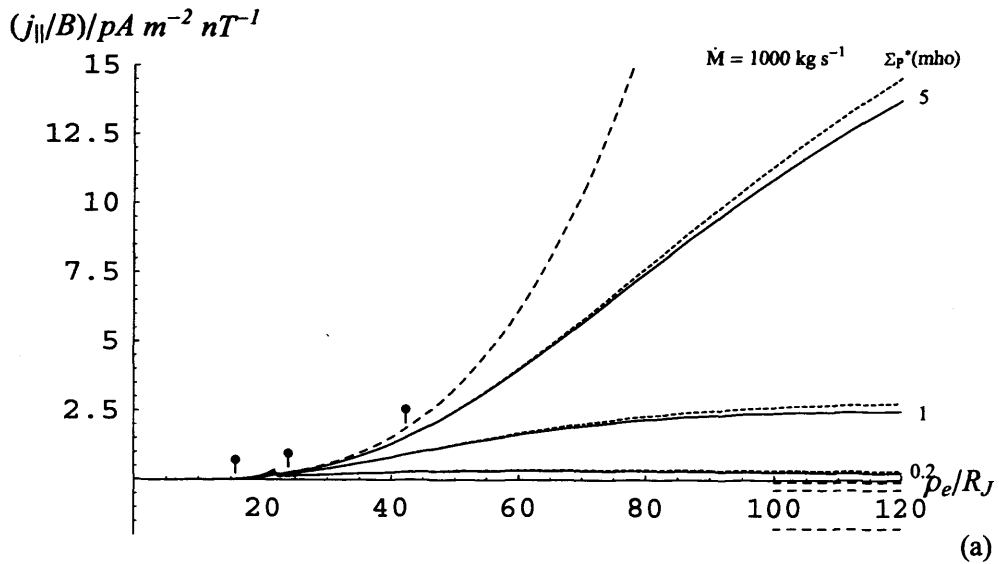


**Figure 4.21** Set of solutions for (a) the equatorial field-aligned current density per unit magnetic flux, and (b) the ionospheric field-aligned current density for the current sheet field model, shown for  $\dot{M}$  held fixed at  $1000 \text{ kg s}^{-1}$  while  $\Sigma_p^*$  takes the values 0.2, 1, and 5 mho as marked. These are plotted versus equatorial radial distance and ionospheric co-latitude respectively. The format follows that in Fig. 4.18, such that the solid lines show values obtained by numerical integration of Eq. (3.27) using the full field model together with Eqs. (3.15) and (3.17), the long-dashed lines show the approximate forms given by Eqs. (4.4e,f) and (4.5e,f) with limits of validity indicated by the tick-marks, while the short-dashed lines show the approximate analytic solution in the power-law field region given by Eqs. (4.27) and (4.33e,f). Again, note that there is only one ‘small- $\rho_e$ ’ approximation (long-dashed) curve in each plot corresponding to the fixed  $\dot{M}$  value, while the three ‘large- $\rho_e$ ’ approximation curves are simply proportional to  $\Sigma_p^*$ .

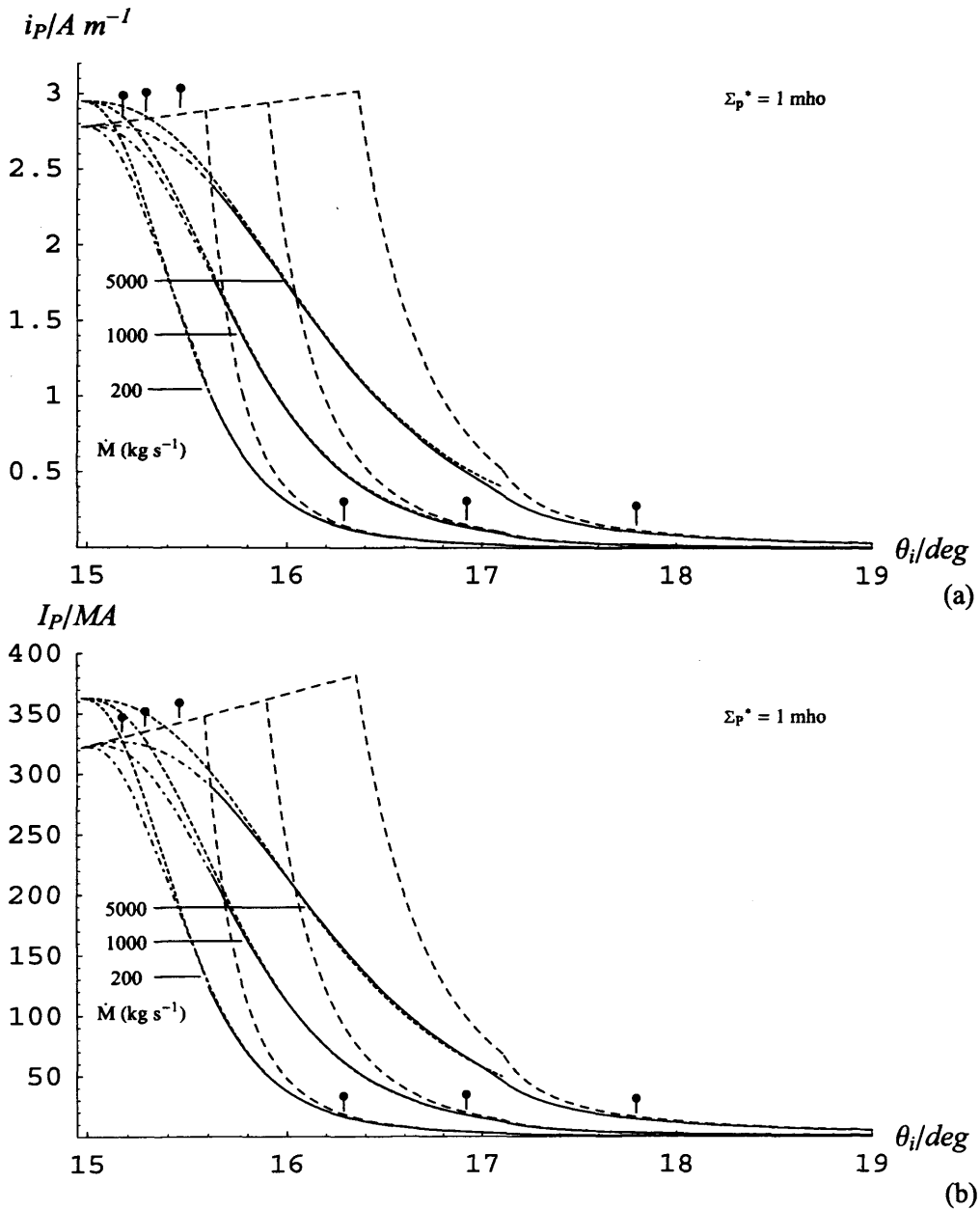


**Figure 4.22** Set of solution curves for (a) the height-integrated Pedersen current intensity, and (b) the azimuth- and height-integrated total ionospheric Pedersen current for the current sheet field model, shown for  $\Sigma_p^*$  held fixed at 1 mho while  $\dot{M}$  takes the values 200, 1000, and 5000  $\text{kg s}^{-1}$ . The format is the same as for Figs. 4.19-4.21. Note that in this case there is only one 'large- $\rho_e$ ' approximation (dashed) curve in each plot corresponding to the fixed  $\Sigma_p^*$  value, while the three 'small- $\rho_e$ ' approximation curves are simply proportional to  $\dot{M}$ .

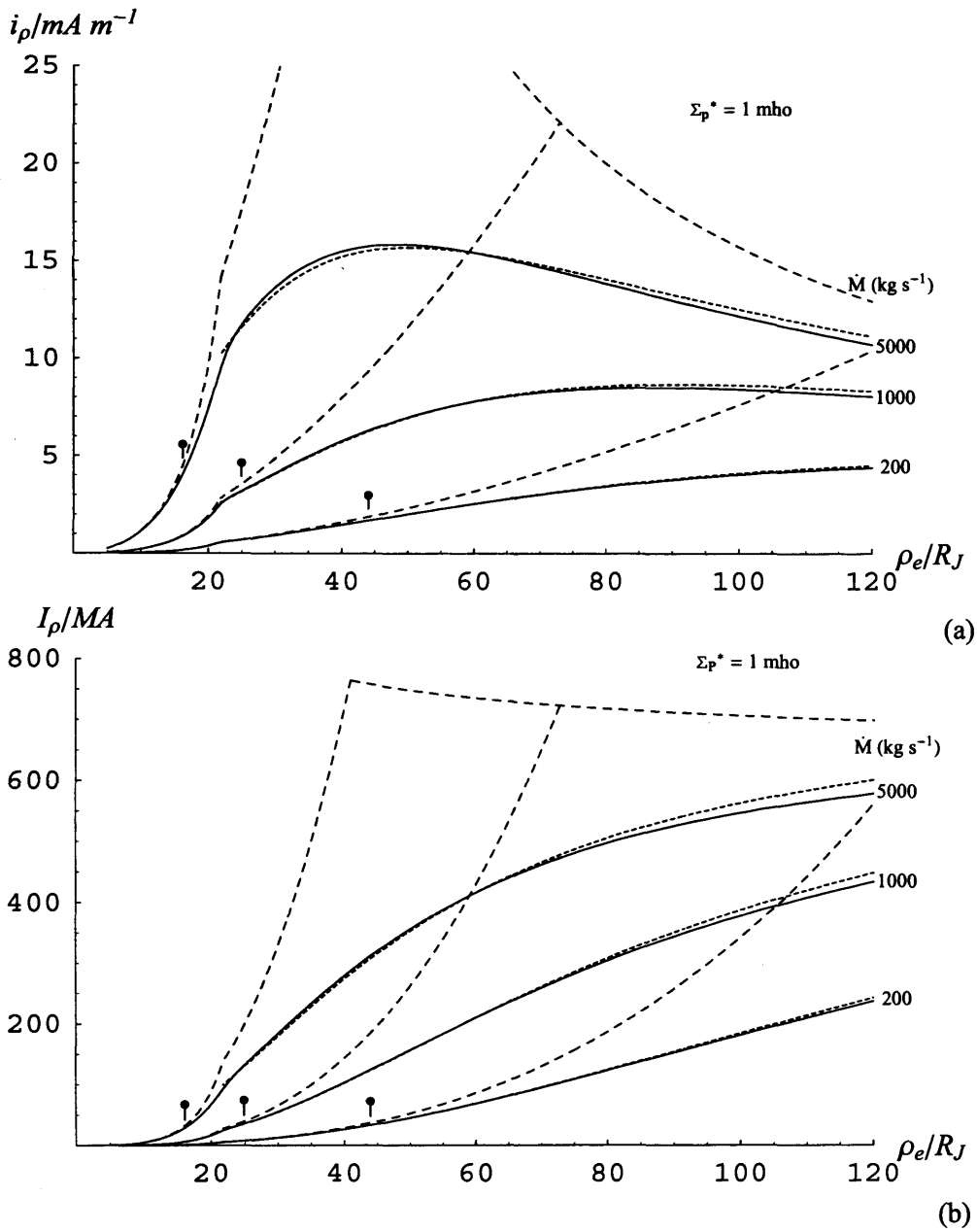


**Figure 4.23** Set of solution curves for (a) the sheet-integrated equatorial radial current intensity, and (b) the azimuth- and sheet-integrated total equatorial radial current for the current sheet field model, shown for  $\Sigma_p^*$  held fixed at 1 mho while  $\dot{M}$  takes the values 200, 1000, and 5000  $\text{kg s}^{-1}$ . The format is the same as for Figs. 4.19-4.21. Again, note that in this case there is only one 'large- $\rho_e$ ' approximation (dashed) curve in each plot corresponding to the fixed  $\Sigma_p^*$  value, while the three 'small- $\rho_e$ ' approximation curves are simply proportional to  $\dot{M}$ .

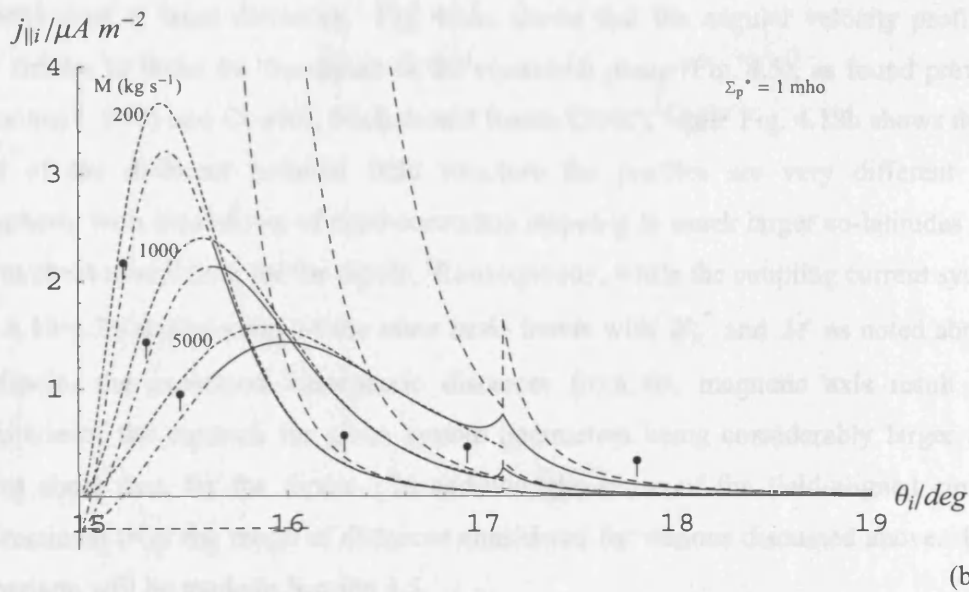
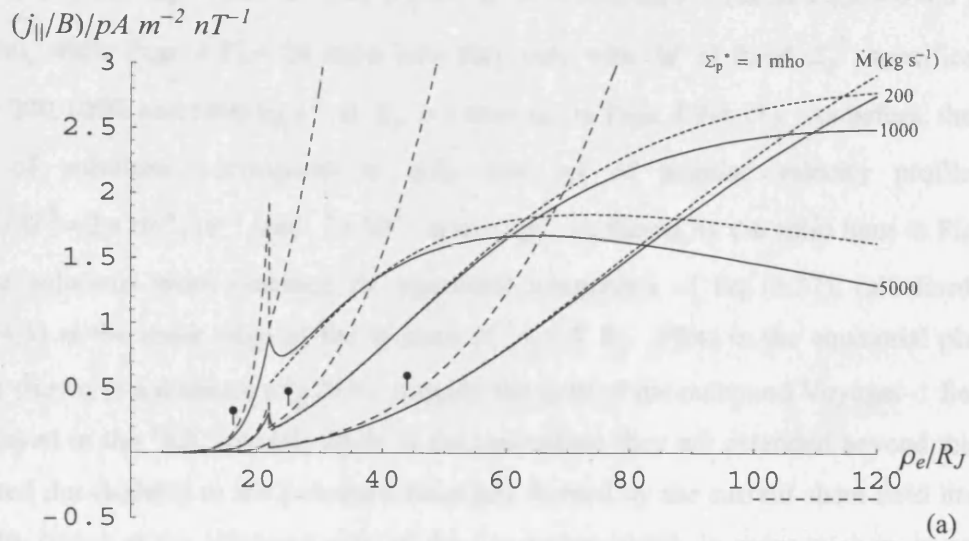


**Figure 4.24** Set of solution curves for (a) the equatorial field-aligned current density per unit magnetic flux, and (b) the ionospheric field-aligned current density for the current sheet field model, shown for  $\Sigma_p^*$  held fixed at 1 mho while  $\dot{M}$  takes the values 200, 1000, and 5000  $\text{kg s}^{-1}$ . The format is the same as for Figs. 4.19-4.21. Again, note that in this case there is only one ‘large- $\rho_e$ ’ approximation (dashed) curve in each plot corresponding to the fixed  $\Sigma_p^*$  value, while the three ‘small- $\rho_e$ ’ approximation curves are simply proportional to  $\dot{M}$ .

also be made between the results for the two fields. Figs. 4.19-4.21 thus show how the current components for the current sheet model vary with  $\Sigma_p^*$  at fixed  $\dot{M}$  (solid lines), specifically for  $\Sigma_p^* = 0.2, 1,$  and  $5$  mho at  $\dot{M} = 1000 \text{ kg s}^{-1}$  (as in Figs. 4.6-4.8 for the dipole), while Figs. 4.22-4.24 show how they vary with  $\dot{M}$  at fixed  $\Sigma_p^*$ , specifically for  $\dot{M} = 200, 1000,$  and  $5000 \text{ kg s}^{-1}$  at  $\Sigma_p^* = 1$  mho (as in Figs. 4.9-4.11). As before, these two sets of solutions correspond to only one set of angular velocity profiles, for  $(\Sigma_p^*/\dot{M}) = 2 \times 10^{-4}, 10^{-3},$  and  $5 \times 10^{-3} \text{ mho s kg}^{-1}$ , as shown by the solid lines in Fig. 4.18. These solutions were obtained by numerical integration of Eq. (3.27), initialised using Eq. (4.3) at the inner edge of the Io torus at  $\rho_e = 5 R_J$ . Plots in the equatorial plane are again shown to a distance of  $120 R_J$ , roughly the limit of the outbound Voyager-1 field data employed in the 'KK' model, while in the ionosphere they are extended beyond this point (plotted dot-dashed) to the poleward boundary formed by the current sheet field line from infinity (lying at the left-hand edge of the ionosphere plots), in order to show in principle the behaviour at large distances. Fig. 4.18a shows that the angular velocity profiles are quite similar to those for the dipole in the equatorial plane (Fig. 4.5), as found previously by Pontius (1997) and Cowley, Nichols and Bunce (2002), while Fig. 4.18b shows that as a result of the different poloidal field structure the profiles are very different in the ionosphere, with breakdown of rigid corotation mapping to much larger co-latitudes for the current sheet model than for the dipole. Consequently, while the coupling current system in Figs. 4.19-4.24 shows many of the same basic trends with  $\Sigma_p^*$  and  $\dot{M}$  as noted above for the dipole, the increased ionospheric distances from the magnetic axis result in the magnitude of the currents for given system parameters being considerably larger for the current sheet than for the dipole. In addition, the sense of the field-aligned current is unidirectional over the range of distances considered for reasons discussed above. Further comparison will be made in Section 4.5.

We now compare the numerical results with the approximate analytic solutions derived above. In order to fix the approximation, it is necessary to choose the value of  $F_o$ , related to the distance from the magnetic axis that the current sheet field lines are taken to map to the ionosphere. Any value can be chosen that is representative of the current sheet field lines in the region considered. Here we take  $F_o$  to be equal to  $F_e$  at a radial distance of  $70 R_J$ , roughly the centre of the power-law field region in the equatorial range considered.

This value is  $\sim 3.22 \times 10^4 \text{ nT } R_J^2$ , corresponding to an ionospheric distance from the magnetic axis of  $\sim 0.27 R_J$ , or a dipole co-latitude of  $15.9^\circ$ . We then find from Eqs. (4.26) and (4.29) that the modified equatorial and ionospheric ‘Hill’ distances are

$$\frac{R_{CSe}}{R_J} \approx 56.38 \left( \frac{\Sigma_p^* (\text{mho})}{\dot{M} (1000 \text{ kg s}^{-1})} \right)^{\frac{1}{2.71}} \quad \text{and} \quad \frac{R_{CSI}}{R_J} \approx 0.0197 \left( \frac{\dot{M} (1000 \text{ kg s}^{-1})}{\Sigma_p^* (\text{mho})} \right)^{\frac{0.71}{2.71}}, \quad (4.39)$$

such that for  $(\Sigma_p^* / \dot{M}) = 2 \times 10^{-4}, 10^{-3},$  and  $5 \times 10^{-3} \text{ mho s kg}^{-1}$  we have  $R_{CSe} \approx 31.1, 56.4,$  and  $79.1 R_J$ , again comparable to the spatial scale of the middle magnetosphere, while  $R_{CSI} \approx 0.013, 0.020,$  and  $0.030 R_J$ , small compared with  $\rho_{i\infty} \approx 0.258 R_J$ , as assumed above.

Using these values, the equatorial angular velocity profiles obtained from Eq. (4.27) with  $K = 0$  are shown by the short-dashed lines in Fig. 4.18, where the ionospheric profiles have been mapped (as for the numerical results) from the equator using the full expression for the flux function (Eq. (3.35b)), rather than using the approximate mapping of Eqs. (4.29) and (4.30). Since the power law field on which the approximation is based is valid in the full model only beyond  $\rho_e^* \approx 21.78 R_J$ , the approximations are plotted only beyond this point (corresponding to  $\theta_i \leq 17.1^\circ$  in the ionosphere). It can be seen that the agreement between the approximations and the numerical results in this region is very good, especially for the larger values of  $(\Sigma_p^* / \dot{M})$ . This being so, we may expect that Eq. (4.33) will also form good approximations for the currents. This is indeed the case as seen in Figs. 4.19-4.24, though the approximations (short-dashed lines) overestimate the currents somewhat at larger distances, particularly in the dot-dashed portions of the ionospheric plots where the choice  $F_0 = F_\infty \approx 2.85 \times 10^4 \text{ nT } R_J^2$  would have led to better estimates. It is also seen in Figs. 4.21b and 4.24b that while the approximate curves for the field-aligned current go to zero at the poleward boundary of the current sheet region as discussed above, the numerical curves reverse sense to small negative values close to the boundary. This results from the fact that in the numerical solutions the total equatorial (and ionospheric) current rises with increasing distance to a maximum value slightly above  $8\pi F_\infty \Sigma_p^* \Omega_J$  before falling with decreasing  $F$  to the latter value at infinity, rather than following the strictly monotonically

rising behaviour of the approximation. However, for the range of system parameters considered, the maximum in the total current and the concurrent reversal in sense of the field-aligned current typically take place at equatorial distances of several hundred to several thousand  $R_J$ , far beyond the limit of physical applicability of the model. Within the region of applicability the agreement between the numerical and approximate analytic results is very good. This statement applies also to the other current components in this region, such that the analytic formulas are found to provide close approximations to the numerical results in the power law region. In Table 4.4 we thus summarise in physical units the peak values and locations of the various current components derived from the approximate formulas for the  $m = 2.71$  power law field. Comparison with Table 4.2 giving related quantities for the dipole field is instructive, and further discussion will be presented below in Section 4.5.

The un-normalised small- and large- $\rho_e$  approximate forms for the current sheet field model are just those given by Eqs. (4.3) to (4.5) and are shown by the long-dashed lines in Figs. 4.18-4.24. The limits of validity are again given by Eq. (4.12) and shown by tick-marks in Figs. 4.18-4.24. The small- $\rho_e$  approximation is drawn to the point where  $(\omega/\Omega_j)_s$  in Eq. (4.3) falls to zero, beyond which the large- $\rho_e$  approximation is shown. The long-dashed lines overall in these figures thus again show the current profiles that would be driven by an angular velocity profile given by  $(\omega/\Omega_j)_s$  to the point where the latter falls to zero, with zero being taken beyond.

As discussed in Section 4.2, Eq. (4.4) shows that in general the departure of the plasma from rigid corotation in the inner region is proportional to  $\dot{M}$  and inversely proportional to  $\Sigma_p^*$ , as already found for the dipole case above. Consequently we again find that the currents in the inner region depend only on  $\dot{M}$  and not on  $\Sigma_p^*$ . Since these currents depend only  $\dot{M}$ , only one small- $\rho_e$  approximation curve is shown in each panel of Figs. 4.19-4.21 where  $\Sigma_p^*$  is varied at fixed  $\dot{M}$ . In this case each numerically-determined solution then follows the same curve at small distances, before falling away from the curve at a distance which increases with increasing  $\Sigma_p^*$  (shown by the tick-marks), as for the corresponding dipole plots in Fig. 4.6-4.8. In Figs. 4.22-4.24, on the other hand, where  $\dot{M}$

Feature	$\left(\frac{\rho_e}{R_j}\right)$	$\left(\frac{\Delta\rho_i}{R_j}\right)$
Maximum sheet-integrated equatorial radial current $i_{\rho \max} \approx$ $8.690 \left( \Sigma_p^* (\text{mho})^{1.71} \dot{M} (10^3 \text{ kg s}^{-1}) \right)^{\frac{1}{2.71}} \text{ mA m}^{-1}$	$91.02 \left( \frac{\Sigma_p^* (\text{mho})}{\dot{M} (10^3 \text{ kg s}^{-1})} \right)^{\frac{1}{2.71}}$	$0.01400 \left( \frac{\dot{M} (10^3 \text{ kg s}^{-1})}{\Sigma_p^* (\text{mho})} \right)^{\frac{0.71}{2.71}}$
Plasma angular velocity falls to $\left(\frac{\omega}{\Omega_j}\right) = 0.5$	$93.15 \left( \frac{\Sigma_p^* (\text{mho})}{\dot{M} (10^3 \text{ kg s}^{-1})} \right)^{\frac{1}{2.71}}$	$0.01377 \left( \frac{\dot{M} (10^3 \text{ kg s}^{-1})}{\Sigma_p^* (\text{mho})} \right)^{\frac{0.71}{2.71}}$
Maximum upward field-aligned current density $(j_{\parallel}/B)_{\max} \approx$ $2.808 \left( \Sigma_p^* (\text{mho})^{3.42} \dot{M} (10^3 \text{ kg s}^{-1})^{-0.71} \right)^{\frac{1}{2.71}} \text{ pA m}^{-2} \text{ nT}^{-1}$ $j_{\parallel \max} \approx$ $2.404 \left( \Sigma_p^* (\text{mho})^{3.42} \dot{M} (10^3 \text{ kg s}^{-1})^{-0.71} \right)^{\frac{1}{2.71}} \text{ mA m}^{-2}$	$134.06 \left( \frac{\Sigma_p^* (\text{mho})}{\dot{M} (10^3 \text{ kg s}^{-1})} \right)^{\frac{1}{2.71}}$	$0.01063 \left( \frac{\dot{M} (10^3 \text{ kg s}^{-1})}{\Sigma_p^* (\text{mho})} \right)^{\frac{0.71}{2.71}}$
Maximum height-integrated ionospheric Pedersen current $i_{p \max} \approx 2.950 \Sigma_p^* (\text{mho}) \text{ A m}^{-1}$	$\infty$	0
Maximum azimuth-integrated total current $I_{p \max} = 2I_{p \max} \approx 725.8 \Sigma_p^* (\text{mho}) \text{ MA}$		
Field-aligned current goes to zero		

**Table 4.4.** Principal features of the plasma angular velocity and coupling current system for the power law current sheet field in physical units, obtained (using  $B_0 = 5.4 \times 10^4 \text{ nT}$ ,  $m = 2.71$ ,  $F_{\infty} \approx 2.85 \times 10^4 \text{ nT R}_j^2$ , and  $F_0 \approx 3.22 \times 10^4 \text{ nT R}_j^2$ ) from the approximate analytic solution of Section 4.4.

is varied at fixed  $\Sigma_p^*$ , the small- $\rho_e$  approximation curves vary in simple proportion to  $\dot{M}$ , and the numerically computed curves follow them to distances which decrease with increasing  $\dot{M}$ , again as for the dipole plots in Figs. 4.9-4.11. This behaviour can readily be quantified within the power-law field region using the analytic approximations derived above, since in this regime (in like manner to the dipole case) we found in the previous section that the small- $\rho_e$  approximations are valid (in the sense of Eq. (4.12)) to a distance which is proportional to  $R_{CS_e}$  (specifically  $\rho_e \approx 0.410R_{CS_e}$ ), and hence to  $(\Sigma_p^*/\dot{M})^{1/m}$ . Thus, for example, the equatorial radial current given by Eq. (4.5c) grows as  $\dot{M}\rho_e^{m-1}$  in the inner power law field region to a distance proportional to  $(\Sigma_p^*/\dot{M})^{1/m}$ , where it thus attains a value proportional to  $(\Sigma_p^{*m-1}\dot{M})^{1/m}$ , in agreement with the normalised form Eq. (4.33c) and with the behaviour observed in Figs. 4.19-4.24 outlined above. Corresponding statements apply to the behaviour of the other current components shown in these figures.

The large- $\rho_e$  forms given by Eq. (4.5) depend only on  $\Sigma_p^*$  and not on  $\dot{M}$  and thus these approximations, to which the numerical results asymptote in Figs. 4.19-4.21, are in simple proportion to  $\Sigma_p^*$ , while only one large- $\rho_e$  approximation curve applies in each panel of Fig. 4.22-4.24. The radial distance at which the approximation becomes valid (shown by the tick-marks in the ionosphere plots in Figs. 4.19-4.24) again varies as  $(\Sigma_p^*/\dot{M})^{1/m}$  according to the approximate analytic results (specifically located at  $\rho_{eL} \approx 5.761R_{CS_e}$  as given above), where the value of the current at the limit again scales as indicated by the normalised forms in Eqs. (4.33).

#### 4.5. Comparison of the system behaviour for the dipole and current sheet field models

In this section we finally provide a summary and comparison of how the major features of the plasma flow and coupling current system vary with  $\Sigma_p^*$  and  $\dot{M}$  for the dipole and current sheet field models. Specifically we consider the location of corotation breakdown,

the magnitudes and locations of the peak values of the various current components, and the latitudinal width in the ionosphere of the region of upward field-aligned current. With the exception of the latter parameter, in effect we here provide plots showing how the quantities in Tables 4.2 (for the dipole) and 4.4 (for the power law field approximation) vary with  $\Sigma_p^*$  and  $\dot{M}$ , augmented in the latter case by spot values obtained by numerical integration using the full current sheet field.

Fig. 4.25 shows how the spatial scale on which plasma corotation breaks down depends  $\Sigma_p^*$  and  $\dot{M}$  for the two fields. Specifically we show the position where  $(\omega/\Omega_e)=0.5$ , as previously given in Tables 4.1-4.4. In Fig. 4.25a the equatorial distance is plotted versus  $\Sigma_p^*$  in log-log format for  $\dot{M} = 100, 1000, \text{ and } 10,000 \text{ kg s}^{-1}$ , while in Fig. 4.25b it is plotted versus  $\dot{M}$  in similar format for  $\Sigma_p^* = 0.1, 1 \text{ and } 10 \text{ mho}$ . Solid lines give results for the dipole field obtained from Eqs. (4.7) and (4.8), showing that the distance increases with the conductivity as  $\Sigma_p^{*1/4}$ , and decreases with the mass outflow rate as  $\dot{M}^{-1/4}$ . The dashed lines show corresponding results obtained from the power law field approximate solutions Eqs. (4.26) and (4.27) (with  $m=2.71$  and  $F_0 \approx 3.22 \times 10^4 \text{ nT R}_J^2$  as above), which of course are not applicable to the full field model at distances smaller than  $\rho_e^* \approx 21.78 \text{ R}_J$ . These increase more rapidly with  $\Sigma_p^*$  and decrease more rapidly with  $\dot{M}$ , as  $\Sigma_p^{*1/2.71}$  and  $\dot{M}^{-1/2.71}$  respectively. Overall, however, the equatorial distances of corotation breakdown are similar for the dipole and current sheet fields as noted above, but are generally somewhat larger for the current sheet model than for the dipole, particularly for larger values of  $\Sigma_p^*$  and smaller values of  $\dot{M}$ . The solid dots in the figures provide spot values obtained by numerical integration of the full current sheet solution, their close association with the dashed lines clearly indicating the values of  $\dot{M}$  (in Fig. 4.25a) and  $\Sigma_p^*$  (in Fig. 4.25b) employed. This close association also confirms that the analytic solutions provide good approximations to the numerical results in the power law regime over essentially the whole parameter range considered here. The only notable deviations occur at small  $\Sigma_p^*$  and large  $\dot{M}$  where corotation breakdown occurs at equatorial distances approaching the radial limit of the power law field region at  $\rho_e^* \approx 21.78 \text{ R}_J$ . In this case

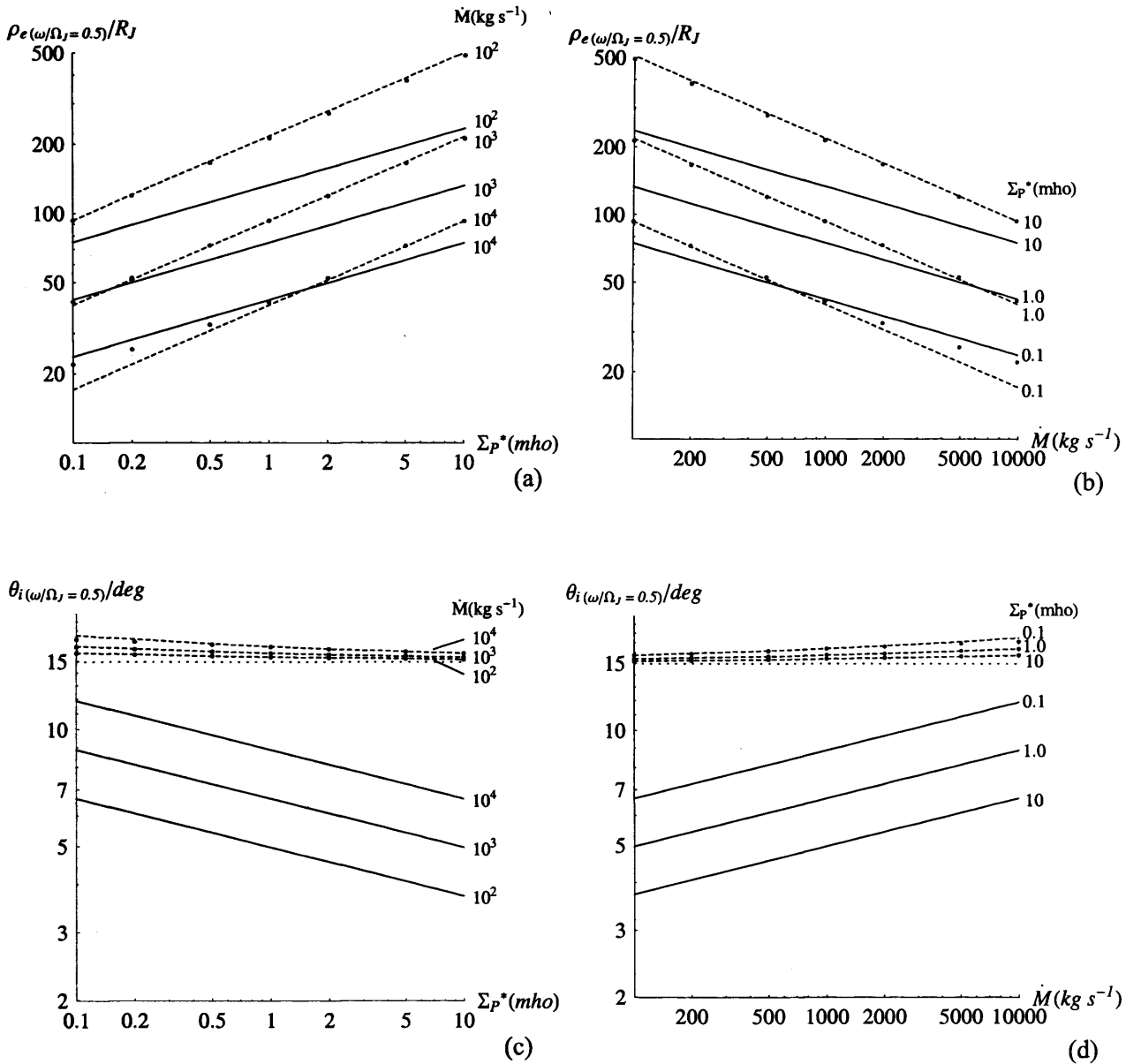


**Figure 4.25** Plots showing the location of plasma corotation breakdown, specifically where  $(\omega/\Omega_J)=0.5$ , and its dependence on the system parameters  $\Sigma_p^*$  and  $\dot{M}$ . Plot (a) shows the equatorial distance at which  $(\omega/\Omega_J)=0.5$  versus  $\Sigma_p^*$  in log-log format for  $\dot{M} = 100, 1000$ , and  $10,000 \text{ kg s}^{-1}$ , while (b) shows this distance similarly plotted versus  $\dot{M}$  for  $\Sigma_p^* = 0.1, 1$  and  $10 \text{ mho}$ . Solid lines give results for the dipole field obtained from Eqs. (4.7) and (4.8), while the dashed lines show corresponding results derived from the power law field approximation solutions for the current sheet model Eqs. (4.26) and (4.27). The solid dots provide spot values obtained from numerical integration of the full current sheet solution, whose  $\dot{M}$  (in (a)) and  $\Sigma_p^*$  (in (b)) values are obvious from their close association with the corresponding dashed lines. Corresponding plots of the ionospheric co-latitude at which  $(\omega/\Omega_J)=0.5$  are shown versus  $\Sigma_p^*$  and  $\dot{M}$  in (c) and (d). The horizontal dotted line shows the latitude of the field line from infinity in the current sheet field model.

the numerical results give somewhat larger distances than the analytic approximation, as also seen in Fig. 4.18a.

Corresponding results projected to the ionosphere are shown in Figs. 4.25c and 4.25d, in a similar format. The horizontal dotted line at  $\theta_i \approx 14.95^\circ$  shows the co-latitude of the current sheet field line from infinity (the corresponding limit for the dipole being, of course, the pole at  $\theta_i = 0^\circ$ ). These plots again emphasise the significantly larger distance from the magnetic axis at which plasma corotation breaks down in the ionosphere for the current sheet field than for dipole, despite the similarity of the equatorial results. They also display the relative lack of response of this distance to the system parameters in the current sheet model, this forming the basis of the ‘current sheet’ approximation  $F_e \approx F_o$  employed to obtain the analytic results in Section 4.3.2.

Turning now to the current components, in Fig. 4.26 we show the behaviour of the magnitude and location of the peak Pedersen current, plotted in a similar format to Fig. 4.25. The magnitude of the peak current, plotted versus  $\Sigma_p^*$  and  $\dot{M}$  in Figs. 4.26a and 4.26b, respectively, shows that for the dipole (solid lines) the peak Pedersen current increases with the conductivity as  $\Sigma_p^{*7/8}$ , while also increasing weakly with the mass outflow rate as  $\dot{M}^{1/8}$  (Eq. (4.15a), while for the current sheet (dashed line) approximations the peak current varies linearly with  $\Sigma_p^*$  but is independent of  $\dot{M}$  (Eq. (4.33a)). The modestly lower numerically-determined spot values in the latter case result from our taking  $F_o = F_e(\rho_e = 70 R_j)$  in the approximation, as above. Very close agreement would have been obtained if we had instead taken  $F_o = F_\infty$ . These plots also show that for given system parameters the peak Pedersen current for the current sheet model exceeds that for the dipole by relatively constant factors of  $\sim 3$  to  $\sim 5$  (typically  $\sim 4$ ). This difference arises from the different ionospheric mappings of corotation breakdown as shown in Figs. 4.25c and 4.25d. Figs. 4.26c and 4.26d show the co-latitude of the peak Pedersen current, which for the dipole field lies typically at  $\sim 5^\circ$  and is such that the distance from the magnetic axis varies with the system parameters as  $\Sigma_p^{*-1/8}$  and  $\dot{M}^{1/8}$  (Eq. (4.9)), while for the current sheet approximation it is located consistently at the poleward boundary of the current sheet field lines at  $\sim 14.95^\circ$  (dotted line) where the plasma angular velocity falls to zero. The numerically computed positions are located at slightly higher co-latitudes, typically by

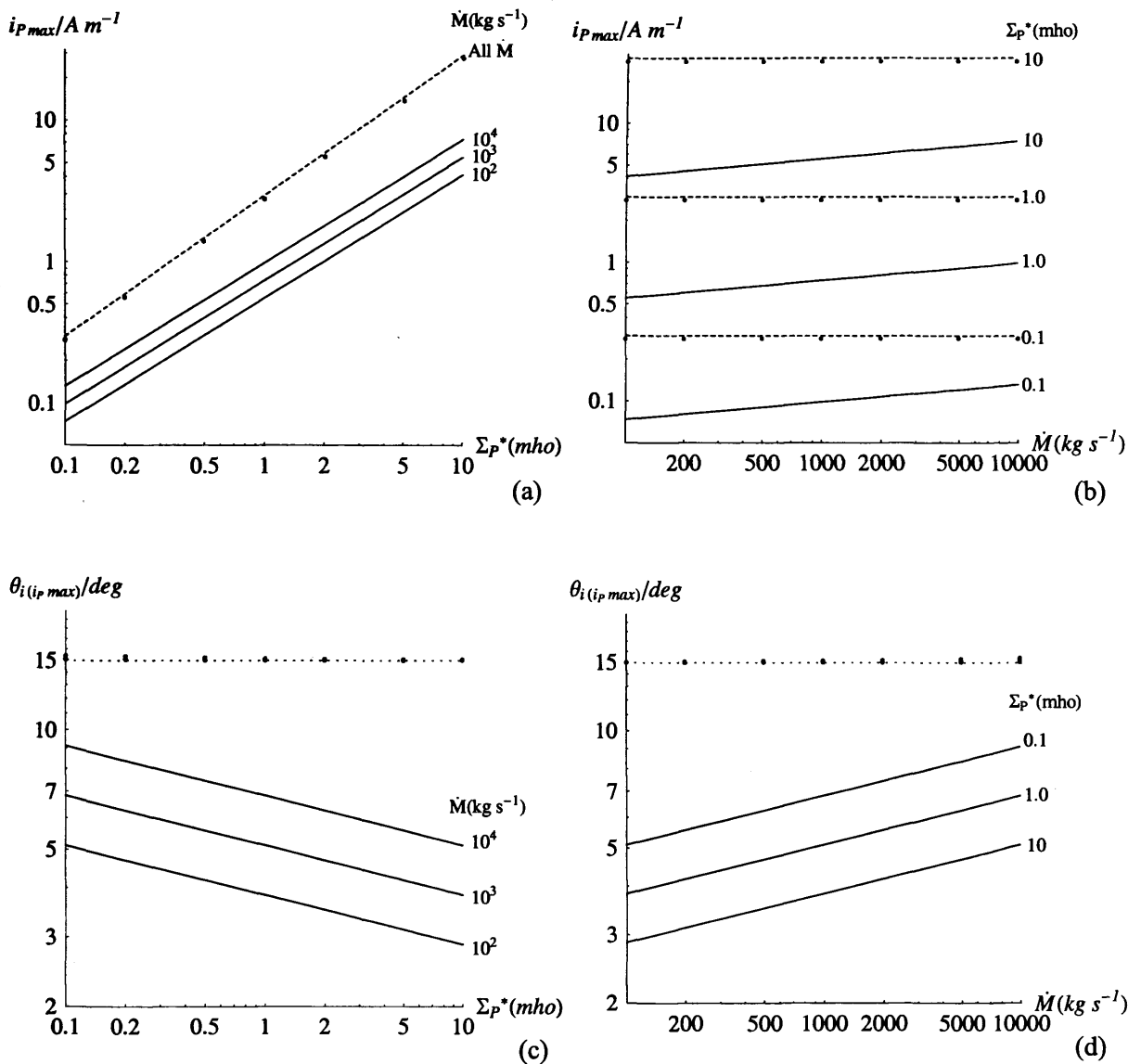
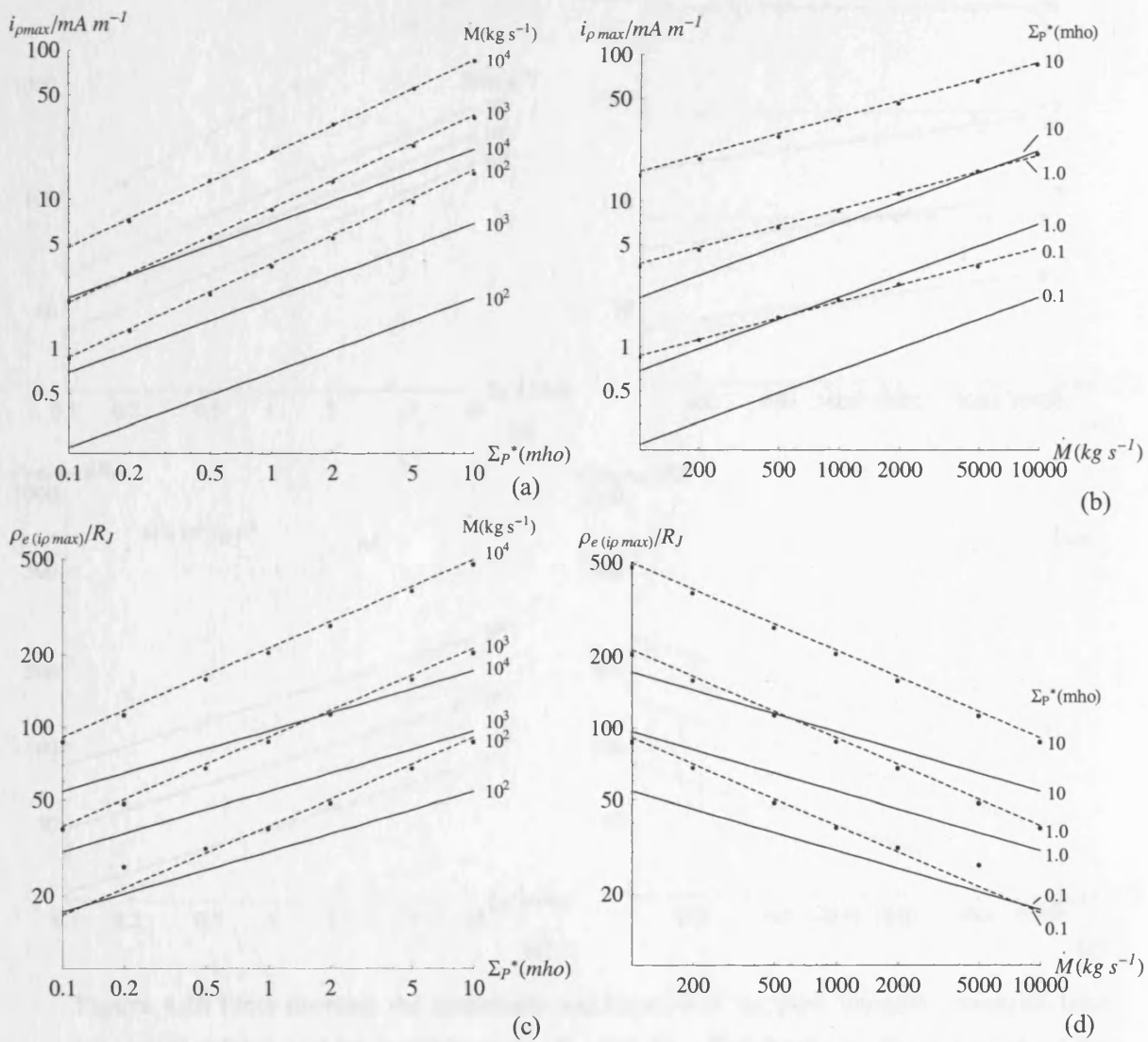


**Figure 4.26** Plots showing the magnitude and location of the peak height-integrated Pedersen current intensity in the ionosphere, and their dependence on  $\Sigma_p^*$  and  $\dot{M}$ . Plot (a) shows the magnitude of the peak Pedersen current plotted versus  $\Sigma_p^*$  in log-log format for  $\dot{M} = 100, 1000$ , and  $10,000 kg s^{-1}$ , while plot (c) show the ionospheric location of the peak. Plots (b) and (d) similarly show the magnitude and location of the peak Pedersen current plotted versus  $\dot{M}$  for  $\Sigma_p^* = 0.1, 1$ , and  $10 mho$ . Solid lines give results for the dipole field obtained from Eq. (4.15a), while the dashed lines show corresponding results derived from the approximate solutions for the power law current sheet field given by Eq. (4.33a). The solid dots show spot values obtained from numerical integration using the full current sheet solution. For the case of the current sheet approximation the peak current depends only on  $\Sigma_p^*$  and not on  $\dot{M}$ , so that only one dashed line is shown in plot (a), valid for all  $\dot{M}$ . The peak current in this case always occurs at the poleward boundary of the current sheet field lines, as indicated by the horizontal dotted lines at  $\sim 14.95^\circ$  in plots (c) and (d).

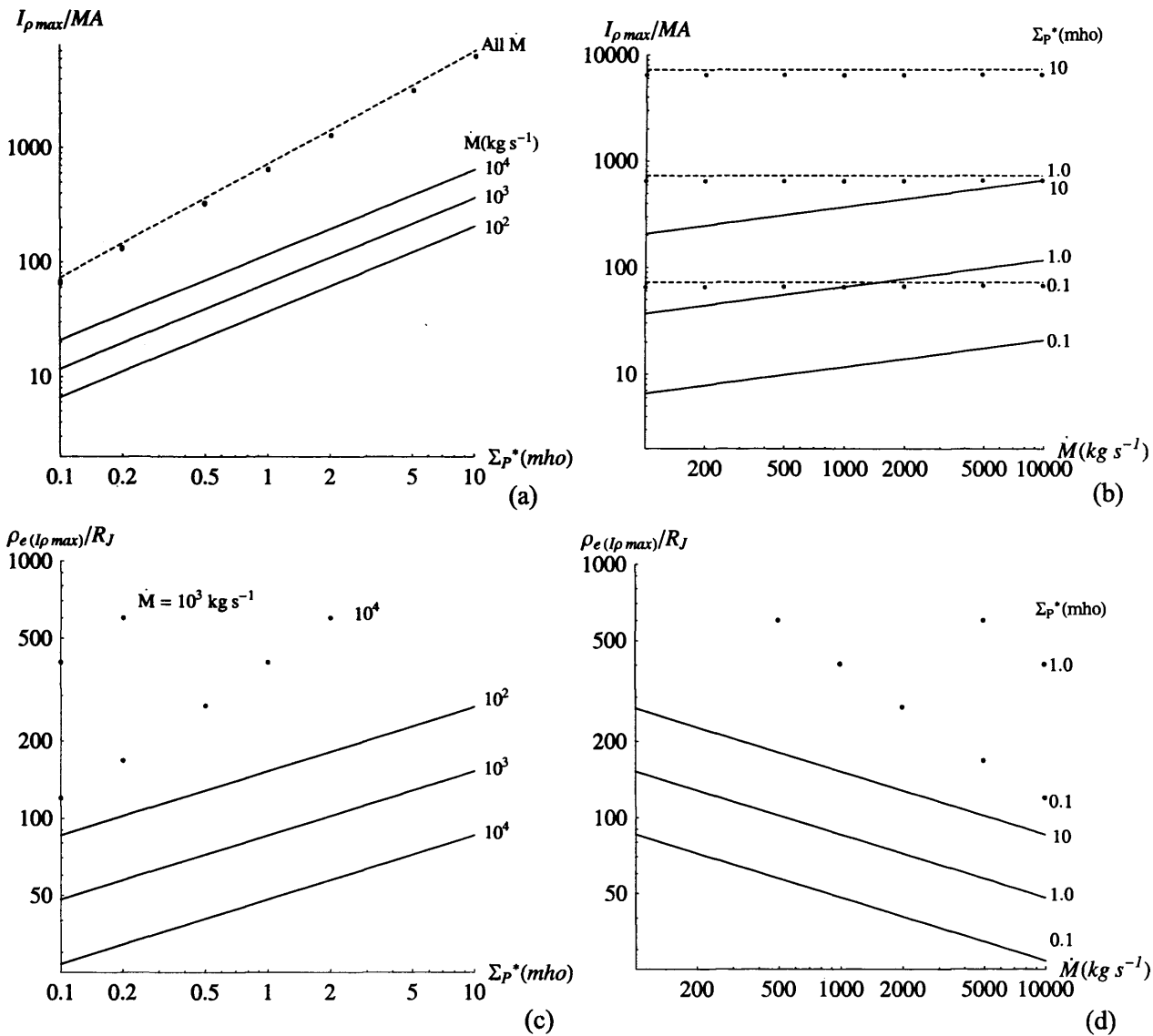
$\sim 0.1^\circ$ . In practical application the peak current will thus be limited instead by the radial extent of the region to which the model is taken to apply, with the peak value occurring at its outer (poleward) boundary. Nevertheless, the results given here should provide an indication of the peak currents involved.

Fig. 4.27 similarly provides results for the peak equatorial radial current, a parameter which relates directly to the magnitude of the azimuthal magnetic field outside of the current sheet (Fig. 3.1) ( $B_\phi(\text{nT}) \approx 0.63 i_p(\text{mA m}^{-1})$ ). Figures 4.27a and 4.27b show that for the dipole field the peak current varies as  $\Sigma_p^{*1/2}$  and  $\dot{M}^{1/2}$  (Eq. (4.15c)), while for the current sheet approximation it varies more strongly with the conductivity as  $\Sigma_p^{*1.71/2.71}$ , and less strongly with the mass outflow rate as  $\dot{M}^{1/2.71}$  (Eq. (4.33c)). The values given by the numerical integrations are in close agreement with the latter. The current sheet model values are again higher than the dipole values by factors of  $\sim 3$  to  $\sim 5$  (typically  $\sim 4$ ), for reasons discussed above. Figs. 4.27c and 4.27d show that the equatorial distance of the peak is typically located at  $\sim 50 R_J$  for the dipole model, varying with the system parameters as  $\Sigma_p^{*1/4}$  and  $\dot{M}^{-1/4}$ , while for the current sheet approximation it is generally located at somewhat larger distances  $\sim 90 R_J$ , and varies more strongly as  $\Sigma_p^{*1/2.71}$  and  $\dot{M}^{-1/2.71}$ . The positions given by the numerical integrations are again in close agreement with the latter, except for small  $\Sigma_p^*$  and large  $\dot{M}$  where the position of the peak approaches  $\rho_e^* \approx 21.78 R_J$ . In fact for small  $\Sigma_p^*$  and large  $\dot{M}$  the peak current in the numerical solutions lies consistently at  $\rho_e^*$  where the field models are joined. Such points are omitted from the plots. At large distances the radial regime of applicability is again limited, such that the peak radial currents will actually occur at the outer boundary of the region for sufficiently large  $\Sigma_p^*$  and/or sufficiently small  $\dot{M}$ , as can be determined from the position of the peak in Figs. 4.27c and 4.27d.

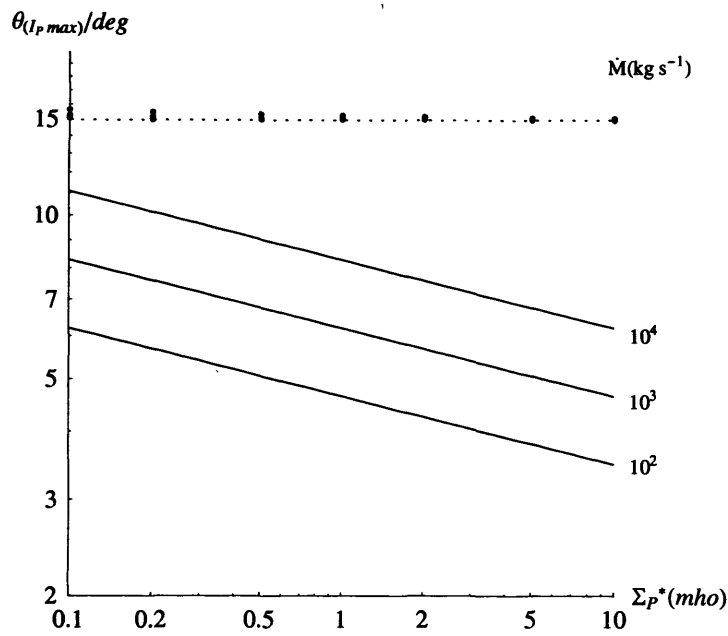
Results for the magnitude and location of the peak azimuth-integrated total equatorial radial current, equal, of course, to twice the peak azimuth-integrated total Pedersen current in each conjugate ionosphere, are shown in Figs. 4.28 and 4.29. Figs. 4.28a and 4.28b show that the magnitude of the peak current for the dipole field increases with the conductivity as



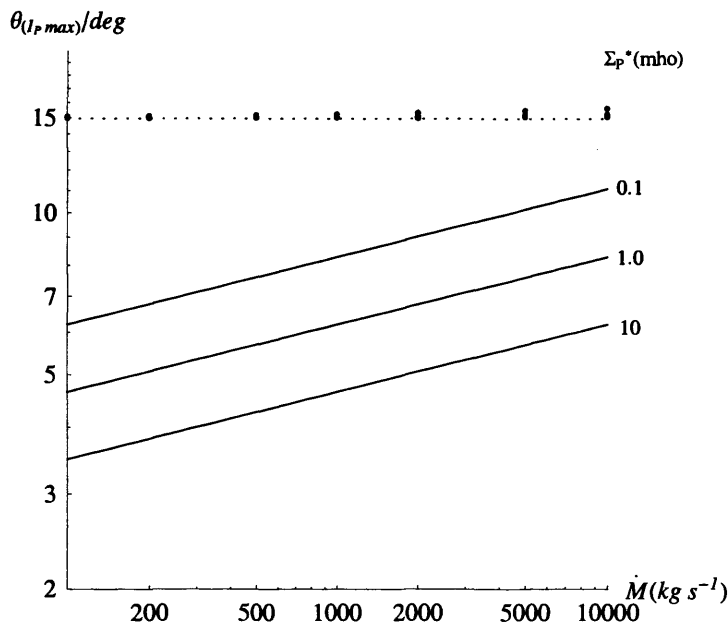
**Figure 4.27** Plots showing the magnitude and location of the peak sheet-integrated equatorial radial current intensity, and their dependence on  $\Sigma_p^*$  and  $\dot{M}$ . Plot (a) shows the magnitude of the peak current versus  $\Sigma_p^*$  in log-log format for  $\dot{M} = 100, 1000,$  and  $10,000 kg s^{-1}$ , while plot (c) shows the corresponding equatorial location of the peak in a similar format. Plots (b) and (d) similarly show the magnitude and location of the peak current versus  $\dot{M}$  for  $\Sigma_p^* = 0.1, 1,$  and  $10 mho$ . Solid lines give results for the dipole field obtained from Eq. (4.15c), while the dashed lines show corresponding results derived from the approximate solutions for the power law current sheet model given by Eq. (4.33c). The solid dots show spot values obtained from numerical integration of the full current sheet solution.



**Figure 4.28** Plots showing the magnitude and location of the peak azimuth-integrated total equatorial current, and its dependence on  $\Sigma_p^*$  and  $\dot{M}$ . Plot (a) shows the magnitude of the peak total equatorial radial current (equal to twice the peak total ionospheric Pedersen current) versus  $\Sigma_p^*$  in log-log format for  $\dot{M} = 100, 1000, \text{ and } 10,000 \text{ kg s}^{-1}$ , while plot (c) shows the corresponding equatorial location of the peak in a similar format. Plots (b) and (d) similarly show the magnitude and location of the azimuth-integrated peak total current versus  $\dot{M}$  for  $\Sigma_p^* = 0.1, 1, \text{ and } 10 \text{ mho}$ . Solid lines give results for the dipole field obtained from Eq. (4.15d), while the dashed lines show corresponding results derived from the approximate solutions for the power law current sheet model given by Eqs. (4.33d). The peak total current in the latter model is independent of  $\dot{M}$ , so that only one dashed line is shown in (a). It occurs at infinity in the equatorial plane so that no dashed lines are shown in (c) and (d). The solid dots show spot values obtained from numerical integration of the full current sheet solution. In this case the peak values occur at large but finite distances such that only the closest of them are included in (c) and (d).



(a)



(b)

**Figure 4.29** Plots showing location of the peak azimuth-integrated total ionospheric Pedersen current, and its dependence on (a)  $\dot{M}$  and (b)  $\Sigma_p^*$  in the same manner as in Fig. 4.28. Solid lines give results for the dipole field obtained from Eq. (4.15b), while the dashed lines show corresponding results derived from the approximate solutions for the power law current sheet model given by Eqs. (4.33b). As in Fig. 4.28, the peak total current in the latter model is independent of  $\dot{M}$ , and occurs at infinity in the equatorial plane, or equivalently at the poleward boundary of current sheet field lines in the ionosphere at  $\sim 14.95^\circ$  as shown here by the dotted line. The solid dots show spot values obtained from numerical integration of the full current sheet solution.

$\Sigma_p^{*3/4}$ , and less strongly with the mass outflow rate as  $\dot{M}^{1/4}$  (Eqs. (4.15b) and (4.15d)), while for the current sheet approximation it is linearly proportional to  $\Sigma_p^*$  and independent of  $\dot{M}$  (Eqs. (4.33b) and (4.33d)). The numerical values shown by the dots in the latter case are a little lower than the dashed line approximation for reasons given above for the Pedersen current. The value of the peak current is factors of  $\sim 5$  to  $\sim 20$  (typically  $\sim 10$ ) larger for the current sheet than for the dipole. The location of the peak in the equatorial plane (where the field-aligned current passes through zero), is shown in Figs. 4.28c and 4.28d. It is located typically at  $\sim 90 R_J$  for the dipole field, scaling as  $\Sigma_p^{*1/4}$  and  $\dot{M}^{-1/4}$ , but occurs at infinity for the current sheet approximation (such that no dashed lines are shown in Figs. 4.28c and 4.28d), or in other words at the outer boundary of the relevant region in practical application. The peak value in the numerical curves, shown by the dots, occurs at large but finite radial distance as mentioned previously in Section 4.3.4, typically well beyond the region of physical applicability ( $\sim 500$  to  $\sim 5000 R_J$ ). Only the closest of them (for small  $\Sigma_p^*$  and large  $\dot{M}$ ) are included in Figs. 4.28c and 4.28d. The corresponding location of the peak azimuth-integrated Pedersen current in the conjugate ionosphere is shown in Figs. 4.29a and 4.29b. It is located typically at  $\sim 6^\circ$  for the dipole field, scaling as  $\Sigma_p^{*-1/8}$  and  $\dot{M}^{1/8}$  as before, but for the current sheet approximation it is located consistently at the poleward boundary of the current sheet field lines at  $\sim 14.95^\circ$  (dotted line).

Figs. 4.30 and 4.31 shows results for the upward-directed field-aligned current density, a parameter of relevance to the origins of the jovian auroras. The magnitude of the peak upward current is shown in Figs. 4.30a and 4.30b in a similar format to the above, where, since  $j_{\parallel}$  and  $(j_{\parallel}/B)$  are simply related through the constant factor  $2B_J$  in the approximation for the ionospheric magnetic field employed here (Eq. (3.14)), one plot serves the purposes of both parameters according to the left and right-hand scales. These plots show that for the dipole field the peak upward current density depends linearly on  $\Sigma_p^*$  and is independent of  $\dot{M}$  (Eqs. (4.15e) and (4.15f)), while for the current sheet approximation it increases somewhat more rapidly with the conductivity as  $\Sigma_p^{*3.42/2.71}$  (i.e. as  $\sim \Sigma_p^{*1.26}$ ), while decreasing slowly with the mass outflow rate as  $\dot{M}^{-0.71/2.71}$  (Eqs. (4.33e) and (4.33f)). The latter values agree well with those obtained from numerical integration, and exceed those obtained for the dipole field by factors of  $\sim 10$  to  $\sim 50$  (typically by  $\sim 25$ ). The position of

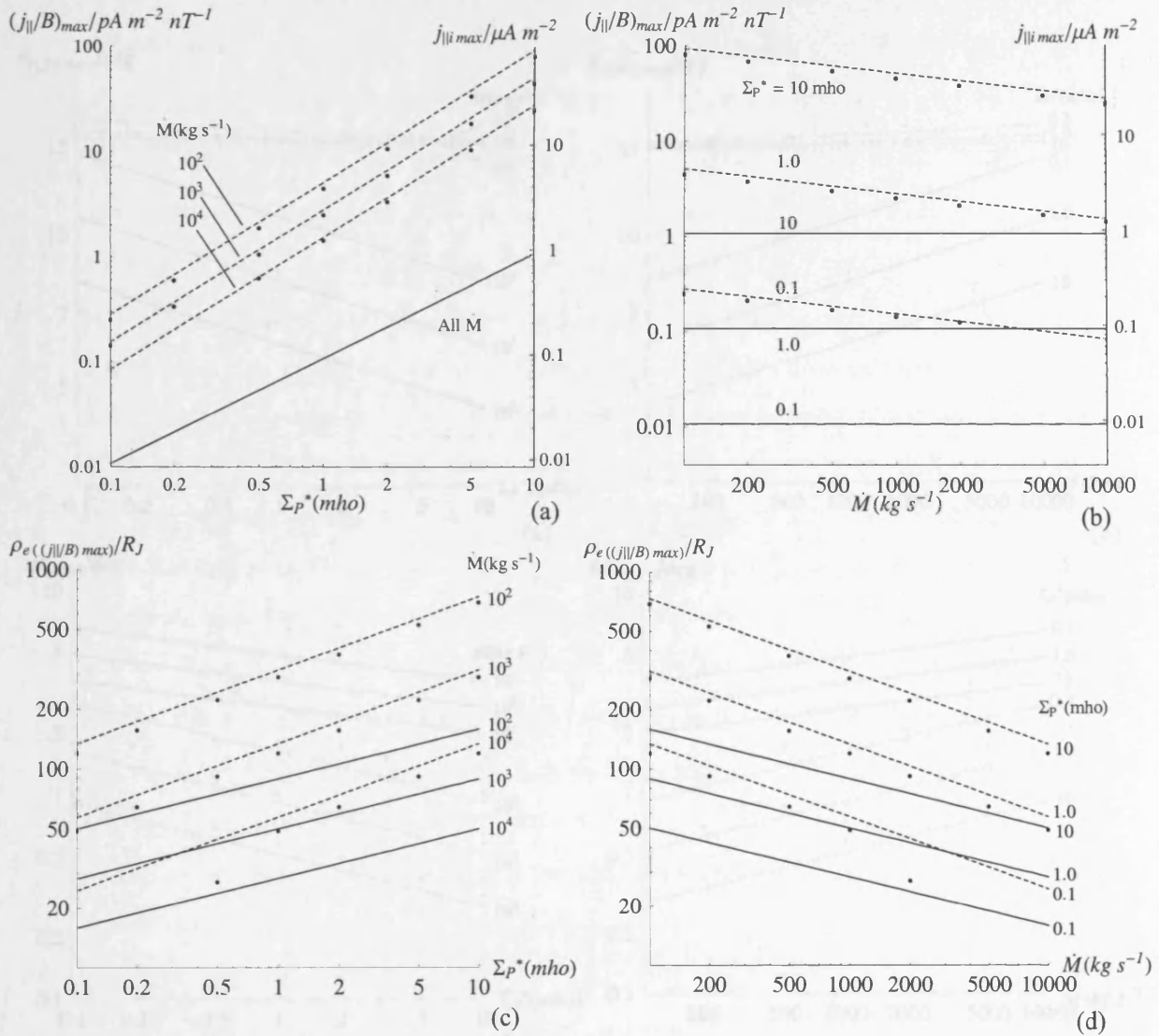


**Figure 4.30** Plots showing the magnitude and equatorial location of the peak upward-directed field-aligned current density, and their dependence on  $\Sigma_p^*$  and  $\dot{M}$ . Plot (a) shows the magnitude of the peak total current density versus  $\Sigma_p^*$  in log-log format for  $\dot{M} = 100, 1000, \text{ and } 10,000 \text{ kg s}^{-1}$ , where the right-hand scale shows the peak current density in the ionosphere, while the left-hand scale shows the peak  $(j_{\parallel}/B)$  value, simply related to the former via Eq. (3.16). Solid lines give results for the dipole field obtained from Eqs. (4.15e) and (4.15f), while the dashed lines show corresponding results derived from the approximate solutions for the power law current sheet model given by Eqs. (4.33e) and (4.33f). The solid dots show spot values obtained from numerical integration of the full current sheet solution. Plot (c) shows the corresponding location of the peak  $(j_{\parallel}/B)$  in the equatorial plane in a similar format. Plots (b) and (d) similarly show the magnitude and equatorial locations of the peak current density versus  $\dot{M}$  for  $\Sigma_p^* = 0.1, 1, \text{ and } 10 \text{ mho}$ .

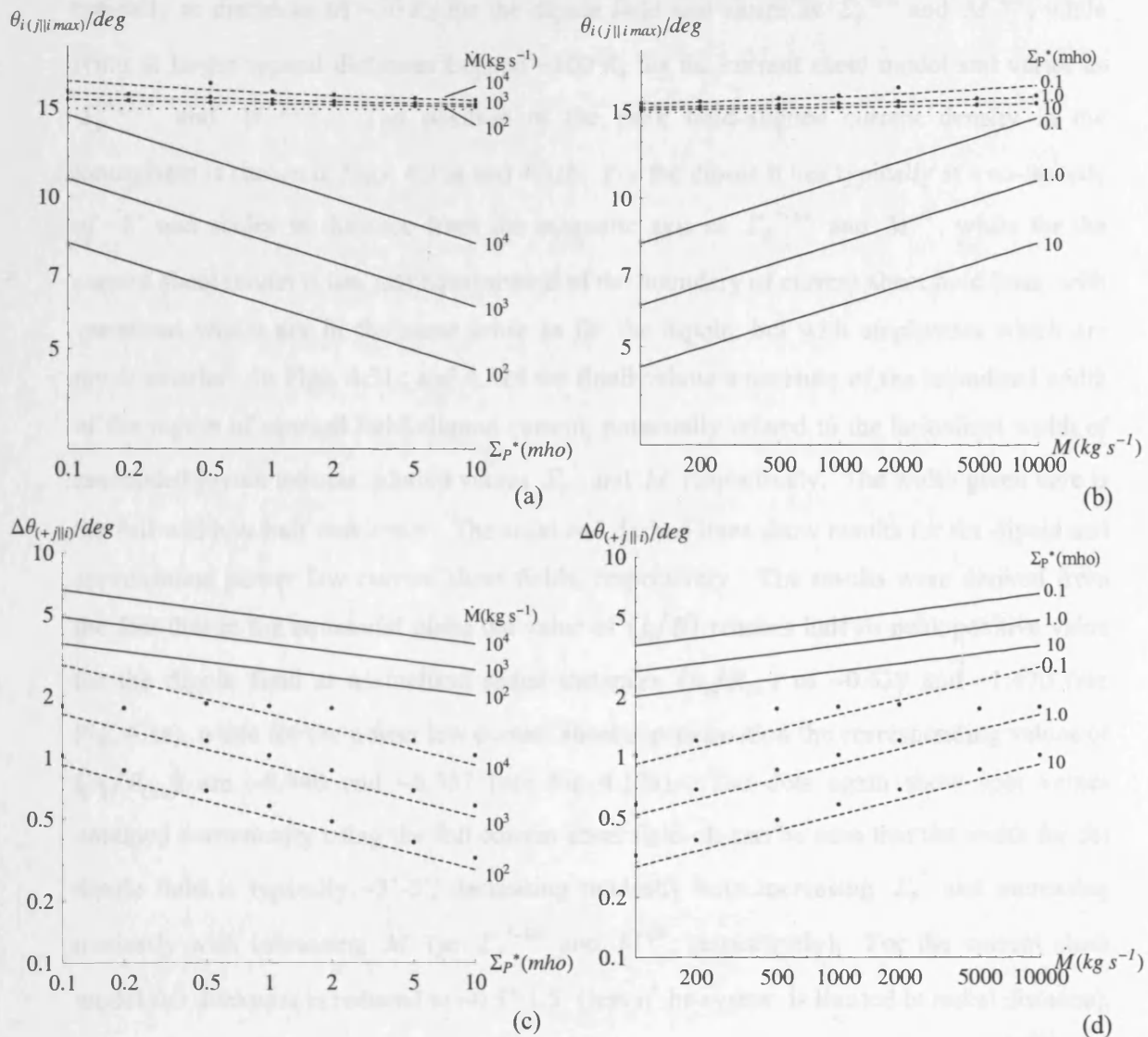


**Figure 4.31** Plots showing the ionospheric location and half-width of the peak upward-directed field-aligned current density, and their dependence on  $\Sigma_p^*$  and  $\dot{M}$ . Plot (a) shows the location of the peak field-aligned current in the ionosphere versus  $\Sigma_p^*$  in log-log format for  $\dot{M} = 100, 1000, \text{ and } 10,000 \text{ kg s}^{-1}$ . Solid lines give results for the dipole field obtained from Eqs. (4.15f), while the dashed lines show corresponding results derived from the approximate solutions for the power law current sheet model given by Eqs. (4.33f). The solid dots show spot values obtained from numerical integration of the full current sheet solution. Plot (b) similarly shows the ionospheric location of the peak current density versus  $\dot{M}$  for  $\Sigma_p^* = 0.1, 1, \text{ and } 10 \text{ mho}$ . Plots (c) and (d) show the latitudinal width of the upward field-aligned current region in the ionosphere in a similar format, defined as the full width at half maximum.

the peak value of  $(j_{\parallel}/B)$  in the equatorial plane is shown in Figs. 4.30c and 4.30d. It lies typically at distances of  $\sim 50 R_J$  for the dipole field and varies as  $\Sigma_p^{*1/4}$  and  $\dot{M}^{-1/4}$ , while lying at larger typical distances beyond  $\sim 100 R_J$  for the current sheet model and varies as  $\Sigma_p^{*1/2.71}$  and  $\dot{M}^{-1/2.71}$ . The position of the peak field-aligned current density in the ionosphere is shown in Figs. 4.31a and 4.31b. For the dipole it lies typically at a co-latitude of  $\sim 8^\circ$  and scales in distance from the magnetic axis as  $\Sigma_p^{*-1/8}$  and  $\dot{M}^{1/8}$ , while for the current sheet model it lies just equatorward of the boundary of current sheet field lines, with variations which are in the same sense as for the dipole, but with amplitudes which are much smaller. In Figs. 4.31c and 4.31d we finally show a measure of the latitudinal width of the region of upward field-aligned current, potentially related to the latitudinal width of associated jovian auroras, plotted versus  $\Sigma_p^*$  and  $\dot{M}$  respectively. The width given here is the full width at half maximum. The solid and dashed lines show results for the dipole and approximate power law current sheet fields, respectively. The results were derived from the fact that in the equatorial plane the value of  $(j_{\parallel}/B)$  reaches half its peak positive value for the dipole field at normalised radial distances  $(\rho_e/R_{De})$  of  $\sim 0.629$  and  $\sim 1.470$  (see Fig. 4.4a), while for the power law current sheet approximation the corresponding values of  $(\rho_e/R_{CSe})$  are  $\sim 0.940$  and  $\sim 8.337$  (see Fig. 4.17a). The dots again show spot values obtained numerically using the full current sheet field. It can be seen that the width for the dipole field is typically  $\sim 3^\circ$ - $5^\circ$ , decreasing modestly with increasing  $\Sigma_p^*$  and increasing modestly with increasing  $\dot{M}$  (as  $\Sigma_p^{*-1/8}$  and  $\dot{M}^{1/8}$ , respectively). For the current sheet model the thickness is reduced to  $\sim 0.5^\circ$ - $1.5^\circ$  (less if the system is limited in radial distance), varying in the above manner more strongly with the system parameters (as  $\sim \Sigma_p^{*-0.26}$  and  $\sim \dot{M}^{0.26}$ ).

#### 4.6. Summary

In this chapter we have considered the steady-state properties of the magnetosphere-ionosphere coupling current system that flows in Jupiter's middle magnetosphere, associated with the enforcement of partial corotation on outward-flowing plasma from the

Io torus. The solutions depend on the values of two parameters, the effective Pedersen conductivity of the jovian ionosphere  $\Sigma_p^*$ , and the mass outflow rate of iogenic plasma  $\dot{M}$ , these being taken to be constants. However, their values remain uncertain at present, thus prompting the study presented here of how the solutions depend on these parameters over wide ranges of the latter. We have also focussed on two models of the magnetospheric poloidal field, taken for simplicity to be axisymmetric. The first is the planetary dipole alone, which constitutes an instructive paradigm. Some general results for this case have previously been given by Hill (1979, 2001) (see Chapter 3). Here we have provided a complete analytic solution for this case, showing how the plasma angular velocity and current components scale in space and in amplitude with  $\Sigma_p^*$  and  $\dot{M}$ . We find that the plasma angular velocity and current components scale in equatorial radial distance as  $(\Sigma_p^*/\dot{M})^{1/4}$  as found previously by Hill (and correspondingly as  $(\dot{M}/\Sigma_p^*)^{1/8}$  in the ionosphere), while each current component scales in amplitude as  $\Sigma_p^{*(1+\gamma)/2} \dot{M}^{(1-\gamma)/2}$ , where  $\gamma$  has a particular value for each component. The scales in space and amplitude then combine to produce current values which depend only on  $\dot{M}$  at a fixed position at small radial distances, and only on  $\Sigma_p^*$  at a fixed position at large radial distances, these dependencies then requiring current variations at small and large distances with particular powers of the distance, as  $\rho_e^{2(1+\gamma)}$  at small distances, and as  $\rho_e^{-2(1-\gamma)}$  at large distances.

These results provide useful background for the second more realistic field model, based on Voyager data, in which the equatorial field strength is significantly less than for the dipole field due to the radial distension of the middle magnetosphere field lines, and is taken to vary with distance as a power law  $\rho_e^{-m}$ . Solutions for a few spot values of  $\Sigma_p^*$  and  $\dot{M}$  have previously been presented by Cowley, Nichols and Bunce (2002) and Cowley, Bunce and Nichols (2003), obtained by numerical integration of the corresponding Hill-Pontius equation. Here we have derived an analytic approximation, applicable to the power law regime, which shows how the plasma angular velocity and current components scale with  $\Sigma_p^*$  and  $\dot{M}$  in this case. We find that these solutions provide accurate approximations to the full numerical results within the power law regime (roughly  $\rho_e > 20 R_J$ ) over very wide ranges of the system parameters, provided  $(\Sigma_p^*/\dot{M})$  is not too small ( $\sim 10^{-4}$  mho s kg<sup>-1</sup> or larger). The results show that the conclusions concerning the nature of the current sheet

solutions, and their relation to the dipole solutions, which were drawn previously on the basis of a limited number of numerical investigations are generally valid over wide ranges of the parameters. In particular it has been shown that in the current sheet model the field-aligned current flows unidirectionally outward from the ionosphere into the current sheet over the whole current sheet, in all cases of interest. The closure of this current must then occur on field lines at higher latitudes which map to the outer magnetosphere and tail, which are not described by the present theory. This situation contrasts with the dipole model, in which (at least in principle) all the flux in the system is described by the theory, such that complete current closure occurs between the equator and the pole. The results for the power law current sheet show that the plasma angular velocity and currents now scale in radial distance as  $(\Sigma_p^*/\dot{M})^{1/m}$ , while each current component again scales in amplitude as  $\Sigma_p^{*(1+\gamma)/2} \dot{M}^{(1-\gamma)/2}$ , where the values of  $\gamma$  for each component exceed those of the corresponding component for the dipole field (at least for  $m > 2$  as considered here). The current components thus scale as a somewhat higher power of  $\Sigma_p^*$  for the current sheet than for the dipole, and as a somewhat lower power of  $\dot{M}$ . These scales in space and amplitude again combine to produce current values which depend only on  $\dot{M}$  at a fixed position at small radial distances, and only on  $\Sigma_p^*$  at a fixed position at large radial distances (both being general properties of the solutions), these dependencies then requiring current variations as  $\rho_e^{m(1+\gamma)/2}$  at small distances, and as  $\rho_e^{-m(1-\gamma)/2}$  at large distances. The absolute values of the currents are also higher for the current sheet model than for the dipole, by factors of  $\sim 4$  for the Pedersen and equatorial currents,  $\sim 10$  for the total current flowing in the circuit, and  $\sim 25$  for the field-aligned current densities. These factors do not vary greatly over the range of system parameters considered here.

## ***Chapter 5***

# ***Magnetosphere-Ionosphere Coupling Currents in Jupiter's Middle Magnetosphere: Effect of Precipitation-Induced Enhancements of the Ionospheric Pedersen Conductivity***

### ***5.1. Introduction***

An important limitation of the calculations of previous authors discussed in Chapter 3 and those in Chapter 4 of this thesis is that they all assume a constant value of the effective ionospheric Pedersen conductivity, though Pontius (1997) discussed the effect of variations of this parameter produced by varying atmospheric 'slippage' associated with the possible onset of instabilities induced by atmospheric velocity shear. However, given the newly-understood linkage with the 'main oval' auroras, it seems clear that a far more important conductivity modulation mechanism results from the ionospheric ionisation produced by precipitating accelerated 'main oval' electrons. For example, as indicated in Chapter 4 Strobel and Atreya (1983) estimated that a Pedersen conductivity of a fraction of a mho produced solely by solar UV radiation could be increased to  $\sim 10$  mho (uncorrected for atmospheric slippage) under conditions of intense auroral precipitation. These conclusions have recently been confirmed by more detailed calculations presented by Millward et al. (2002), using the JIM jovian coupled ionosphere-thermosphere model of Achilleos et al. (1998). Millward et al. (2002) calculated the effect on the ionospheric conductivity of precipitating monoenergetic electron beams, and found, for example, that a beam of  $\sim 60$  keV electrons (comparable to the energies determined by Cowley and Bunce (2001b)) associated with an upward field-aligned current of  $\sim 1 \mu\text{A m}^{-2}$  (on the high side of those determined here) will produce an increase in height-integrated Pedersen conductivity from

a background value of less than 0.1 mho to a value of  $\sim 7.5$  mho (uncorrected for atmospheric slippage).

It is the primary purpose of this chapter to investigate the effect on the plasma angular velocity profiles, and on the magnetosphere-ionosphere current circuit, of precipitation-induced changes in the ionospheric conductivity. In so doing, we will also address two other issues left open from previous studies. The first is the issue addressed specifically by Pontius (1997), which concerns the fact that observed values of the plasma angular velocity in the outer part of the middle magnetosphere do not fall as fast with increasing radial distance as anticipated from simple constant-conductivity models (e.g. Kane et al., 1995; Krupp et al., 2001). Cowley and Bunce (2001b) anticipated that such effects could result from precipitation-induced enhancements in the ionospheric conductivity and the consequent atmospheric torque. The second concerns the radial profile of the outward-directed field-aligned currents which feed the radial current in the equatorial plasma. In the constant-conductivity models derived previously, these currents are broadly distributed over the whole middle magnetosphere region, such that the equatorial radial current, integrated over local time, grows monotonically with increasing distance (see Chapter 4), closing in the exterior region outside the middle magnetosphere not described by the model. However, analysis of Galileo magnetometer data presented by Khurana (2001) indicates that the outward field-aligned current into the equatorial plane is actually concentrated in the inner region between radial distances of  $\sim 10$  and  $\sim 30 R_J$ , peaking near  $20 R_J$ , such that the total radial current, integrated in local time, is approximately constant at distances beyond. These results for the location of the upward field-aligned current are also in rough accord with the observed locations of the ‘main oval’ auroras (Clarke et al. 1998; Prangé et al., 1998; Grodent et al., 2003). Here we will show that the effect of precipitation-induced enhancement of the ionospheric conductivity is just such as to concentrate the upward current into the inner middle magnetosphere region, as deduced from the Galileo data.

This chapter will be organised as follows. In the next section an update to the ‘current sheet’ field model (see Chapter 3) to be used in the calculations in this chapter will be described. In Section 5.3 we then derive an empirical model of how the conductivity depends on the field-aligned current, estimated from the results presented by Millward et al. (2002). In Section 5.4 we present solutions for the plasma angular velocity and the

current using simplified conductivity models motivated by the empirical results, allowing us to investigate the nature of the solutions and their relation to the previous solutions derived for constant conductivity. In Section 5.5 we then present results using the full empirical conductivity model, and compare them with the current profiles derived by Khurana (2001) from Galileo data.

## 5.2. Magnetic field model

In the modelling work described in previous chapters we have used the ‘Voyager-1 / Pioneer-10’ model of Connerney et al. (1981) (the ‘CAN’ model) at small distances, and the Voyager-1 model of Khurana and Kivelson (1993) (the ‘KK’ model) at large distances, the models being joined at an equatorial radial distance of  $\rho_e^* \approx 21.78 R_J$ , where the two model curves meet (see Section 3.3.6). Although there is then no discontinuity in the field magnitude at this point, there is a discontinuity in the first derivative. Here instead we employ a field model which is very close to that previously used, but is continuous over the range of interest. The model equatorial field is given by

$$B_{ze}(\rho_e) = - \left\{ B_0 \left( \frac{R_J}{\rho_e} \right)^3 \exp \left[ - \left( \frac{\rho_e}{\rho_{e0}} \right)^{5/2} \right] + A \left( \frac{R_J}{\rho_e} \right)^m \right\} \quad (5.1a)$$

where  $B_0 = 3.335 \times 10^5$  nT,  $\rho_{e0} = 14.501 R_J$ ,  $A = 5.4 \times 10^4$  nT and  $m = 2.71$ . The second term in this expression is simply the KK model, applicable at large distances, while the first term is a modified dipole in form. The corresponding flux function is given by

$$F_e(\rho_e) = F_\infty + \frac{B_0 R_J^3}{2.5 \rho_{e0}} \Gamma \left[ -\frac{2}{5}, \left( \frac{\rho_e}{\rho_{e0}} \right)^{5/2} \right] + \frac{A}{(m-2)} \left( \frac{R_J}{\rho_e} \right)^{m-2}, \quad (5.1b)$$

where  $F_\infty \approx 2.841 \times 10^4$  nT  $R_J^2$  is the value of the flux function at infinity, and  $\Gamma(a,z)$  is the incomplete gamma function given by Eq. (4.28). This field model is such that the values of both  $B_{ze}$  and  $F_e$  at the inner edge of the middle magnetosphere current sheet at  $\rho_e = 5 R_J$  are

exactly those given by the CAN model (in the Edwards et al. (2001) approximations). These values are  $\sim 3177$  nT and  $\sim 8.819 \times 10^4$  nT  $R_J^2$ , compared with  $\sim 3411$  nT and  $\sim 8.528 \times 10^4$  nT  $R_J^2$  for the dipole field alone, the differences reflecting the stretched out nature of the field due to the presence of the current sheet. The model is also such that the flux threading through the current sheet between  $5 R_J$  and infinity is exactly equal to that of the CAN/KK model employed previously, such that the values of  $F_\infty$  in the two models are also exactly equal. Consequently, the models map into exactly the same dipole latitude band in the ionosphere, spanning dipole co-latitudes between  $\sim 27^\circ$  and  $\sim 15^\circ$  for radial distances between  $5 R_J$  and infinity. In Fig. 5.1 we show plots of  $|B_{ze}|$  (the actual values of  $B_{ze}$  are, of course, all negative),  $F_e$ , and the ionospheric co-latitude  $\theta_i$  versus equatorial radial distance over the range 0 to  $100 R_J$  (as employed throughout this chapter). The solid lines show the values for the above field model, while the dashed lines show the values for the planetary dipole alone. The dotted lines in the  $|B_{ze}|$  plot show the values for the CAN/KK model, which are only clearly visible when they are projected beyond  $\rho_e^*$ . The ionospheric mapping is given by Eqs. (3.2) and (3.3) such that the outermost field line in the plot, mapping to  $100 R_J$  in the equatorial plane, maps to  $\sim 15.7^\circ$  in the ionosphere. The horizontal dashed lines in the  $F_e$  and  $\theta_i$  plots show the asymptotic values of these quantities at large distances.

### ***5.3. Dependence of the Pedersen conductivity on the field-aligned current***

Recent modelling work presented by Millward et al. (2002) has investigated how the height-integrated conductivities in Jupiter's auroral zones are enhanced by auroral electron precipitation. In their model runs the precipitating electrons were taken to be a monoenergetic electron beam with energy ranging from 1 to 100 keV, thus spanning the range expected from the initial studies of Cowley and Bunce (2001b), Cowley, Nichols and Bunce (2002), and Cowley, Bunce and Nichols (2003). In their paper, results are shown for two cases of electron flux, one for a fixed flux of  $6.25 \times 10^{12} \text{ m}^{-2} \text{ s}^{-1}$  (corresponding to a

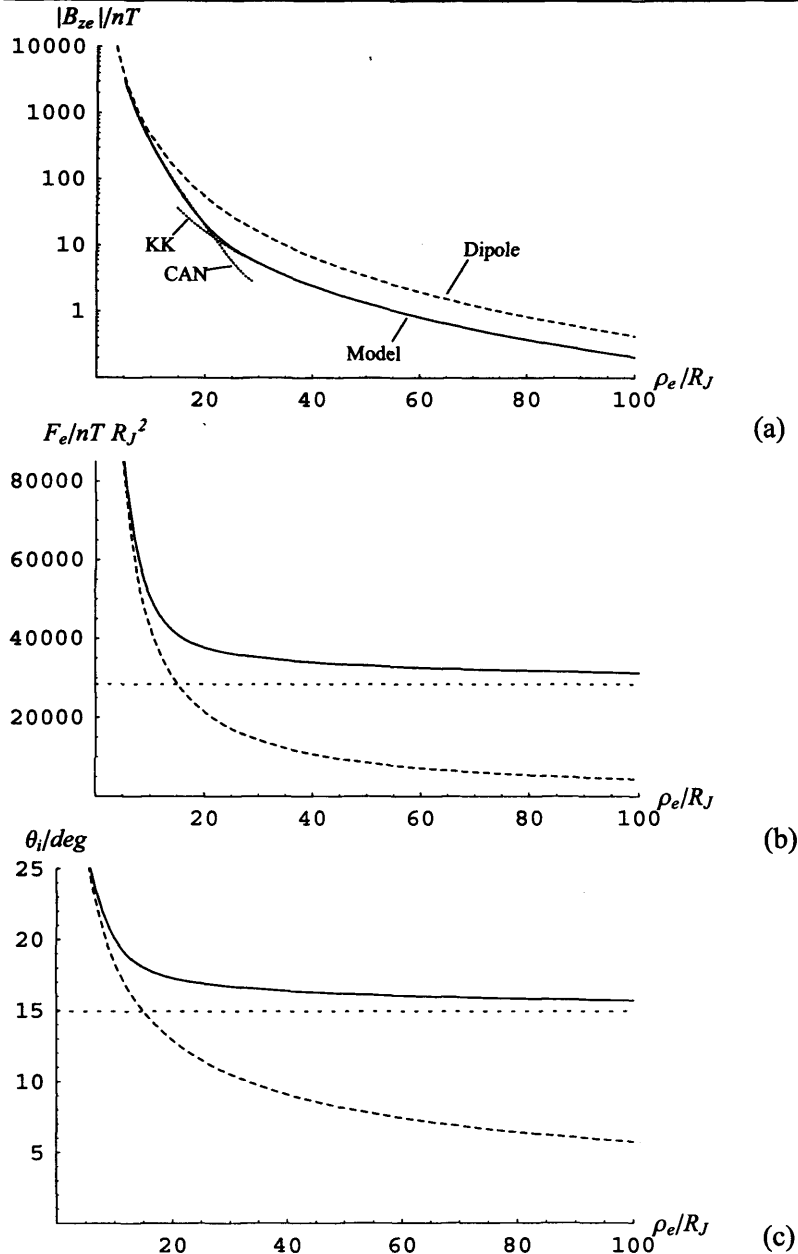


**Figure 5.1.** Plots showing the parameters of the current sheet field model employed in this chapter (solid lines) compared with values for the planetary dipole field alone (dashed lines). Plot (a) is a log-linear plot of the modulus of the north-south component of the equatorial magnetic field  $|B_{ze}|$  in nT threading the equatorial plane, shown versus jovicentric equatorial radial distance  $\rho_e$ , and where we note that the actual values are negative (i.e. the field points south). The solid line shows the field model employed in this paper, given by Eq. (5.1a), which is based on the CAN-KK model described in Section 3.3.6. The dotted lines show the CAN and KK models themselves, plotted beyond their intersection for ease of visibility. Plot (b) similarly shows the equatorial flux function of the model field  $F_e$  in  $nT m^2$  versus jovicentric equatorial radial distance  $\rho_e$ , given by Eq. (5.1b). The dotted line shows the value of the flux function at infinity,  $F_\infty$ . Plot (c) shows the mapping of the field lines between the equatorial plane and the ionosphere, determined from Eqs. (3.2) and (3.3). The ionospheric co-latitude of the field line  $\theta_i$  is plotted versus jovicentric equatorial radial distance  $\rho_e$ . The dotted line shows the ionospheric co-latitude of the field line which maps to infinity in the equatorial plane for our current sheet field model.

current density of  $1 \mu\text{A m}^{-2}$ ), their Fig. 7, the other for a fixed energy flux of  $10 \text{ mW m}^{-2}$ , their Fig. 8 (we note that in their paper the units of the fixed flux are misprinted as  $\text{cm}^{-2} \text{ s}^{-1}$ ). The empirical conductivity models employed here are based on the results shown in these two figures (kindly provided in digital form by G.H. Millward, personal communication, 2003).

Millward et al.'s (2002) results show that, for a given value of the number flux, the enhancement in the Pedersen conductivity is dependent on the precipitating electron energy, strongly peaking in the energy band between  $\sim 50$  to  $\sim 80$  keV, where the electrons deposit most of their energy within the Pedersen layer. Electrons e.g. of significantly higher energies deposit their energy too low down in the atmosphere to significantly affect the conductivity. In order to estimate the conductivity enhancement associated with a given field-aligned current (and hence number flux) we thus also need to estimate the energy of the precipitating electrons. To do this we employ the kinetic theory of Knight (1973), as discussed in Section 3.3.3. Specifically, we use Eq. (3.20) for the minimum field-aligned voltage required to drive a given field-aligned current and Eq. (3.23) for the corresponding precipitating energy flux. The approximations in Eqs. (3.20) and (3.23) correspond to the case where  $j_{\parallel} \gg j_{\parallel io}$ , as will generally be satisfied in the middle magnetosphere, as discussed previously by Cowley and Bunce (2001b), Cowley, Nichols and Bunce (2002), and Cowley, Bunce and Nichols (2003). In this case, therefore, the electron population will indeed form an essentially monoenergetic beam at high altitudes, because  $e\Phi \gg W_{th}$ . Consequently, the results presented by Millward et al. (2002) indicate that the ionospheric conductivity will be strongly enhanced when the field-aligned current passes through values such that the accelerating voltage lies in the range  $\sim 50$  to  $80$  keV, and will be significantly smaller outside this range. However, judging from the case of the Earth (see e.g. Paschmann et al. (2002), chapter 4), the monoenergetic beam will be strongly scattered by wave-particle interactions underneath the accelerating region, forming a broad distribution covering a wide range of energies, thus smoothing the variation of conductivity with current. This seems the most likely scenario at the present time, and is the case which will be assumed here.

Specifically, we have assumed that the auroral electron distribution is isotropic over the downward-going hemisphere (due to the large increase in field strength between the acceleration region at a few  $R_J$  altitude and the top of the ionosphere), and is given as a function of electron velocity  $v$  by

$$f(v) = \frac{f_0}{\left[ \left( \frac{v}{v_0} \right)^\alpha + \left( \frac{v}{v_0} \right)^\beta \right]}, \quad (5.2)$$

such that for  $\beta > \alpha$ , the distribution varies as  $v^{-\alpha}$  for  $v < v_0$ , and  $v^{-\beta}$  for  $v > v_0$ . The velocity where the spectrum 'breaks' between exponents  $\alpha$  and  $\beta$  is taken to be given by the accelerating voltage  $\Phi$ , i.e.

$$\frac{m_e v_0^2}{2} = e\Phi, \quad (5.3)$$

such that the population with slope  $\alpha$  for  $v < v_0$  corresponds to degraded primary particles, while that with slope  $\beta$  for  $v > v_0$  corresponds to a steeply falling high energy tail produced by the wave-particle interactions. The value of  $f_0$  is determined by the requirement that the downward-going particles carry current  $j_{||}$ , i.e.

$$f_0 = \left( \frac{j_{||}}{\pi e} \right) / \int_0^\infty \frac{dv v^3}{\left[ \left( \frac{v}{v_0} \right)^\alpha + \left( \frac{v}{v_0} \right)^\beta \right]}, \quad (5.4)$$

and, for the examples employed here, for a given value of  $\alpha$  we have determined the value of  $\beta$  such that the total precipitating energy flux is just that given by Eq. (3.23). Example distributions are shown in Figs. 5.2a and 5.2b for the cases  $\alpha = 0, \beta = 10$  and  $\alpha = 2, \beta = 8$  respectively. In each case we show the distributions (plotted versus electron energy  $W_e = m_e v^2 / 2$  in keV) corresponding to both  $j_{||} = 0.1 \mu\text{A m}^{-2}$  and  $1.0 \mu\text{A m}^{-2}$ , where the magnetospheric 'parent' population has a density  $N = 0.01 \text{ cm}^{-3}$  and a thermal energy

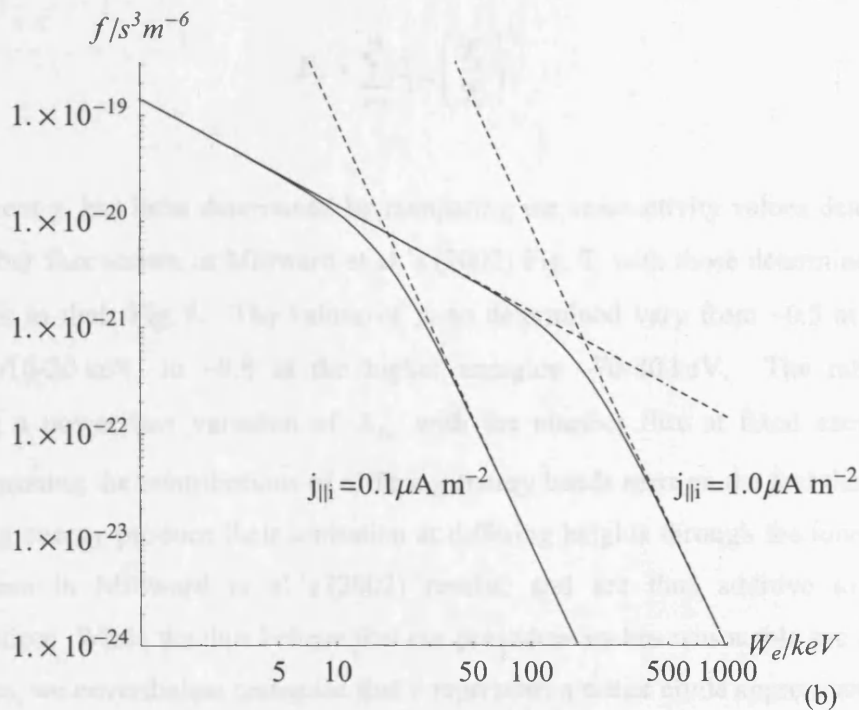
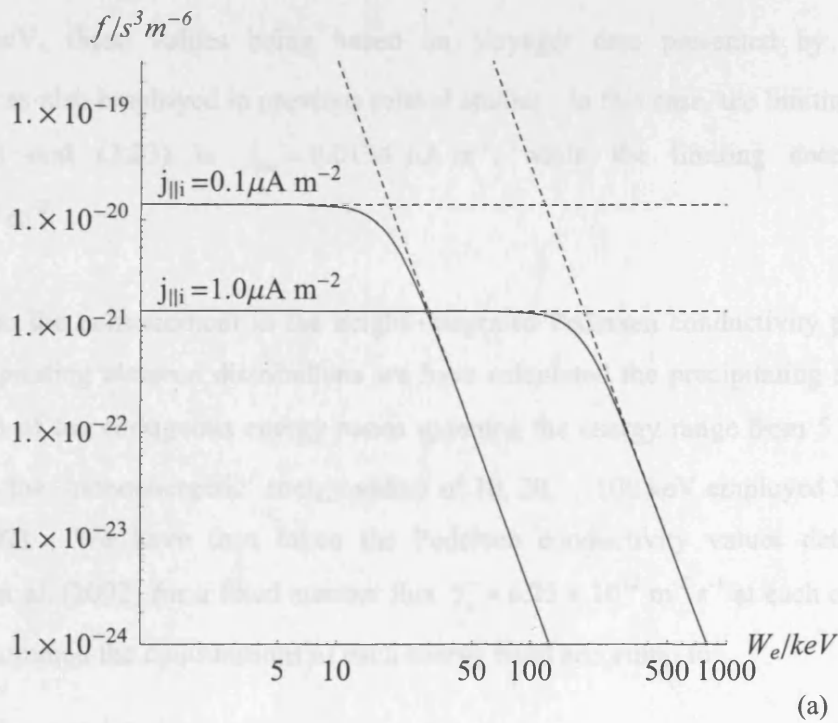


**Figure 5.2.** Two examples of auroral electron distribution functions, plotted versus electron energy  $W_e = m_e v^2/2$  in keV, determined from Eqs. (5.2)-(5.4), employed here with  $N = 0.01 \text{ cm}^{-3}$  and  $W_{th} = 2.5 \text{ keV}$ . Plot (a) shows the case for  $\alpha = 0$  and  $\beta = 10$ , while plot (b) shows the case for  $\alpha = 2$  and  $\beta = 8$ . In both plots the distributions are shown for  $j_{\parallel} = 0.1 \mu A m^{-2}$  and  $1.0 \mu A m^{-2}$ . The dashed lines show the asymptotes of the respective power law variations.

$W_e = 2.5$  keV, these values being based on Voyager data presented by Scudder et al. (1981), as also employed in previous related studies. In this case, the limiting current in Eqs. (3.20) and (3.23) is  $j_{\parallel 0} = 0.0134 \mu\text{A m}^{-2}$ , while the limiting energy flux is  $0.067 \text{ mW m}^{-2}$ .

To estimate the enhancement in the height-integrated Pedersen conductivity produced by such precipitating electron distributions we have calculated the precipitating number flux  $\mathcal{F}_n$  in each of ten contiguous energy bands spanning the energy range from 5 to 105 keV, centred on the ‘monoenergetic’ energy values of 10, 20, ... 100 keV employed by Millward et al. (2002). We have then taken the Pedersen conductivity values determined by Millward et al. (2002) for a fixed number flux  $\mathcal{F}_0 = 6.25 \times 10^{12} \text{ m}^{-2} \text{ s}^{-1}$  at each energy,  $\Sigma_{Pn}$ , and have summed the contributions of each energy band according to

$$\Sigma_P = \sum_{n=1}^{10} \Sigma_{Pn} \left( \frac{\mathcal{F}_n}{\mathcal{F}_0} \right)^{\gamma_n} . \quad (5.5)$$

The exponent  $\gamma_n$  has been determined by comparing the conductivity values determined at fixed number flux shown in Millward et al.’s (2002) Fig. 7, with those determined at fixed energy flux in their Fig. 8. The values of  $\gamma_n$  so determined vary from  $\sim 0.5$  at the lower energies  $\sim 10$ -20 keV, to  $\sim 0.8$  at the higher energies  $\sim 70$ -80 keV. The rationale for employing a power law variation of  $\Sigma_{Pn}$  with the number flux at fixed energy, while linearly summing the contributions of differing energy bands rests on the fact that electrons of differing energy produce their ionisation at differing heights through the ionosphere, as can be seen in Millward et al.’s (2002) results, and are thus additive to a lowest approximation. While we thus believe that our procedure makes reasonable use of existing information, we nevertheless recognise that it represents a rather crude approximation.

The solid lines in Fig. 5.3 show how  $\Sigma_P$  depends on  $j_{\parallel i}$  for four model auroral distribution functions ( $\alpha, \beta$  values) for a hot magnetospheric ‘source’ electron population with the above values of  $N$  and  $W_{th}$ . It can be seen that the curves are reasonably similar, rising from small values for small currents to values of  $\sim 2$  mho for  $j_{\parallel i} \sim 0.4 \mu\text{A m}^{-2}$  (a slope of

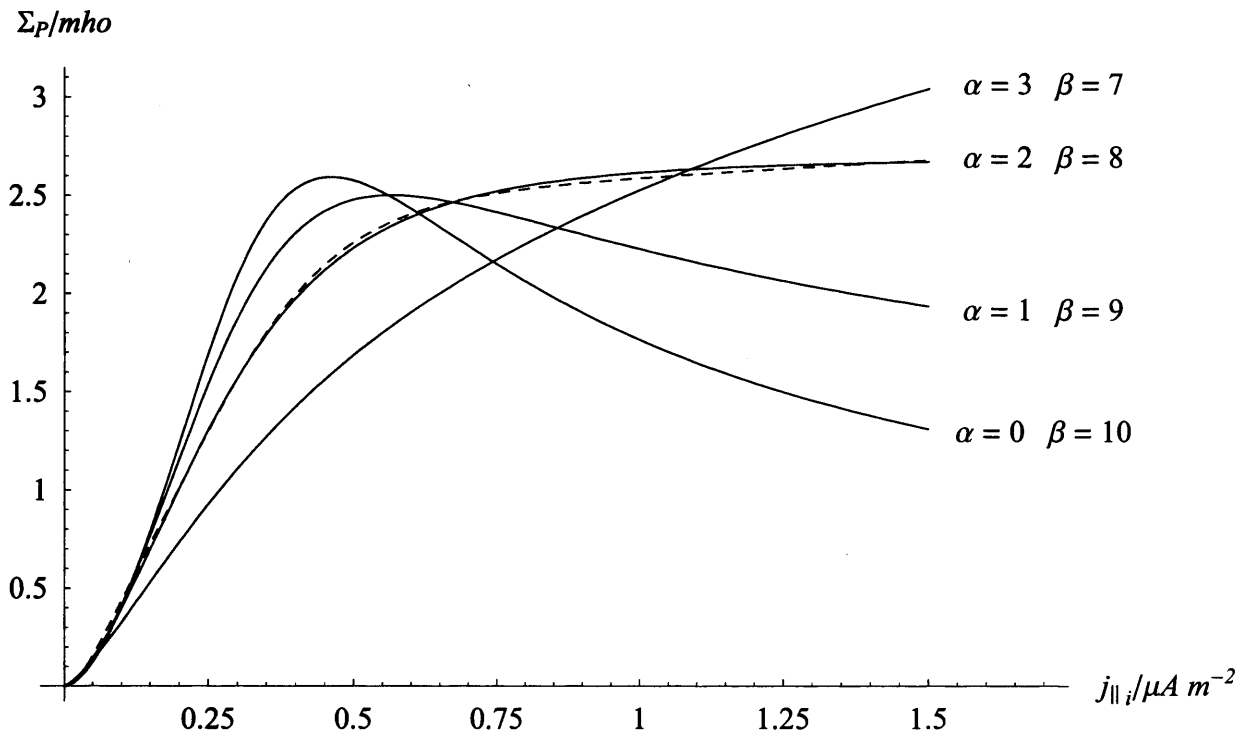


**Figure 5.3.** Plots of the height integrated Pedersen conductivity  $\Sigma_p$  in mho versus ionospheric field-aligned current density  $j_{\parallel i}$  ( $\mu\text{A m}^{-2}$ ) using four models of the auroral electron distribution functions. The respective  $\alpha$  and  $\beta$  values are indicated on the plot. The results are based on Millward et al.'s (2002) computations, using Eq. (5.5). The dashed line shows the analytic form given by Eq. (5.6).

$\sim 5$  mho ( $\mu\text{A m}^{-2}$ )<sup>-1</sup>). For larger currents, the behaviour of the conductivity depends rather more on the assumed spectrum, specifically on the slope at small energies, below that produced by the voltage drop. However, rather than employing these curves directly, which would be impractical in the numerical integrations which follow, we have instead employed a simple analytical form taken to be representative of these results. This is given, for  $j_{\parallel i} > 0$ , by

$$\Sigma_p(j_{\parallel i}) = 0.16j_{\parallel i} + 2.45 \left[ \frac{(j_{\parallel i}/0.075)^2}{1 + (j_{\parallel i}/0.075)^2} \right] \frac{1}{\left[ 1 + \exp(-(j_{\parallel i} - 0.22)/0.12) \right]}, \quad (5.6)$$

where  $\Sigma_p$  is in mho and  $j_{\parallel i}$  is in  $\mu\text{A m}^{-2}$ . This form is shown by the dashed line in Fig. 5.3.

It should be realised that the results shown in Fig. 5.3 are appropriate only to the above values of the magnetospheric hot electron source parameters, and that differing dependencies of the conductivity on the current will be appropriate to other values. In general, therefore, the conductivity will be a function of both the field-aligned current and the position (i.e. the flux function). For simplicity, however, and in the absence of any established model of the properties of the hot magnetospheric electrons, we have taken the source parameters to be constant throughout the middle magnetosphere, as seems appropriate to an initial investigation. We have thus employed a fixed conductivity model  $\Sigma_p = \Sigma_p(j_{\parallel i})$ , independent of position, in all the solutions derived in this chapter. Two further points should also be made. The first is that the quantity  $\Sigma_p$  derived above and shown in Fig. 5.3 is our estimate of the true value of the height-integrated Pedersen conductivity, while the value required by the theory in Section 3.3.2 is the ‘effective’ value, reduced from the true value by atmospheric slippage. This is related to the true value by Eqs. (3.11) and (3.9), thus depending on parameter  $k$ . The value of  $k$  is not well known at present, but recent work with the JIM model indicates that  $k \sim 0.5$  for large current values of  $\sim 1 \mu\text{A m}^{-2}$  (G.H. Millward, personal communication, 2003). Application of Eq. (5.6) in Section 5.5 is thus modified by the multiplication of the true conductivity by the factor  $(1-k)$ , where we assume that  $k \sim 0.5$ . Second, noting that the analytical form Eq. (5.6)

goes to zero as  $j_{||i} \rightarrow 0$ , we also add a small constant value  $\sim 0.05$  mho, representing the residual conductivity (produced, for example, by solar illumination) in the absence of precipitation. Further details will be given below.

#### **5.4. Solutions for near-linear variations of the conductivity**

Rather than proceed directly to the discussion of solutions tailored specifically to jovian conditions, employing the empirical conductivity model given by Eq. (5.6), in this section we first discuss the results of a somewhat wider investigation using simplified conductivity models, which provide insight into the nature of the solutions and their relation to those derived in earlier studies using constant conductivity.

##### **5.4.1. Method of obtaining solutions**

We first discuss the method adopted to obtain the solutions required. In the case where  $\Sigma_p^*$  is considered to be a constant, as discussed in previous chapters, the equation to be solved is the Hill-Pontius equation, Eq. (3.27). This is a first order linear equation for  $\omega$ , which can be solved numerically with the use of one initial or boundary condition, i.e. with the arbitrary choice of the value of  $\omega$  at one particular position  $\rho_e$ . However, for a given position  $\rho_e$ , there is only one choice for  $\omega$  which satisfies the physical requirement that the plasma near-rigidly corotates at small radial distances, the latter corresponding to the solutions first derived by Hill (1979) and Pontius (1997). All other solutions diverge at small  $\rho_e$ , those starting with a smaller value of  $\omega$  eventually diverging to large negative values, while those starting with a larger value of  $\omega$  diverging to large positive values. Some examples of such divergent solutions are shown in the Appendix of the paper by Cowley and Bunce (2003a). The required solution which does not diverge at the origin can then be found by iterating the value of  $\omega$  at the ‘boundary’ position.

If we now consider the variable conductivity problem in which  $\Sigma_p^*$  depends on  $j_{\parallel i}$  according to some model such as Eq. (5.6), then two equations must be solved simultaneously. That is Eq. (3.16) for parallel current, and the Hill-Pontius equation Eq. (3.27) for the plasma angular velocity, which now depends on the parallel current through the dependence of  $\Sigma_p^*$ . We thus must solve two coupled first order equations for  $j_{\parallel i}$  and  $\omega$ , thus requiring the choice of two boundary or initial conditions. These choices are conveniently the values of  $j_{\parallel i}$  and  $\omega$  at a given point,  $\rho_e$ , taken throughout here to be the outer boundary of the model at  $100 R_J$ . The choice of  $j_{\parallel i}$  at the outer boundary also fixes the value of  $\Sigma_p^*$  at the boundary, of course, through the chosen conductivity model. For a given value of  $j_{\parallel i}$  (and  $\Sigma_p^*$ ) at the outer boundary we then iterate  $\omega$  to find the physically acceptable solution which near-rigidly corotates at small radial distances, using the divergent behaviour of the Hill-Pontius equation at small radial distances outlined above, which applies here also to the general problem. It is found that  $\omega$  must generally be specified to very many (typically  $\sim 13$ ) decimal places at  $100 R_J$  in order to follow the required solution in towards the quasi-dipolar inner magnetosphere without diverging either to large positive or negative values. In practice this procedure has typically been used to track the required solution in from  $100 R_J$  to  $\rho_e \sim 10$  to  $20 R_J$ , the solution then being completed by the use of an approximation which is appropriate to the inner region, as we now discuss.

#### 5.4.2. *Inner region approximations*

The behaviour of the physically required solutions in the inner region where the plasma near-rigidly corotates has been discussed previously in Chapter 4 for the case of constant conductivity, and is now applied here to the more general case. It was found in Section 4.2 that the amount of (small) slippage from rigid corotation required to drive the current  $i_p$  which maintains near-rigid corotation is given by Eq. (4.3), valid for the situation where  $(1 - \omega/\Omega_r) \ll 1$ . Hence in this regime the azimuth-integrated equatorial radial current  $I_p$  and the ionospheric field-aligned current  $j_{\parallel i}$  were found to be given by Eqs. (4.4d) and

(4.4f) respectively. It was therefore shown that the currents in the innermost region depend only on  $\dot{M}$  and the model of the poloidal field and not on  $\Sigma_p^*$  (or the model dependence of  $\Sigma_p^*$  on  $j_{\parallel i}$ ), though of course the radial extent of the region to which Eqs. (4.4d) and (4.4f) apply does depend on  $\Sigma_p^*(j_{\parallel i})$  as we will find. However, the plasma angular velocity in the inner region then does depend on  $\Sigma_p^*(j_{\parallel i})$  (with  $j_{\parallel i}$  determined from Eq. (4.4f)), the departure from rigid corotation varying inversely with the conductivity.

It will be noted from Eq. (4.4f) that  $j_{\parallel i}$  approaches small values in the inner region, being given by

$$j_{\parallel i} \approx \frac{3\dot{M}\Omega_J}{\pi B_J} \rho_e^4 \quad (5.7)$$

where the field is quasi-dipolar, i.e.  $|B_{ze}| \approx B_J R_J^3 / \rho_e^3$  (Eq. (5.7) is simply the equatorial mapping of Eq. (4.23f), and is related to the latter via Eq. (3.3)). The ionospheric conductivity thus perforce approaches the small constant value  $\Sigma_p^* = \Sigma_p^*(j_{\parallel i} = 0)$  in the inner region. An additional iterative approach to approximation in the inner region can then be useful in cases where the conductivity does not vary strongly with the parallel current. We can then first solve the Hill-Pontius equation using the constant conductivity  $\Sigma_p^*(j_{\parallel i} = 0)$ , from which an approximation to  $j_{\parallel i}$  is derived, which can be used to derive a varying conductivity profile from the model for  $\Sigma_p^*(j_{\parallel i})$  which is an explicit function of position. This can then be used to solve the Hill-Pontius equation again, yielding a ‘first iteration’ to the angular velocity and currents, from which a modified varying conductivity profile is derived. In principle this procedure can then be repeated to find successive iterations to the solution in the inner region.

### 5.4.3. Results for a near-linear conductivity model

We now present results, derived as discussed above, for a simplified conductivity model in which the Pedersen conductivity has a small near-constant value for  $j_{\parallel i}$  negative (i.e. downward field-aligned current), while increasing near-linearly with the field-aligned current density when  $j_{\parallel i}$  is positive (i.e. upward field-aligned current). Specifically the function employed is

$$\Sigma_P^*(j_{\parallel i}) = \Sigma_{P_0}^* + \left(\frac{S}{2}\right) \left(\sqrt{j_{\parallel i}^2 + j_w^{*2}} + j_{\parallel i}\right), \quad (5.8)$$

which is such that  $\Sigma_P^* \approx \Sigma_{P_0}^*$  for  $j_{\parallel i} \ll -|j_w^*|$ , and  $\Sigma_P^* \approx \Sigma_{P_0}^* + S j_{\parallel i}$  for  $j_{\parallel i} \gg |j_w^*|$ . The value of the limiting conductivity in the inner region of the system is then

$$\Sigma_P^*(j_{\parallel i} = 0) = \Sigma_{P_0}^* + \left(\frac{S j_w^*}{2}\right). \quad (5.9)$$

In the results presented here we have taken  $\Sigma_{P_0}^* = 0.05$  mho (motivated, e.g., by the results of Hill (1980) obtained from analysis of plasma angular velocity profiles in the innermost region),  $j_w^* = 0.01 \mu\text{A m}^{-2}$  (a somewhat arbitrary small value, which is such that the conductivity varies between the above two behaviours over a narrow range of  $j_{\parallel i} \sim 0.01 \mu\text{A m}^{-2}$  about  $j_{\parallel i} = 0$ ), and three values of the slope  $S = 0.1, 1.0$  and  $10$  mho  $(\mu\text{A m}^{-2})^{-1}$ . We show these three models for the conductivity in Fig. 5.4, plotted versus  $j_{\parallel i}$  over the physically interesting range out to  $1 \mu\text{A m}^{-2}$ . We note that the initial slopes of the empirical curves for the true value of the Pedersen conductivity (as opposed to the ‘effective’ value discussed here) shown in Fig. 5.3, lie between the two larger of these values of  $S$ . Results for the smallest value,  $S = 0.1$  mho  $(\mu\text{A m}^{-2})^{-1}$ , are included in order to address the issue of the relation between the solutions derived here and those obtained for constant conductivity in previous studies.

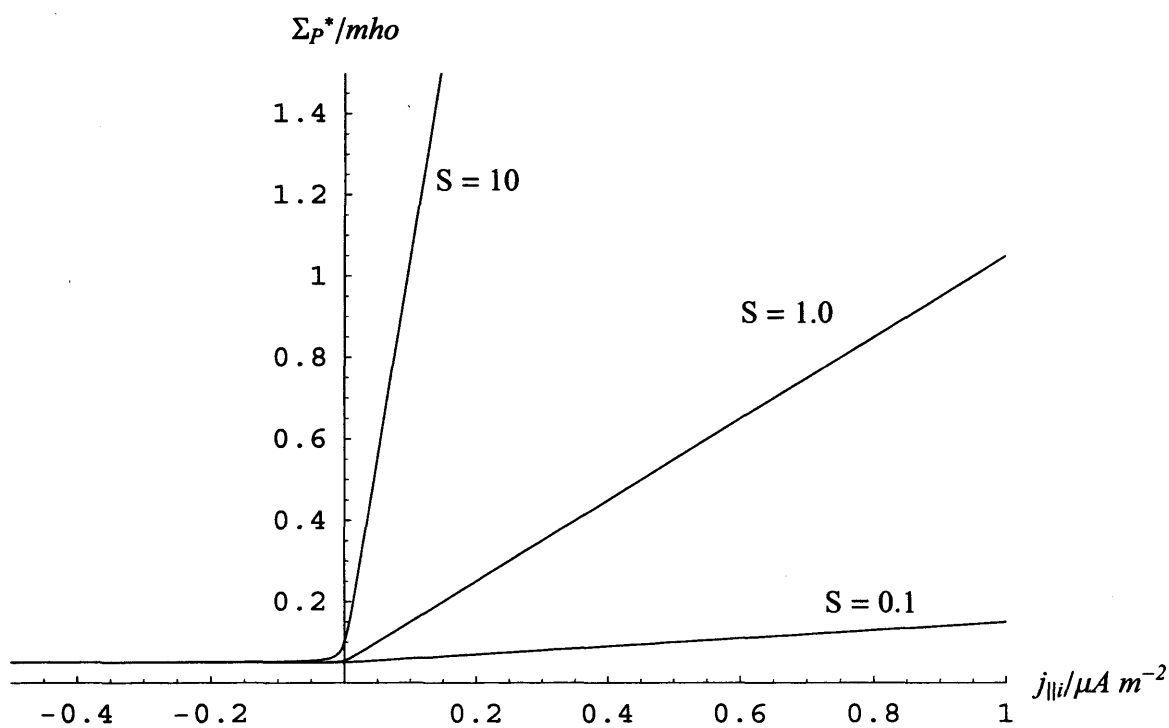


**Figure 5.4.** Plots of the effective height integrated Pedersen conductivity  $\Sigma_p^*$  in mho versus ionospheric field-aligned current density  $j_{||i}$  ( $\mu A m^{-2}$ ) using the near-linear conductivity model given by Eq. (5.8). Three cases are shown for  $S = 0.1, 1,$  and  $10 \text{ mho } (\mu A m^{-2})^{-1}$ , as indicated.

We thus begin here with the latter case,  $S = 0.1 \text{ mho } (\mu\text{A m}^{-2})^{-1}$ , and also choose  $\dot{M} = 1000 \text{ kg s}^{-1}$  as a typical value as indicated above. In Figs. 5.5 and 5.6 we show results in a standard form that will be used throughout the chapter. The two panels of the first figure (Fig. 5.5) show, respectively, the plasma angular velocity normalised to  $\Omega_J$  and the azimuth-integrated equatorial radial current  $I_\rho$  in MA, while the two panels of the second figure (Fig. 5.6) show the field-aligned current density at the top of the ionosphere  $j_{\parallel i}$  in  $\mu\text{A m}^{-2}$ , and the effective height-integrated Pedersen conductivity  $\Sigma_p^*$  in mho, all plotted versus radial distance  $\rho_e$ . The last two quantities, of course, correspond to the values at the respective feet of the field lines concerned, but they have been plotted here versus  $\rho_e$  so that the relationships between all these quantities can be most readily appreciated. In the next section we will also show solutions projected into the ionosphere and plotted versus dipole co-latitude, so that the ionospheric distributions can also be appreciated.

The dot-dashed lines in the figure panels show the small- $\rho_e$  approximations given by Eqs. (4.3), (4.4d), and (4.4f), with  $\Sigma_p^*$  evaluated at  $j_{\parallel i}$  given by Eq. (4.4f). These approximations should be valid in the inner region where the departure of the plasma from rigid corotation is small. The dashed lines also show the solution obtained, as in previous works, if the conductivity is taken to be the constant value  $\Sigma_p^*(j_{\parallel i} = 0)$ , equal (from Eq. (5.9)) to 0.0505 mho in this case. According to the above discussion, these are then the curves to which our solutions should asymptote in the inner region as  $j_{\parallel i}$  falls to small values, such that the conductivity falls to  $\Sigma_p^*(j_{\parallel i} = 0)$ . It can be seen that  $j_{\parallel i}$  for this solution peaks at a value of  $\sim 0.055 \mu\text{A m}^{-2}$  at  $\sim 30 R_J$ , and falls to  $\sim 0.028 \mu\text{A m}^{-2}$  at the outer boundary at  $100 R_J$ . We note that such values of  $j_{\parallel i}$  result in only modest increases in the conductivity according to our assumed model, e.g. reaching  $\sim 0.0562 \text{ mho}$  for  $j_{\parallel i} \approx 0.056 \mu\text{A m}^{-2}$ . If we then choose a value of  $j_{\parallel i}$  at the outer boundary at  $100 R_J$  which is close to that of the constant conductivity curve, we may expect to derive a closely similar solution. This solution is shown by the central solid curve in each of the panels in Figs. 5.5 and 5.6, which shows the solution obtained by numerical integration of Eqs. (3.16) and (3.27) which near-rigidly corotates at small  $\rho_e$  and has the value  $j_{\parallel i} = 0.03 \mu\text{A m}^{-2}$  at

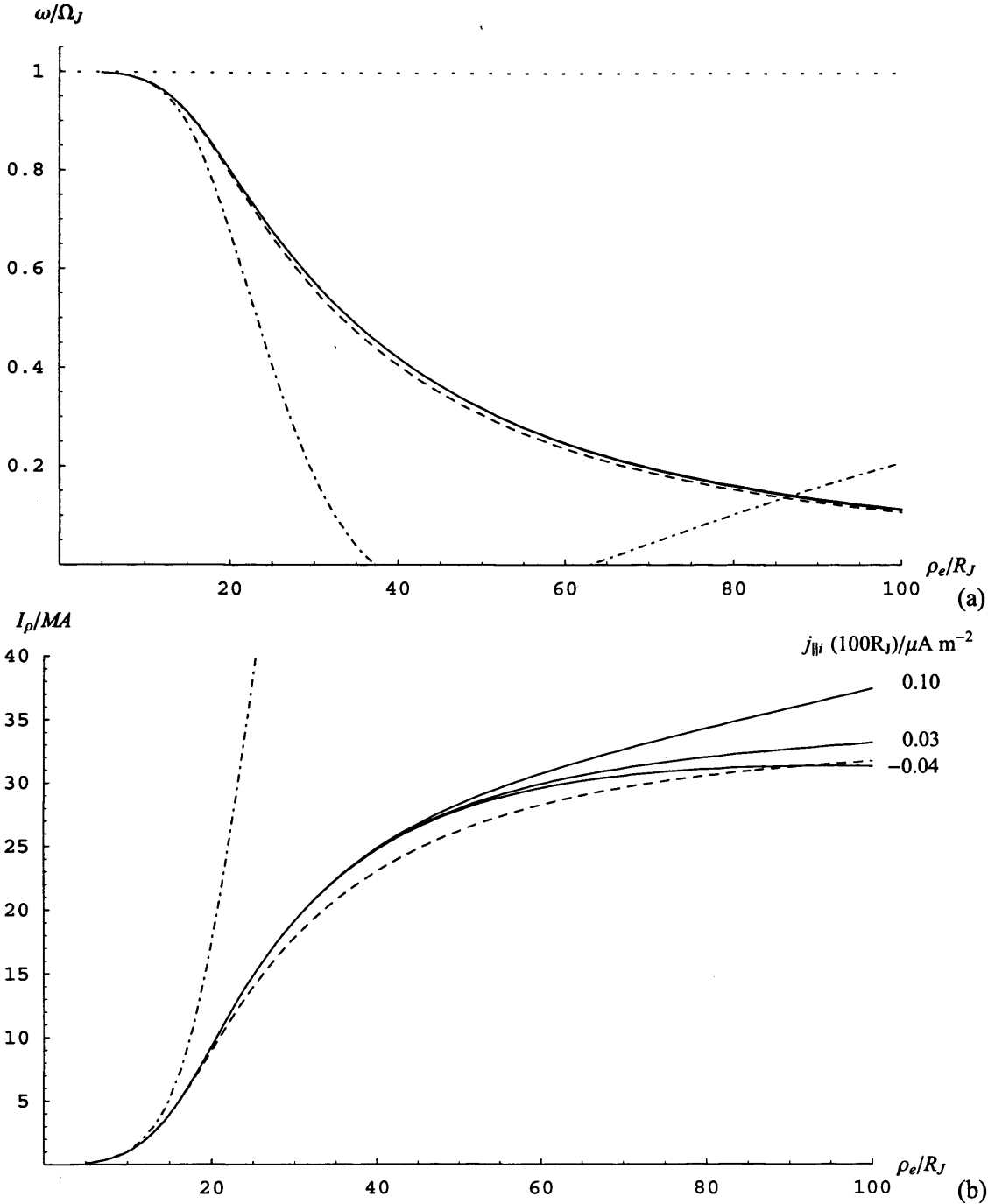


**Figure 5.5.** Plots of (a) the plasma angular velocity  $\omega$  normalised to the planet's angular velocity  $\Omega_J$ , and (b) the azimuth-integrated equatorial radial current  $I_\rho$  in MA for the near-linear conductivity model (Eq. (5.8)) with slope  $S = 0.1$  mho  $(\mu A m^{-2})^{-1}$  (solid lines), for constant conductivity  $\Sigma_p^*(j_{||} = 0) = 0.0505$  mho (dashed lines), and the near-rigid corotation approximations given by Eqs. (4.3) and (4.4d) (dot-dashed lines). The three solid lines represent boundary condition choices of  $j_{||}(100 R_J) = 0.10, 0.03$  and  $-0.04 \mu A m^{-2}$  as indicated in plot (b). In plot (a) the three solid curves are closely similar to one another, and are therefore not labelled. The solutions in each case are tracked to  $13 R_J$ , inside which they are completed by the 'first-iteration' approximation discussed in Section 5.4.2. Both parameters are plotted versus joventric equatorial radial distance  $\rho_e$ .

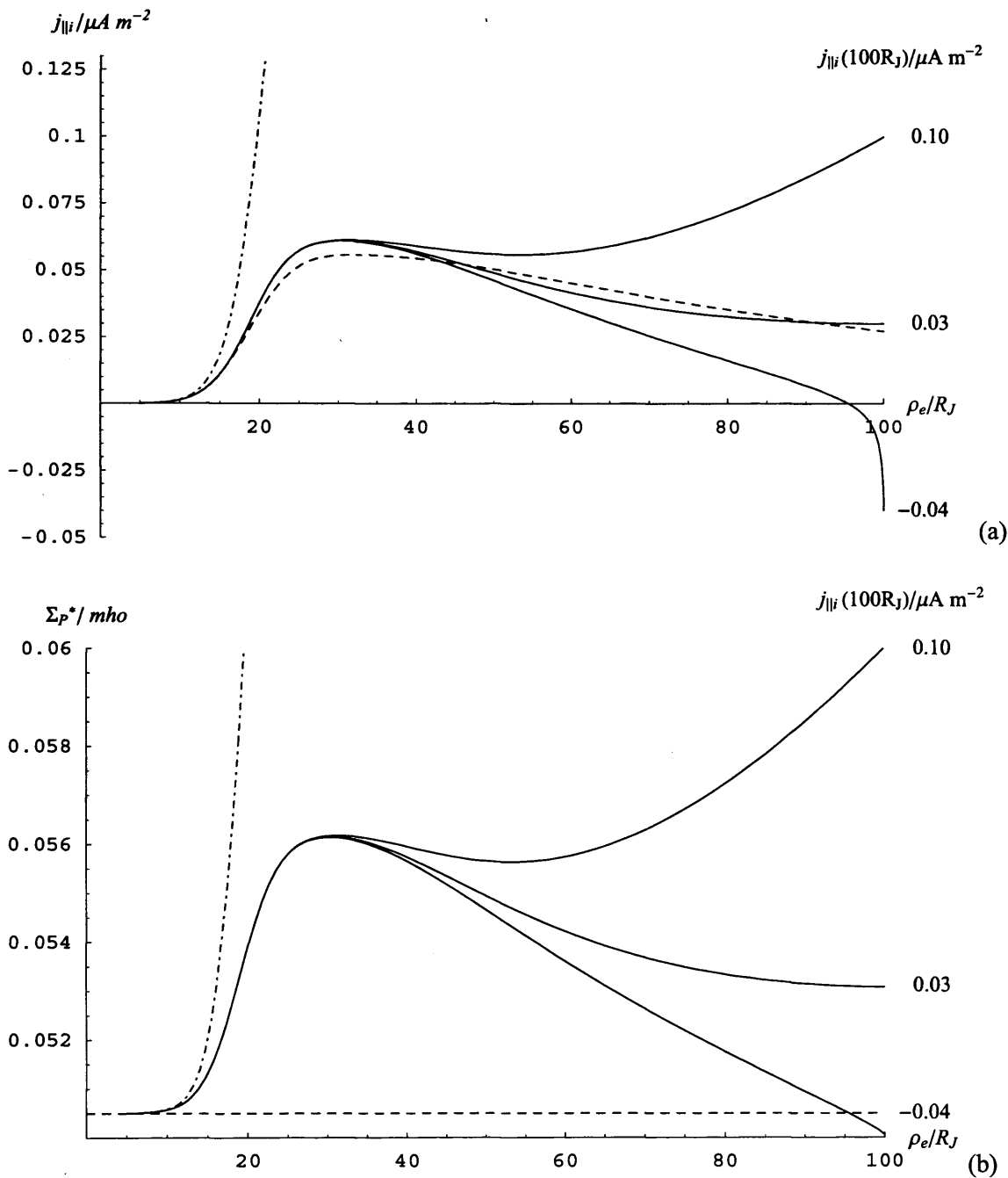


**Figure 5.6.** Plots of (a) the field-aligned current density at the feet of the field lines  $j_{\parallel i}$  in  $\mu A m^{-2}$ , and (b) the effective height-integrated Pedersen conductivity  $\Sigma_p^*$  in mho for the near-linear conductivity model (Eq. (5.8)) with slope  $S = 0.1$  mho  $(\mu A m^{-2})^{-1}$  (solid lines), for constant conductivity  $\Sigma_p^*(j_{\parallel i} = 0) = 0.0505$  mho (dashed lines), and the near-rigid corotation approximation given by Eq. (4.4f) (dot-dashed lines). The three solid lines represent boundary condition choices of  $j_{\parallel i}(100 R_J) = 0.10$ ,  $0.03$  and  $-0.04$   $\mu A m^{-2}$  as indicated. Again, the solutions in each case are tracked to  $13 R_J$ , inside which they are completed by the ‘first-iteration’ approximation discussed in Section 5.4.2. Both parameters are plotted versus jovicentric equatorial radial distance  $\rho_e$ .

$\rho_e = 100 R_J$ . (Note, however, that in Fig. 5.5a the solid lines are so close to each other that they are essentially indistinguishable). It can be seen that, as expected, this solution is very close to the constant conductivity solution over the whole range of distances. The iterated value of  $\omega/\Omega_J$  at  $100 R_J$ , for example, is  $(\omega/\Omega_J) \approx 0.1114$  compared with  $(\omega/\Omega_J) \approx 0.1065$  for the constant conductivity solution. We thus confirm that the solutions obtained here reduce to those found previously for constant conductivity in the appropriate limit.

Two other variable conductivity solutions are also shown in Figs. 5.5 and 5.6, for  $j_{\parallel i} = 0.10 \mu\text{A m}^{-2}$  and  $j_{\parallel i} = -0.04 \mu\text{A m}^{-2}$  at  $\rho_e = 100 R_J$ , such that the current at the outer boundary deviates considerably from that of the constant conductivity solution, one to larger positive values, the other to negative values. It can be seen that these solutions are closely similar to that for  $j_{\parallel i} = 0.03 \mu\text{A m}^{-2}$  in the inner region, diverging only at larger distances towards the boundary condition imposed at  $100 R_J$ . If the solution curves are projected (somewhat unphysically) beyond  $100 R_J$ , it is found that the solution for negative  $j_{\parallel i}$  at the boundary diverges to large negative currents at a radial distance just beyond  $100 R_J$ , while the solutions for positive currents at the boundary grow approximately linearly with the distance (results not shown). However, as can be seen in Fig. 5.5a, the solutions for  $(\omega/\Omega_J)$  in all cases remain very close to that for the constant conductivity  $\Sigma_p^* = \Sigma_p^*(j_{\parallel i} = 0) = 0.0505$  mho, shown by the dashed line.

We now turn to cases with significantly larger values of the slope  $S$  in the conductivity model, such that the enhancement of the conductivity with current is by a more substantial factor. For example, for  $S = 1 \text{ mho } (\mu\text{A m}^{-2})^{-1}$  the conductivity increases from 0.055 mho when  $j_{\parallel i} = 0$  to 0.150 mho when  $j_{\parallel i} = 0.1 \mu\text{A m}^{-2}$ , while for  $S = 10 \text{ mho } (\mu\text{A m}^{-2})^{-1}$  the corresponding increase is from 0.1 to 1.052 mho (see Fig. 5.4). Results for these values of  $S$  are shown in Figs. 5.7 and 5.8, and 5.9 and 5.10, respectively, where again we take  $\dot{M} = 1000 \text{ kg s}^{-1}$ . The format of the figures is similar to Figs. 5.5 and 5.6. It can be seen in Figs. 5.7a and 5.9a that in the innermost region the plasma angular velocity decreases from near-rigid corotation with increasing distance, in line with expectations based on the

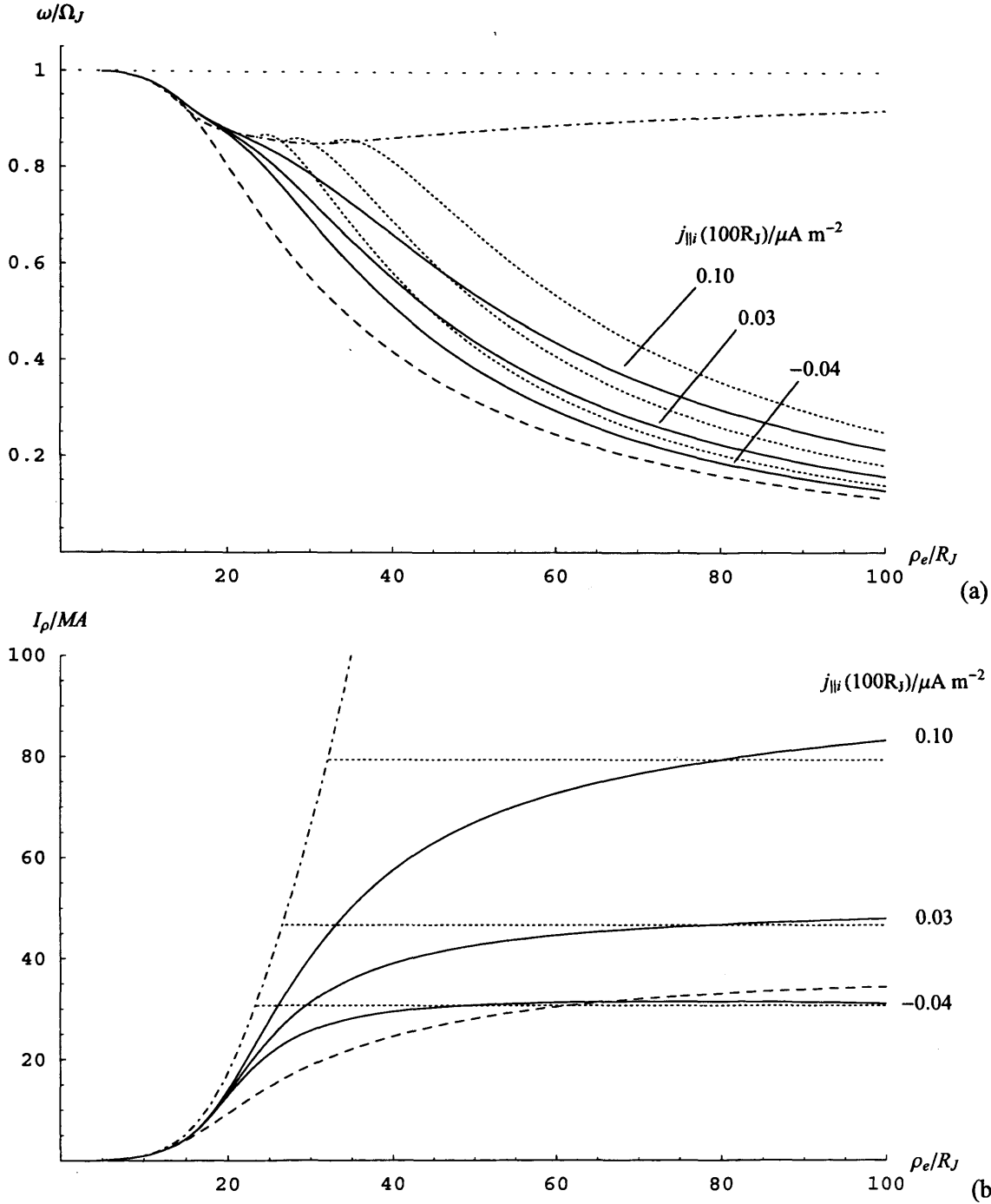


**Figure 5.7.** Plots of (a) the plasma angular velocity  $\omega$  normalised to the planet's angular velocity  $\Omega_J$ , and (b) the azimuth-integrated equatorial radial current  $I_\rho$  in MA, for the near-linear conductivity model (Eq. (5.8)) with slope  $S = 1.0$  mho  $(\mu A m^{-2})^{-1}$  (solid lines), for constant conductivity  $\Sigma_p^*(j_{||i} = 0) = 0.055$  mho (dashed lines), and the near-rigid corotation approximations given by Eqs. (4.3) and (4.4d) (dot-dashed lines). Also shown by the dotted lines is the outer region approximation calculated from Eqs. (5.10)-(5.13). The three solid lines represent boundary condition choices of  $j_{||i}(100 R_J) = 0.10, 0.03$  and  $-0.04 \mu A m^{-2}$  as indicated, as in Fig. 5.5. The solutions in each case are tracked to  $13 R_J$ , inside which they are completed by the 'first-iteration' approximation discussed in Section 5.4.2. All parameters are plotted versus jovicentric equatorial radial distance  $\rho_e$ .

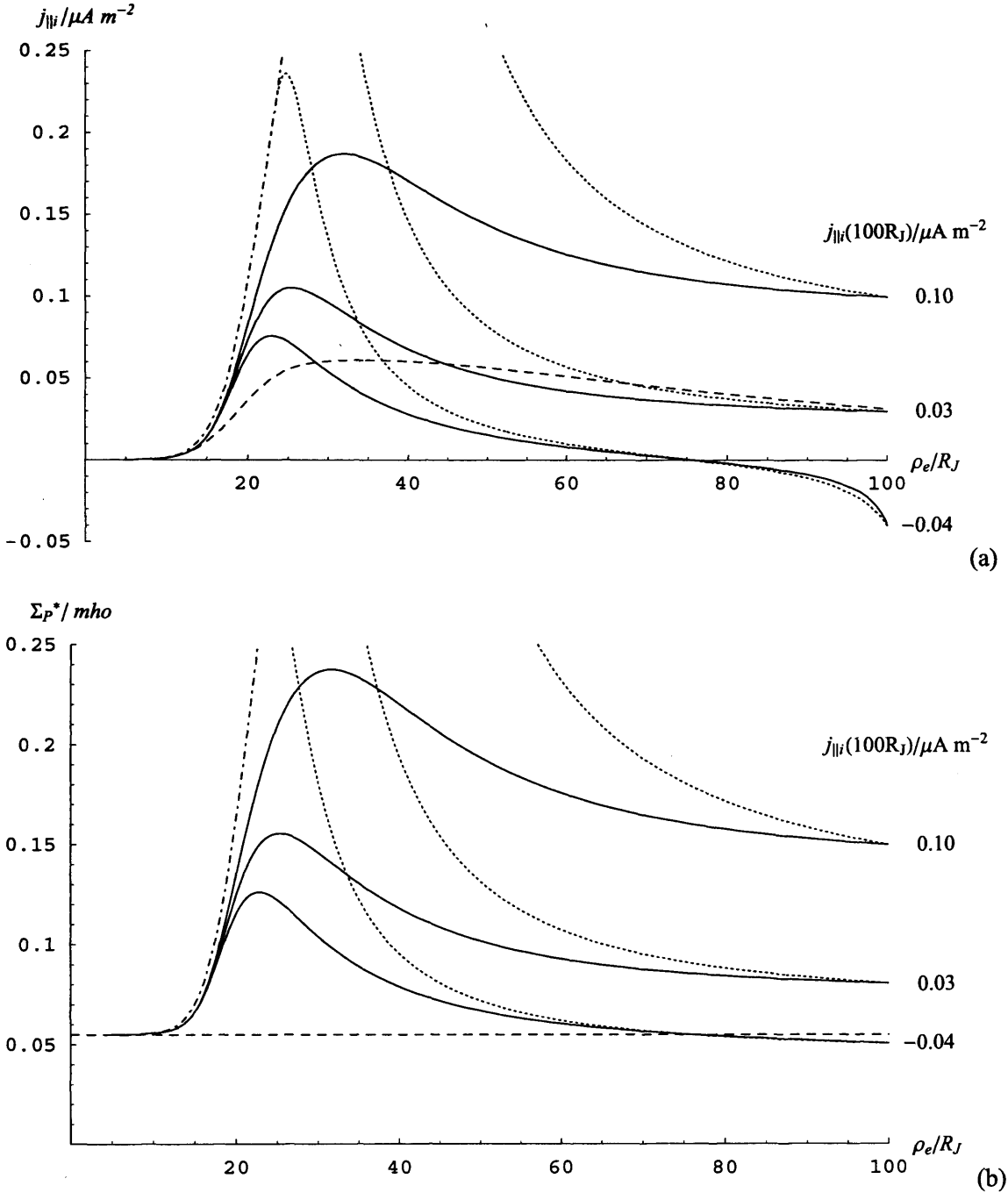


**Figure 5.8.** Plots of (a) the field-aligned current density at the feet of the field lines  $j_{\parallel i}$  in  $\mu A m^{-2}$ , and (b) the effective height-integrated Pedersen conductivity  $\Sigma_p^*$  in mho, for the near-linear conductivity model (Eq. (5.8)) with slope  $S = 1.0 mho (\mu A m^{-2})^{-1}$  (solid lines), for constant conductivity  $\Sigma_p^*(j_{\parallel i} = 0) = 0.055 mho$  (dashed lines), and the near-rigid corotation approximation given by Eq. (4.4f) (dot-dashed lines). Also shown by the dotted lines is the outer region approximation calculated from Eqs. (5.10)-(5.13). The three solid lines represent boundary condition choices of  $j_{\parallel i}(100 R_J) = 0.10, 0.03$  and  $-0.04 \mu A m^{-2}$  as indicated, as in Fig. 5.6. The solutions in each case are tracked to  $13 R_J$ , inside which they are completed by the ‘first-iteration’ approximation discussed in Section 5.4.2. All parameters are plotted versus jovicentric equatorial radial distance  $\rho_e$ .

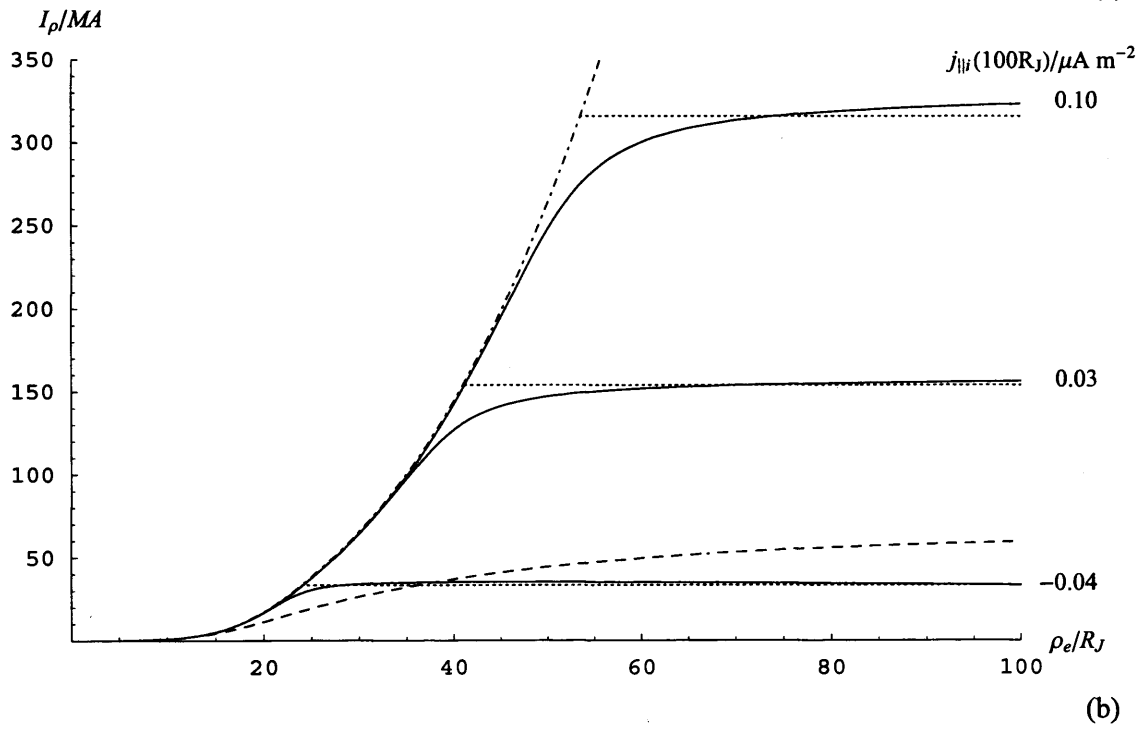
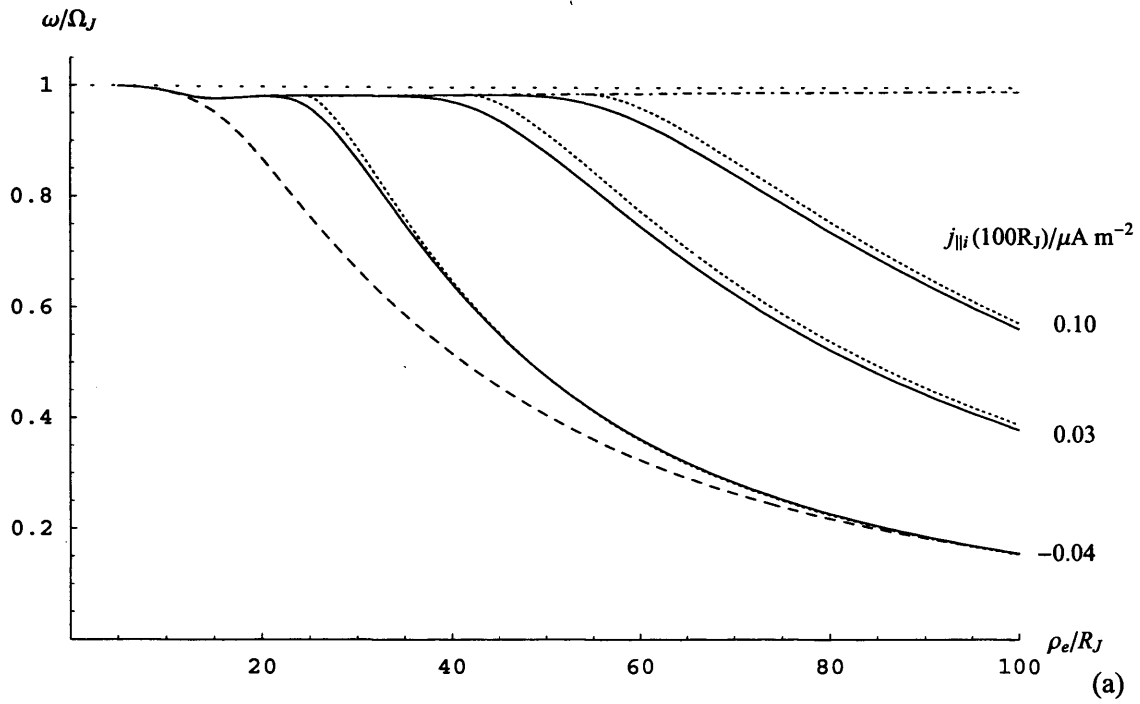
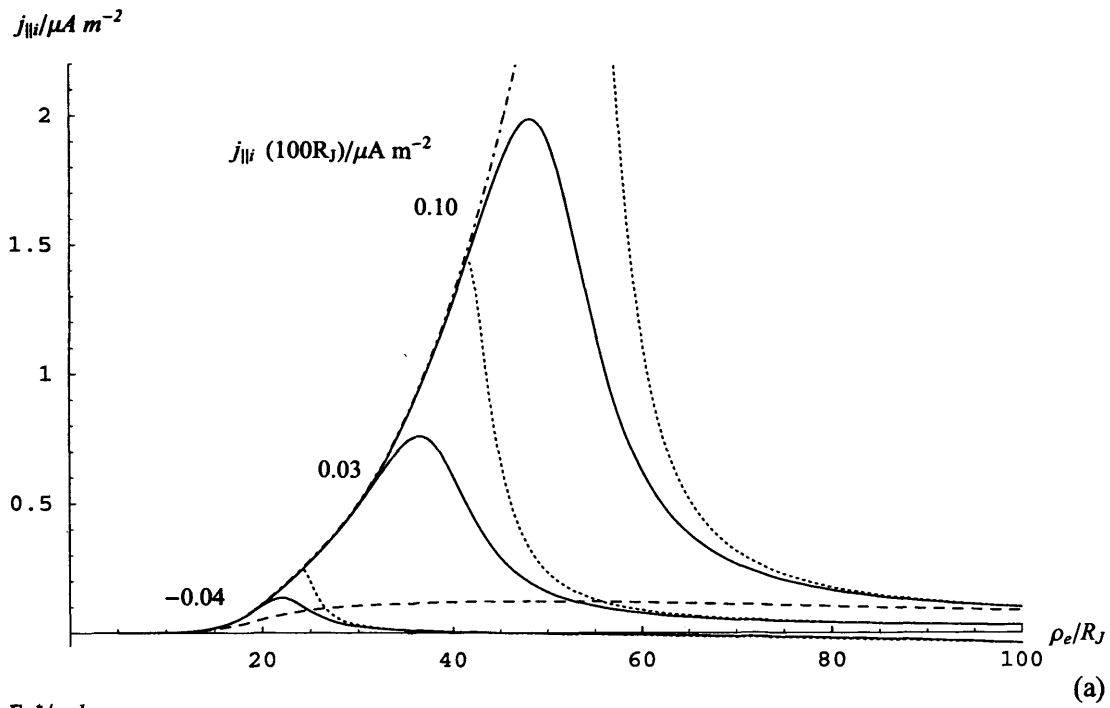
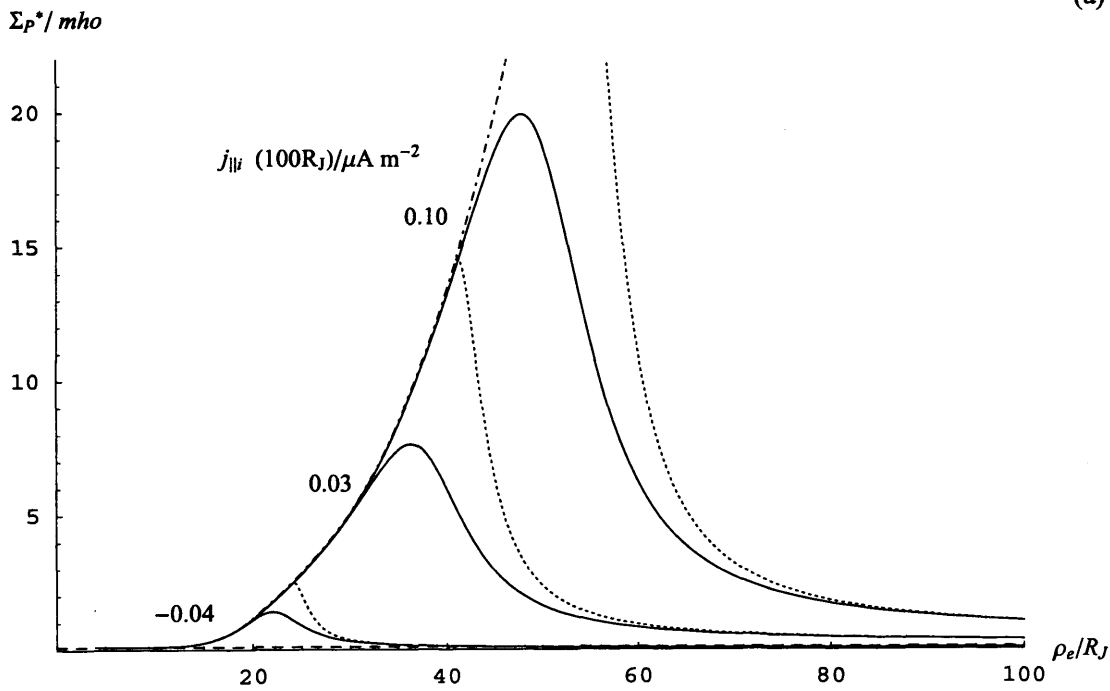


Figure 5.9. As for Fig. 5.7 but with  $S = 10 \text{ mho } (\mu\text{A m}^{-2})^{-1}$ .



(a)



(b)

Figure 5.10. As for Fig. 5.8 but with  $S = 10 \text{ mho } (\mu\text{A m}^{-2})^{-1}$ .

constant conductivity solution with  $\Sigma_p^* = \Sigma_p^*(j_{\parallel i} = 0)$  shown by the long-dashed line, and the near-rigid approximation Eq. (4.3), shown by the dot-dashed line. The field-perpendicular and field-parallel current components shown in Figs. 5.7b and 5.8a, and 5.9b and 5.10a correspondingly increase in accordance with Eqs. (4.4d) and (4.4f). However, as the parallel current increases in accordance with Eq. (4.4f), so does the ionospheric Pedersen conductivity in accordance with Eq. (5.8), such that when the increase in conductivity becomes comparable with or larger than  $\Sigma_p^*(j_{\parallel i} = 0)$ , the plasma angular velocity departs from the constant conductivity solution (long-dashed line), and falls less rapidly with distance, in accordance with Eq. (4.3) (dot-dashed line). The onset of this behaviour occurs at smaller radial distances for larger values of  $S$ , and hence at smaller departures of the angular velocity from rigid corotation, as can be seen by comparing Figs. 5.7a and 5.9a. Beyond this point, the increase of the conductivity with the parallel current given by Eq. (4.4f) is such that the angular velocity given by Eq. (4.3) (dot-dashed line) shows a shallow minimum, with  $(\omega/\Omega_J) \approx 0.85$  at  $\rho_e \approx 25 R_J$  for  $S = 1 \text{ mho } (\mu\text{A m}^{-2})^{-1}$  in Fig. 5.7a, and with  $(\omega/\Omega_J) \approx 0.97$  at  $\rho_e \approx 15 R_J$  for  $S = 10 \text{ mho } (\mu\text{A m}^{-2})^{-1}$  in Fig. 5.9a, before slowly increasing again at larger distances (the departure from rigid corotation decreasing as  $\sim \rho_e^{-(m-2)}$  in this regime, where  $m$  is the exponent of the KK field model in Eq. (5.1a)). Equations. (4.3), (4.4d), and (4.4f) thus imply that for  $S \geq 1 \text{ mho } (\mu\text{A m}^{-2})^{-1}$  the enhancement in the ionospheric conductivity can be such that near-rigid corotation conditions (given by Eq. (4.3)) can be maintained to large distances, and with it the growth of the current components according to Eq. (4.4d) and (4.4f). The numerical results (solid lines) show that this is indeed the case, the computed solutions for the angular velocity following the near-rigid corotation value given by Eq. (4.3) (approximately for  $S = 1 \text{ mho } (\mu\text{A m}^{-2})^{-1}$  in Fig. 5.7a, and very closely for  $S = 10 \text{ mho } (\mu\text{A m}^{-2})^{-1}$  in Fig. 5.9a) out to a certain radial distance determined by the outer boundary condition before falling to lower values at larger distances. The distance to which the near-rigid corotation approximation is followed increases with the chosen value of  $j_{\parallel i}$  (and hence  $\Sigma_p^*$ ) at the outer boundary at  $100 R_J$ , as can be seen in the figures. These results therefore confirm the conjecture of Cowley and Bunce (2001b) that precipitation-induced enhancements of the Pedersen conductivity can act to maintain the plasma angular

velocity closer to rigid corotation to much larger radial distances than anticipated on the basis of previously presented solutions using typical constant ‘background’ Pedersen conductivities of a few tenths of a mho.

The corresponding behaviour of the current components shown in Figs. 5.7b and 5.8a, and 5.9b and 5.10a is thus that in the inner region they follow the near-rigid corotation approximations given by Eqs. (4.4d) and (4.4f), increasing rapidly with increasing distance depending on  $\dot{M}$  and the equatorial magnetic model  $|B_{ze}|$ , over the radial range where the angular velocity remains close to the near-rigid corotation approximation Eq. (4.3). Beyond this distance, where the angular velocity falls away from this behaviour, the field-aligned current also falls away to smaller positive values, rapidly in the case of  $S = 10 \text{ mho } (\mu\text{A m}^{-2})^{-1}$  shown in Fig. 5.10a, to the value of the chosen boundary condition at  $\rho_e = 100 R_J$ . Correspondingly, the value of the Pedersen conductivity also falls with distance in the outer region, as seen in Figs. 5.8b and 5.10b, while the total current  $I_\rho$  shown in Figs. 5.7b and 5.9b tends towards a constant value. Overall it can be seen that in cases where the conductivity increases rapidly with the current density (i.e.  $S$  is large), the form of the current profiles differ significantly from those derived previously for constant conductivity. In the latter case the upward field-aligned current density tends to be broadly distributed over the middle magnetosphere current sheet outside of  $\sim 20 R_J$  for typical parameters (see, e.g., the solutions in Chapter 4), such that the total radial current  $I_\rho$  grows gradually with increasing distance. In the solutions found here for large  $S$ , however, the field-aligned current input to the current sheet is instead concentrated in the inner part of the region where the conductivity is also enhanced, and then falls to smaller but still positive values in the region beyond, the radial extent of the main upward field-aligned current region then depending on the outer boundary condition. The total radial current then grows with distance according to Eq. (4.4d) within the main region of field-aligned current in the inner region, while plateauing at almost constant values in the region beyond.

#### 5.4.4. Outer region approximations

Approximate solutions based on these results can then be developed for the outer region, using the governing equations given in Section (2). Specifically we replace Eq. (3.16) by

$$I_p = 8\pi\Sigma_p^* F_e \Omega_J \left(1 - \frac{\omega}{\Omega_J}\right) \approx \text{constant} \quad , \quad (5.10)$$

in which case the Hill-Pontius equation, in the form given by Eq. (3.26), can be integrated directly to give

$$\left(\frac{\omega}{\Omega_J}\right) \approx \left(\frac{\rho_e'}{\rho_e}\right)^2 \left(\frac{\omega}{\Omega_J}\right)' + \frac{I_p}{M\Omega_J\rho_e^2} \left(F_e(\rho_e') - F_e(\rho_e)\right) \quad , \quad (5.11)$$

where  $(\omega/\Omega_J)'$  is a known value of the angular velocity at some radial distance  $\rho_e'$ . We then assume that the angular velocity and current components follow the near-rigid corotation approximations given by Eqs. (4.3), (4.4d), and (4.4f) out to distance  $\rho_e'$ , then breaking away to the behaviour defined by Eqs. (5.10) and (5.11) at larger distances, such that  $j_{\parallel}$  and hence  $\Sigma_p^*$  reach the value specified at the outer boundary  $\rho_e = \rho_{eB}$  (100  $R_J$  in the results presented here). Thus, introducing Eq. (4.4d) into Eq. (5.10), the position  $\rho_e'$  where the break occurs is determined from the imposed boundary conditions by solving the equation

$$\frac{2\dot{M}\Omega_J}{\left|B_{ze}(\rho_e')\right|} = 8\pi\Sigma_p^*(\rho_{eB})F_e(\rho_{eB})\Omega_J \left(1 - \left(\frac{\omega}{\Omega_J}\right)_B\right) \quad , \quad (5.12)$$

where from Eq. (5.11)

$$\left(\frac{\omega}{\Omega_J}\right)_B \approx \left(\frac{\rho_e'}{\rho_{eB}}\right)^2 \left(\frac{\omega}{\Omega_J}\right)' + \frac{2}{\rho_{eB}^2 |B_{ze}(\rho_e')|} \left(F_e(\rho_e') - F_e(\rho_{eB})\right), \quad (5.13)$$

and  $(\omega/\Omega_J)'$  is determined from Eq. (4.3) evaluated at  $\rho_e'$ . With the value  $\rho_e'$  so determined, the approximate angular velocity profile is given by Eq. (5.11), the constant value of  $I_p$  by Eq. (4.4d) evaluated at  $\rho_e'$ , and the conductivity profile from Eq. (5.10). The parallel current is determined by inversion of the expressions for the conductivity model given by Eq. (5.8). These approximations are shown by the dotted curves in Figs. 5.7 to 5.10, and are seen to agree quite well with the numerical solutions, particularly with the results for  $S = 10 \text{ mho } (\mu\text{A m}^{-2})^{-1}$  shown in Figs. 5.9 and 5.10.

#### 5.4.5. Solution dependence on $\dot{M}$

The results shown above in Figs. 5.5 to 5.10 have all employed a fixed typical value of the iogenic plasma mass outflow rate  $\dot{M}$  of  $1000 \text{ kg s}^{-1}$ . Here we consider how the solutions depend on  $\dot{M}$  for a given conductivity model. In Figs. 5.11 and 5.12 we show results in our standard format for  $\dot{M} = 1000, 2000, \text{ and } 3000 \text{ kg s}^{-1}$  (our particular interest in larger values becoming clearer in Section 5.5), for  $S = 10 \text{ mho } (\mu\text{A m}^{-2})^{-1}$ , and for the fixed boundary condition that  $j_{\parallel i} = 0.03 \mu\text{A m}^{-2}$  at  $\rho_e = 100 R_J$ . In this case, however, three constant conductivity solutions are now shown in each plot for  $\Sigma_p^*(j_{\parallel i} = 0) = 0.1 \text{ mho}$ , corresponding to the three values of  $\dot{M}$  (dashed lines as marked), and also three curves for the near-rigid corotation approximations given by Eqs. (4.3), (4.4d) and (4.4f). However, for the case of the plasma angular velocity shown in Fig. 5.11a, although the departure of the angular velocity from rigid corotation is proportional to  $\dot{M}$  in the innermost region where  $\Sigma_{p0}^* > S j_{\parallel i}$  in Eq. (5.8), over most of the radial range, where the opposite inequality applies, the near-rigid corotation approximation depends only on the slope  $S$  and not on the mass outflow rate  $\dot{M}$ . That is, if we put  $\Sigma_p^* = S j_{\parallel i}$  over most of the range, as given by Eq. (5.8), then substituting for  $j_{\parallel i}$  from Eq. (4.4f) into Eq. (4.3) yields

$$\frac{\omega}{\Omega_J} \approx 1 - \frac{\rho_e |B_{ze}|^2}{4S\Omega_J B_J F_e \left| \frac{dB_{ze}}{d\rho_e} \right|}, \quad (5.14)$$

such that the departure from rigid corotation is inversely proportional to  $S$  (as can be seen in Figs. 5.7a and 5.9a), but is independent of  $\dot{M}$ . The angular velocity profiles in Fig. 5.11a thus follow essentially the same curves as each other in the inner region, before falling away from the near-rigid corotation approximation at larger distances. This latter distance decreases with increasing  $\dot{M}$  (for fixed boundary condition) as can be seen in Fig. 5.11a, such that the plasma angular velocity at the outer boundary falls with increasing  $\dot{M}$ . Similarly, the current components and conductivity grow more rapidly in the inner region in proportion to  $\dot{M}$ , as shown in Figs. 5.11b to 5.12b and as expected from Eqs. (4.4d) and (4.4f), while also falling away from this behaviour at smaller radial distances with increasing  $\dot{M}$ . The overall effect is that the main region of field-aligned current flow into the current sheet moves inwards as  $\dot{M}$  increases, for a given value of  $j_{\parallel i}$  at the outer boundary. The value at which the total radial current ‘plateaus’ in the outer region is also found to increase modestly with  $\dot{M}$  under these conditions, as can be seen in Fig. 5.11b.

#### 5.4.6. Results for a more realistic conductivity model

The final point we wish to discuss in this section concerns the effect of the behaviour of the ionospheric Pedersen conductivity with the field-aligned current, it being assumed in the above calculations via Eq. (5.8) that the current increases essentially linearly with the current for all positive values of the latter (Fig. 5.4). This potentially results in very large values of the conductivity being obtained, as can be seen, for example, in Figs. 5.10b and 5.12b. It may be noted in the results presented in Section 5.3, however, that near-linear behaviour of the conductivity may only prevail for sufficiently small values of the field-aligned current density, with the conductivity tending to plateau or possibly even fall in value for larger values of  $j_{\parallel i}$ . We now investigate the effect of such conductivity behaviour by modifying the  $S = 10 \text{ mho } (\mu\text{A m}^{-2})^{-1}$  model such that beyond a certain value of the field-

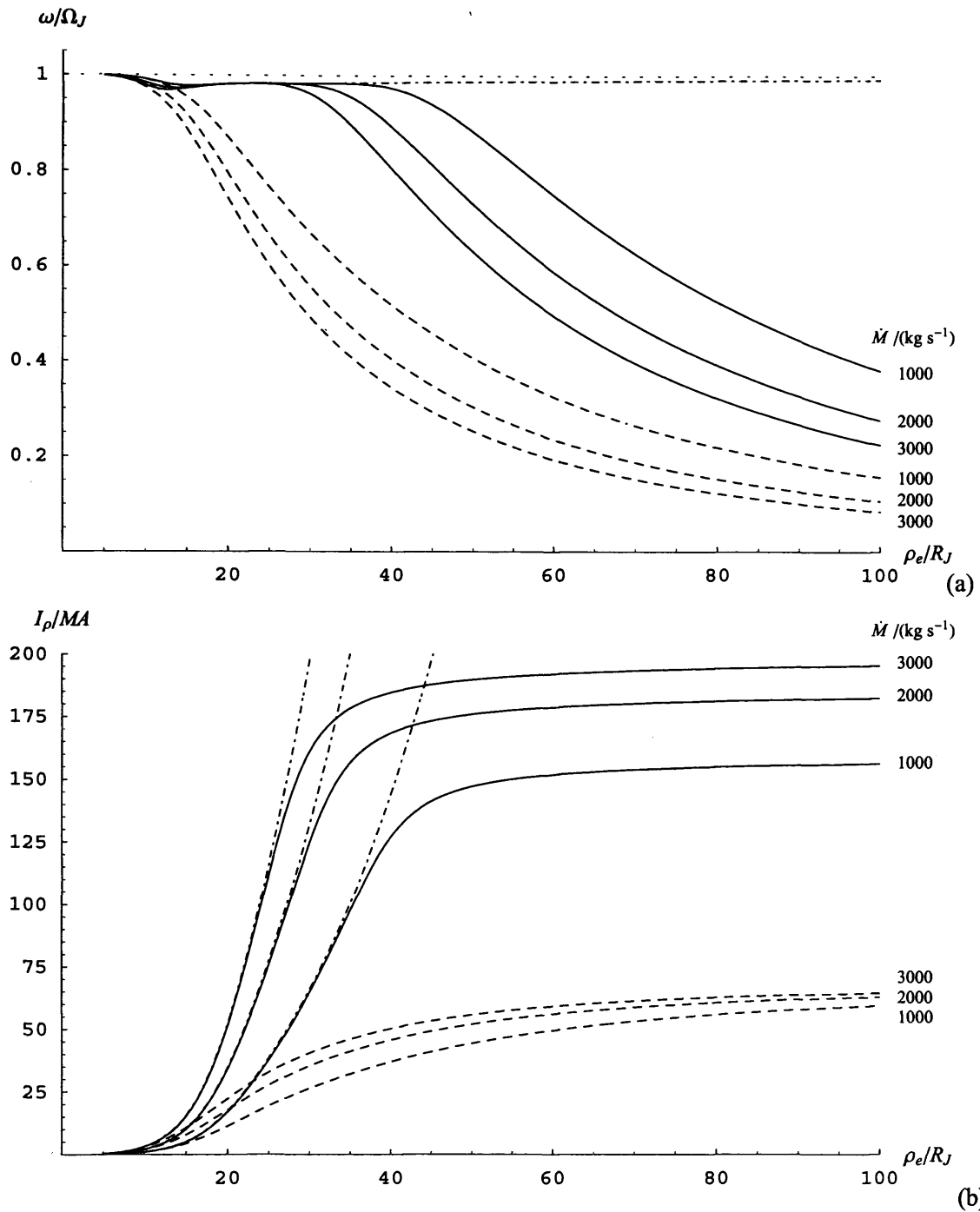


**Figure 5.11.** Plots of (a) the plasma angular velocity  $\omega$  normalised to the planet's angular velocity  $\Omega_J$ , and (b) the azimuth-integrated equatorial radial current  $I_\rho$  in MA for the near-linear conductivity model (Eq. (5.8)) with slope  $S = 10 \text{ mho } (\mu\text{A m}^{-2})^{-1}$  (solid lines), for a constant conductivity  $\Sigma_p^*(j_{\parallel} = 0) = 0.1 \text{ mho}$  (dashed lines), and the near-rigid corotation approximation given by Eqs. (4.3) and (4.4d) (dot-dashed lines) for three values of the iogenic plasma mass outflow rate  $\dot{M} = 1000, 2000$  and  $3000 \text{ kg s}^{-1}$  (as indicated). The solutions in each case are tracked to  $13 R_J$ , inside which they are completed by the near-rigid corotation approximation. All parameters are plotted versus joventric equatorial radial distance  $\rho_e$ .

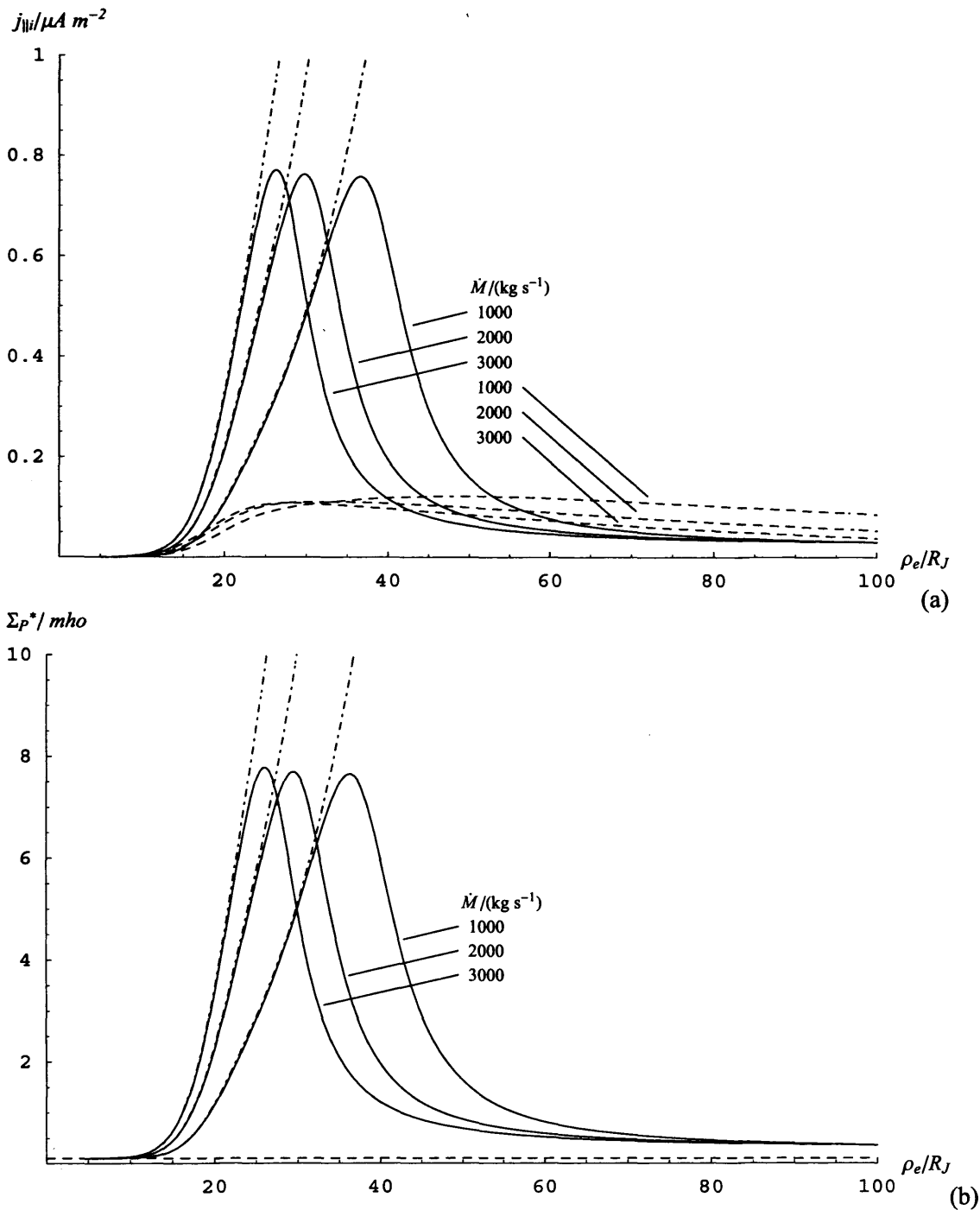


**Figure 5.12.** Plots of (a) the field-aligned current density at the feet of the field lines  $j_{\parallel}$  in  $\mu A m^{-2}$ , and (b) shows the effective height-integrated Pedersen conductivity  $\Sigma_p^*$  in mho for the near-linear conductivity model (Eq. (5.8)) with slope  $S = 10 \text{ mho } (\mu A m^{-2})^{-1}$  (solid lines), for a constant conductivity  $\Sigma_p^*(j_{\parallel} = 0) = 0.1 \text{ mho}$  (dashed lines), and the near-rigid corotation approximation given by Eq. (4.4f) (dot-dashed lines) for three values of the iogenic plasma mass outflow rate  $\dot{M} = 1000, 2000$  and  $3000 \text{ kg s}^{-1}$  (as indicated). The solutions in each case are tracked to  $13 R_J$ , inside which they are completed by the near-rigid corotation approximation. Both parameters are plotted versus jovicentric equatorial radial distance  $\rho_e$ .

aligned current density the conductivity increases much less rapidly than for small values of the current. Specifically, the model adopted is

$$\Sigma_P^*(j_{\parallel i}) = \Sigma_{P_0}^* + \frac{1}{2} \left\{ S_1 + \frac{S_2}{\left[ 1 + \left( \frac{j_{\parallel i}}{j_{\parallel i}^{**}} \right)^n \right]^{\frac{1}{n}}} \right\} \left( \sqrt{j_{\parallel i}^2 + j_{\parallel i}^{*2}} + j_{\parallel i} \right), \quad (5.15)$$

which is such that  $\Sigma_P^* \simeq \Sigma_{P_0}^*$  for  $j_{\parallel i}$  negative, varies as  $\Sigma_P^* \simeq \Sigma_{P_0}^* + (S_1 + S_2)j_{\parallel i}$  for positive  $j_{\parallel i}$  less than  $j_{\parallel i}^{**}$  and greater than  $j_{\parallel i}^*$ , and then as  $\Sigma_P^* \simeq (\Sigma_{P_0}^* + S_2 j_{\parallel i}^{**}) + S_1 j_{\parallel i}$  for  $j_{\parallel i}$  greater than  $j_{\parallel i}^{**}$ . Here we have taken  $\Sigma_{P_0}^* = 0.05$  mho and  $j_{\parallel i}^* = 0.01 \mu\text{A m}^{-2}$ , as before, together with  $S_1 = 0.1$  mho  $(\mu\text{A m}^{-2})^{-1}$ ,  $S_2 = 9.9$  mho  $(\mu\text{A m}^{-2})^{-1}$ ,  $j_{\parallel i}^{**} = 0.25 \mu\text{A m}^{-2}$  and  $n = 8$ . This function is shown in Fig. 13 (solid line), together with the  $S = 10$  mho  $(\mu\text{A m}^{-2})^{-1}$  model given by Eq. (5.8) (dashed line). It can be seen that the two models are essentially identical for small positive and all negative values of  $j_{\parallel i}$ , the conductivity increasing at the rate of  $\sim 10$  mho  $(\mu\text{A m}^{-2})^{-1}$  for positive  $j_{\parallel i}$  less than  $j_{\parallel i}^{**} = 0.25 \mu\text{A m}^{-2}$ . Above this value of the current, however, the conductivity curve rapidly flattens to increase at the much reduced rate of  $0.1$  mho  $(\mu\text{A m}^{-2})^{-1}$ .

Results using this conductivity model are shown in Figs. 5.14 and 5.15 in the same format as Figs. 5.5 to 5.12. Here we compare the solution obtained with the above model with that obtained with the  $S = 10$  mho  $(\mu\text{A m}^{-2})^{-1}$  model of Eq. (5.8), for the same value of  $\dot{M} = 1000 \text{ kg s}^{-1}$ , and with the same boundary condition  $j_{\parallel i} = 0.03 \mu\text{A m}^{-2}$  at  $\rho_e = 100 R_J$ . We note that the dashed line showing the constant conductivity solution for  $\Sigma_P^* = \Sigma_P^*(j_{\parallel i} = 0) = 0.1$  mho is the same for both models. The current profiles of the near-rigid corotation approximations Eqs. (4.4d) and (4.4f), shown by the dot-dashed lines, are also the same for the two calculations, being dependent only on  $\dot{M}$  and the equatorial magnetic field model. However, the angular velocity profiles in the latter approximation given by Eq. (4.3) are in general different, being dependent on the conductivity model. As can be seen in Fig. 5.14a, the two profiles are very similar to each other in the inner region

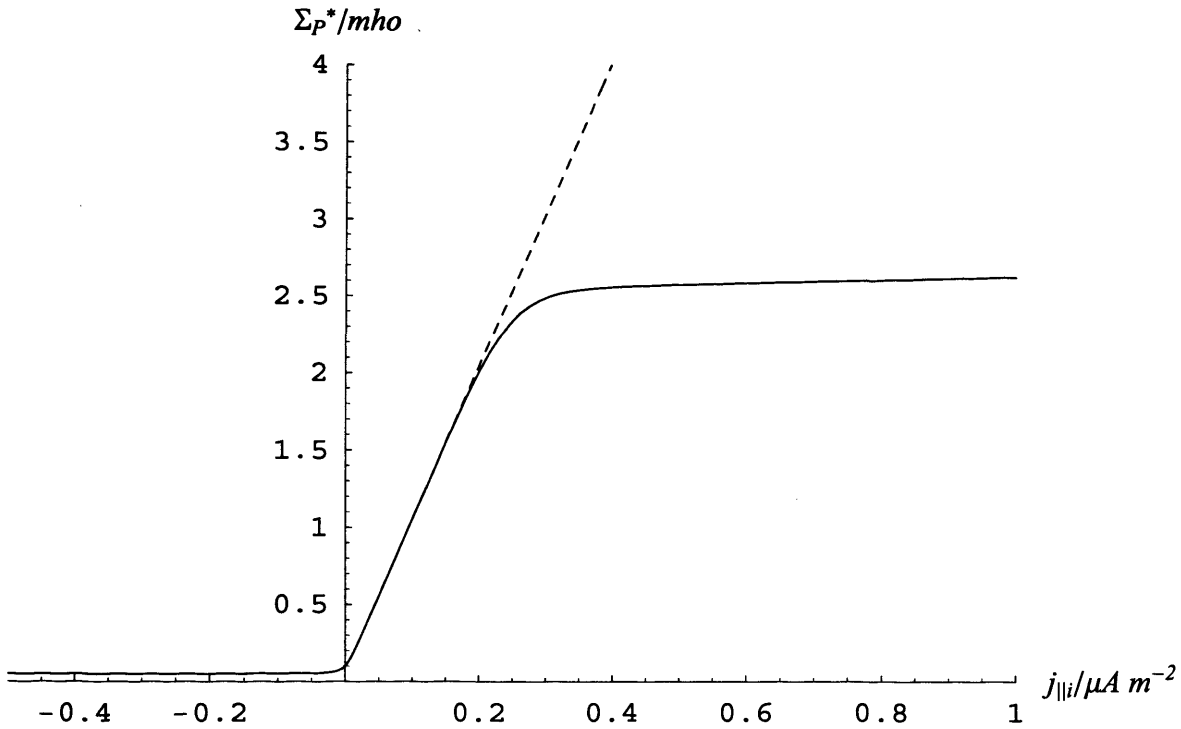


**Figure 5.13.** Plot of the effective height integrated Pedersen conductivity  $\Sigma_p^*$  in mho versus ionospheric field-aligned current density  $j_{\parallel i}$  ( $\mu A m^{-2}$ ) using the revised conductivity model given by Eq. (5.15) (solid line). This is compared with the near-linear conductivity model given by Eq. (5.8) with slope  $S = 10$  mho ( $\mu A m^{-2}$ )<sup>-1</sup> (dashed line).

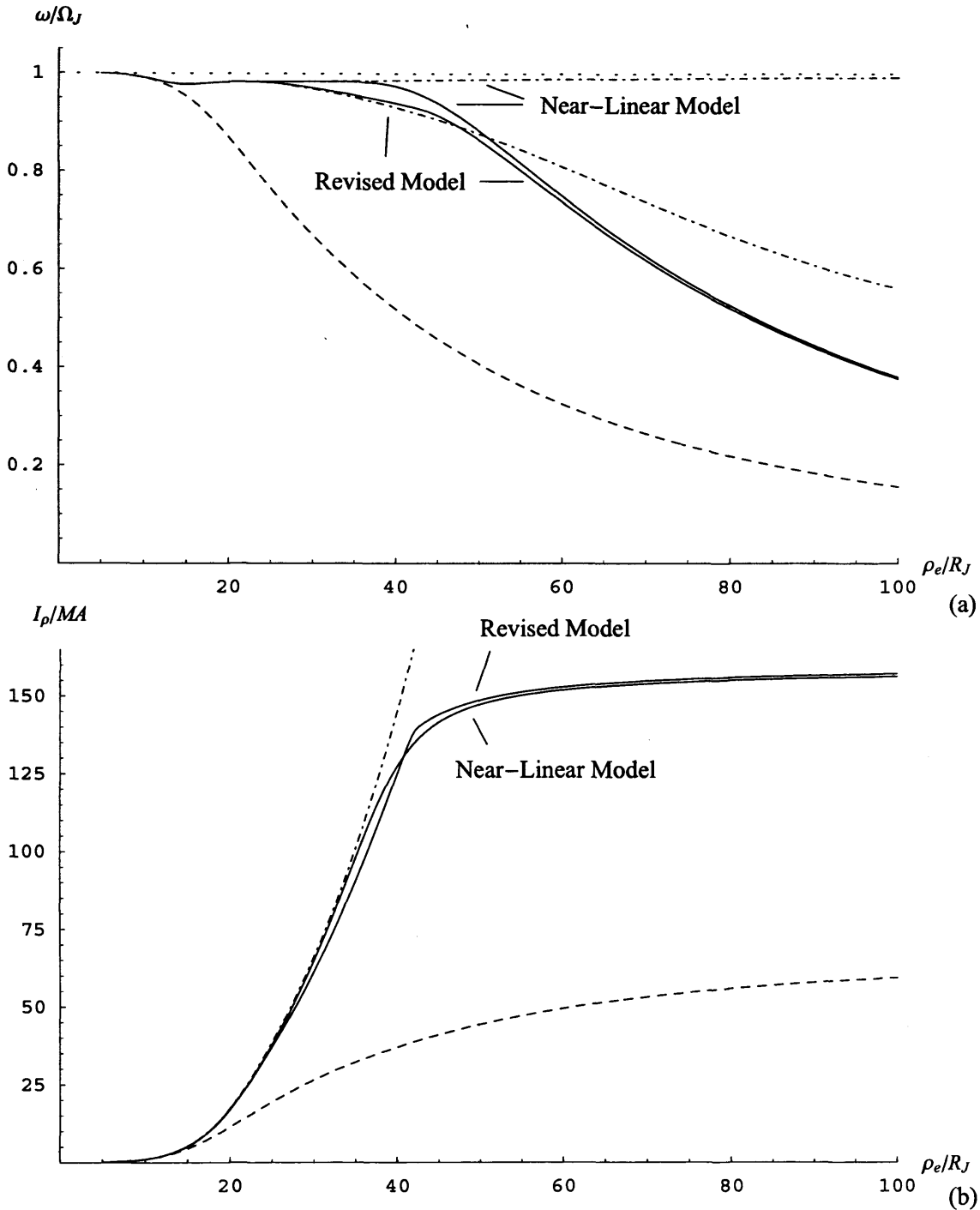


**Figure 5.14.** Plots of (a) the plasma angular velocity  $\omega$  normalised to the planet's angular velocity, and (b) the azimuth-integrated equatorial radial current  $I_\rho$  in MA for the near-linear conductivity model (Eq. (5.8)) with slope  $S = 10 \text{ mho } (\mu\text{A m}^{-2})^{-1}$ , and the revised conductivity model (Eq. (5.15)) (solid lines as labelled), for constant conductivity  $\Sigma_P^*(j_{\parallel i} = 0) = 0.1 \text{ mho}$  (dashed lines) and for the near-rigid corotation approximations given by Eqs. (4.3) and (4.4d) (dot-dashed lines). The solutions are tracked to  $13 R_J$  and  $21 R_J$  for the near-linear and revised models respectively, inside which they are completed by the near-rigid approximation. Both parameters are plotted versus jovicentric equatorial radial distance  $\rho_e$ .

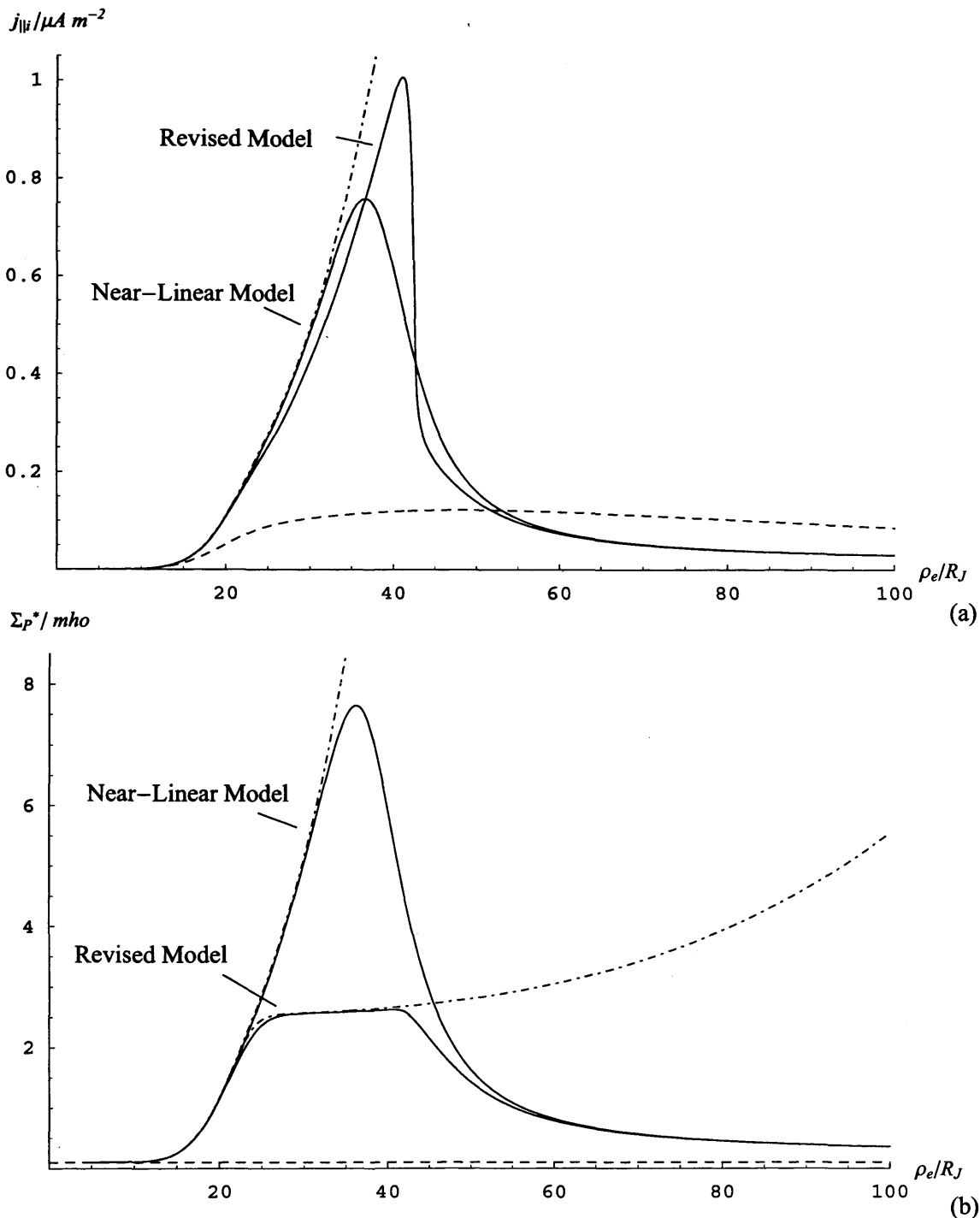


**Figure 5.15.** Plots of (a) the field-aligned current density at the feet of the field lines  $j_{||}$  in  $\mu A m^{-2}$ , and (b) the effective height-integrated Pedersen conductivity  $\Sigma_p^*$  in mho for the near-linear conductivity model (Eq. (5.8)) with slope  $S = 10 \text{ mho} (\mu A m^{-2})^{-1}$ , and the revised conductivity model (Eq. (5.15)) (solid lines as labelled), for constant conductivity  $\Sigma_p^*(j_{||} = 0) = 0.1 \text{ mho}$  (dashed lines) and for the near-rigid corotation approximation given by Eqs. (4.4f) (dot-dashed lines). The solutions are tracked to  $13 R_J$  and  $21 R_J$  for the near-linear and revised models respectively, inside which they are completed by the near-rigid approximation. Both parameters are plotted versus jovicentric equatorial radial distance  $\rho_e$ .

where the field-aligned current given by Eq. (4.4f) lies below  $j_{\parallel}^{**} = \sim 0.25 \mu\text{A m}^{-2}$ , such that the model  $\Sigma_p^*$  values are closely similar to each other. However, the field-aligned current approximation exceeds this value at and beyond  $\rho_e \sim 25 R_J$ , such that in the revised model the conductivities then fall significantly below those given by the near-linear model with  $S = 10 \text{ mho } (\mu\text{A m}^{-2})^{-1}$  (Fig. 5.13), and with it, the departure of the plasma from rigid corotation given by Eq. (4.3) also significantly increases. It can be seen in Fig. 5.14a that in the inner region the numerically integrated angular velocity profiles follow their respective approximations, closely in the case of the  $S = 10 \text{ mho } (\mu\text{A m}^{-2})^{-1}$  near-linear model out to  $\sim 40 R_J$ , and approximately in the case of the revised conductivity model given by Eq. (5.15) out to  $50 R_J$ , before falling more rapidly in the outer region to values which are quite similar at the outer boundary. The current profiles shown in Figs. 5.14b and 5.15a are also similar to each other. The parallel current for the revised conductivity model in Fig. 5.15a lies modestly below that of the  $S = 10 \text{ mho } (\mu\text{A m}^{-2})^{-1}$  model beyond  $\sim 20 R_J$ , while peaking at a larger value at a larger distance, before falling precipitately to small values beyond  $\sim 40 R_J$ . The total radial current profiles shown in Fig. 5.14b behave in a corresponding manner, with closely similar values being achieved at the outer boundary at  $\rho_e = 100 R_J$ . Turning now to the conductivity profile shown in Fig. 5.15b, it can be seen that the effect of the revised conductivity model is to truncate the increase in conductivity in the central regions to reach a peak of only  $\sim 3 \text{ mho}$ , compared with  $\sim 7.5 \text{ mho}$  for the near-linear model. Nevertheless, the elevation of the conductivity in the revised model is still sufficient to maintain the plasma angular velocity and the current components close to the values given by the near-rigid corotation approximation out to significant distances. The main distinction between the two models is that the angular velocity is more significantly depressed from rigid corotation in the revised model, such as to maintain similar values of the currents.

### ***5.5. Solutions appropriate to jovian conditions***

In this section we examine solutions for the angular velocity and current components which are appropriate to conditions in the jovian magnetosphere, and consider how well they fit to

available observations. Specifically, we derive solutions based on the empirical conductivity model given by Eq. (5.6), shown by the dashed line in Fig. 5.3, and we also choose boundary conditions that yield solutions appropriate to the jovian system.

### 5.5.1. *Observed radial current profile*

The jovian observations to which we refer are the radial profiles of the radial equatorial current  $i_\rho$  derived from Galileo magnetometer data by Khurana (2001). As discussed in the introduction, the radial current is associated with bending of the magnetic field lines out of meridian planes, and hence with the appearance of a  $B_\phi$  field which reverses in sense about the centre of the equatorial current sheet, as shown in Fig. 3.1. Applying Ampère's law to an azimuthally aligned loop passing through the current sheet and closing in the region outside we find

$$i_\rho = \mp \frac{2\Delta B_\phi}{\mu_0}, \quad (5.16)$$

where  $\Delta B_\phi$  is the azimuthal field outside the current sheet (the planetary azimuthal field is negligible at middle magnetosphere distances). The upper sign applies to observations north of the current sheet, while the lower sign applies to observations south of the sheet, and we assume north-south symmetry of the field line bending. In Fig. 5.16b we show the radial profile of the radial current derived from Galileo data, kindly provided at increased  $5 R_J$  radial resolution by K.K. Khurana (personal communication, 2002). This has been derived using Eq. (5.16) from magnetic data outside the current sheet, within a 3 hour local time sector centred on midnight. Data from this sector have been chosen since it is less likely to contain systematic contributions from other effects that produce magnetospheric  $B_\phi$ , such as field line bending associated with the day-night asymmetry of the magnetospheric cavity due to the dynamic pressure of the solar wind. The resulting values of  $i_\rho$  derived from Eq. (5.16) have then been multiplied by  $2\pi\rho_e$  in order to represent the total radial current integrated in azimuth, as seems appropriate as a first approximation (see also Khurana (2001)). It can be seen that the total radial current inferred from these data

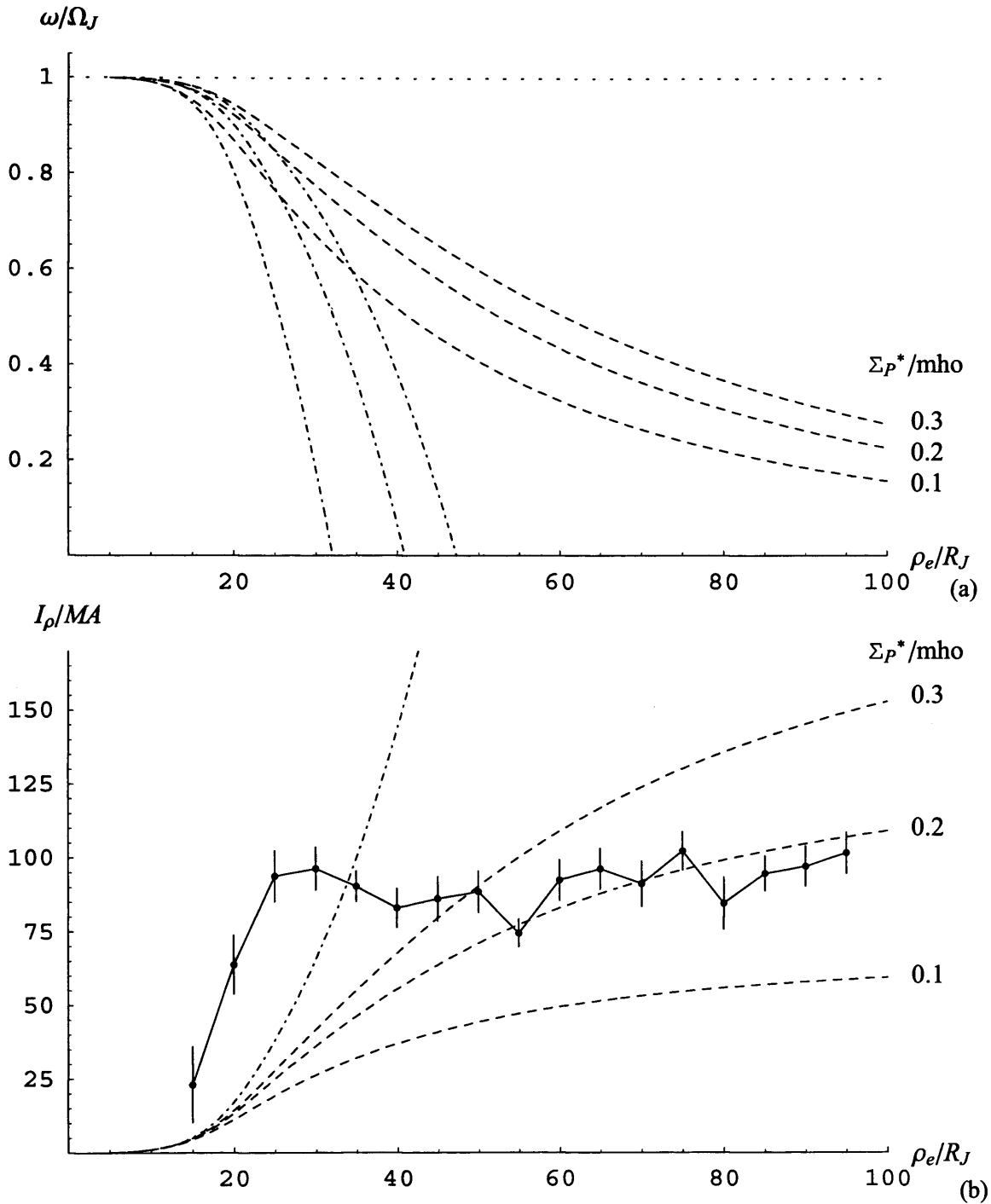


**Figure 5.16.** Plots of (a) the plasma angular velocity  $\omega$  normalised to the planet's angular velocity  $\Omega_J$ , and (b) the azimuth-integrated equatorial radial current  $I_\rho$  in MA using  $\dot{M} = 1000 \text{ kg s}^{-1}$  and constant effective height-integrated Pedersen conductivities of 0.1, 0.2 and 0.3 mho (dashed lines as labelled), together with the near-rigid corotation approximations given by Eqs. (4.3) and (4.4d) (dot-dashed lines). Both parameters are plotted versus jovicentric equatorial radial distance  $\rho_e$ . In plot (b) the theoretical curves are compared with the radial profile of the radial current derived from Galileo data in the midnight sector, as described in the text.

increases rapidly in the inner region, between  $\sim 15$  and  $25 R_J$ , before plateauing at a value of  $\sim 100$  MA at distances beyond, out to  $\sim 100 R_J$ . As noted previously by Khurana (2001), these results imply that the upward-directed field-aligned currents which feed the current sheet are concentrated in the inner region, centred near  $\sim 20 R_J$ , with the upward field-aligned current density in the ionosphere derived from the slope of the curve in this region being typically  $\sim 0.2 - 0.3 \mu\text{A m}^{-2}$ .

### 5.5.2. Comparison with constant conductivity model results

The dashed lines in Fig. 5.16b show solution curves for  $I_\rho$  derived for the typical value of  $\dot{M} = 1000 \text{ kg s}^{-1}$  and various constant values of the effective Pedersen conductivity, 0.1, 0.2 and 0.3 mho, as marked, in the range used in previously published studies. These are plotted together with the limiting value of the current given by Eq. (4.4d), shown by the dot-dashed line. Other parameters of these solutions are also shown, specifically  $(\omega/\Omega_J)$  in Fig. 5.16a and  $j_{\parallel}$  in Fig. 5.17. It can be seen that although these constant conductivity solutions produce  $I_\rho$  profiles which are comparable to that derived from the Galileo data in certain regions, they do not provide a good overall fit, for any reasonable values of the system parameters  $\Sigma_p^*$  and  $\dot{M}$ . The ‘best fit’ solutions (e.g. that for  $\dot{M} = 1000 \text{ kg s}^{-1}$  and  $\Sigma_p^* = 0.2$  to  $0.3$  mho in Fig. 5.16b) tend to rise too gradually in the inner region and to overshoot at larger distances, associated with the broadly-distributed profile of the upward field-aligned current shown in Fig. 5.17.

In Figs. 5.18-5.20 we also show for future reference the plasma angular velocity and current components for these constant conductivity solutions mapped along field lines into the ionosphere, using Eqs. (3.2) and (3.3). In this format the plots extend from a co-latitude of  $\sim 15.7^\circ$ , mapping to  $100 R_J$  in the equatorial plane, to  $19^\circ$ , mapping to  $\sim 12.1 R_J$ . In Fig. 5.18a we show the angular velocity profiles (dashed), together with the approximate forms (dot-dashed), while in Figs. 5.18b and 5.19a we show the total height-integrated Pedersen current integrated in azimuth, equal to half the conjugate equatorial current  $I_\rho$ , together with the similarly halved Galileo data, and the field-aligned current density,

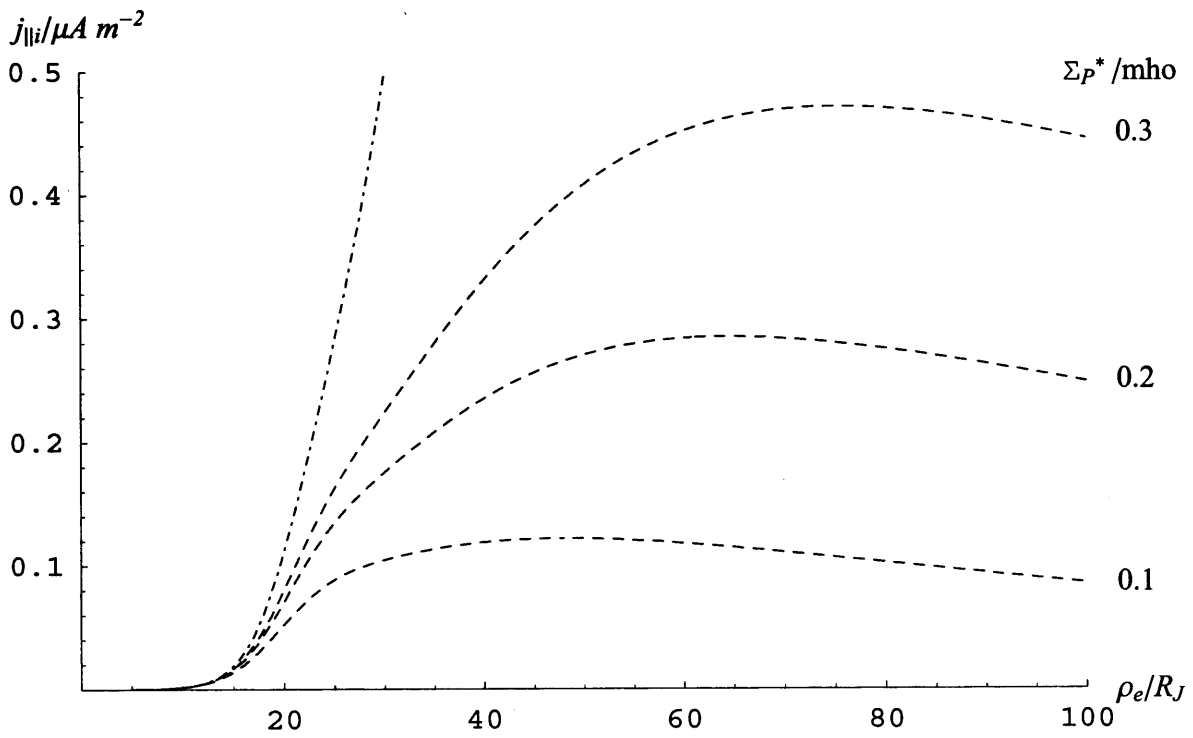
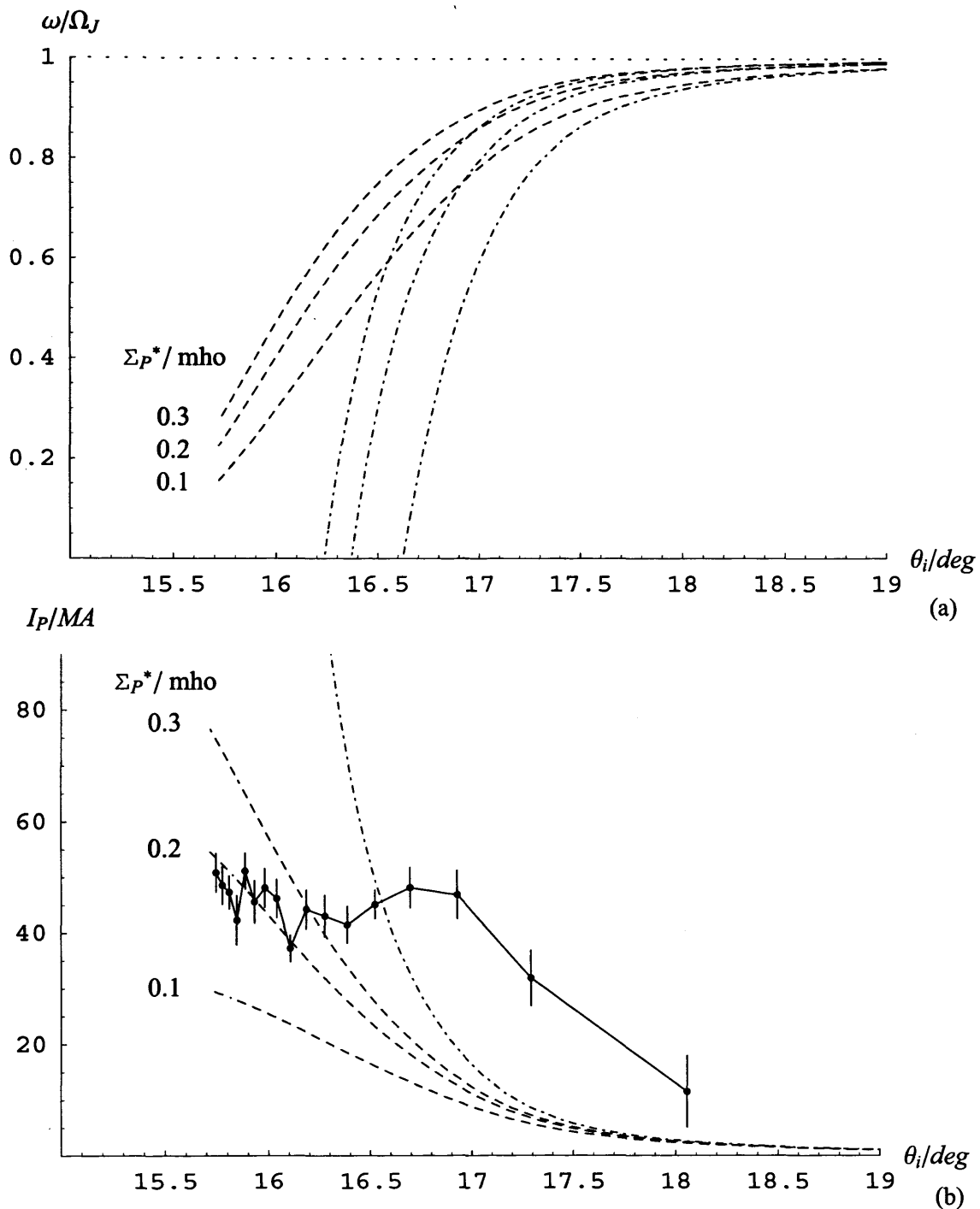
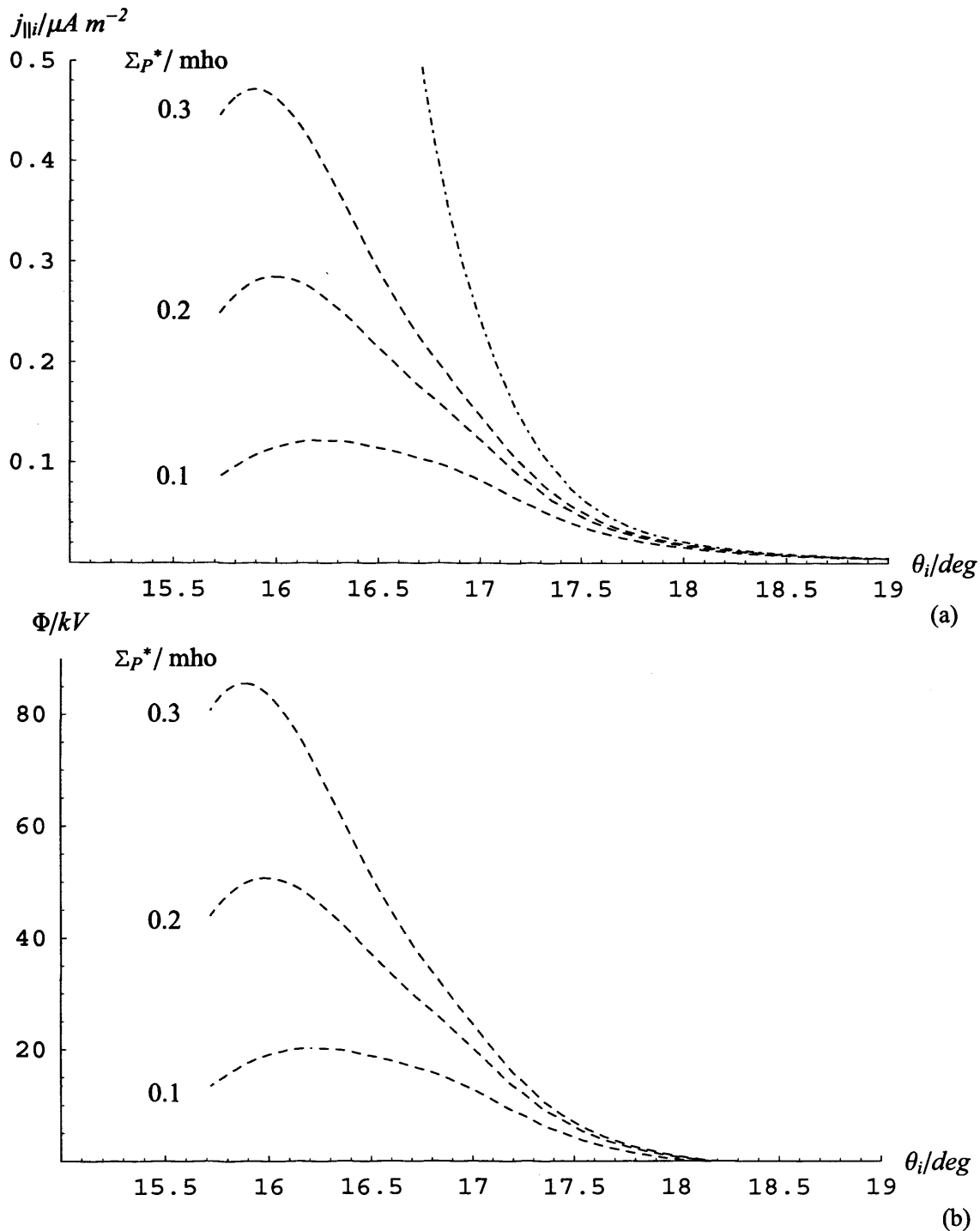


Figure 5.17. As for Fig. 5.16, but showing the field-aligned current density at the feet of the field lines  $j_{\parallel i}$  in  $\mu A m^{-2}$ .



**Figure 5.18.** Plots of (a) the plasma angular velocity  $\omega$  normalised to the planet's angular velocity  $\Omega_J$ , and (b) the azimuth-integrated equatorial radial current  $I_p$  in MA for constant conductivity along with the Galileo data shown previously in Fig. 5.16, but now projected along current sheet model magnetic field lines into the jovian ionosphere and plotted versus dipole co-latitude  $\theta_i$ , using Eq. (3.6). In panel (b) the equatorial radial current  $I_p$  has also been divided by a factor of two to show the azimuth-integrated Pedersen current flowing in one ionosphere,  $I_P$ .



**Figure 5.19.** Plots of (a) the field-aligned current density at the feet of the field lines  $j_{\parallel i}$  in  $\mu A m^{-2}$  as shown previously in Fig. 5.17, but now projected along current sheet model magnetic field lines into the jovian ionosphere and plotted versus dipole co-latitude  $\theta_i$ , using Eq. (3.6), and (b) the minimum accelerating voltage  $\Phi$  in kV required to drive the field-aligned current obtained from the exact form of Eq. (3.20), also plotted versus dipole co-latitude  $\theta_i$ .

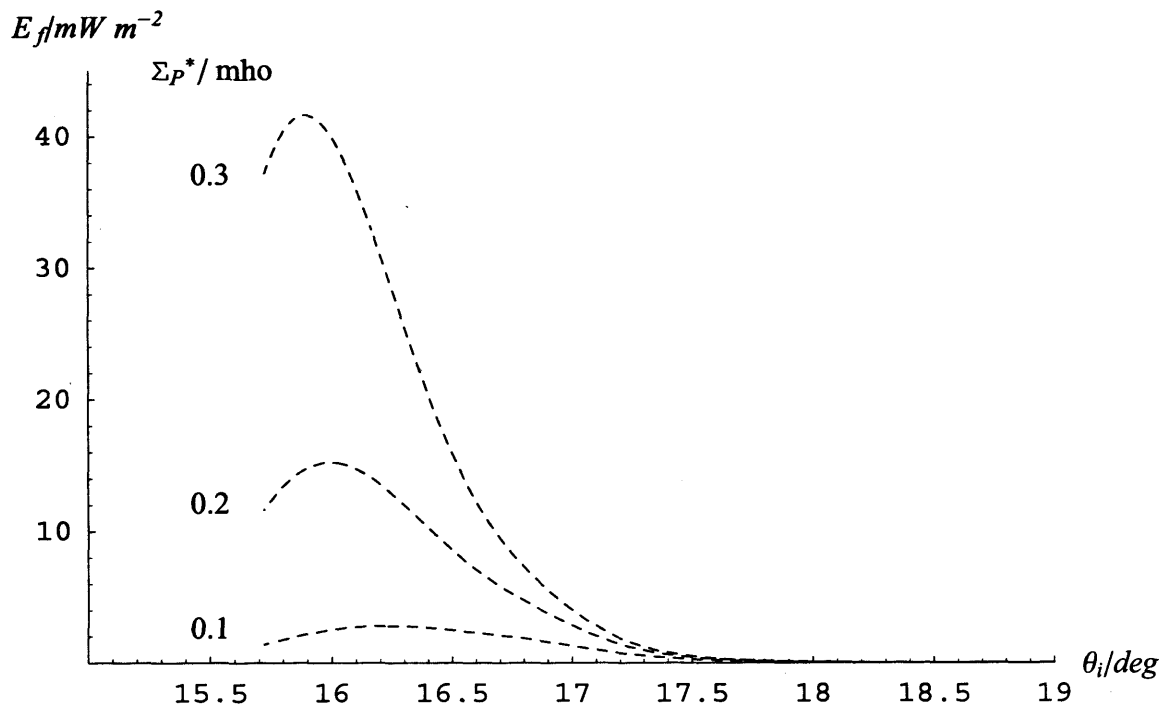


**Figure 5.20.** Plot of the precipitating energy flux as a consequence of the field-aligned current shown in Fig. 5.19a,  $E_f$  in  $\text{mW m}^{-2}$ , obtained from the exact form of Eq. (3.23), plotted versus dipole co-latitude  $\theta_i$ .

respectively, in a similar format. These theoretical plots are entirely representative of previously-published results, showing, for example, the field-aligned current density peaking at a few tenths of a  $\mu\text{A m}^{-2}$  near the poleward boundary of the ionospheric region mapping to the middle magnetosphere, and falling to small values over a latitudinal scale of  $\sim 1.5^\circ$  FWHM (i.e.  $\sim 2000$  km) in the ionosphere. In Figs. 5.19b and 5.20 we also show estimates of the auroral accelerating voltage and the precipitating auroral electron energy flux, derived from Eqs. (3.20) and (3.23) (using the full formulae rather than the approximate forms), with magnetospheric electron parameters  $N = 0.01 \text{ cm}^{-3}$  and  $W_{ih} \approx 2.5 \text{ keV}$ , as employed in previous chapters and in Section 5.3 of this chapter. These show that accelerating voltages of several tens of kV are anticipated, together with precipitating energy fluxes of a few tens of  $\text{mW m}^{-2}$ , in line with previous results (e.g. Cowley and Bunce, 2001b; Cowley, Nichols and Bunce, 2002; and Cowley, Bunce and Nichols, 2003). We recall that at  $\sim 20\%$  conversion efficiency, an energy flux of  $10 \text{ mW m}^{-2}$  corresponds to a UV luminosity of  $\sim 100 \text{ kR}$ , such that typical luminosities are expected to be of this order, as observed.

### 5.5.3. *Empirical conductivity model*

We now turn to the results for varying conductivity, and first discuss the conductivity model to be employed. As indicated above, this is based on the empirical form Eq. (5.6) derived in Section 5.3 above from the modelling results presented by Millward et al. (2002). However, the quantity estimated above is the true height-integrated Pedersen conductivity  $\Sigma_P$ , while the value required here is the ‘effective’ value  $\Sigma_P^*$ , equal to  $(1-k)\Sigma_P$ , reduced from the true value by atmospheric ‘slippage’ discussed in Section 3.3.2 above. The appropriate value of  $k$  is not conclusively known at the present time, but recent modelling results (G.H. Millward, personal communication, 2003) indicate that  $k \approx 0.5$  under circumstances appropriate to those discussed in this chapter. Here we will therefore adopt this value, such that we will take the factor  $(1-k) = 0.5$  in Eq. (3.11). Noting that the empirical form Eq. (5.6) goes to zero for  $j_{\parallel} = 0$ , we will also add a small constant conductivity  $\Sigma_{P_0}^*$ . As found in Section 5.4, the value of  $\Sigma_{P_0}^*$  governs the nature of the

angular velocity profile at small distances where  $j_{\parallel i}$  becomes small. This value of  $\Sigma_{p_0}^*$  has thus been determined from the results presented by Hill (1980), who examined Voyager-1 angular velocity data in the inner region (from  $\sim 12 R_J$  to  $\sim 20 R_J$ ) and compared the data with constant conductivity solutions for a dipole field model (which is reasonably realistic in the inner region). The theoretical angular velocity profiles depend on the quotient  $\Sigma_p^*/\dot{M}$ , the results obtained by Hill (1980) indicating that  $\Sigma_p^*/\dot{M} \approx 2.75 \times 10^{-5}$  mho ( $\text{kg s}^{-1}$ ). Although it is not a major point of our study, we have therefore employed here  $\Sigma_{p_0}^* = 0.0275 \times \dot{M} (1000 \text{ kg s}^{-1})$  mho, such that the calculated angular velocity profile perforce asymptotes to the form determined by Hill (1980) in the inner region (and by which we do not wish to imply that the ‘background’ ionospheric conductivity is somehow physically determined by the mass outflow rate from Io). In summary, therefore, here we employ the following empirical conductivity model

$$\Sigma_p^* = 0.0275\dot{M} + 0.08j_{\parallel i} + 1.225 \left[ \frac{(j_{\parallel i}/0.075)^2}{1 + (j_{\parallel i}/0.075)^2} \right] \frac{1}{1 + \exp[-(j_{\parallel i} - 0.22)/0.12]}, \quad (5.17)$$

where  $\dot{M}$  is in units of  $1000 \text{ kg s}^{-1}$ , and  $j_{\parallel i}$  is in  $\mu\text{A m}^{-2}$ . In Fig. 5.21 we show  $\Sigma_p^*$  versus  $j_{\parallel i}$  for  $\dot{M} = 1000, 2000$  and  $3000 \text{ kg s}^{-1}$ , as employed below.

#### 5.5.4. *Results using the empirical conductivity model*

Results using the empirical conductivity model given by Eq. (5.17) are shown in our ‘standard’ format in Figs. 5.22 and 5.23. The solid lines show three numerically computed solutions for  $\dot{M} = 1000, 2000$  and  $3000 \text{ kg s}^{-1}$ , each employing differing values of  $j_{\parallel i}$  at the boundary at  $\rho_e = 100 R_J$ , such that the total current  $I_p$  at  $100 R_J$  is equal to  $100 \text{ MA}$ , in approximate agreement with the values obtained at large distance from the Galileo data. The values of  $j_{\parallel i} (100 R_J)$  employed are  $\sim 0.264, \sim 0.171$  and  $\sim 0.133 \mu\text{A m}^{-2}$  for  $\dot{M} = 1000, 2000$  and  $3000 \text{ kg s}^{-1}$  respectively. The dot-dashed lines show the corresponding ‘near-rigid’ corotation approximations given by Eqs. (4.3), (4.4d) and (4.4f), while the dashed

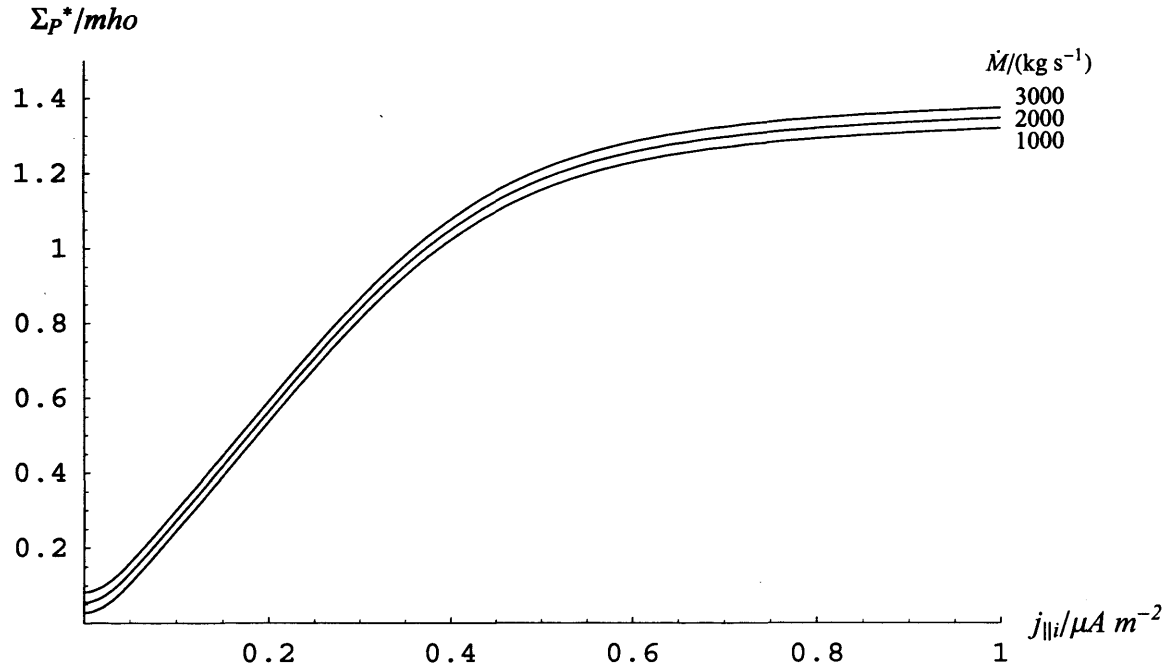


**Figure 5.21.** Plot of the effective height integrated Pedersen conductivity  $\Sigma_P^*$  in mho versus ionospheric field-aligned current density  $j_{||i}$  ( $\mu\text{A m}^{-2}$ ) using the empirical conductivity model given by Eq. (5.17).

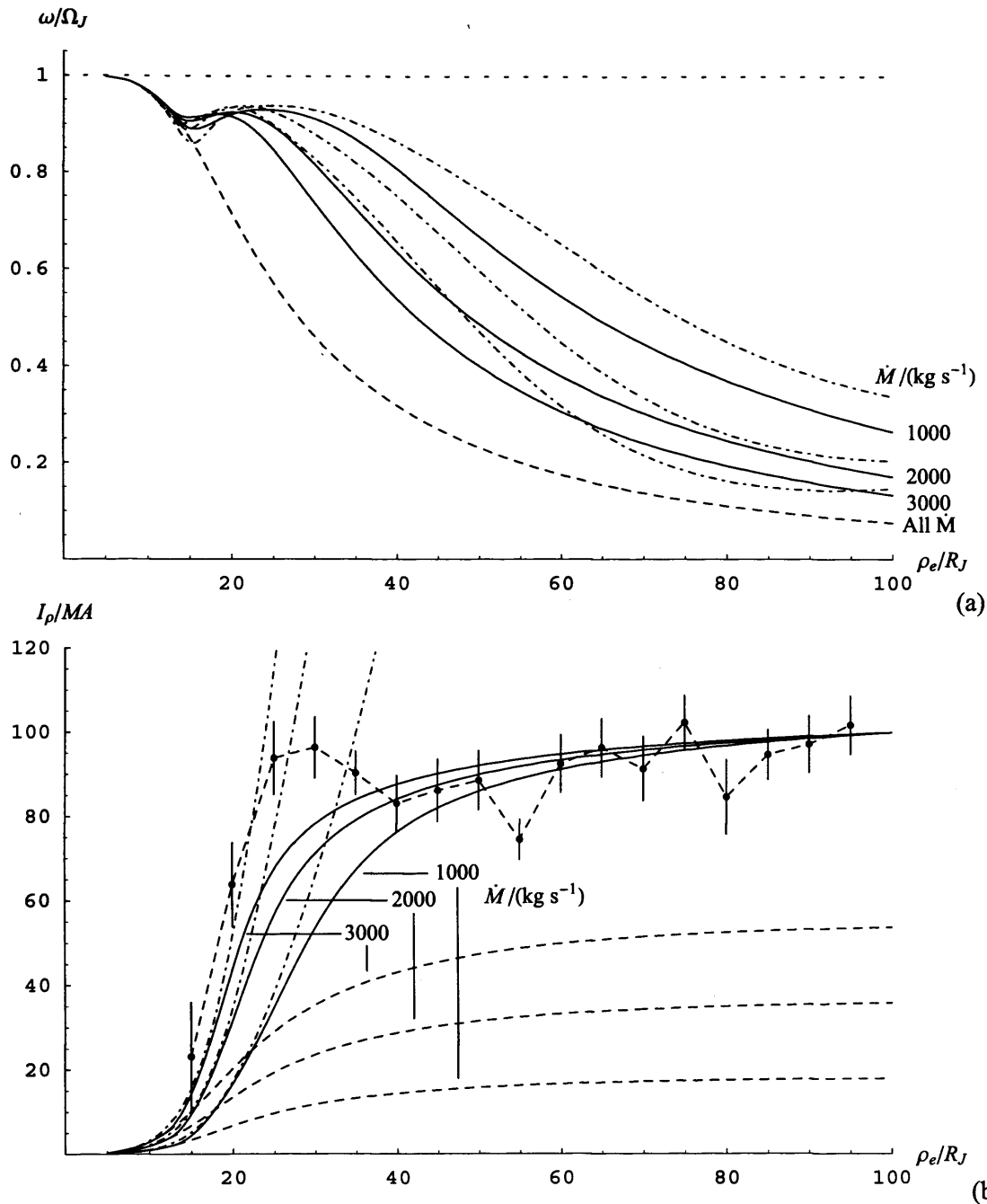


**Figure 5.22.** Plots of (a) the plasma angular velocity  $\omega$  normalised to the planet's angular velocity  $\Omega_J$ , and (b) the azimuth-integrated equatorial radial current  $I_\rho$  in MA obtained using the empirical conductivity model (Eq. (5.17)) (solid lines), constant conductivity  $\Sigma_P^* = \Sigma_P^*(j_{||} = 0)$  (dashed lines), and the near-rigid corotation approximations given by Eqs. (4.3) and (4.4d) (dot-dashed lines), for three values of the iogenic plasma mass outflow rate  $\dot{M} = 1000, 2000$  and  $3000 \text{ kg s}^{-1}$  (as indicated). The empirical conductivity model solutions have the boundary condition on  $j_{||}$  set such that the value of the azimuth-integrated equatorial radial current in each case is equal to 100 MA at  $100R_J$ . The solutions are tracked numerically to  $12 R_J$ , inside which they are completed by the 'first-iteration' approximation of Section 5.4.2. Both parameters are plotted versus jovicentric equatorial radial distance  $\rho_e$ . In plot (b) the theoretical curves are shown together with the radial profile of the radial current derived from Galileo  $B_\phi$  data provided by K.K. Khurana.

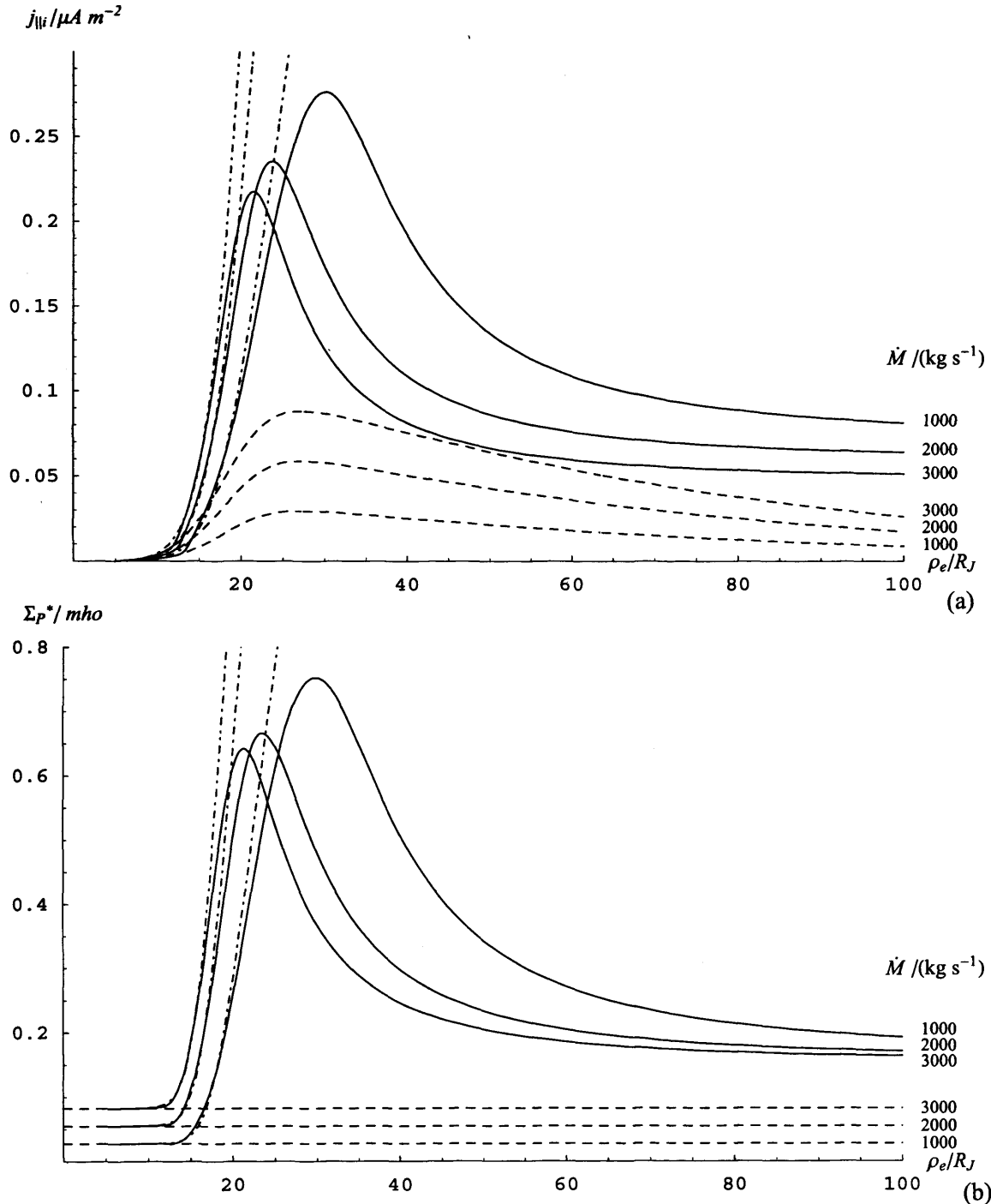


**Figure 5.23.** Plots of (a) the field-aligned current density at the feet of the field lines  $j_{\parallel i}$  in  $\mu\text{A m}^{-2}$ , and (b) the effective height-integrated Pedersen conductivity  $\Sigma_p^*$  in mho obtained using the empirical conductivity model (Eq. (5.17)) (solid lines), constant conductivity  $\Sigma_p^* = \Sigma_p^*(j_{\parallel i} = 0)$  (dashed lines), and the near-rigid corotation approximation given by Eqs. (4.4f) (dot-dashed lines), for three values of the iogenic plasma mass outflow rate  $\dot{M} = 1000, 2000$  and  $3000 \text{ kg s}^{-1}$  (as indicated). The empirical conductivity model solutions have the boundary condition on  $j_{\parallel i}$  set such that the value of the azimuth-integrated equatorial radial current in each case is equal to 100 MA at  $100R_J$ . The solutions are tracked numerically to  $12 R_J$ , inside which they are completed by the ‘first-iteration’ approximation of Section 5.4.2. Both parameters are plotted versus jovicentric equatorial radial distance  $\rho_e$ .

lines show the constant conductivity solutions with  $\Sigma_p^* = \Sigma_p^*(j_{||} = 0)$ . There is only one constant conductivity solution for the angular velocity due to the above choice of the form of  $\Sigma_{p0}^*$ .

We begin by comparing the  $I_\rho$  profiles shown in Fig. 5.22b with the values derived from the Galileo data. It can be seen that the shape of the theoretical curves agree reasonably well with the Galileo data, consisting of a sharp rise in the inner region, followed by an extended region of almost constant values. However, it can be seen that the initial rise in the current occurs at too large a radial distance for  $\dot{M} = 1000 \text{ kg s}^{-1}$ , and approaches more satisfactory agreement as  $\dot{M}$  increases to 2000 and 3000  $\text{kg s}^{-1}$ , thus explaining our interest in larger values of  $\dot{M}$  indicated above. However, even the results for 3000  $\text{kg s}^{-1}$  do not quite reach the mean of the Galileo data in the innermost region, while the observational estimates outlined in the Introduction suggest an upper limit of the mass transport rate of  $\sim 2000 \text{ kg s}^{-1}$ , with smaller values of  $\sim 1000 \text{ kg s}^{-1}$  being more typical. The implication may therefore be that the mean  $|B_{ze}|$  in the model employed here is too large (see, e.g. Eq. (4.4d)) in the critical upward current region, a possibility that needs to be carefully examined in future study.

Turning now to the results for the field-aligned current, shown in Fig. 5.23a, we see that the  $j_{||}$  profiles all strongly peak in the inner region with similar peak values of between  $\sim 0.22$  and  $\sim 0.28 \mu\text{A m}^{-2}$  for  $\dot{M} = 3000 \text{ kg s}^{-1}$  and  $1000 \text{ kg s}^{-1}$  respectively, before falling rapidly at larger distances. However, as may be expected from the results discussed in Fig. 5.22b, the position of the peak moves in towards the planet as  $\dot{M}$  increases, from  $\rho_e \approx 30 R_J$  when  $\dot{M} = 1000 \text{ kg s}^{-1}$ , to  $\rho_e \approx 20 R_J$  when  $\dot{M} = 3000 \text{ kg s}^{-1}$ . The Pedersen conductivity curves in Fig. 5.23b show a corresponding behaviour, peaking in the inner region at  $\sim 0.7 \text{ mho}$ .

Finally, the corresponding angular velocity curves are shown in Fig. 5.22a. These show similar initial decreases to each other in the innermost region (as guaranteed by the choice of  $\Sigma_{p0}^*$ ), before rising again outside  $\sim 15 R_J$  in line with the ‘near-rigid’ corotation

approximation Eq. (4.3) shown by the dot-dashed lines, and then falling more gradually at larger distances to values at the outer boundary which decrease with increasing  $\dot{M}$ . These results show how it is possible to deduce small values of  $\Sigma_p^*$  (for typical values of  $\dot{M}$ ) from plasma angular velocity profiles in the inner region, as found by Hill (1980), while values at larger distances are much higher than would be anticipated on this basis, as found, e.g. by Kane et al. (1995) and Krupp et al. (2001).

In Figs. 5.24-5.26 we show these parameters mapped along the current sheet model field lines into the ionosphere, together with auroral parameters derived from Eqs. (3.20) and (3.23), as in Figs. 5.19b and 5.20. Figure 5.24a shows that the elevated conductivity conditions produced by the auroral precipitation maintains near-rigid corotation conditions up to dipole co-latitudes of  $\sim 17^\circ$ , before falling rapidly to smaller values over  $\sim 1^\circ$  latitude in the poleward region. The total height-integrated Pedersen current curves ( $I_p = I_\rho/2$ ) shown in Fig. 5.24b exhibit related behaviour, with values elevated between  $\sim 16.5^\circ$  and  $17.5^\circ$  by the precipitation-enhanced Pedersen conductivity. The field-aligned current profiles shown in Fig. 5.25a show similar curves peaking between  $\sim 0.22$  and  $\sim 0.28 \mu\text{A m}^{-2}$  for  $\dot{M} = 3000 \text{ kg s}^{-1}$  and  $1000 \text{ kg s}^{-1}$  respectively, at colatitudes moving equatorward from  $16.7^\circ$  to  $17.2^\circ$  as  $\dot{M}$  increases from  $1000 \text{ kg s}^{-1}$  to  $3000 \text{ kg s}^{-1}$ , in corresponding behaviour with the  $I_p$  curves. Comparison with the profiles for constant conductivity shown in Fig. 5.19a show that the current distributions are now significantly narrower, with a width (FWHM) of  $\sim 1^\circ$  ( $\sim 1300 \text{ km}$ ). The conductivity profiles in Fig. 5.25b show corresponding behaviour, peaking at  $\sim 0.7 \text{ mho}$  at  $\sim 17^\circ$ . This is significantly larger than both the 'background conductivity' and the assumed constant conductivity values which have been taken in previous chapters. The estimated accelerating voltages and precipitating energy fluxes which produce the elevated conductivities are shown in Figs. 5.26a and 5.26b respectively. The peak voltages are  $\sim 50 \text{ kV}$ , falling somewhat with increasing  $\dot{M}$ , with peak energy fluxes of  $\sim 14 \text{ mW m}^{-2}$ , again falling somewhat with increasing  $\dot{M}$ , in a region whose width (FWHM) is  $\sim 0.6^\circ$  ( $\sim 800 \text{ km}$ ), significantly narrower than the profiles for constant conductivity shown in Fig. 5.20. These energy fluxes correspond to a UV luminosity of  $\sim 80\text{-}140 \text{ kR}$  in this region, which compares reasonably with 'main oval' observations (Clarke et al. 1998; Prangé et al., 1998; Grodent et al., 2003).

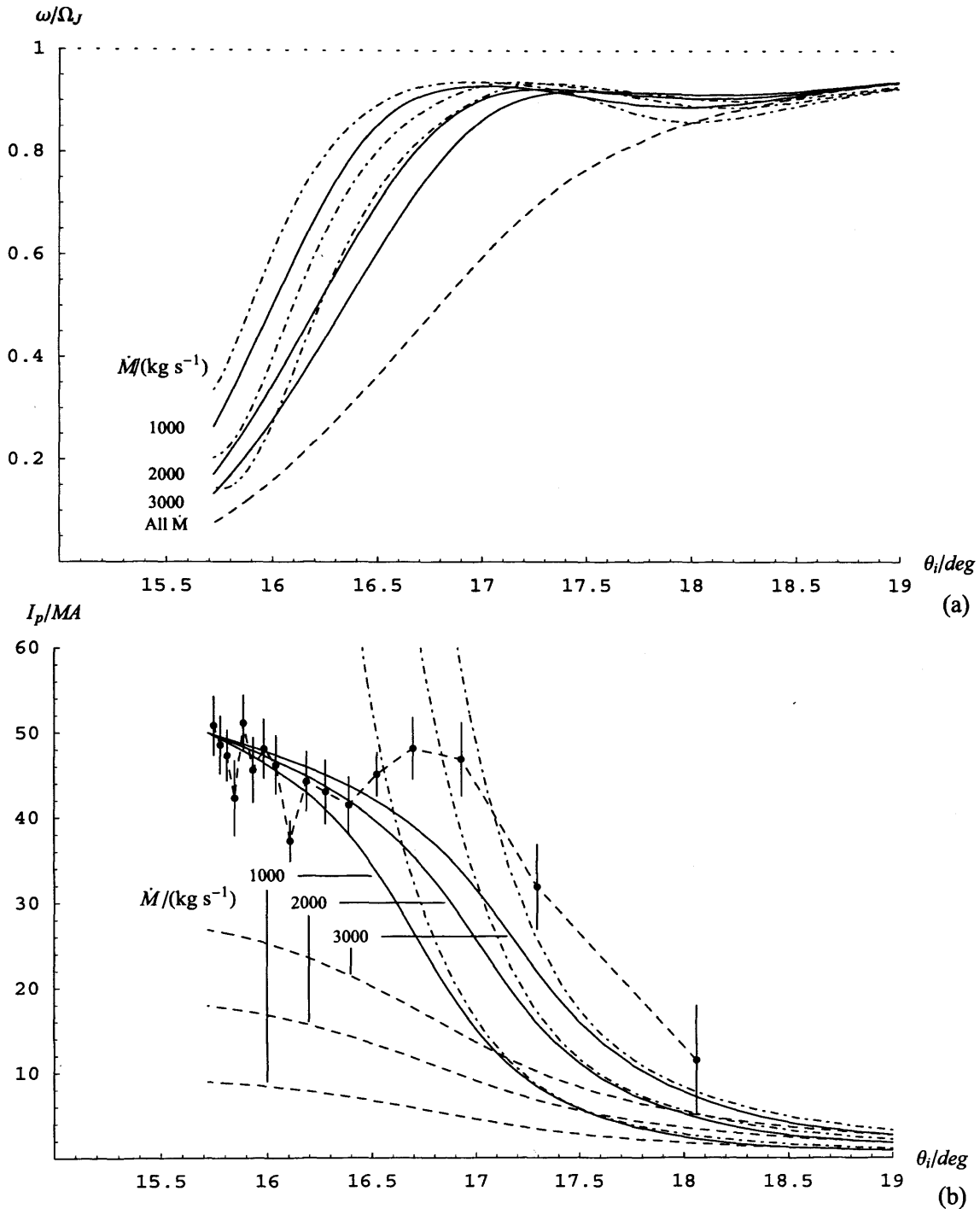


**Figure 5.24.** Plots of the solutions shown in Fig. 5.22 are shown projected along the field lines into the ionosphere, using the same line style format. Both parameters are plotted versus dipole co-latitude  $\theta_i$ . Plot (a) shows the plasma angular velocity  $\omega$  normalised to the planet's angular velocity  $\Omega_J$ , plot (b) shows the azimuth-integrated ionospheric Pedersen current  $I_p$  in MA, together with the Pedersen current derived from Galileo data.

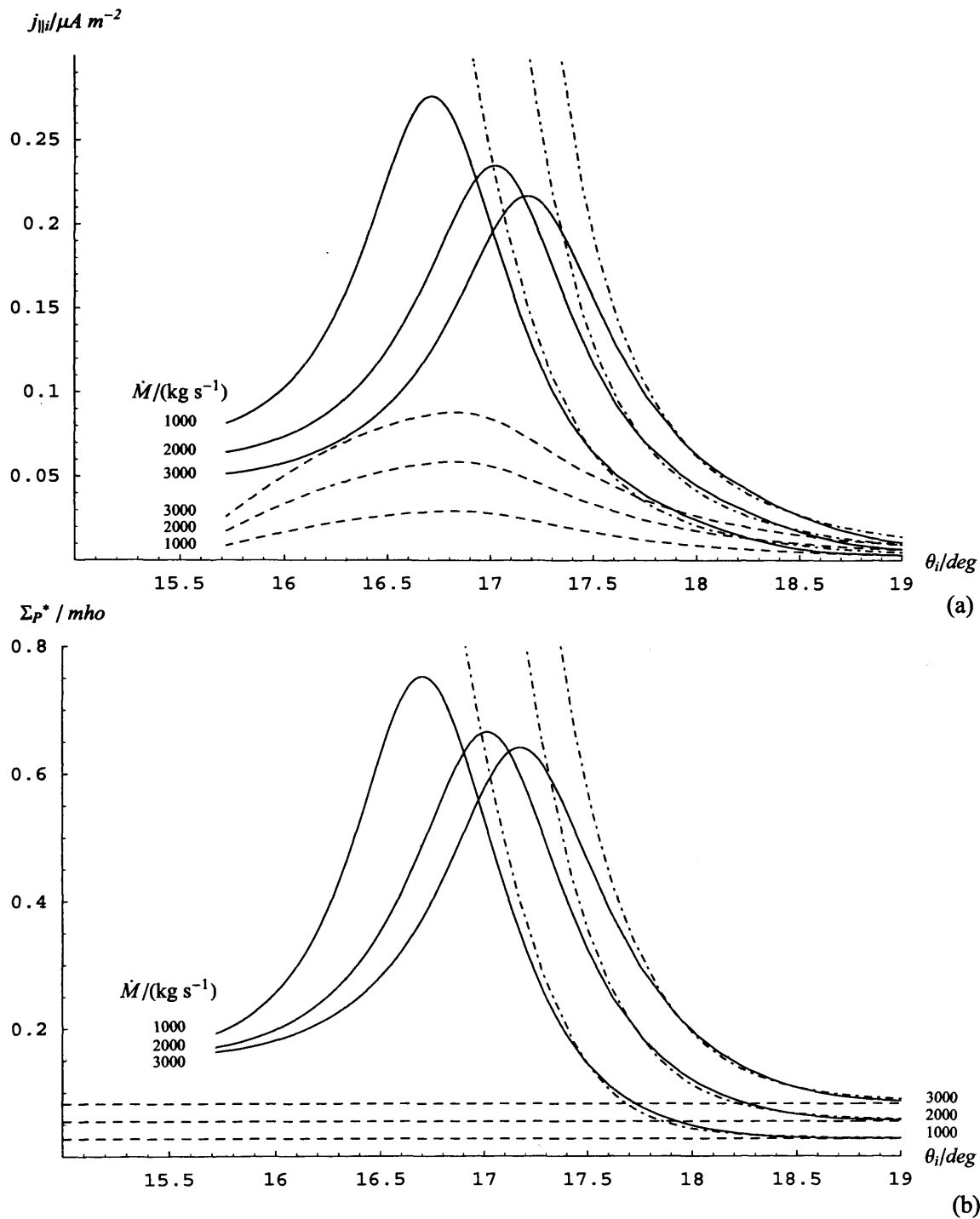


**Figure 5.25.** Plots of the solutions shown in Fig. 5.23 are shown projected along the field lines into the ionosphere, using the same line style format. Both parameters are plotted versus dipole co-latitude  $\theta_i$ . Plot (a) shows the field-aligned current density at the feet of the field lines  $j_{\parallel}$  in  $\mu\text{A m}^{-2}$ , while plot (b) shows the effective height-integrated Pedersen conductivity  $\Sigma_p^*$  in mho.

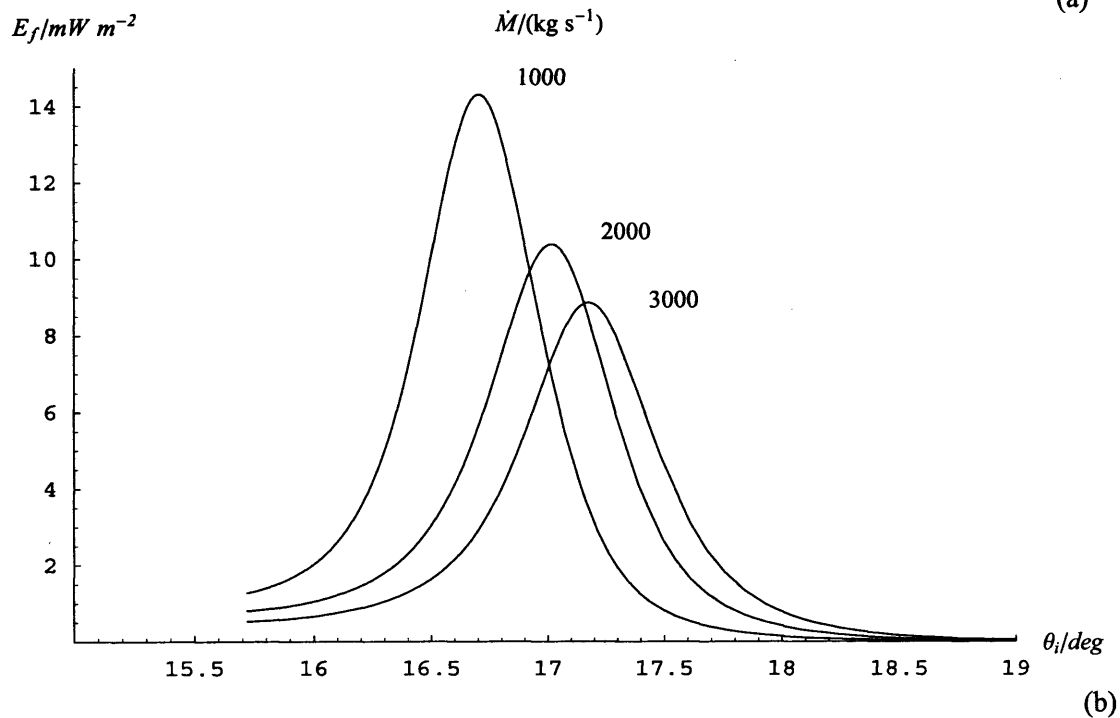
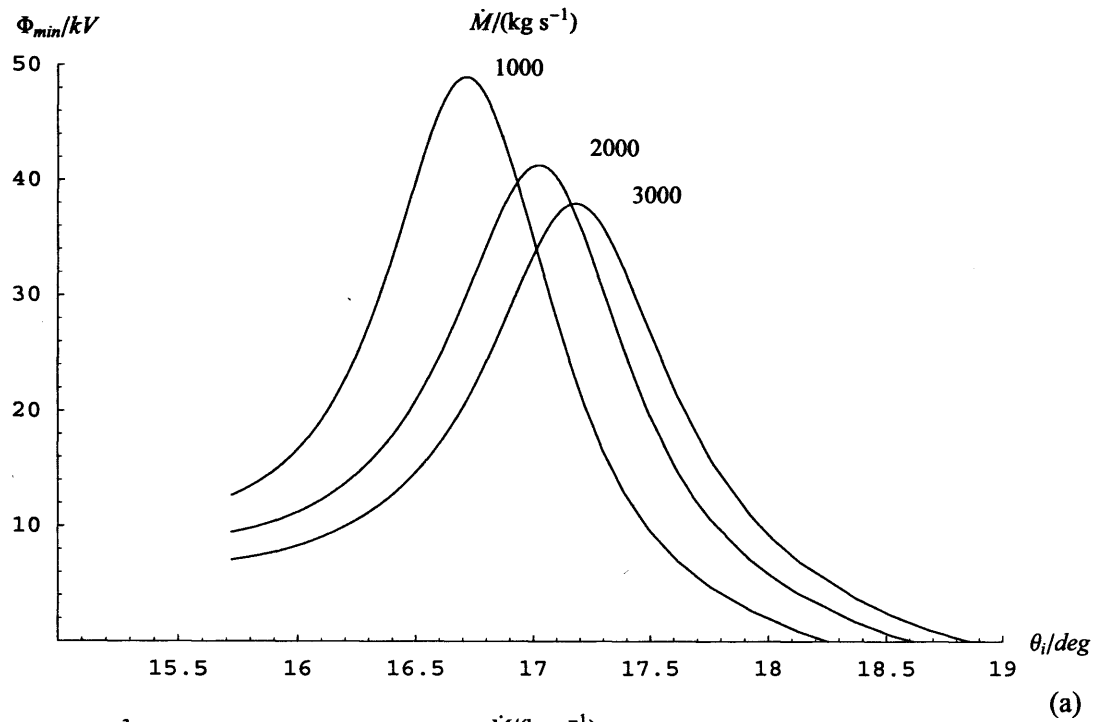


**Figure 5.26.** Plot (a) shows the minimum accelerating voltage  $\Phi$  in kV required to drive the field-aligned current shown in Figs. 5.22a and 5.24a, obtained from the exact form of Eq. (3.20), while plot (b) shows the precipitating energy flux  $E_f$  in  $\text{mW m}^{-2}$  obtained from the exact form of Eq. (3.23).

Finally, in order to display results which cover a reasonable range of variations within the jovian magnetosphere, in Figs. 5.27-5.34 we show results in a similar format for the same conductivity model, but where the value of the radial current at the outer boundary at  $100 R_J$  is fixed at values which are a factor of 1.5 larger (Figs. 5.27-5.30) and 1.5 smaller (Fig. 5.31-5.34) than in Figs. 5.22-5.26, i.e. at 150 MA and 67 MA, respectively. In order to keep the presentation reasonably compact, however, we simply show the plasma angular velocity and total equatorial radial current plotted versus  $\rho_e$  in Figs. 5.27 and 5.31, the angular velocity and Pedersen current plotted versus co-latitude in Figs. 5.28 and 5.32, the field-aligned current and Pedersen conductivity plotted versus co-latitude in Figs. 5.29 and 5.33, and finally the accelerating voltage and precipitating electron flux plotted versus co-latitude in Figs. 5.30 and 5.34 respectively. Comparison with Figs. 5.22-5.25 show that when the field-perpendicular current is increased to 150 MA, the angular velocities are elevated and the field-aligned current is increased by a factor of  $\sim 1.8$ , while its spatial distribution is shifted polewards by  $\sim 0.2^\circ$ . Consequently, the accelerating voltages are increased to  $\sim 100$  kV in this case, and the peak energy fluxes to  $\sim 50 \text{ mW m}^{-2}$ , corresponding to an enhanced UV auroral luminosity of 500 kR. The latitudinal region in which the energy fluxes achieve such values is  $\sim 0.5^\circ$  (FWHM), corresponding to 650 km in the ionosphere. By contrast, when the total current is reduced to 67 MA at the boundary at  $100 R_J$ , the field-aligned currents are correspondingly reduced in rough proportion, as are the accelerating voltages to  $\sim 25$  kV, while the precipitating energy flux then falls to  $\sim 5 \text{ mW m}^{-2}$ , corresponding to a weak UV luminosity of 50 kR. This extends over a latitudinal region  $\sim 0.7^\circ$  (FWHM), corresponding to 910 km.

## **5.6. Summary**

In this chapter we have considered the problem of the coupling current system that flows between the ionosphere and the middle magnetosphere current sheet in the jovian system, which imparts angular momentum to the plasma outflowing from the Io torus. In modelling this current system we have for the first time considered the enhancement in the ionospheric Pedersen conductivity which is produced by the precipitating energetic electrons in regions of upward-directed field-aligned current flow. The properties of the

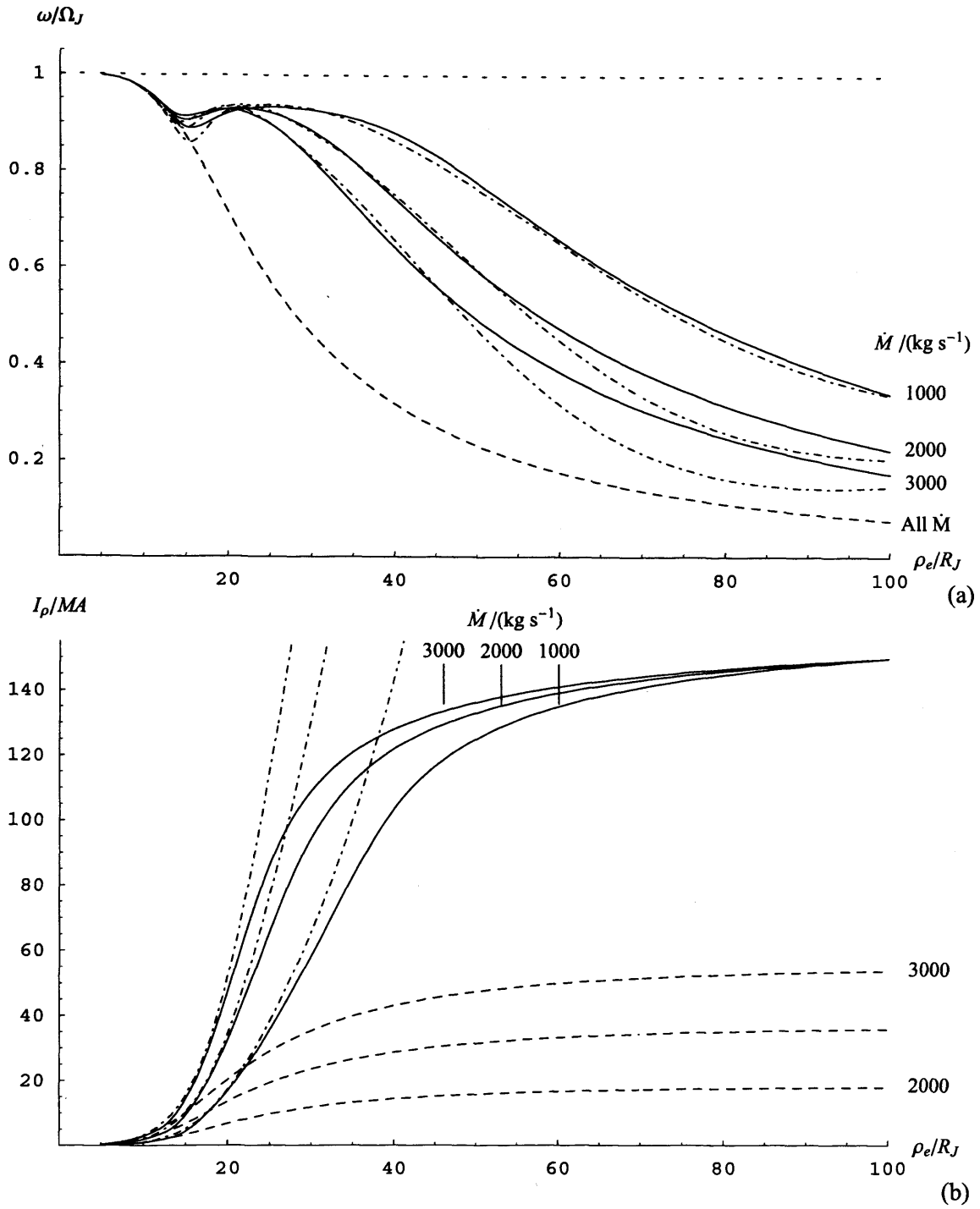


Figure 5.27. As Fig. 5.22, except with the boundary condition  $I_\rho(100R_J) = 150 \text{ MA}$ .

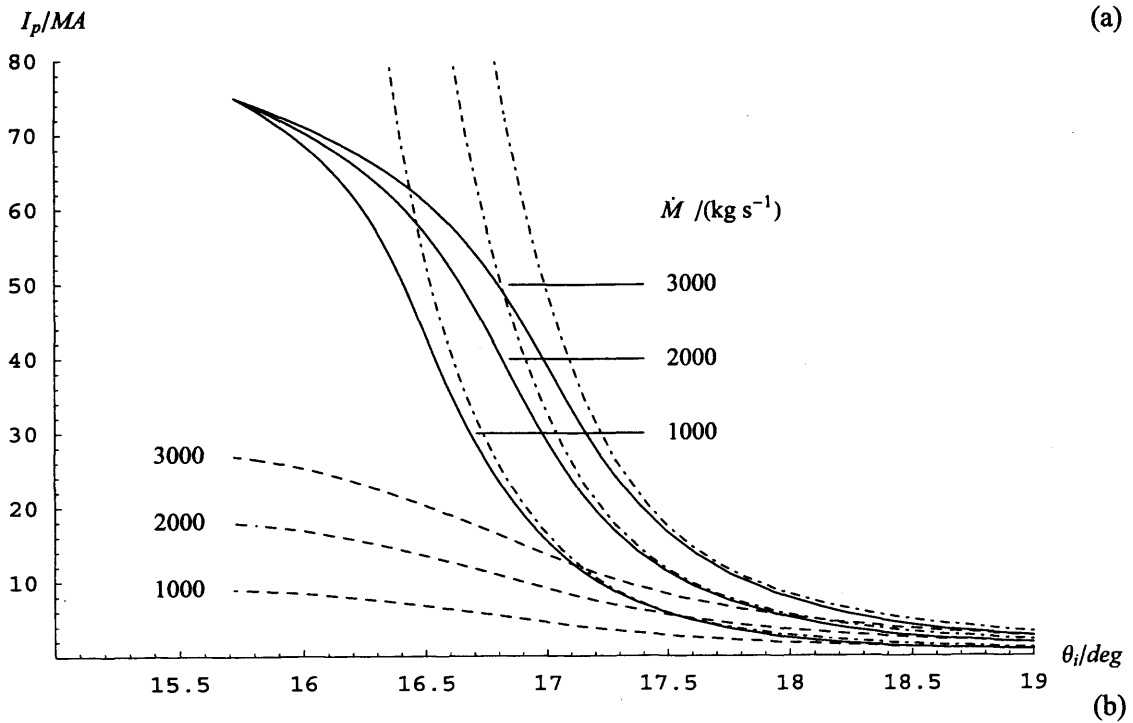
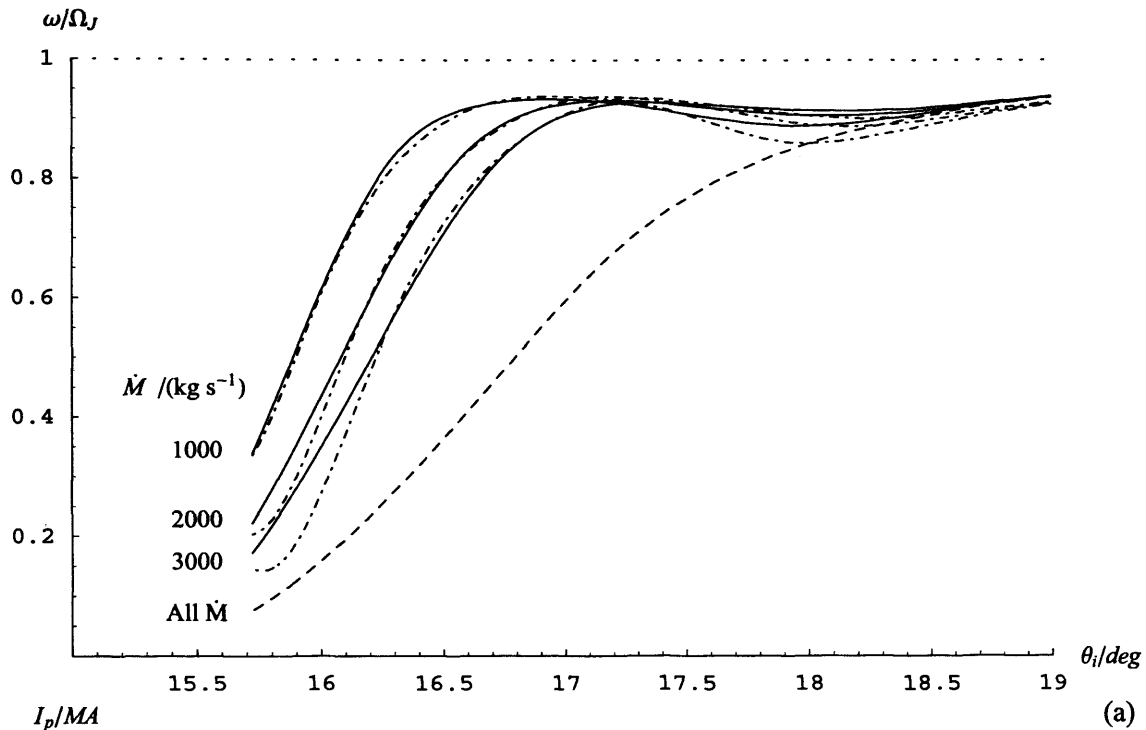


Figure 5.28. As Fig. 5.24, except with the boundary condition  $I_p(100R_J) = 150 \text{ MA}$ .

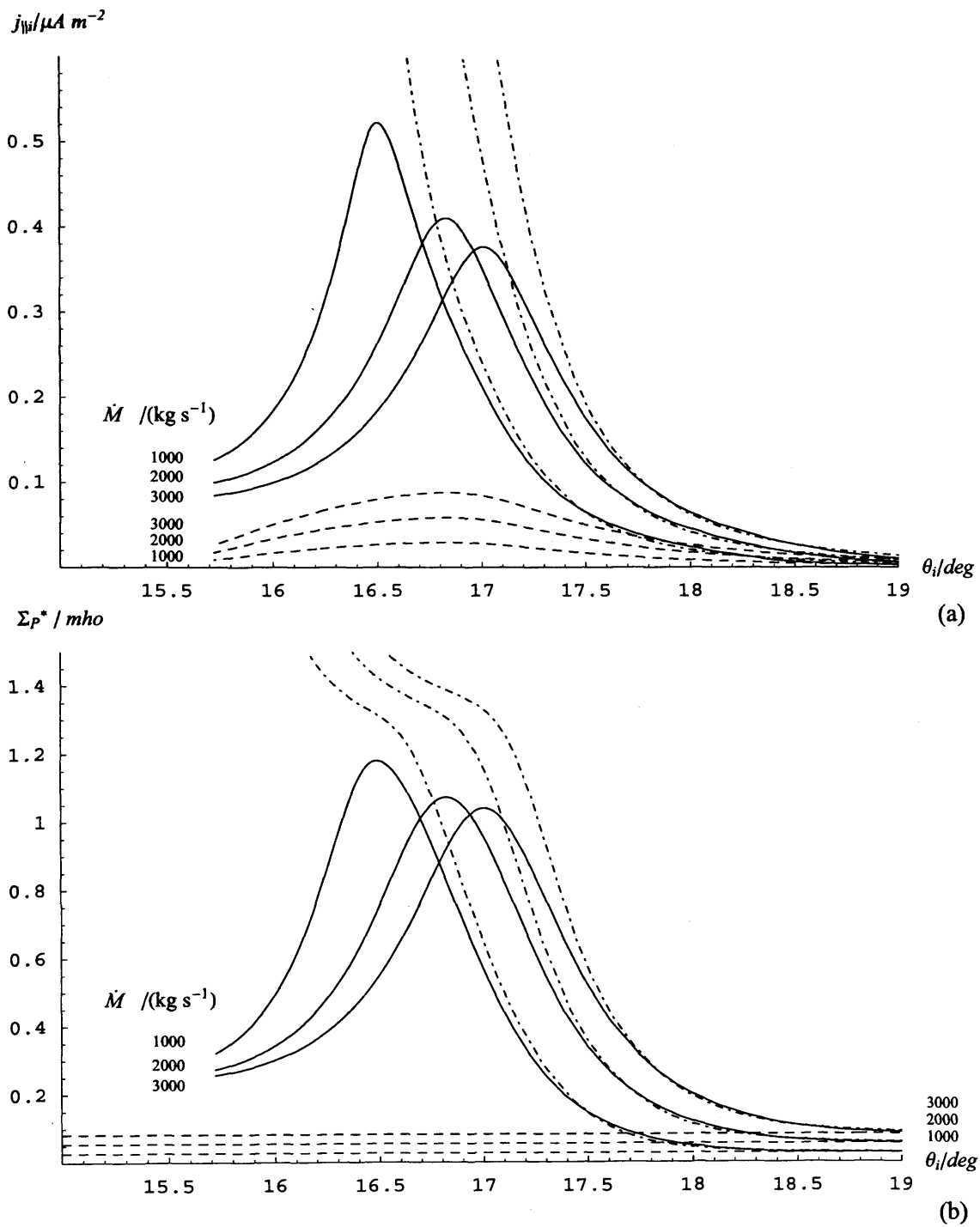


Figure 5.29. As Fig. 5.25, except with the boundary condition  $I_p(100R_J) = 150$  MA.

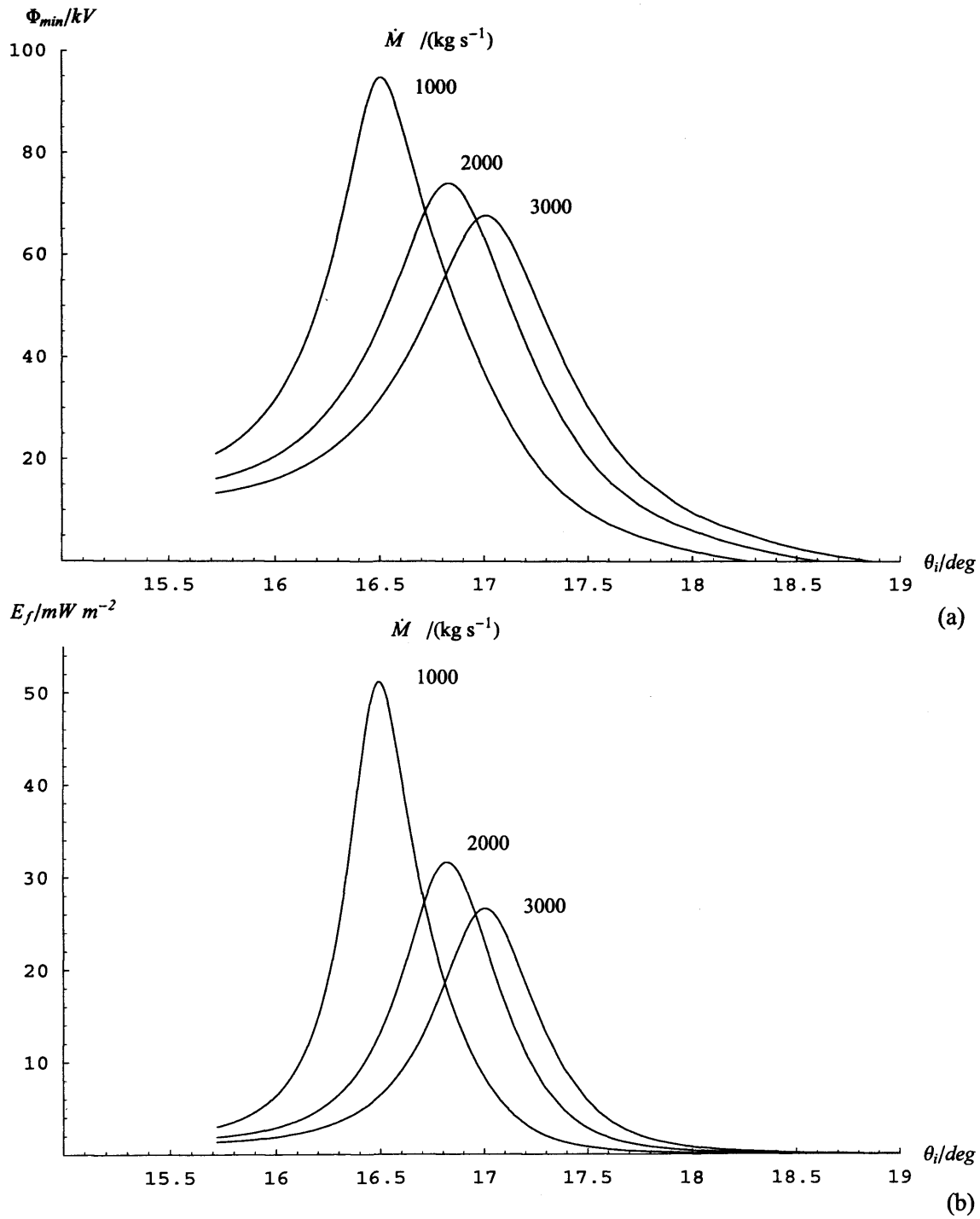


Figure 5.30. As Fig. 5.26, except with the boundary condition  $I_\rho(100R_j) = 150$  MA.

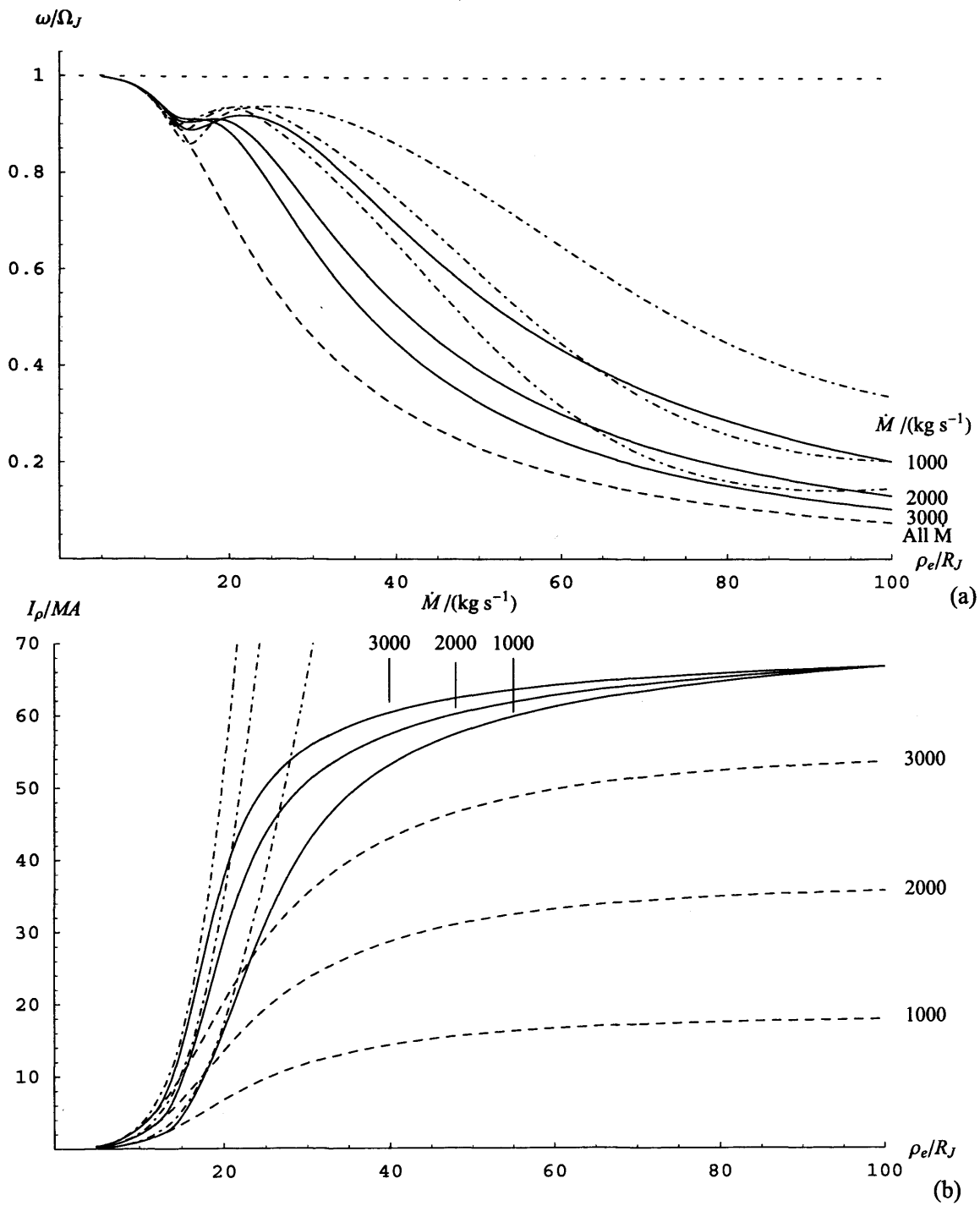


Figure 5.31. As Fig. 5.22, except with the boundary condition  $I_\rho(100R_J) = 67 MA$ .

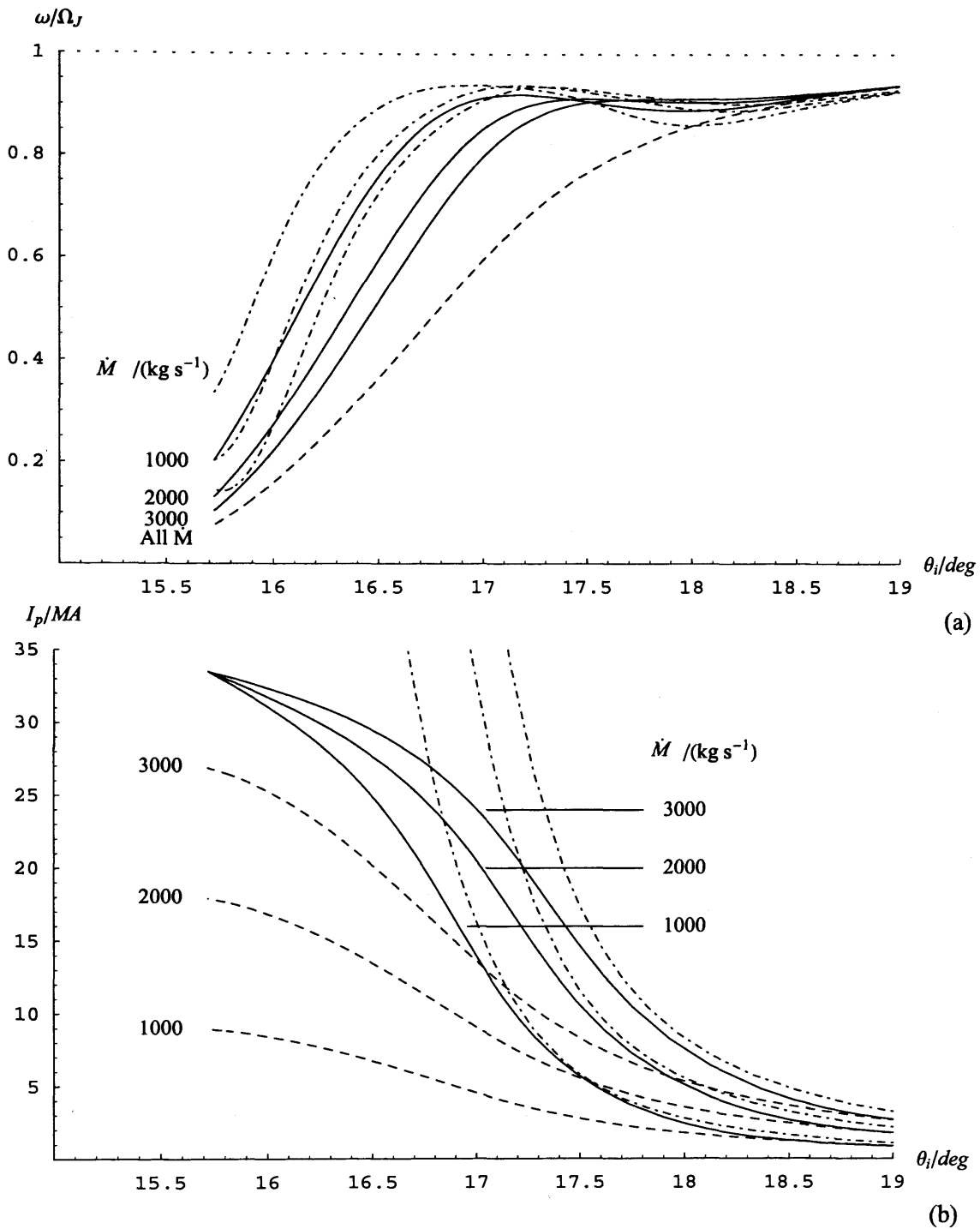


Figure 5.32. As Fig. 5.24, except with the boundary condition  $I_p(100R_J) = 67$  MA.

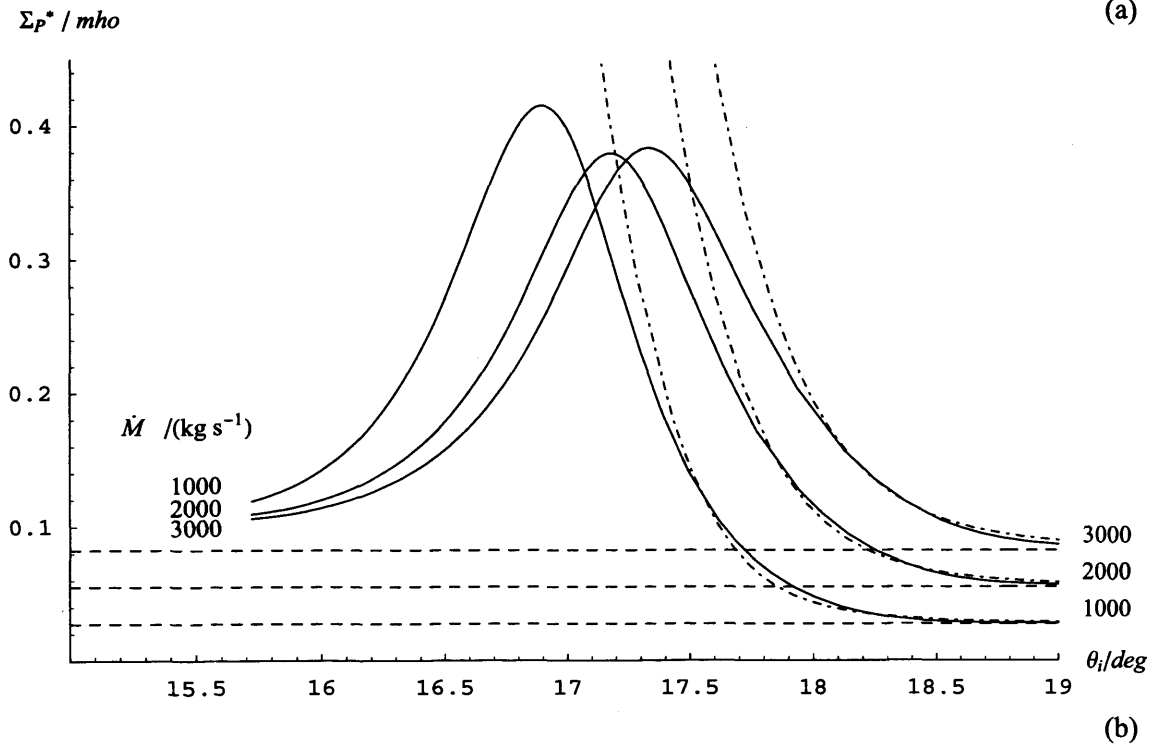
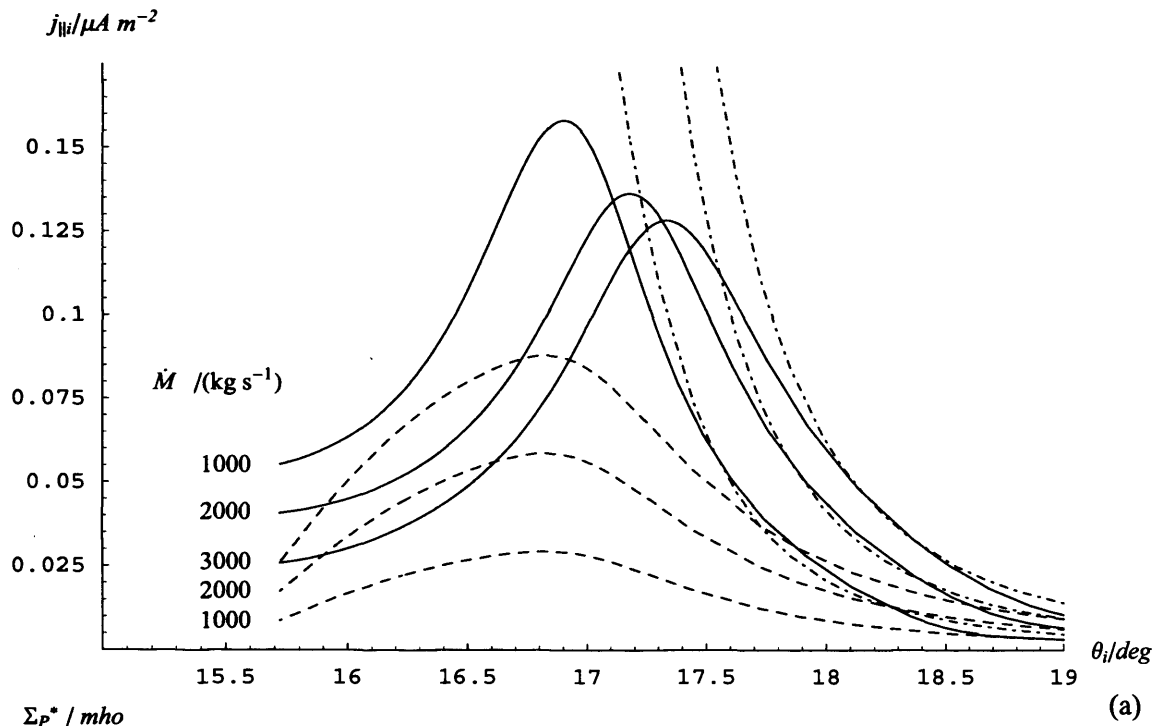


Figure 5.33. As Fig. 5.25, except with the boundary condition  $I_p(100R_J) = 67$  MA.

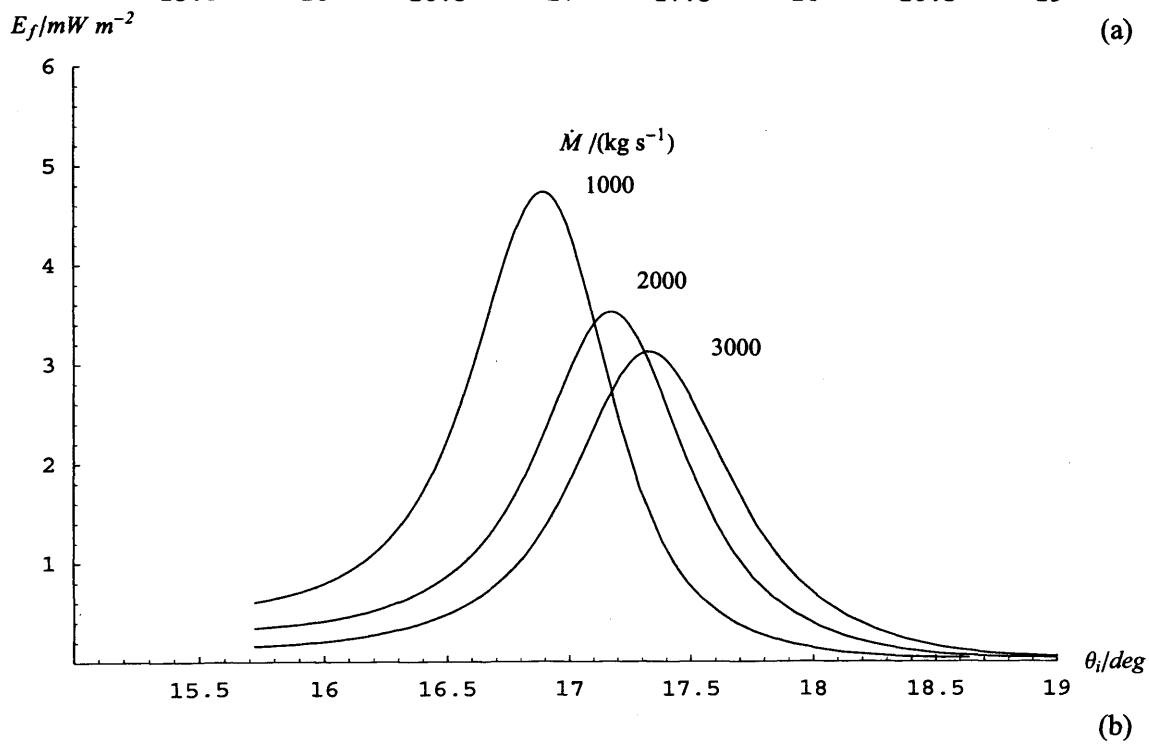
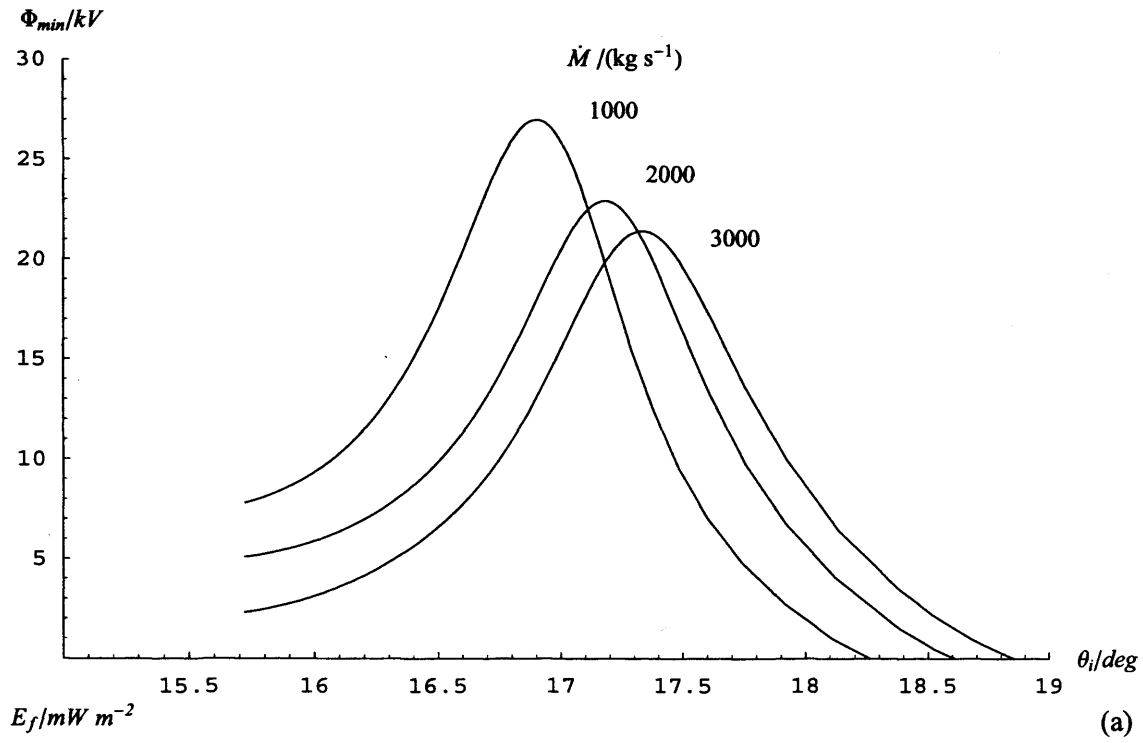


Figure 5.34. As Fig. 5.26, except with the boundary condition  $I_\rho(100R_J) = 67\ MA$ .

electron precipitation are estimated from Knight's (1973) kinetic theory, while the effects on the ionospheric conductivity have been determined using Millward et al.'s (2002) modelling results. For simplicity we have employed these inputs to derive a model for the dependence of the effective height-integrated Pedersen conductivity on the upward field-aligned current density, which is taken to be valid at all points in the middle magnetosphere. Inclusion of the effects of spatial dependence would require development of models of the spatial dependence of the properties of the hot magnetospheric source electron population, that do not exist at present. We have also employed a number of other simplified models of the conductivity dependence on the field-aligned current, which have allowed us to examine how the results depend on the properties of the model. We have then incorporated these models into the description of the M-I system, solving for the currents with the changing conductivity self-consistently included. One element of inconsistency which remains, however, is that the Knight (1973) theory requires the presence of field-aligned voltages of ~20-100 kV on the auroral field lines, whose effects are not included in our mapping of the flow between the magnetosphere and ionosphere, where we have assumed equipotential field lines. This factor is considered in the analysis presented in Chapter 6.

Following definition of the Pedersen conductivity model as discussed above, two coupled first-order differential equations must then be solved simultaneously, the first being the Hill-Pontius equation for the plasma angular velocity based on Newton's laws, the second being the current continuity equation (Eqs. (3.27) and (3.16)). To define a particular solution then requires choice of two boundary conditions, one of which is set by the requirement that the plasma angular velocity does not diverge at small radial distances, but rather that the plasma rigidly corotates with the planet in this limit. Practically, however, solution of the equations requires the choice of values of the plasma angular velocity and field-aligned current at one 'boundary' location, taken here to be the outer boundary of the model current sheet at  $100 R_J$ , the choice of the field-aligned current also being equivalent to the choice of the ionospheric conductivity at the outer boundary, via the conductivity model employed. In the majority of calculations we have then held the field-aligned current (and therefore also the ionospheric conductivity) constant at the boundary and have then iterated the angular velocity to find the solution that does not diverge at small distances.

The solutions so obtained show a number of important features which are different from those obtained previously with constant assumed ionospheric conductivities, and which potentially resolve some outstanding issues concerning the distribution of plasma angular velocity and current in Jupiter's middle magnetosphere. First, concerning the plasma angular velocity, because the field-aligned current density falls to small values in the innermost regions, the precipitation-induced enhancement of the ionospheric conductivity is also small in this region. The angular velocity thus tends to fall relatively rapidly with distance in the innermost region, out to  $\sim 15 R_J$  in the models derived in Section 5.5, which were intended to represent reasonably realistic conditions in the jovian magnetosphere. Thus, for example, Hill (1980) derived values of the Pedersen conductivity of  $\sim 0.05$  mho for typical iogenic source rates of  $\sim 2000 \text{ kg s}^{-1}$  from Voyager-1 angular velocity data in the inner region. However, the field-aligned current and conductivity grow rapidly on field lines that map to the equator at distances beyond  $\sim 15 R_J$  (corresponding to dipole co-latitudes poleward of  $\sim 18^\circ$  in the ionosphere), thus maintaining the plasma angular velocity at much higher values in the outer region than would be obtained from the conductivities deduced in the inner region. This result thus confirms the conjecture of Cowley and Bunce (2001b) to this effect, and provides an explanation of the elevated angular velocities deduced from energetic ion anisotropies in the outer region by Kane et al. (1995) and by Krupp et al. (2001). In our 'realistic' models we then find that the field-aligned current peaks at values  $\sim 0.22 - 0.28 \mu\text{A m}^{-2}$  on field lines which map in the equatorial plane to distances of  $\sim 20 - 30 R_J$  ( $16.7^\circ - 17.3^\circ$  co-latitude in the ionosphere), the peak field-aligned currents corresponding to peak ionospheric Pedersen conductivities of  $\sim 0.7$  mho according to our model. The field-aligned currents and conductivities then fall to smaller values at larger distances, determined by the choice of boundary condition. In our 'realistic' models this has been set by imposing the condition that the total radial current flowing in the equatorial current sheet reaches 100 MA at  $100 R_J$ , in conformity with the results derived from Galileo azimuthal magnetic field data by Khurana (2001). The resulting solutions for the current system are then found to be very similar in form to that derived from the magnetospheric field data, with the upward-directed field-aligned current input into the current sheet being concentrated in the inner part of the system at  $\sim 25 R_J$  in the equatorial plane, with the equatorial radial current becoming plateaued at near-constant values at distances beyond. However, matching the position of the field-aligned current input

deduced from Galileo data, centred at  $\sim 20 R_J$ , favours large values of the iogenic source rate, of around  $3000 \text{ kg s}^{-1}$  or more. Such large values seem rather unrealistic when compared with a range of previous estimates of the plasma production rate within the torus, and the (smaller) outward transport rate within the equatorial plasma disc. These suggest instead an upper limit on the outward plasma transport rate of  $\sim 2000 \text{ kg s}^{-1}$ , with  $\sim 1000 \text{ kg s}^{-1}$  being a more typical value. A possible explanation of this discrepancy, which is suggested by Eq. (4.4d) (which should be valid in the region in question), is that the strength of the north-south field threading through the current sheet in this region is too large in existing models. This possibility should be examined in future work.

We finally note that the location of the upward-directed field-aligned currents deduced in this model are comparable with the observed location of the jovian main auroral oval deduced from HST and Galileo data (e.g. Prangé et al., 1998; Clarke et al., 1998; Vasavada et al., 1999; Grodent et al., 2003). Although the field-aligned current is directed out of the ionosphere into the equatorial current sheet over the whole of the current sheet, as found in previous calculations (such that the current must close outside of the middle magnetosphere in the poleward region not described by the model) the concentration of the field-aligned current in the inner region, relative to solutions with constant conductivity, leads to a related concentration in the ionosphere. We then find in our 'realistic' models that the peaks in the field-aligned current map to  $16.7^\circ - 17.3^\circ$  co-latitude in the ionosphere for mass outflow rates of  $1000 - 3000 \text{ kg s}^{-1}$  respectively, in a region whose FWHM is  $\sim 1^\circ$  (1200 km north – south). The corresponding accelerating field-aligned voltages required by Knight's (1973) theory are then  $\sim 50 \text{ kV}$ , and the peak precipitating electron energy fluxes are  $\sim 14 \text{ mW m}^{-2}$ , located in a region of FWHM  $\sim 0.6^\circ$  ( $\sim 800 \text{ km north - south}$ ), the latter energy flux then resulting in a 'main oval' UV aurora of  $\sim 140 \text{ kR}$ .

## ***Chapter 6***

# ***Magnetosphere-ionosphere coupling currents in Jupiter's middle magnetosphere: Effect of magnetosphere-ionosphere decoupling by field- aligned auroral voltages***

### ***6.1. Introduction***

In the calculations in Chapters 4 and 5 of this thesis, as well as those of previous authors, there is one inconsistency that remains. This is that the calculations of the plasma angular velocities and the coupling currents were performed assuming perfect mapping of the electric field and plasma flow along equipotential field lines between the equatorial plane and the ionosphere. The associated field-aligned voltages were then calculated from the field-aligned current using Knight's (1973) theory. In principle, however, this field-aligned voltage would modify the mapping of the electric field, and hence the plasma flow, between these two regions. This topic was considered briefly by Cowley and Bunce (2001b), who showed that the field-aligned voltages of order  $\sim 50$ - $100$  kV are small compared to the field-perpendicular voltages associated with plasma corotation, which are several MV across the middle magnetosphere region considered. Hence they suggested that only modest modification of the potential structures across the field lines are implied.

It is the purpose of this chapter to examine quantitatively the effects of the magnetosphere-ionosphere decoupling due to the field-aligned voltages, and hence to test Cowley and Bunce's (2001b) suggestion. In the following section we derive the governing equations, while in Sect. 6.3 we go on to present the results of their numerical evaluation.

## 6.2. Governing equations

### 6.2.1 Magnetosphere-ionosphere decoupling by field-aligned voltages

The primary new feature of the calculations presented here is the inclusion of field-aligned voltages  $\Phi_{\parallel}(j_{\parallel i})$  calculated from Knight's (1973) kinetic theory, between the magnetosphere and ionosphere, which imply that the ionospheric electric field and flow values are not simply obtained by mapping the equatorial values along equipotential magnetic field lines. In this section we derive the relationship between the ionospheric and equatorial plasma angular velocities when a field-aligned voltage is present. We note that the current sheet model for the equatorial field  $B_{ze}$  used in this chapter is that discussed in Sect. 5.2.

For the purposes of derivation it is convenient to use the flux function  $F$  as the spatial coordinate, related to the physical coordinates  $\rho_e$  and  $\theta_i$  through Eqs. (3.3) and (3.4), such that the equatorial and ionospheric plasma angular velocities and the field-aligned voltage are given by the functions  $\omega_e(F)$ ,  $\omega_i(F)$  and  $\Phi_{\parallel}(F)$ , respectively. We assume a steady flow, such that the electric field  $\mathbf{E} = -\mathbf{v} \times \mathbf{B}$  can be described by a scalar potential  $\Phi$ , through  $\mathbf{E} = -\nabla\Phi$ . It is then easy to show using  $\mathbf{B} = (1/\rho)\nabla F \times \hat{\phi}$  that the plasma angular velocity is related to the gradient of  $\Phi$  by

$$\nabla\Phi = \omega\nabla F \quad , \quad (6.1)$$

such that

$$\omega_e(F) = \frac{d\Phi_e(F)}{dF} \quad \text{and} \quad \omega_i(F) = \frac{d\Phi_i(F)}{dF} \quad (6.2a,b)$$

in the equatorial plane and the ionosphere, respectively. Now if  $\Phi_{\parallel}(F)$  is the field-aligned voltage, taken to be positive when the ionosphere has a higher potential than the equatorial

plane (i.e. the case for upward-directed electric field and corresponding downward precipitating electrons), then

$$\Phi_i(F) = \Phi_e(F) + \Phi_{\parallel}(F) \quad , \quad (6.3)$$

which, when differentiated with respect to  $F$  and combined with Eqs. (6.2a,b), yields

$$\omega_i(F) = \omega_e(F) + \frac{d\Phi_{\parallel}(F)}{dF} \quad . \quad (6.4)$$

This is the equation which relates the ionospheric and equatorial angular velocities in the presence of a field-aligned voltage, and which we refer to as the magnetosphere-ionosphere decoupling equation. We note that  $\omega_i > \omega_e$  in regions where  $\Phi_{\parallel}$  increases with increasing  $F$ , while  $\omega_i < \omega_e$  in regions where  $\Phi_{\parallel}$  decreases with increasing  $F$ .

It is also necessary to specify how  $\Phi_{\parallel}$  depends on the physical conditions present in the magnetosphere. Here, in common with work discussed in previous chapters, we use Knight's (1973) kinetic theory, which gives the field-aligned voltage required to drive a given field-aligned current  $j_{\parallel i}$  which exceeds the maximum value  $j_{\parallel i0}$  that can be carried by unaccelerated precipitating magnetospheric electrons alone. For a magnetospheric population which is isotropic and Maxwellian,  $j_{\parallel i0}$  is given by Eq. (3.19). Knight's (1973) theory then shows that the minimum field-aligned voltage required to drive a current greater than  $j_{\parallel i0}$  is given by Eq. (3.20). In principle  $\Phi_{\parallel}$  will vary with  $F$  on differing flux shells due to variations in the magnetospheric electron source population parameters  $N$  and  $W_{th}$ . However, in the absence of any detailed models for these parameters at present, we here employ the constant values used in previous chapters based on Voyager data, i.e.  $N = 0.01 \text{ cm}^{-3}$  and  $W_{th} = 2.5 \text{ keV}$ . In this case  $\Phi_{\parallel}$  varies with  $F$  due to variations in  $j_{\parallel i}$  only. Substitution of Eq. (3.20) into Eq. (6.4) then gives

$$\omega_i(F) = \omega_e(F) + \frac{W_{th}}{e j_{\parallel i0}} \frac{dj_{\parallel i}}{dF} \quad . \quad (6.5)$$

This equation is strictly valid only for  $j_{\parallel} \geq j_{\parallel 0}$ . However, this condition is met essentially everywhere in the middle magnetosphere, except in the innermost region where the field-aligned current drops to small values. Here, therefore, we assume that Eq. (6.5) is valid for all  $j_{\parallel} > 0$ , i.e. that it is valid throughout the middle magnetosphere. This is equivalent to making the approximation on the RHS of Eq. (3.20), which is generally well satisfied throughout the middle magnetosphere. It is also worth recalling at this point that the corresponding precipitating energy flux is then given by Eq. (3.23).

### 6.2.2 *Current circuit equations*

In this section we outline the calculation of the components of the current system illustrated in Fig. 3.1. This is essentially the same as that given previously in Chapter 3 except that we now specifically use the ionospheric plasma angular velocity  $\omega_i$  to derive the ionospheric electric field in the rest frame of the neutral atmosphere and hence the Pedersen and field-aligned currents.

As in previous works, we define a quantity  $\Omega_j^*$  which represents the angular velocity in the inertial frame of the neutral atmosphere in the Pedersen layer, which is reduced from the planet's angular velocity  $\Omega_j$  ( $1.76 \times 10^{-4}$  rad s<sup>-1</sup>) due to ion-neutral collisional drag. This slippage can be parameterised by the factor  $k$  in the equation

$$(\Omega_j - \Omega_j^*) = k(\Omega_j - \omega_i) , \quad (6.6)$$

such that when  $k$  takes a value between 0 and 1,  $\Omega_j^*$  takes a value between  $\Omega_j$  and  $\omega_i$ . The value of  $k$  is not well known at present, but recent modelling work (Millward et al., 2004) suggests that  $k \approx 0.5$  under the circumstances appropriate to the jovian auroral ionosphere. Assuming to a sufficient approximation that the polar magnetic field is vertical and equal to  $2B_j$  in strength, the equatorward ionospheric electric field in the rest frame of the neutral atmosphere is given by

$$E_i = 2(\Omega_j^* - \omega_i)\rho_i B_j , \quad (6.7)$$

where  $\rho_i$  is again the perpendicular distance from the magnetic axis. Hence employing Eq. (6.6), the ionospheric equatorward-directed height-integrated Pedersen current is given by

$$i_p = 2\Sigma_p (\Omega_J^* - \omega_i) \rho_i B_J = 2\Sigma_p^* (\Omega_J - \omega_i) \rho_i B_J, \quad (6.8)$$

where  $\Sigma_p^*$  is the effective value of the height-integrated Pedersen conductivity, related to the true value  $\Sigma_p$  by Eq. (3.11).

Current continuity in the circuit shown in Fig. 3.1 requires that  $\rho_e i_\rho = 2\rho_i i_p$ , taking account of both north and south hemispheres, such that the equatorial radial current  $i_\rho$  is given by

$$i_\rho = \frac{4\Sigma_p^* F (\Omega_J - \omega_i)}{\rho_e}, \quad (6.9)$$

where we have used  $F = B_J \rho_i^2$  on a flux shell from Eq. (3.3). We hence find that the total radial current, integrated in azimuth, is

$$I_\rho = 2\pi\rho_e i_\rho = 8\pi\Sigma_p^* \Omega_J F \left(1 - \frac{\omega_i}{\Omega_J}\right), \quad (6.10)$$

which is equal, of course, to twice the azimuth-integrated Pedersen current in each conjugate ionosphere  $I_p$ . The field-aligned current density is then calculated from the divergence of either  $I_\rho$  or  $I_p$ . Using the former, we have

$$j_{\parallel i} = -\frac{B_J}{2\pi} \frac{dI_\rho}{dF} = -4\Sigma_p^* B_J \Omega_J \frac{d}{dF} \left[ F \left(1 - \frac{\omega_i}{\Omega_J}\right) \right], \quad (6.11)$$

this being the parallel current to be substituted in Eq. (6.5) in order to determine the difference between  $\omega_i$  and  $\omega_e$  for given source parameters. Note that in deriving

Eq. (6.11) we have assumed for simplicity that  $\Sigma_p^*$  is constant (see Sect. 3.3.2 for a full explanation of this derivation).

### 6.2.3 Conservation of angular momentum (the Hill-Pontius equation)

The analysis is completed by consideration of conservation of angular momentum of the equatorial plasma. Following Hill (1979) and Pontius (1997), this is described by the equation

$$\frac{d}{dF} \left( \rho_e^2 \frac{\omega_e}{\Omega_J} \right) = -\frac{I_\rho}{\dot{M}\Omega_J}, \quad (6.12)$$

where  $\dot{M}$  is the iogenic plasma mass outflow rate, assumed to be constant in space and time. Note that this form uses the flux function  $F$  as the spatial coordinate, but recalling that  $dF = \rho_e B_{ze} d\rho_e$  from Eq. (3.4) we recover the more usual form

$$\frac{d}{d\rho_e} \left( \rho_e^2 \frac{\omega_e}{\Omega_J} \right) = -\frac{\rho_e B_{ze} I_\rho}{\dot{M}\Omega_J}. \quad (6.13)$$

Substitution of Eq. (6.10) for  $I_\rho$  into Eq. (6.12) then yields the modified Hill-Pontius equation

$$\frac{d}{dF} \left( \rho_e^2 \frac{\omega_e}{\Omega_J} \right) = -\frac{8\pi\Sigma_p^* F}{\dot{M}} \left( 1 - \frac{\omega_i}{\Omega_J} \right), \quad (6.14)$$

where we note that the LHS now specifically contains  $\omega_e$ , the angular velocity of the equatorial plasma, while the RHS, representing the ionospheric torque on the equatorial plasma, contains  $\omega_i$ .

### 6.2.4 Governing equation

There are three equations to be solved, these being the decoupling equation in the form incorporating Knight's (1973) theory, i.e. Eq. (6.5), the equation for the parallel current Eq. (6.11), and the Hill-Pontius equation Eq. (6.14). Substitution of Eq. (6.11) into Eq. (6.5) yields

$$\frac{\omega_e}{\Omega_J} = \frac{\omega_i}{\Omega_J} + \frac{4\Sigma_P^* B_J W_{th}}{ej_{\parallel io}} \frac{d^2}{dF^2} \left[ F \left( 1 - \frac{\omega_i}{\Omega_J} \right) \right]. \quad (6.15)$$

Introducing the dimensionless parameter  $\varepsilon$  given by

$$\varepsilon = \frac{4\Sigma_P^* W_{th}}{ej_{\parallel io} R_J^2}, \quad (6.16)$$

and noting that the first term in the differential vanishes, Eq. (6.15) becomes

$$\frac{\omega_e}{\Omega_J} = \frac{\omega_i}{\Omega_J} - \varepsilon B_J R_J^2 \frac{d^2}{dF^2} \left( F \frac{\omega_i}{\Omega_J} \right). \quad (6.17)$$

Note that in all the works described in previous chapters, solutions have been obtained in the limit  $\varepsilon \rightarrow 0$ , such that  $\omega_e \rightarrow \omega_i$ . The value of  $\varepsilon$  can be made arbitrarily small by choosing  $W_{th}/ej_{\parallel io} \rightarrow 0$ , in which case  $\Phi_{\parallel} \rightarrow 0$  according to Eq. (3.20). For canonical system parameters  $\Sigma_P^* = 0.1$  mho,  $j_{\parallel io} \approx 0.01 \mu\text{A m}^{-2}$ , and  $W_{th} = 2.5$  keV, for example, we find  $\varepsilon \approx 1.5 \times 10^{-5}$ . Substitution of Eq. (6.17) into the Hill-Pontius equation Eq. (6.14), finally yields the governing equation for  $\omega_i$  as

$$\frac{d}{dF} \left( \rho_e^2 \frac{\omega_i}{\Omega_J} \right) = -\frac{8\pi\Sigma_P^* F}{M} \left( 1 - \frac{\omega_i}{\Omega_J} \right) + \varepsilon B_J R_J^2 \frac{d}{dF} \left[ \rho_e^2 \frac{d^2}{dF^2} \left( F \frac{\omega_i}{\Omega_J} \right) \right]. \quad (6.18)$$

This is a third order linear inhomogeneous equation for  $\omega_i$ , from which  $\omega_e$  can be obtained from Eq. (6.17), and the current system and field-aligned voltage from Eqs. (6.10), (6.11) and (3.20).

### 6.2.5 Series solution of the governing equation

The general solution of Eq. (6.18) is the sum of a complementary function which solves the homogeneous equation and contains three arbitrary constants, together with some particular integral. The physical solution which we require here, however, is the particular integral which reduces to our previous solutions in the limit that  $\varepsilon \rightarrow 0$ . This solution may be obtained as a power series in  $\varepsilon$  given by

$$\left( \frac{\omega_i}{\Omega_J} \right) = \sum_{n=0}^{\infty} \varepsilon^n \left( \frac{\omega_i}{\Omega_J} \right)_{(n)}, \quad (6.19)$$

where each of the coefficients  $(\omega_i/\Omega_J)_{(n)}$  is a function of  $F$ . Substitution of Eq. (6.19) into Eq. (6.18) gives

$$\begin{aligned} \frac{d}{dF} \left( \rho_e^2 \sum_{n=0}^{\infty} \varepsilon^n \left( \frac{\omega_i}{\Omega_J} \right)_n \right) = & -\frac{8\pi\Sigma_p^* F}{M} \left( 1 - \sum_{n=0}^{\infty} \varepsilon^n \left( \frac{\omega_i}{\Omega_J} \right)_n \right) + \\ & + B_J R_J^2 \frac{d}{dF} \left[ \rho_e^2 \frac{d^2}{dF^2} \left( F \sum_{n=0}^{\infty} \varepsilon^{n+1} \left( \frac{\omega_i}{\Omega_J} \right)_n \right) \right], \end{aligned} \quad (6.20)$$

from which the required functions are found by equating terms of the same power of  $\varepsilon$ . For the zeroth order, i.e.  $n = 0$ , we have

$$\frac{d}{dF} \left[ \rho_e^2 \left( \frac{\omega_i}{\Omega_J} \right)_{(0)} \right] = -\frac{8\pi\Sigma_p^* F}{M} \left[ 1 - \left( \frac{\omega_i}{\Omega_J} \right)_{(0)} \right], \quad (6.21)$$

which is identical to the Hill-Pontius equation that has been solved in previous chapters. The solution required is the particular integral for which  $(\omega_i/\Omega_J) \rightarrow 1$  as  $\rho_e \rightarrow 0$ , i.e. for which the plasma rigidly corotates at small distances. For  $n \geq 1$  we have

$$\frac{d}{dF} \left[ \rho_e^2 \left( \frac{\omega_i}{\Omega_J} \right)_{(n)} \right] = \frac{8\pi\Sigma_p^* F}{M} \left[ \left( \frac{\omega_i}{\Omega_J} \right)_{(n)} \right] + B_J R_J^2 \frac{d}{dF} \left\{ \rho_e^2 \frac{d^2}{dF^2} \left[ F \left( \frac{\omega_i}{\Omega_J} \right)_{(n-1)} \right] \right\}, \quad (6.22)$$

which is a first order linear inhomogeneous equation for  $(\omega_i/\Omega_J)_{(n)}$ , in which the inhomogeneous term contains the derivative of the solution of the previous order,  $(\omega_i/\Omega_J)_{(n-1)}$ . The solutions required of these equations are the particular integrals which satisfy  $(\omega_i/\Omega_J)_{(n)} \rightarrow 0$  as  $\rho_e \rightarrow 0$  for all  $n \geq 1$ . In principle we can then solve Eqs. (6.21) and (6.22) in sequence to any desired order in  $\varepsilon$ . Here we will obtain solutions up to second order ( $n = 2$ ).

The other parameters of interest are obtained by substitution of Eq. (6.19) and equating powers of  $\varepsilon$ . Thus for  $\omega_e$  we obtain from Eq. (6.17)

$$\left( \frac{\omega_e}{\Omega_J} \right)_{(0)} = \left( \frac{\omega_i}{\Omega_J} \right)_{(0)}, \quad (6.23a)$$

which was our original formulation, while for  $n \geq 1$  we have

$$\left( \frac{\omega_e}{\Omega_J} \right)_{(n)} = \left( \frac{\omega_i}{\Omega_J} \right)_{(n)} - B_J R_J^2 \frac{d^2}{dF^2} \left[ F \left( \frac{\omega_i}{\Omega_J} \right)_{(n-1)} \right]. \quad (6.23b)$$

The total radial and field-aligned currents follow from Eqs. (6.10) and (6.11), respectively. The former is then given by the power series

$$I_\rho = \sum_{n=0}^{\infty} \varepsilon^n I_{\rho(n)}, \quad (6.24a)$$

where for  $n = 0$  we have

$$I_{\rho(0)} = 8\pi\Sigma_p^* \Omega_J F \left[ 1 - \left( \frac{\omega_i}{\Omega_J} \right)_{(0)} \right], \quad (6.24b)$$

while for  $n \geq 1$ , we have

$$I_{\rho(n)} = -8\pi\Sigma_p^* \Omega_J F \left( \frac{\omega_i}{\Omega_J} \right)_{(n)}. \quad (6.24c)$$

The field-aligned current is similarly given by

$$j_{\parallel i} = \sum_{n=0}^{\infty} \varepsilon^n j_{\parallel i(n)}, \quad (6.25a)$$

where for  $n = 0$  we have

$$j_{\parallel i(0)} = -4\Sigma_p^* B_J \Omega_J \frac{d}{dF} \left\{ F \left[ 1 - \left( \frac{\omega_i}{\Omega_J} \right)_{(0)} \right] \right\}, \quad (6.25b)$$

and for  $n \geq 1$  we have

$$j_{\parallel i(n)} = 4\Sigma_p^* B_J \Omega_J \frac{d}{dF} \left[ F \left( \frac{\omega_i}{\Omega_J} \right)_{(n)} \right]. \quad (6.25c)$$

Since we can write from Eqs. (3.20) and (6.11)

$$\Phi_{\parallel} = \sum_{n=0}^{\infty} \varepsilon^n \Phi_{\parallel(n)} \approx \varepsilon \frac{R_J^2 j_{\parallel i}}{4\Sigma_p^*} = -\varepsilon B_J R_J^2 \Omega_J \frac{d}{dF} \left[ F \left( 1 - \frac{\omega_i}{\Omega_J} \right) \right] \quad (6.26a)$$

in the approximation employed here, we have on substituting Eq. (6.19) for  $(\omega_i/\Omega_J)$

$$\Phi_{\parallel(0)} = 0 \quad , \quad (6.26b)$$

i.e. to lowest order the parallel voltage is zero as in previous published solutions, while for  $n = 1$  we have

$$\Phi_{\parallel(1)} = -B_J R_J^2 \Omega_J \frac{d}{dF} \left\{ F \left[ 1 - \left( \frac{\omega_i}{\Omega_J} \right)_{(0)} \right] \right\} \quad , \quad (6.26c)$$

and for  $n \geq 2$  we have

$$\Phi_{\parallel(n)} = B_J R_J^2 \Omega_J \frac{d}{dF} \left[ F \left( \frac{\omega_i}{\Omega_J} \right)_{(n-1)} \right] \quad . \quad (6.26d)$$

Hence, if we evaluate  $(\omega_i/\Omega_J)$  and  $(\omega_e/\Omega_J)$  to second order, for example, we can determine the parallel voltage to third order, etc.

With regard to the precipitating energy flux, we have from Eqs. (3.20) and (3.23)

$$E_f \approx \frac{E_{f0}}{2} \left( \frac{e\Phi_{\parallel}}{W_{th}} \right)^2 \quad . \quad (6.27)$$

Therefore we express  $E_f$  to the same order as  $\Phi_{\parallel}$ , such that if we determine the plasma flows to a given order, we can compute the precipitating energy flux to the next highest order.

### 6.2.6 Inner region approximations

Series solutions for  $(\omega_i/\Omega_J)$  can also be obtained for the inner region, i.e. where  $\rho_e$  is small, which describe the initial breakdown of rigid corotation. As in Chapter 4, we employ  $(\dot{M}/\Sigma_p^*)$  as the formal expansion parameter to write

$$\left(\frac{\omega_i}{\Omega_j}\right) = \sum_{m=0}^{\infty} a_m \left(\frac{\dot{M}}{\Sigma_p^*}\right)^m, \quad (6.28)$$

which we substitute into Eq. (6.22) and then equate the coefficients of equal powers of  $(\dot{M}/\Sigma_p^*)$ . We find that  $a_0=1$ , which represents rigid corotation at smallest distances, while for higher orders we have the following recurrence relation

$$a_m = \frac{1}{8\pi F} \left\{ \frac{d}{dF} [\rho_e^2 a_{m-1}] - \varepsilon B_j R_j^2 \frac{d}{dF} \left[ \rho_e \frac{d^2}{dF^2} (F a_{m-1}) \right] \right\}. \quad (6.29)$$

In particular, with  $a_0=1$ , we find

$$a_1 = \frac{2}{8\pi F B_{ze}}, \quad (6.30a)$$

$$a_2 = \frac{2}{(8\pi)^2 F} \left\{ \frac{d}{dF} \left( \frac{\rho_e^2}{F B_{ze}} \right) - \varepsilon B_j R_j^2 \frac{d}{dF} \left[ \rho_e^2 \frac{d^2}{dF^2} \left( \frac{1}{B_{ze}} \right) \right] \right\}, \quad (6.30b)$$

and

$$a_3 = \frac{2}{(8\pi)^3 F} \left\{ \begin{aligned} & \frac{d}{dF} \left[ \frac{\rho_e^2}{F} \frac{d}{dF} \left( \frac{\rho_e^2}{F B_{ze}} \right) \right] - \\ & - \varepsilon B_j R_j^2 \frac{d}{dF} \left\{ \frac{\rho_e^2}{F} \left[ \frac{d}{dF} \left( \rho_e^2 \frac{d^2}{dF^2} \left( \frac{1}{B_{ze}} \right) \right) + F \frac{d^3}{dF^3} \left( \frac{\rho_e^2}{F B_{ze}} \right) \right] \right\} + \\ & + \varepsilon^2 B_j^2 R_j^4 \frac{d}{dF} \left\{ \rho_e^2 \frac{d^3}{dF^3} \left[ \rho_e^2 \frac{d^2}{dF^2} \left( \frac{1}{B_{ze}} \right) \right] \right\} \end{aligned} \right\}, \quad (6.30c)$$

and so on. Note that  $a_1$  is independent of  $\varepsilon$ ,  $a_2$  contains a term proportional to  $\varepsilon$ , while  $a_3$  contains up to  $\varepsilon^2$ . In general,  $a_m$  contains terms up to  $\varepsilon^{m-1}$ . Collecting terms with specific powers of  $\varepsilon$ , we obtain the small- $\rho_e$  expressions for the  $n$ th order solutions for

$(\omega_i/\Omega_J)$ , i.e.  $(\omega_i/\Omega_J)_{(0)}$ ,  $(\omega_i/\Omega_J)_{(1)}$ , etc. From Eq. (6.30) we thus have, correct to third order in  $(\dot{M}/\Sigma_p^*)$

$$\left(\frac{\omega_i}{\Omega_J}\right)_{(0)} \approx 1 + \frac{2\dot{M}}{8\pi\Sigma_p^*FB_{ze}} + \frac{2\dot{M}^2}{(8\pi)^2\Sigma_p^{*2}F} \frac{d}{dF} \left( \frac{\rho_e^2}{FB_{ze}} \right) + \frac{2\dot{M}^3}{(8\pi)^3\Sigma_p^{*3}F} \frac{d}{dF} \left[ \frac{\rho_e^2}{F} \frac{d}{dF} \left( \frac{\rho_e^2}{FB_{ze}} \right) \right] + \dots, \quad (6.31a)$$

$$\begin{aligned} \left(\frac{\omega_i}{\Omega_J}\right)_{(1)} \approx & -\frac{2B_J R_J^2 \dot{M}^2}{(8\pi)^2 \Sigma_p^{*2} F} \frac{d}{dF} \left[ \rho_e^2 \frac{d^2}{dF^2} \left( \frac{1}{B_{ze}} \right) \right] - \\ & - \frac{2B_J R_J^2 \dot{M}^3}{(8\pi)^3 \Sigma_p^{*3} F} \frac{d}{dF} \left\{ \frac{\rho_e^2}{F} \left[ \frac{d}{dF} \left( \rho_e^2 \frac{d^2}{dF^2} \left( \frac{1}{B_{ze}} \right) \right) + F \frac{d^3}{dF^3} \left( \frac{\rho_e^2}{FB_{ze}} \right) \right] \right\} - \dots \end{aligned} \quad (6.31b)$$

and

$$\left(\frac{\omega_i}{\Omega_J}\right)_{(2)} \approx \frac{2B_J^2 R_J^4 \dot{M}^3}{(8\pi)^3 \Sigma_p^{*3} F} \frac{d}{dF} \left\{ \rho_e^2 \frac{d^3}{dF^3} \left[ \rho_e^2 \frac{d^2}{dF^2} \left( \frac{1}{B_{ze}} \right) \right] \right\} + \dots \quad (6.31c)$$

From these equations it can be seen that the lowest order term in the expansion of  $(\omega_i/\Omega_J)_{(n)}$  is a term proportional to  $(\dot{M}/\Sigma_p^*)^{n+1}$ . The implication of this result is that the lowest order term describing the breakdown of rigid corotation in the ionosphere, proportional to  $(\dot{M}/\Sigma_p^*)$ , does not depend on  $\varepsilon$ , i.e. to that order  $(\omega_i/\Omega_J)$ , and consequently the currents in the inner region, are independent of  $\varepsilon$  and the field-aligned voltage. Specifically, this approximation is

$$\left(\frac{\omega_i}{\Omega_J}\right) \approx 1 + \frac{\dot{M}}{4\pi\Sigma_p^*FB_{ze}} + \dots, \quad (6.32)$$

where we recall that  $B_{ze}$  is negative. This is the same approximation for  $\omega$  as found in previous analyses (Eq. 4.3), which is such that the currents in the inner region are given by

Eqs. (4.4d) and (4.4f). That is, in the inner region the behaviour of  $\omega_i$  and the currents remain unchanged compared with previous solutions to a lowest approximation. Physically this is because the lowest order approximation provides a current in Eq. (6.14) that is just such as to maintain rigid corotation of the plasma. Thus if we put  $(\omega_e/\Omega_J)=1$  as the lowest approximation in the LHS of the Hill-Pontius equation Eq. (6.14), we then find

$$\left(1 - \frac{\omega_i}{\Omega_J}\right) = -\frac{\dot{M}\rho_e}{4\pi\Sigma_p^*F} \frac{d\rho_e}{dF}, \quad (6.33)$$

which, when we recall that  $dF/d\rho_e = \rho_e B_{ze}$ , leads to Eq. (6.32). This is not true for  $\omega_e$ , however. To lowest order in  $(\dot{M}/\Sigma_p^*)$  (i.e. considering up to linear terms only), we have from Eq. (6.17)

$$\left(\frac{\omega_e}{\Omega_J}\right) = 1 + \frac{\dot{M}}{4\pi\Sigma_p^*FB_{ze}} - \frac{\varepsilon\dot{M}}{4\pi\Sigma_p^*} B_J R_J^2 \frac{d^2}{dF^2} \left(\frac{1}{B_{ze}}\right) + \dots, \quad (6.34)$$

which is such that the departure from rigid corotation of  $(\omega_e/\Omega_J)$  required to drive the currents in Eqs. (4.4d) and (4.4f) is slightly smaller than obtained in previous analyses.

It is illuminating to evaluate these approximations for a dipole magnetic field, for which  $F_e = B_J R_J^3 / \rho_e$  and  $B_{ze} = -B_J R_J^3 / \rho_e^3$ , and which should be a valid approximation in the inner region of the system. Introducing the Hill distance  $R_{De}$ , given by Eq. (4.7) as a characteristic length scale for the plasma angular velocity profiles, we find for the ionospheric plasma angular velocity to second order in  $(\dot{M}/\Sigma_p^*)^2$

$$\left(\frac{\omega_i}{\Omega_J}\right) = 1 - \frac{1}{2} \left(\frac{\rho_e}{R_{De}}\right)^4 + \frac{3}{4} \left(\frac{\rho_e}{R_{De}}\right)^8 \left[1 - 14\varepsilon \left(\frac{\rho_e}{R_J}\right)\right] + \dots, \quad (6.35)$$

which is the equivalent of Eqs. (6.31a) and Eq. (6.31b), while for the angular velocity in the equatorial plane we have from Eq. (6.17)

$$\left(\frac{\omega_e}{\Omega_J}\right) = 1 - \frac{1}{2}\left(\frac{\rho_e}{R_{De}}\right)^4 \left[1 - 12\varepsilon\left(\frac{\rho_e}{R_J}\right)\right] + \frac{3}{4}\left(\frac{\rho_e}{R_{De}}\right)^8 \left[1 - 70\varepsilon\left(\frac{\rho_e}{R_J}\right)\right] + \dots \quad (6.36)$$

We note that in the limit that  $\varepsilon \rightarrow 0$  both Eqs. (6.35) and (6.36) reduce to Eq. (4.11), which is the small- $\rho_e$  approximation to the plasma angular velocity for the dipole given previously in Chapter 4.

### 6.3. Results

In this section we present the results of the numerical evaluation of the equations discussed in Sect. 6.2 in order to assess the significance of the effects of field-aligned voltages under typical jovian conditions. In this study we have used our ‘canonical’ values of  $\Sigma_p^* = 0.1$  mho and  $\dot{M} = 1000$  kg s<sup>-1</sup>, along with magnetospheric electron ‘source’ population parameters of  $j_{\parallel io} \approx 0.01$   $\mu\text{A m}^{-2}$ , and  $W_{th} = 2.5$  keV. Under these conditions we find  $\varepsilon \approx 1.5 \times 10^{-5}$ , as indicated above, which is small, such that a power series solution in  $\varepsilon$  seems appropriate.

We begin with a brief outline of the zeroth order solution, which is identical to those given in previous chapters, and which forms a basis against which the higher order terms may be compared. We then go on to present the first and second order terms of the series solution, along with their sum, for the plasma angular velocity, azimuth-integrated equatorial radial current, and field-aligned current. We finally show overall profiles of the current system parameters including the zeroth, first and second order terms, and compare them with the zeroth order solution.

Figures 6.1 to 6.4 show the results of the zeroth order solution (i.e. for  $n = 0$ ), which is the basic solution representative of those published previously. Figures 6.1 and 6.2 show system parameters plotted versus jovicentric radial distance  $\rho_e$ , while Figs. 6.3 and 6.4 shows profiles mapped along field lines into the ionosphere and plotted versus co-latitude. The solid lines in the figures show the full solution obtained by solving Eq. (6.21) for the

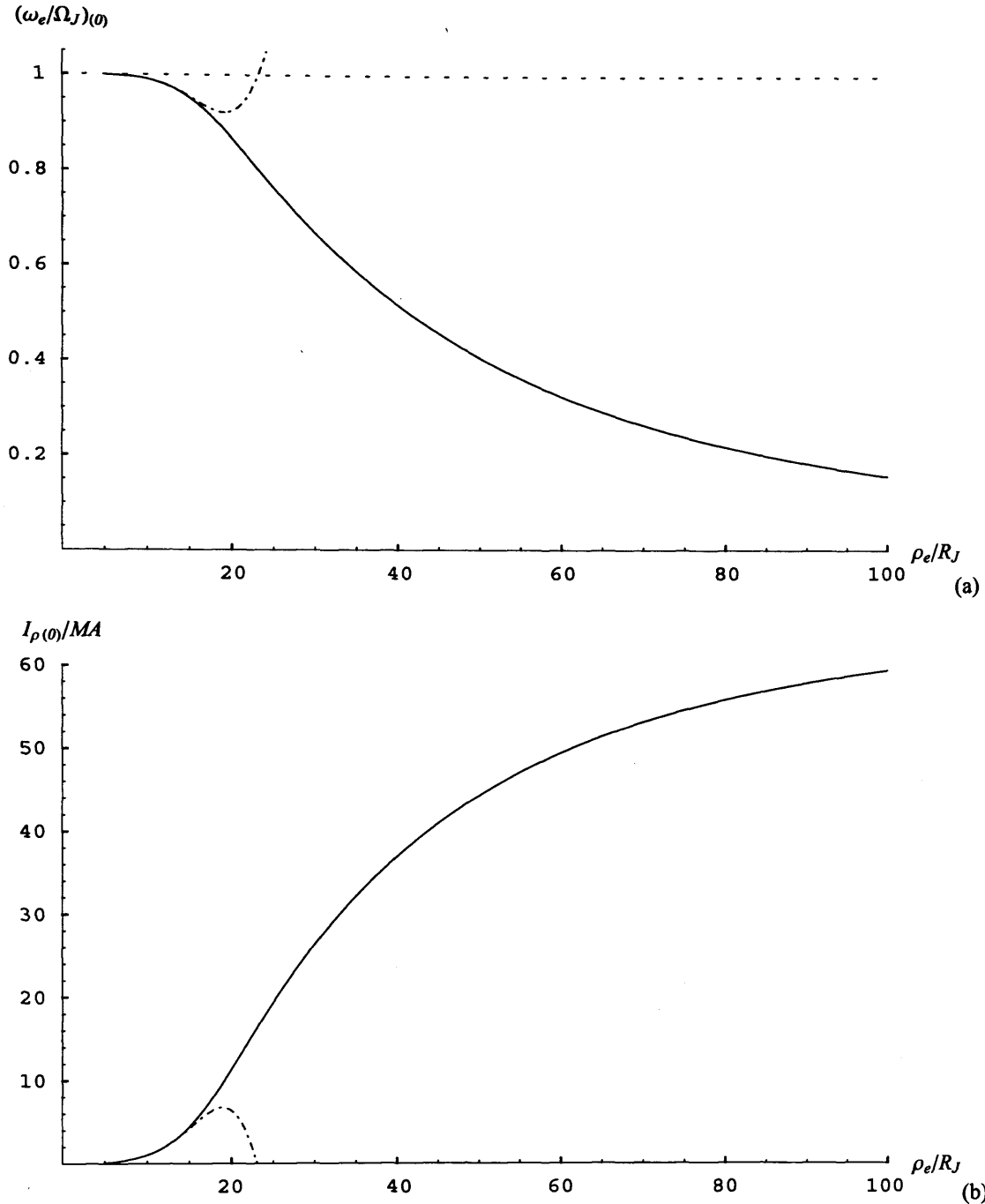


**Figure 6.1.** Plots of the magnetosphere-ionosphere coupling current system parameters for the zeroth order solution, i.e. for  $n=0$ . Both parameters are plotted versus joventric radial distance  $\rho_e$ . The solid lines represent the full solution obtained by integrating Eq. (6.21), while the dot-dashed lines show the small- $\rho_e$  approximation computed from Eq. (6.31), shown here to second order in  $(\dot{M}/\Sigma_p^*)$ . Panel (a) shows the equatorial plasma angular velocity normalised to that of the planet (equal in this case to the ionospheric angular velocity on the same field lines). The horizontal dotted line represents rigid corotation. Panel (b) shows the total equatorial radial current given by Eq. (35b) in MA.

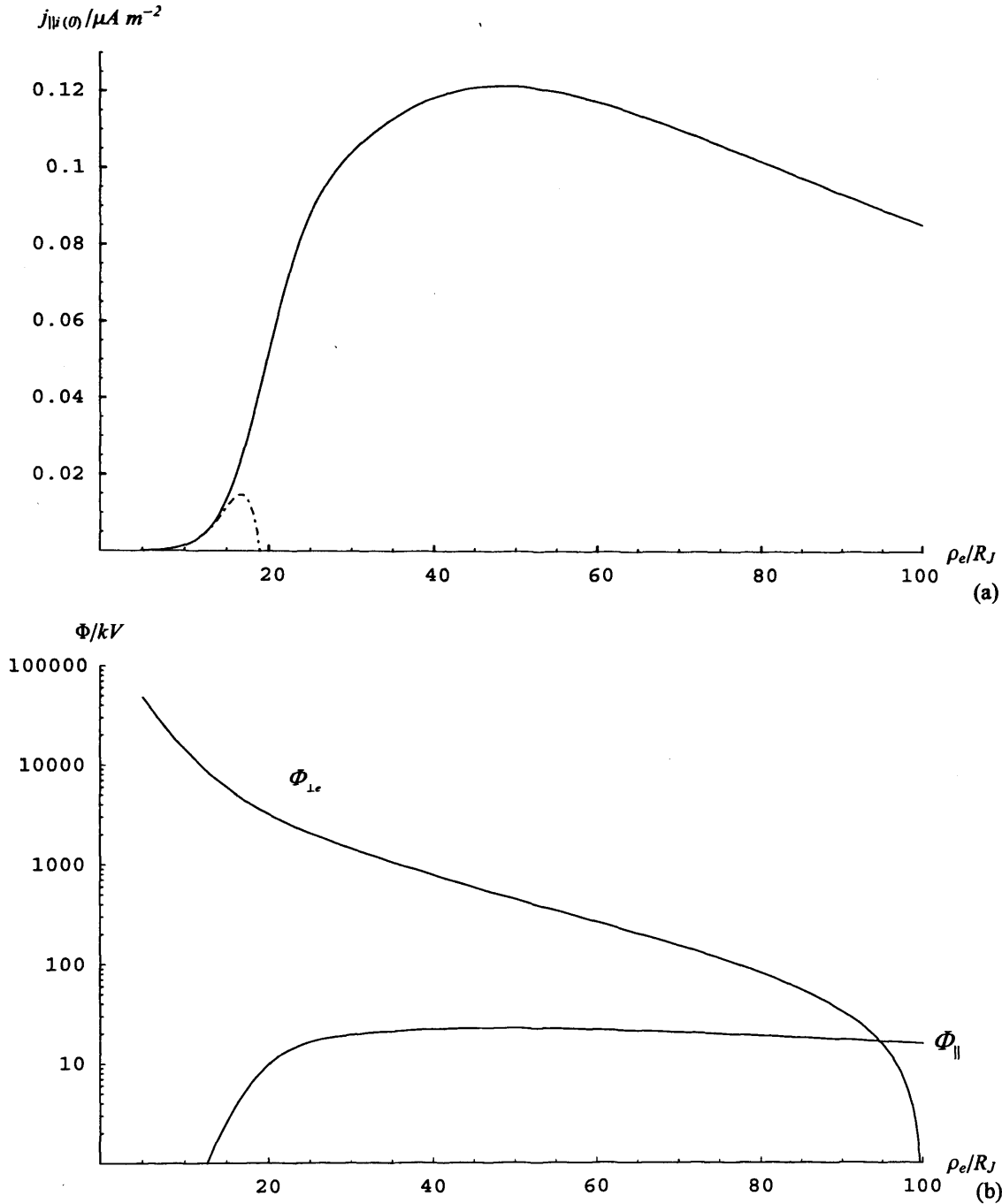


**Figure 6.2.** Plots of the magnetosphere-ionosphere coupling current system parameters for the zeroth order solution, i.e. for  $n=0$ . Both parameters are plotted versus joventric radial distance  $\rho_e$ . As in Fig. 6.1, the solid lines represent the full solution obtained by integrating Eq. (6.21), while the dot-dashed lines show the small- $\rho_e$  approximation computed from Eq. (6.31), shown here to second order in  $(\dot{M}/\Sigma_p^*)$ . Panel (a) shows the field-aligned current at the feet of the field lines given by Eq. (6.25b) in  $\mu A m^{-2}$ . Panel (b) shows a log-linear plot of the zeroth order electrostatic potential  $\Phi_{\perp e}$  obtained from Eq. (6.37) in kV, together with the first order field-aligned voltage  $\Phi_{\parallel}$  calculated from the angular velocity profile shown in panel (a) through Eq. (6.26c).

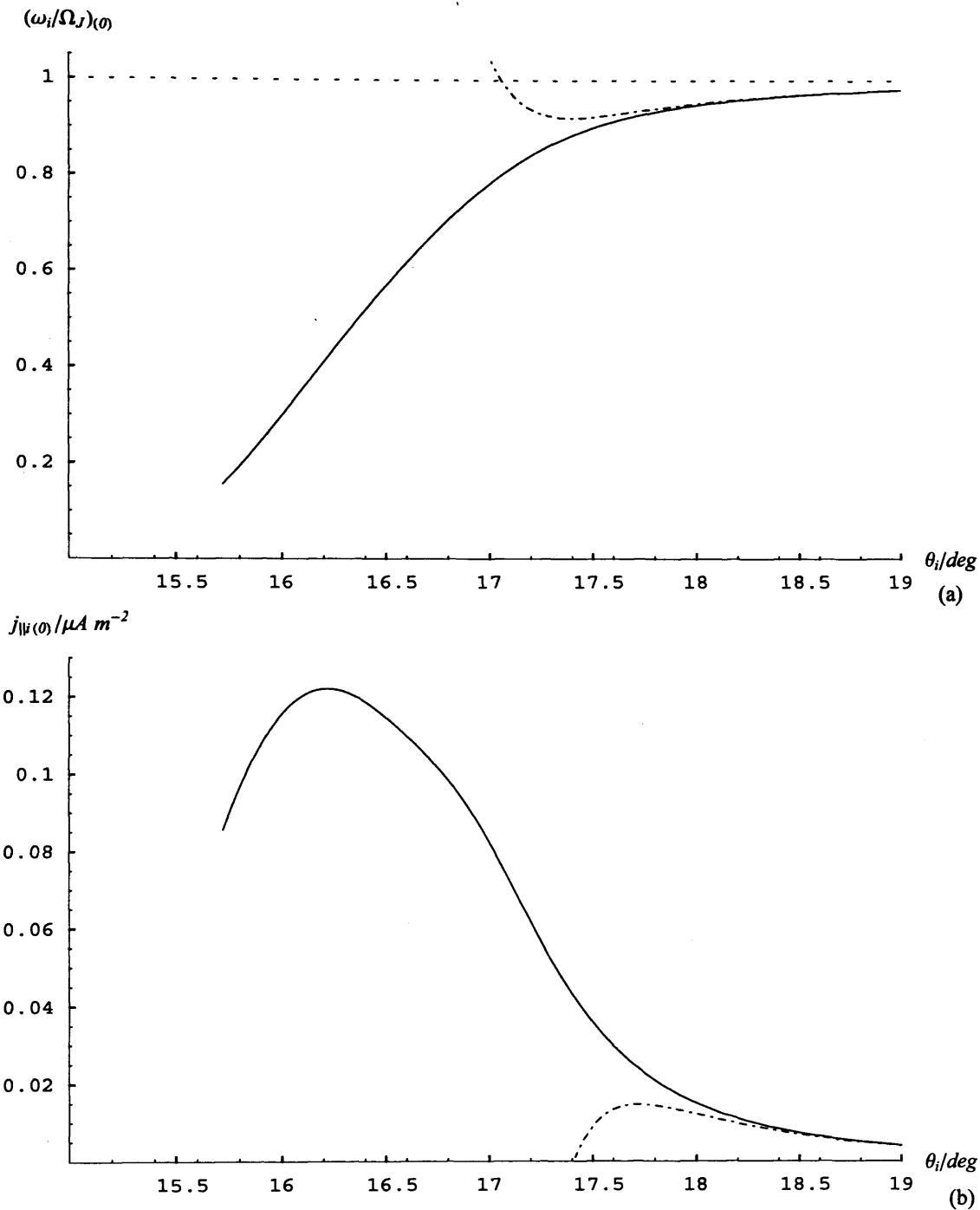


**Figure 6.3.** Plots of the magnetosphere-ionosphere coupling current system parameters for the zeroth order solution, plotted here versus ionospheric co-latitude  $\theta_i$ . The format is the same as in Fig. 6.1. Panel (a) shows the ionospheric plasma angular velocity normalised to that of the planet. Panel (b) shows the field-aligned current at the feet of the field lines given by Eq. (6.25b) in  $\mu A m^{-2}$ .

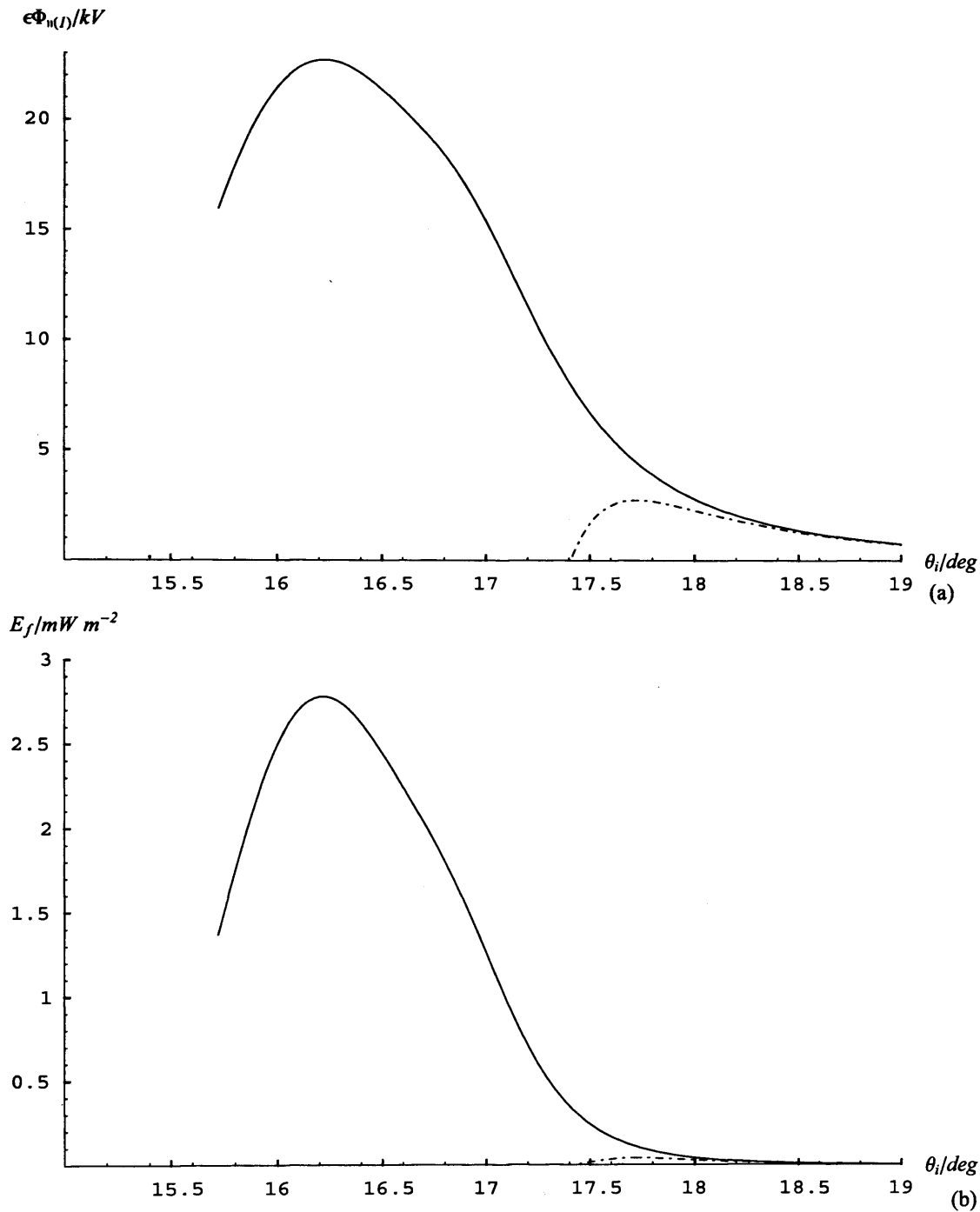


**Figure 6.4.** Plots of the magnetosphere-ionosphere coupling current system parameters for the zeroth order solution, together with the first order field-aligned voltage as in Fig. 6.2, plotted here versus ionospheric co-latitude  $\theta_i$ . The format is the same as in Fig. 6.3. Panel (a) shows the first order field-aligned voltage calculated from the angular velocity profile shown in Fig. 6.3a through Eq. (6.26c). Panel (b) shows the precipitating energy flux calculated from the profile shown in panel (a) through Eq. (6.27).

plasma angular velocity, while the dot-dashed lines show the small- $\rho_e$  approximation given by the series in Eq. (6.31a) (shown here to second order in  $(\dot{M}/\Sigma_p^*)$ ). The plasma angular velocity profile is shown in Fig. 6.1a. In this case  $(\omega_i/\Omega_J)_{(0)} = (\omega_e/\Omega_J)_{(0)}$  since there is no decoupling between the equatorial plane and the ionosphere at zeroth order, as indicated by Eq. (6.23a). It can be seen that the angular velocity is near to rigid corotation in the inner magnetosphere, and falls monotonically to  $\sim 0.2 \Omega_J$  at the outer edge of the model at  $100 R_J$ . The numerical solution was initialised at  $\rho_e = 5 R_J$  using the value of the second order small- $\rho_e$  approximation at this point. It can be seen that the numerical solution closely follows the small- $\rho_e$  approximation out to a distance of  $\sim 15 R_J$ , after which the approximation diverges to large values. The ionospheric mapping of the angular velocity profile is shown in Fig. 6.3a, in which it can be seen that the drop in angular velocity occurs over a region  $\sim 2.5^\circ$  in latitudinal width. Figure 6.1b shows the azimuth-integrated equatorial radial current which follows from the angular velocity profile shown in Fig. 6.1a, calculated using Eq. (6.24b). It can be seen that the current has small values in the inner region and rises monotonically to  $\sim 60$  MA at  $100 R_J$ . Figure 6.2a similarly shows the field-aligned current profile computed from Eq. (6.25b). Note that this is the field-aligned current at the feet of the field lines, mapped into the equatorial plane and plotted versus  $\rho_e$  for ease of comparison with the other parameters. Large field-aligned currents occur beyond  $\sim 20 R_J$ , with a peak value of  $\sim 0.12 \mu\text{A m}^{-2}$  at  $\sim 48 R_J$ . The ionospheric profile of the field-aligned current is shown in Fig. 6.3b, in which it can be seen that the large currents occur over a region  $\sim 2.5^\circ$  wide in latitude, with the peak at  $\sim 16.2^\circ$  co-latitude. Finally, the ‘upper’ line in Fig. 6.2b shows the associated zeroth order electrostatic potential  $\Phi_{\perp e}$  versus radial distance in the equatorial plane, calculated from

$$\Phi_{\perp e} = \int_F^{F(100R_J)} \omega_e(F) dF \quad , \quad (6.37)$$

where the arbitrary zero of potential is taken to be at the outer edge of the model at  $100 R_J$ . Note that in the zeroth order solution the field-aligned voltage is taken to be zero, such that this one potential profile corresponds to both the equatorial plane and the ionosphere. We also note that the voltage drop across the region associated with large field-aligned currents, between  $20 R_J$  and the outer edge of the model at  $100 R_J$ , is  $\sim 3$  MV. This is approximately

two orders of magnitude larger than the first order field-aligned voltage computed from the zeroth order angular velocity profile through Eq. (6.26c), which is shown for comparison by the ‘lower’ line in Fig. 6.2b. The ionospheric mapping of the first-order field-aligned voltage is shown in Fig. 6.4a, while the precipitating energy flux calculated from this voltage using Eq. (6.27) is shown in Fig. 6.4b.

As indicated above, the profiles shown in Figs. 6.1 to 6.4, while being representative of previously presented results, are considered in this chapter to be just the first terms in a series, the higher orders of which introduce the decoupling due to field-aligned voltages. It is to these higher order terms which we now turn in Fig. 6.5, which shows the first and second order terms for the plasma angular velocity, given the ‘typical’ jovian parameters outlined above. Specifically, Figs. 6.5a and 6.5b show the first and second order terms  $\varepsilon(\omega/\Omega_J)_{(1)}$  and  $\varepsilon^2(\omega/\Omega_J)_{(2)}$ , plotted versus radial distance  $\rho_e$ , while Fig. 6.6 shows the sum of these two ( $\Delta\omega/\Omega_J$ ). The solid lines in the figures show the higher order terms for the ionospheric plasma angular velocity calculated from Eq. (6.22), while the long-dashed lines show the same terms for the equatorial plasma angular velocity obtained from Eq. (6.23b). Also shown in the figures (and in all succeeding plots) are the small- $\rho_e$  approximations to these profiles, shown up to the leading term in  $(\dot{M}/\Sigma_p^*)$ , i.e. to second order in  $(\dot{M}/\Sigma_p^*)$  for the first order term and to third order in  $(\dot{M}/\Sigma_p^*)$  for the second order term. The small- $\rho_e$  approximations to the ionospheric angular velocity terms, given by Eqs. (6.31b,c) for the first and second order ionospheric profiles, respectively, are shown by the dot-dashed lines. The small- $\rho_e$  approximations to the equatorial plasma angular velocity, obtained from Eq. (6.23b), are shown by the double-dot-dashed lines. Considering the first order ionospheric angular velocity term shown in Fig. 6.5a, it can be seen that the profile initially takes small negative values in the inner region, dropping to a minimum value of  $\sim -0.0015$  at  $\sim 21 R_J$ . After a second minor minimum at  $\sim 36 R_J$  the values then monotonically rise, passing through zero at  $\sim 41 R_J$  and reaching  $\sim 0.008$  at the outer edge of the model at  $100 R_J$ . The initial variations of this profile in the region inside  $\sim 40 R_J$  results from the nature of the  $B_{ze}$  model used, which exhibits relatively sharp behaviour in the transition region at  $\sim 20 R_J$  between the dipolar form and the power law form (Fig. 5.1a), along with the fact that the inhomogeneous term in Eq. (6.22) for  $(\omega_i/\Omega_J)_{(1)}$  involves the

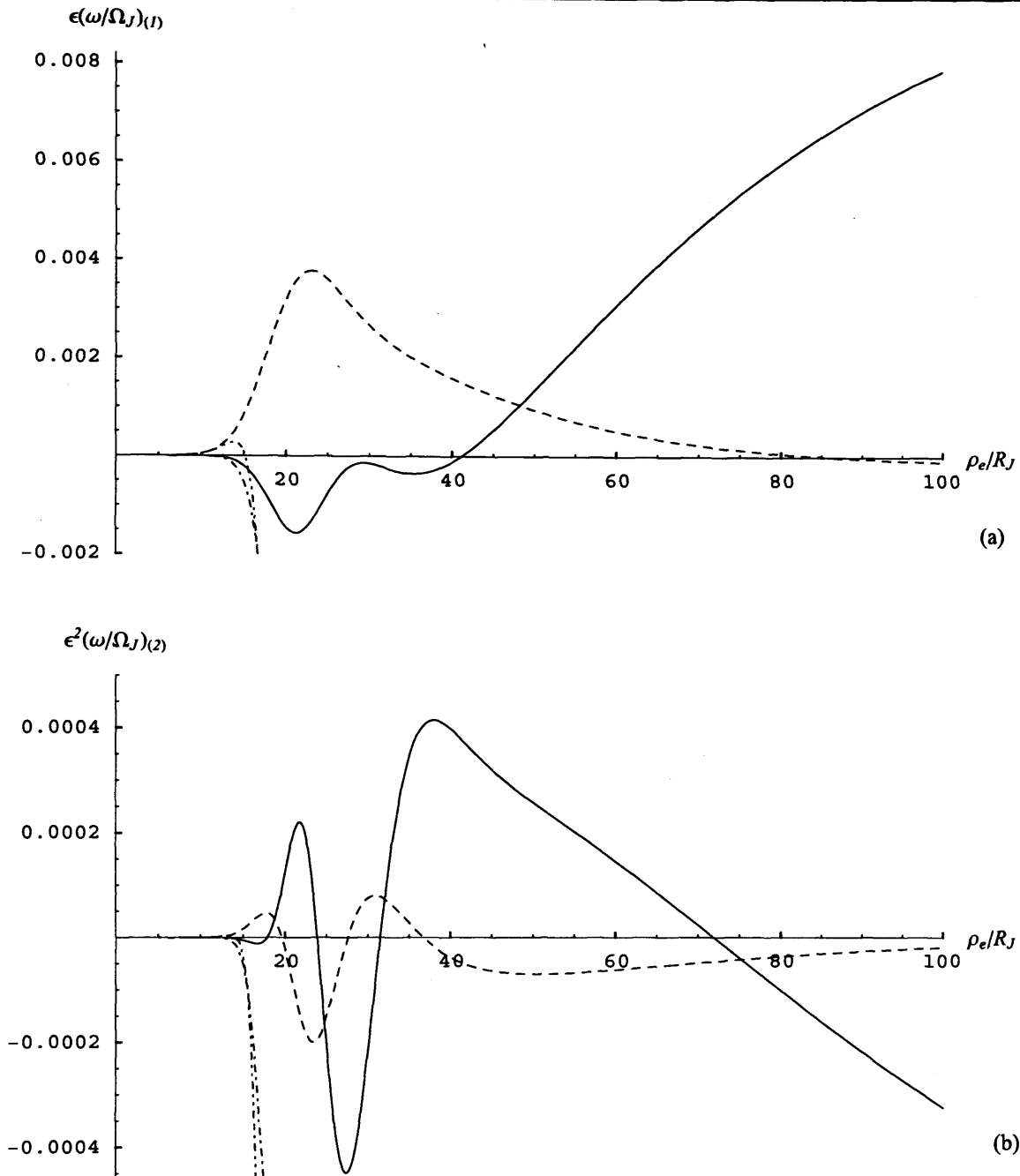


**Figure 6.5.** Plots of higher order terms in the series solution for the plasma angular velocity. Panel (a) shows the first order term  $\varepsilon(\omega/\Omega_J)_{(1)}$ , and panel (b) shows the second order term  $\varepsilon^2(\omega/\Omega_J)_{(2)}$ , both plotted versus radial distance  $\rho_e$ . The solid lines represent the ionospheric plasma angular velocity profiles calculated from Eq. (6.22) with  $n=1,2$  for panels (a) and (b), respectively. The dashed lines show the equatorial plasma angular velocity profiles obtained from the ionospheric solution through Eq. (6.23b), with  $n=1,2$  as appropriate. The single-dot-dashed lines represent the small- $\rho_e$  approximations to the ionospheric angular velocity, given by Eqs. (6.31b,c) for the first and second order profiles, respectively. The double-dot-dashed lines show the small- $\rho_e$  approximations to the equatorial plasma angular velocity, obtained from the ionospheric approximations through Eq. (6.23b). Both approximations are shown up to the leading term in  $(\dot{M}/\Sigma_p^*)$ , i.e. to second order in  $(\dot{M}/\Sigma_p^*)$  for the first order term shown in panel (a), and to third order in  $(\dot{M}/\Sigma_p^*)$  for the second order term shown in panel (b).

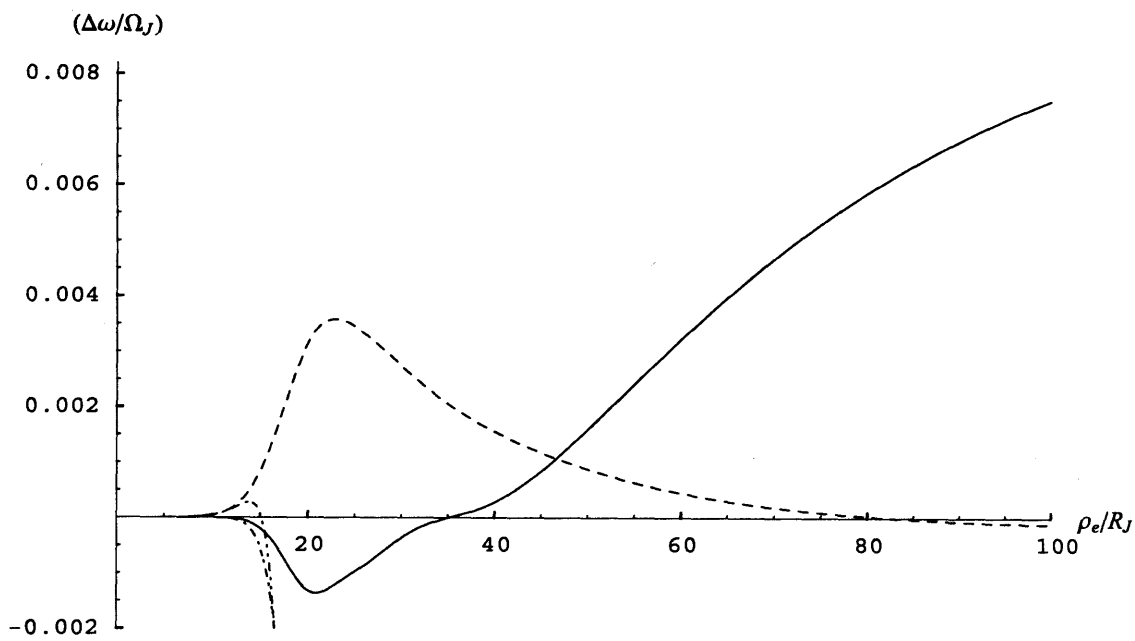


**Figure 6.6.** Plot of the sum of the first and second order terms for the plasma angular velocity shown in Fig. 6.5,  $(\Delta\omega/\Omega_J)$ , plotted versus  $\rho_e$ . The format is the same as in Fig. 6.5.

third order derivative of  $(\omega/\Omega_J)_{(0)}$ . Such rapid variations do not occur if a simple dipole model is used in place of our empirical current sheet model, though the overall nature of the results remain similar. The main point, however, is that the magnitude of the first order term, of order a few thousandths of the planetary angular velocity, is approximately two orders below that of the zeroth order angular velocity profile shown in Fig. 6.1a, such that the first order term can be considered to be very small with respect to the zeroth order term. For the second order ionospheric angular velocity term shown in Fig. 6.5b, it can be seen that the magnitude is even smaller, approximately one order below the first order term. Relatively rapid variations again occur in the region within  $\sim 40 R_J$ , although they are in anti-phase with those in the first order profile. The effect of this can be seen in Fig. 6.6, where the first and second order terms are summed, and the profile appears to be similar to the first order term, but is somewhat smoother in the region inside  $\sim 40 R_J$ . The overall effect of the field-aligned voltage, therefore, is that the ionospheric angular velocity is modestly less than calculated in previous analyses in the region within  $\sim 35 R_J$ , and slightly greater in the region beyond. Considering now the equatorial plasma angular velocity terms, it can be seen that the first order term shown in Fig. 6.5a initially takes positive values, rising to a peak of  $\sim 0.004$  at  $\sim 23 R_J$ , before falling slowly to small negative values at  $100 R_J$ . We note that the equatorial and ionospheric first order terms are equal to each other at  $\rho_e \approx 48 R_J$ , meaning that at this point the total equatorial and ionospheric angular velocities are equal to first order. This occurs at the point where the zeroth order field-aligned current, and consequently the first order field-aligned voltage, reach their maximum values, such that the second term on the RHS of the decoupling equation Eq. (6.4) is zero. The second order term in the equatorial angular velocity, shown in Fig. 6.5b, exhibits peak displacements of  $\sim +8.5 \times 10^{-5}$  and  $\sim -2 \times 10^{-4}$ , which are much smaller than the magnitude of the peak displacements of the first order term, such that the sum of the first and second order terms shown in Fig. 6.6 looks very similar to the first order profile alone.

Figures 6.7 and 6.8 show, in a format similar to Figs. 6.5 and 6.6, the first and second order terms for the azimuth-integrated equatorial radial current given by Eq. (6.24c), along with their sum. It can be seen that the profile of the first order term  $\varepsilon I_{\rho(1)}$  shown in Fig. 6.7a is similar in shape, but opposite in sign, to the first order ionospheric angular velocity term shown in Fig. 6.5a. It rises initially to a peak of  $\sim 0.14$  MA at  $\sim 21 R_J$ , followed by a minor peak at  $\sim 36 R_J$ , and then monotonically decreases to  $\sim -0.56$  MA at  $100 R_J$ . The magnitude

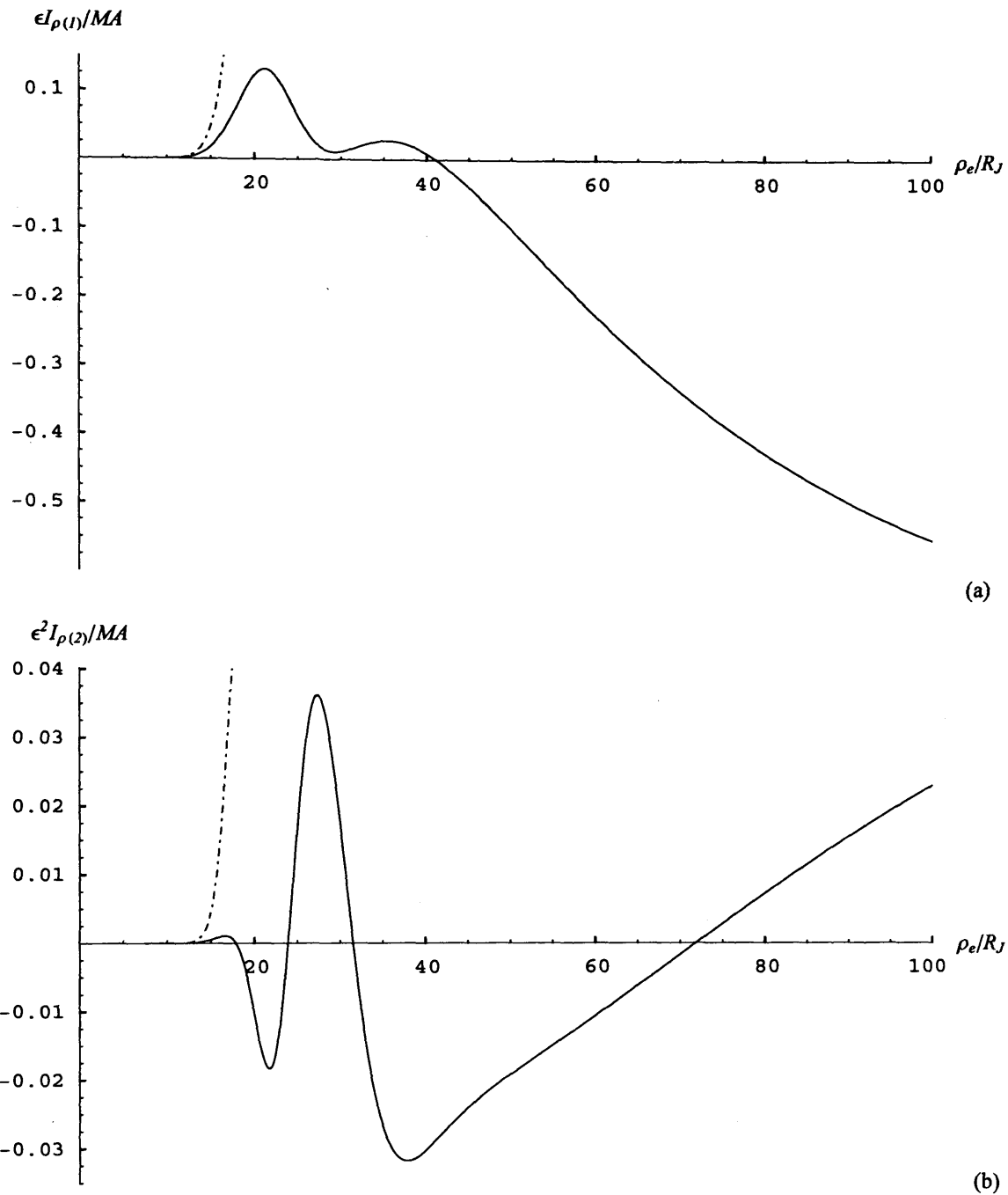


**Figure 6.7.** Plots of higher order terms for the azimuth-integrated equatorial radial current in MA. Panel (a) shows the first order term  $\varepsilon I_{\rho(1)}$ , and panel (b) shows the second order term  $\varepsilon^2 I_{\rho(2)}$ , both plotted versus radial distance  $\rho_e$ . The solid lines represent the radial current profiles calculated from Eq. (6.24c) with  $n=1,2$  for panels (a) and (b), respectively. The dot-dashed lines represent the small- $\rho_e$  approximations to the radial current, calculated from the appropriate small- $\rho_e$  approximations to the ionospheric plasma angular velocity shown in Fig. 6.5.

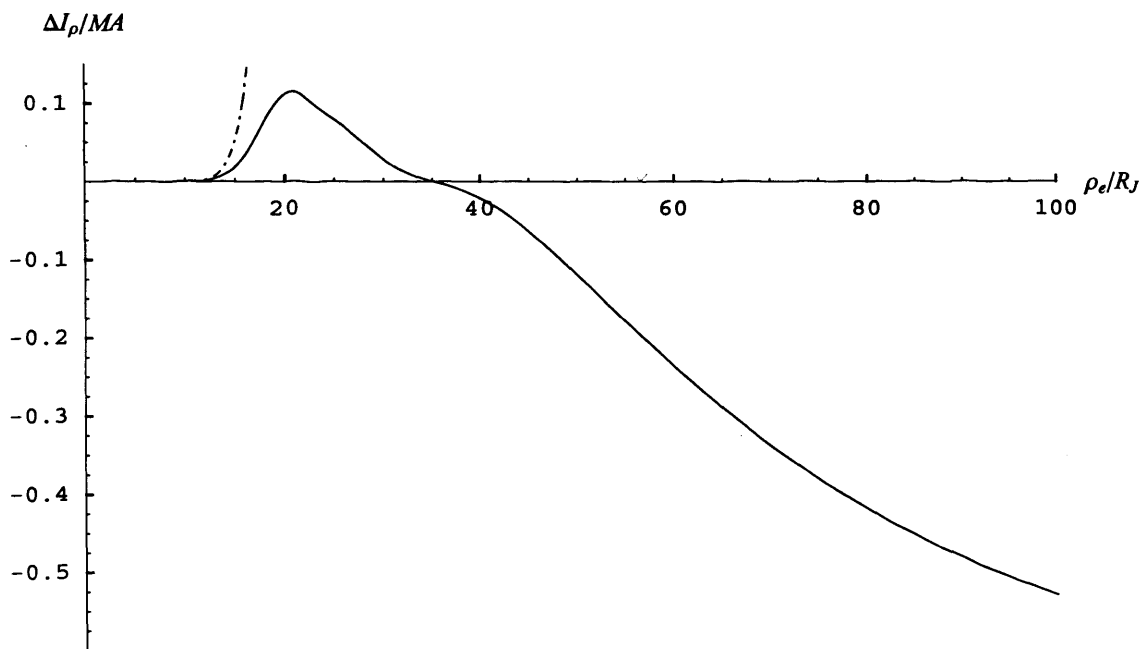


**Figure 6.8.** Plot of the sum of the first and second order terms for the azimuth-integrated equatorial radial current shown in Fig. 6.7,  $\Delta j_{||}$ , plotted versus  $\rho_e$ . The format is as in Fig. 6.7.

of this term is, as with the angular velocity, approximately two orders smaller than that of the zeroth order solution shown in Fig. 6.1b. The second order term  $\varepsilon^2 I_{\rho(2)}$  shown in Fig. 6.7b also takes a similar shape to the second order ionospheric angular velocity profile shown in Fig. 6.5b, but reversed in sign. Again, the magnitude of the second order term is approximately an order below that of the first order term, such that the sum of the two terms  $\Delta I_{\rho}$ , shown in Fig. 6.8, is similar to the first order term, but with less variation within  $\sim 40 R_J$ .

Turning now to the field-aligned current, Figs. 6.9 and 6.10 similarly show the first and second order terms given by Eq. (6.25c), along with their sum. Note that as in Fig. 6.2a, this ionospheric parameter has been mapped along the field lines into the equatorial plane and plotted versus  $\rho_e$  for ease of comparison with the other current system parameters. The first order term for the parallel current  $\varepsilon j_{\parallel(1)}$  shown in Fig. 6.9a exhibits variations within  $\sim 40 R_J$  in a similar manner to the angular velocity and the radial current, after which it drops to negative values, peaking at  $\sim -0.0036 \mu\text{A m}^{-2}$  at  $\sim 75 R_J$ . Again, the magnitude of this term is approximately two orders below the zeroth order term. As with the angular velocity and radial current, the second order field-aligned current term  $\varepsilon^2 j_{\parallel(2)}$  shown in Fig. 6.9b also shows relatively large variations within  $\sim 40 R_J$ , after which the value becomes almost constant at  $\sim 3 \times 10^{-4} \mu\text{A m}^{-2}$ , approximately an order of magnitude below the magnitude of the first order term. The variations in the second order term are again in anti-phase with those in the first order term, such that the sum of the two terms  $\Delta j_{\parallel}$  shown in Fig. 6.10 is relatively smooth below  $\sim 40 R_J$ . The main feature in the  $\Delta j_{\parallel}$  profile is the minimum of  $\sim -0.0033 \mu\text{A m}^{-2}$  at  $\sim 72 R_J$ , implying a slight reduction in the amplitude of the field-aligned current compared with the zeroth order solution.

We finally show in Figs. 6.11 to 6.14, in a similar manner to Figs. 6.1 and 6.4, the sums of the zeroth, first, and second order terms for the system parameters shown as solid lines, along with the appropriate small- $\rho_e$  approximations, and compare them with the zeroth order solution, which is shown by the short-dashed lines. Figure 6.11a shows the sum of the equatorial plasma angular velocity terms  $(\omega_e/\Omega_J)'$ , i.e. the sum of the profile in Fig. 6.1a with the dashed-line profile in Fig. 6.6. It can be seen that this profile is closely

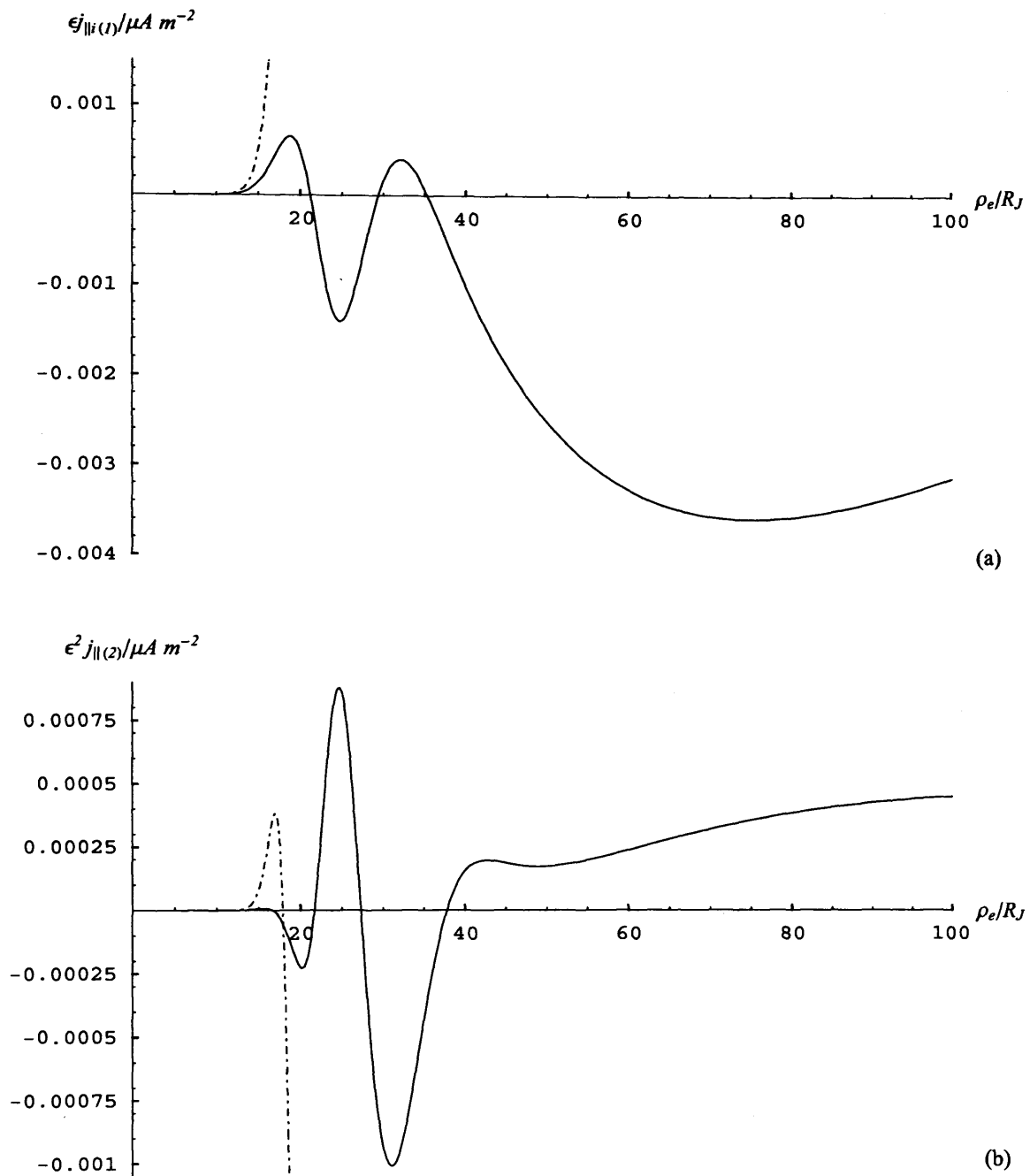


**Figure 6.9.** Plots of higher order terms for the ionospheric field-aligned current in  $\mu A m^{-2}$ . Panel (a) shows the first order term  $\epsilon j_{||}^{(1)}$ , and panel (b) shows the second order term  $\epsilon^2 j_{||}^{(2)}$ , both plotted versus radial distance  $\rho_e$ . The solid lines represent the field-aligned current profiles calculated from Eq. (6.25c) with  $n=1,2$  for panels (a) and (b), respectively. The dot-dashed lines represent the small- $\rho_e$  approximations to the field-aligned current, calculated from the appropriate small- $\rho_e$  approximations to the ionospheric plasma angular velocity shown in Fig. 6.5.

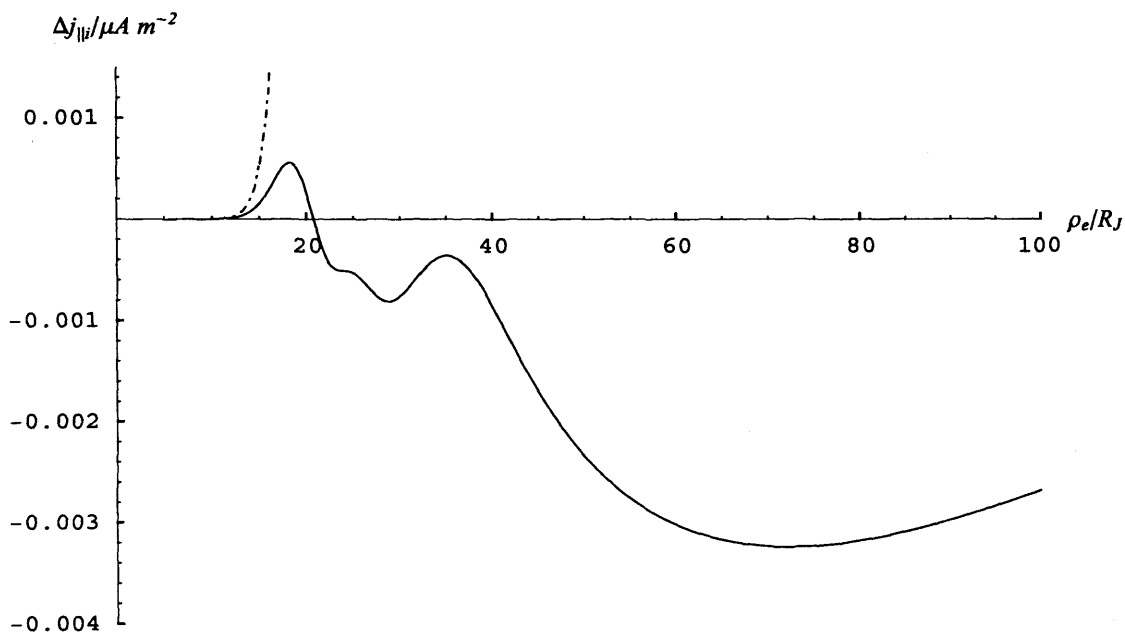


**Figure 6.10.** Plot of the sum of the first and second order terms for the ionospheric field-aligned current shown in Fig. 6.9,  $\Delta j_{||}$ , plotted versus  $\rho_e$ . The format is the same as in Fig. 6.9.

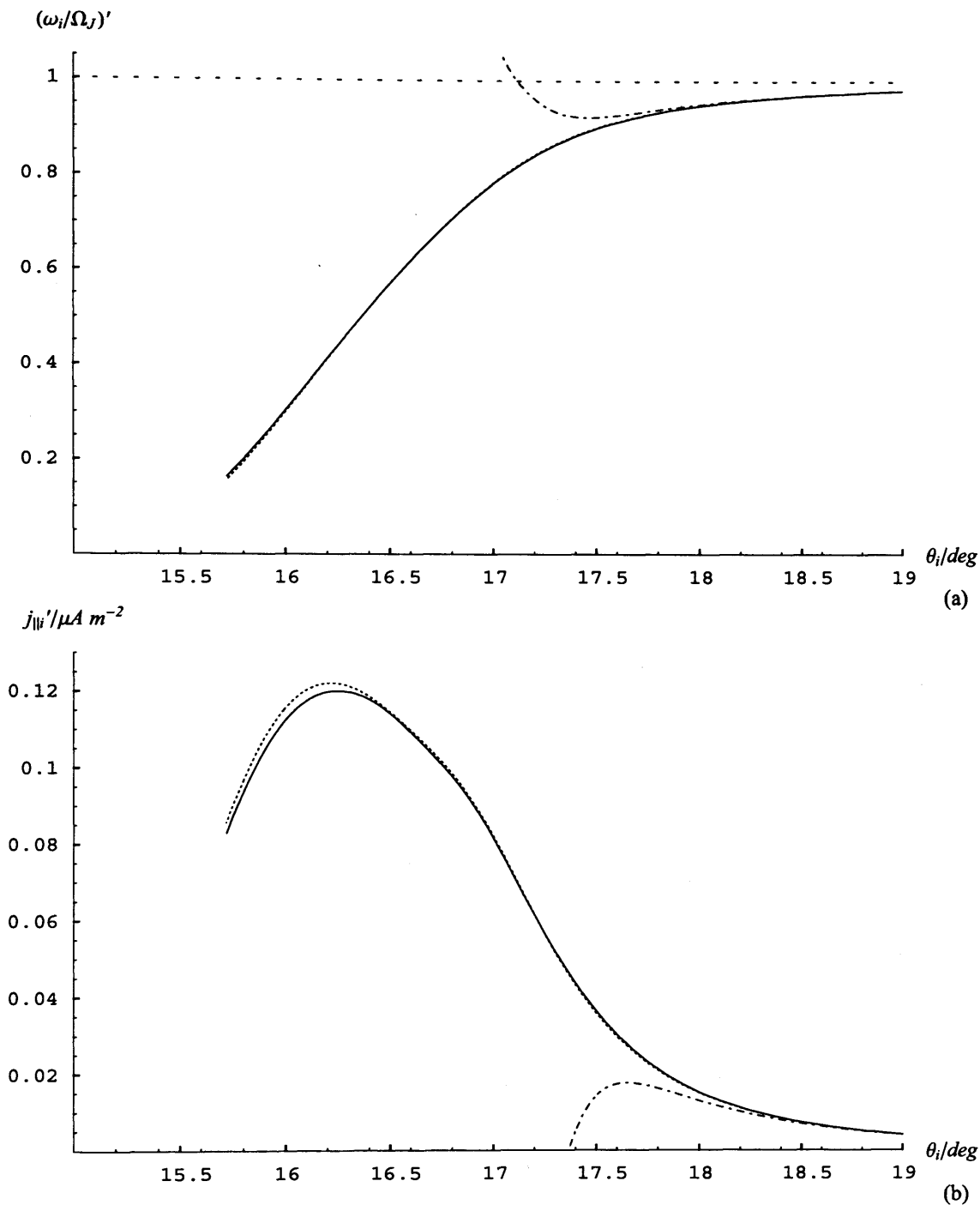


**Figure 6.13.** Plots of the sums of the zeroth, first, and second order terms for the current system parameters. All parameters are plotted versus ionospheric co-latitude  $\theta_i$ . The format is the same as in Fig. 6.10. Panel (a) shows the sum of the ionospheric plasma angular velocity terms  $(\omega_i/\Omega_J)'$ . Panel (b) shows the sum of the field-aligned current terms  $j_{\parallel i}'$  in  $\mu A m^{-2}$ .

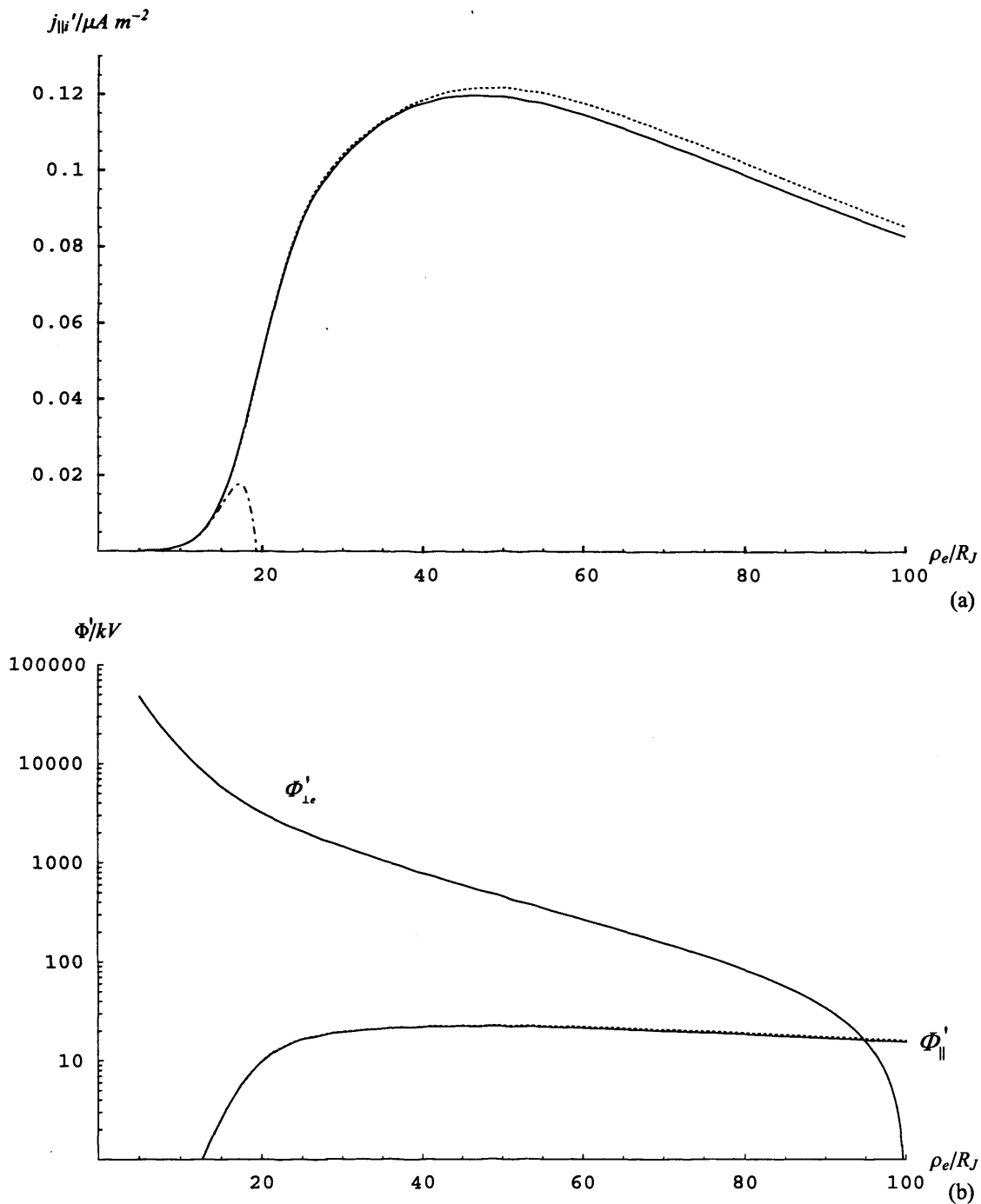


**Figure 6.12.** Plots of the sums of the zeroth, first, and second (and third in the case of the field-aligned voltage) order terms for the system parameters. All parameters are plotted versus radial distance  $\rho_e$ . The format is the same as in Fig. 6.11. Panel (a) shows the sum of the field-aligned current terms  $j_{\parallel}'$  in  $\mu A m^{-2}$ . Panel (b) is a log-linear plot of the equatorial electrostatic potential  $\Phi_{\perp e}'$  in kV calculated from the equatorial plasma angular velocity profile shown in panel (a) using Eq. (6.37), together with the sum of the field-aligned voltage terms  $\Phi_{\parallel}'$  calculated from the ionospheric plasma angular velocity profile shown in Fig. 6.13a using Eq. (6.26d) with  $n = 3$ .

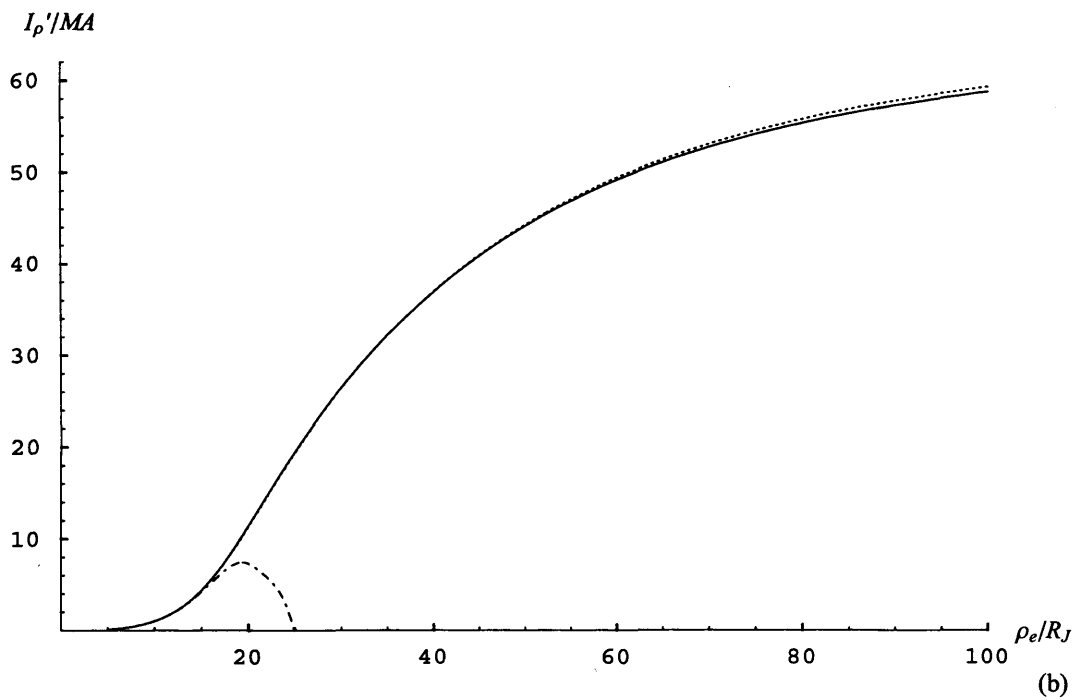
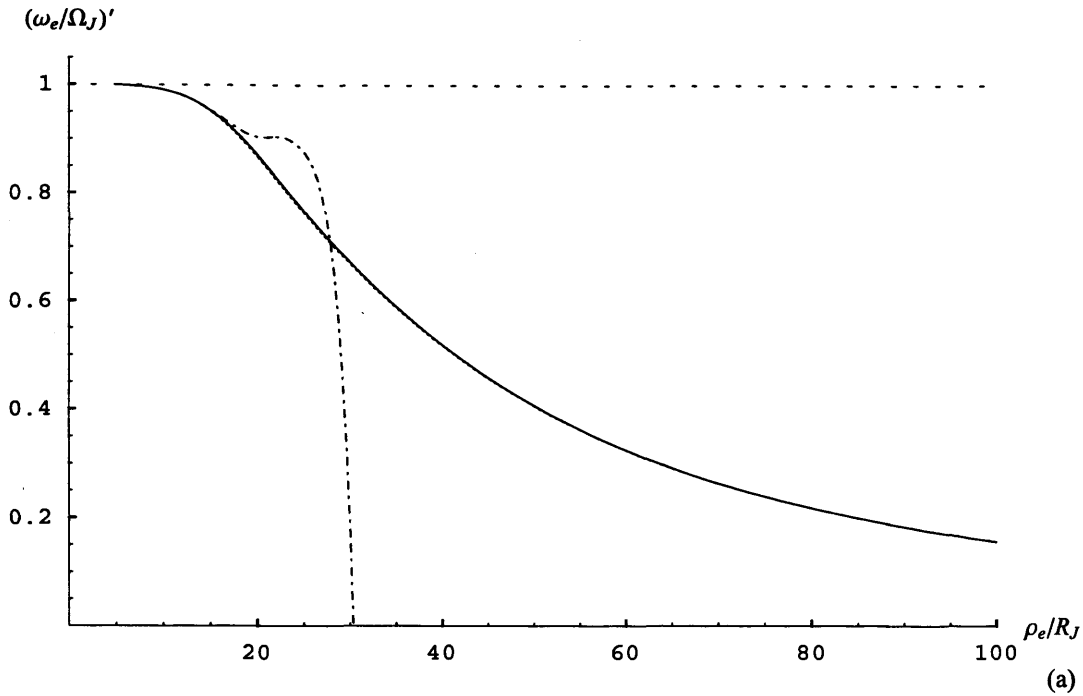


**Figure 6.11.** Plots of the sums of the zeroth, first, and second order terms for the system parameters. All parameters are plotted versus radial distance  $\rho_e$ . The format is the same as in Fig. 6.1, except that the zeroth order solution is also shown by the short-dashed lines for comparison. Panel (a) shows the sum of the equatorial plasma angular velocity terms  $(\omega_e/\Omega_J)'$ . Panel (b) shows the sum of the azimuth-integrated equatorial radial current terms  $I_\rho'$  in MA.

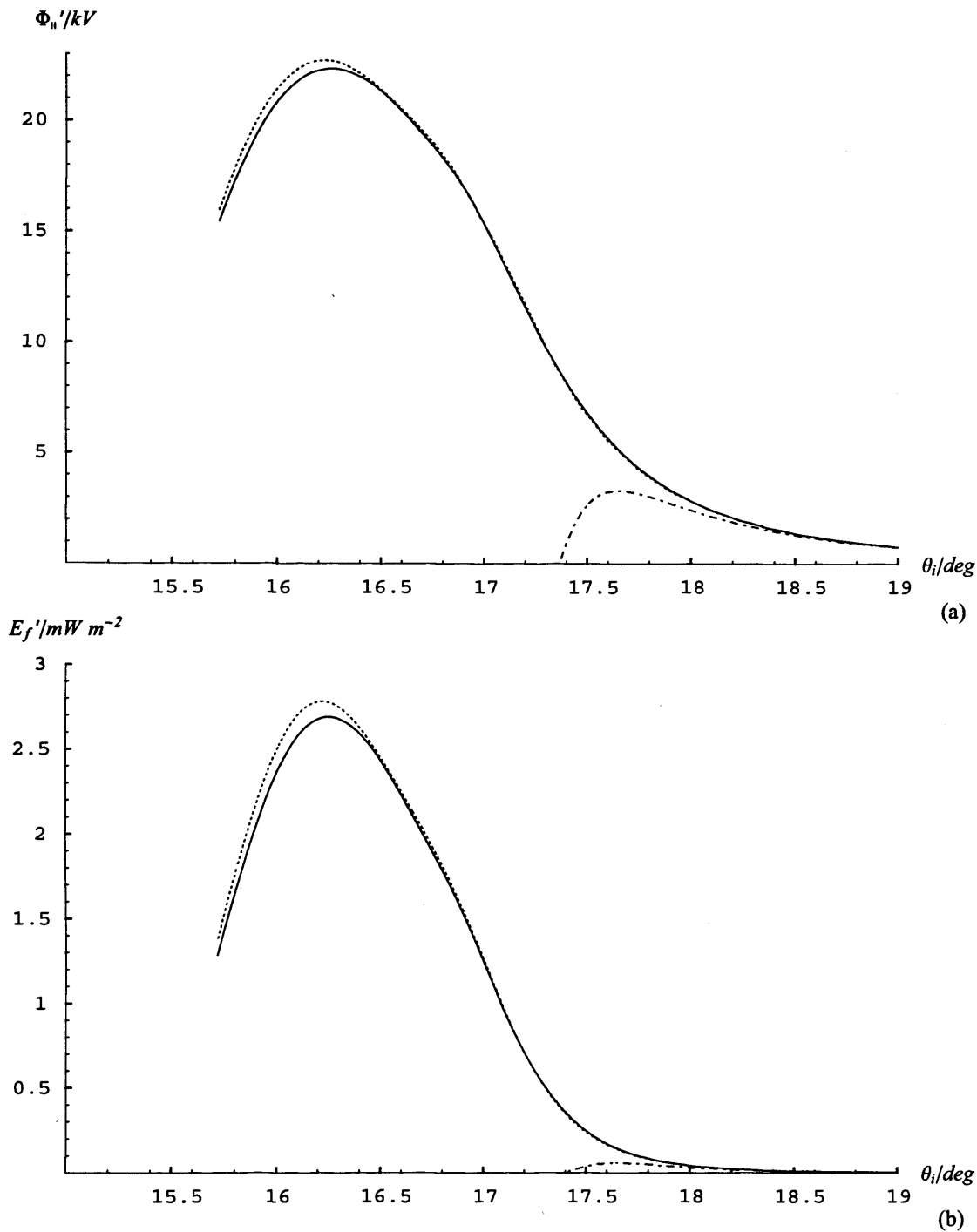


**Figure 6.14.** Plots of the sums of the zeroth, first, and second (and third in the case of the field-aligned voltage) order terms for the current system parameters. All parameters are plotted versus ionospheric co-latitude  $\theta_i$ . The format is the same as in Fig. 6.10. Panel (a) shows the sum of the field-aligned voltage terms  $\Phi_{||}'$  in kV. Panel (b) shows the precipitating energy flux  $E_f'$  calculated from the field-aligned voltage profile shown in panel (a) through Eq. (6.37).

similar to the zeroth order profile above, such that the effect of adding the  $(\Delta\omega_e/\Omega_J)$  profile shown in Fig. 6.6 can hardly be distinguished on this scale. The same is true for the equivalent plot for the ionospheric plasma angular velocity  $(\omega_i/\Omega_J)'$  (i.e. the sum of the profile in Fig. 6.3a and the solid line profile in Fig. 6.6), shown in Fig. 6.13a. It is only really possible to see the difference in the very poleward region, corresponding to the relatively large positive values of  $(\Delta\omega_i/\Omega_J)$  in the outer region of Fig. 6.6, and even here the difference is very small. Figure 6.11b shows the corresponding sum of the terms for the azimuth-integrated equatorial radial current  $I_\rho'$ , i.e. the sum of the profiles shown in Figs. 6.1b and 6.8. It can be seen that, as with the angular velocity, the profiles are very similar, with a modest reduction in the current amplitude in the outer region corresponding to the negative values of  $\Delta I_\rho$  in the outer region of Fig. 6.8. Figure 6.12a shows the sum of terms for the field-aligned current  $j_{\parallel}'$ , i.e. the sum of the profiles shown in Figs. 6.2a and 6.10. Again, the difference between this profile and the zeroth order profile is small. The peak in the current is reduced by  $\sim 0.0033 \mu\text{A m}^{-2}$ , a value which is approximately two orders of magnitude below the peak amplitude of  $\sim 0.12 \mu\text{A m}^{-2}$ , and is shifted inward by  $\sim 2 R_J$ , a distance that is small considering the peak covers the majority of the middle magnetosphere. The ionospheric mapping of the field-aligned current is shown in Fig. 6.13b, where it can be seen that the inward shift of the peak in the current in the equatorial plane corresponds to a slight equatorward shift of the peak in the ionosphere by  $\sim 0.1^\circ$ , which is small with respect to the  $\sim 2.5^\circ$  width of the peak. Considering now the voltages shown in Fig. 6.12b, the 'upper' solid line in the figure shows the equatorial electrostatic potential  $\Phi_{\perp e}'$  computed from the equatorial plasma angular velocity profile shown in Fig. 6.11a using Eq. (6.37). The difference between this and the zeroth order profile is negligible, such that the difference cannot be seen on this scale. As in Fig. 6.2b, the field-aligned voltage  $\Phi_{\parallel}'$  calculated from this order of the angular velocity is also plotted in the 'lower' solid line in Fig. 6.12d, such that the field-aligned voltage here is shown to the next, i.e. third, order (Eq. (6.26d)). On this log scale the difference between this and the first order voltage, shown dashed, is not easily visible, and may more readily be distinguished on the ionospheric mapping of the field-aligned voltage  $\Phi_{\parallel}'$  shown in Fig. 6.14a. It can be seen that the difference in the field-aligned voltage is similar to that

for the field-aligned current, i.e. a slight decrease in magnitude and a  $\sim 0.1^\circ$  equatorward shift of the peak. The same is true for the precipitating energy flux  $E_f'$  shown in Fig. 6.14b, which is calculated from the field-aligned voltage shown in Fig. 6.14a using Eq. (6.27).

#### 6.4. *Summary and conclusion*

In this chapter we have considered the magnetosphere-ionosphere coupling current system that flows in Jupiter's middle magnetosphere and is believed to be associated with the jovian main auroral oval. Previous works have assumed perfect mapping of the electric field and flow along equipotential field lines between the ionosphere and the magnetosphere, while it is known that substantial field-aligned voltages must exist to drive the currents responsible for the main oval auroras. However, Cowley and Bunce (2001b) noted that these field-aligned voltages, generally of order a few tens of kV, are much smaller than the radial voltage due to plasma corotation, which is of order  $\sim 3$  MV across the middle magnetosphere, and they therefore suggested that the effect on the system would not be great. In this chapter we have, for the first time, self-consistently incorporated these field-aligned voltages into the modelling of the system. The inclusion of field-aligned potential drops has the effect of decoupling the magnetospheric and ionospheric electric fields, such that the plasma angular velocities in these two regions will generally differ from each other, with consequences for the currents flowing in the system. The field-aligned voltages were incorporated into the model using Knight's (1973) kinetic theory, which gives the potential drop required to drive a given field-aligned current. This dependency of the field-aligned voltage on the field-aligned current is incorporated into the equation which decouples the ionospheric and the magnetospheric angular velocity (Eq. (6.5) above), which is one of three first order differential equations that must be solved. The other two consist of the current continuity equation that gives the parallel current from the ionospheric Pedersen current, and the Hill-Pontius equation for the plasma angular velocity, which is based on Newton's second law (Eqs. (6.11) and (6.14)). These three equations can be combined to form one third order linear inhomogeneous equation for the ionospheric plasma angular velocity (Eq. (6.18)) that can be solved as a power series in  $\varepsilon$ , given that  $\varepsilon$  is small. The dimensionless parameter  $\varepsilon$  is related to the magnetospheric

'source' electron parameters that determine the field-aligned voltages, but in principle could be set arbitrarily large or small, representing large or small field-aligned voltages. However, given the values of the system parameters expected to exist at Jupiter, and which we have used in this and previous chapters, we find that  $\varepsilon$  is small, of order  $\sim 1.5 \times 10^{-5}$ . Hence a power series solution is appropriate to the jovian system. The zeroth order solution corresponds to those which have been presented previously, in which there is no decoupling between the ionosphere and magnetosphere. Higher orders then introduce the decoupling due to field-aligned voltages, such that the ionospheric and equatorial plasma angular velocity profiles are modified, as are the resulting current profiles. In this chapter the solution was taken to second order.

The results of the numerical evaluation of the equations showed that for the given values of the system parameters taken in this study, representative of the jovian conditions, the decoupling effect due to the existence of field-aligned voltages is small, as suggested by Cowley and Bunce (2001b). The overall effect on the equatorial plasma angular velocity is such that over the majority of the middle magnetosphere it is raised above the zeroth order result by values peaking approximately two orders of magnitude below those of the zeroth order term, such that the effect is very small. The ionospheric plasma angular velocity is modified by similar factors, initially dropping below the zeroth order result in the inner region, while rising above the latter in the outer region, although again the effect is small. The field-perpendicular and field-aligned current values are similarly reduced by values approximately two orders of magnitude below the zeroth order results, and the peak in the field-aligned current is shifted equatorward by  $\sim 0.1^\circ$ , which is small compared to its  $\sim 2.5^\circ$  latitudinal width. The field-aligned voltage and precipitating energy flux are likewise slightly reduced and shifted. Overall, we find that the effect of the field-aligned voltages in this study is small for typical jovian conditions, thus validating the procedures adopted in previous chapters, and the results obtained, as reasonable approximations.

## ***Chapter 7***

### ***Summary and Future Work***

#### ***7.1. Introduction***

The magnetosphere of Jupiter is the largest object in the solar system. It is unfortunate that it is not visible from Earth, because if it were it would appear to be as large as the Sun in the sky. However, the jovian magnetosphere has been under scrutiny from Earth since the 1950s, when the nature of the magnetic field was inferred from jovian radio emissions. In the 1970s the study of Jupiter changed from being astronomy to space science when the first spacecraft reached the planet, imaging the planet and observing the plasma environment. To date, seven spacecraft have visited Jupiter, these being Pioneer-10 and -11, Voyager-1 and -2, Ulysses, Galileo, and Cassini. What was discovered was a magnetosphere vastly different from our own. The large strength of the planetary field, the rapid spin of the planet, and the existence of the most volcanic moon in the solar system, Io, combine to create a magnetosphere, the dynamics of which are largely driven by internal processes rather than external processes as in the case of the Earth. The Io plasma source is estimated to have a sulphur and oxygen plasma production rate of order one tonne per second, a value which is equivalent to that of an active comet. The iogenic plasma is accelerated by the rapidly spinning magnetic field and diffuses centrifugally outwards. Conservation of angular momentum causes the plasma angular velocity to reduce as the plasma diffuses radially outwards, a process which is resisted by ion-neutral collisions at the ionospheric end of the field lines. As a consequence, a current system is set up, the result of which is that equatorial plasma is accelerated back up towards corotation with the planet. A key feature of the current system is the existence of substantial upward-directed field-aligned currents, which are believed to be associated with the 'main oval' aurorae on Jupiter. The first theoretical model for the magnetosphere-ionosphere coupling current system was provided by Hill (1979), who considered the case of the dipole field. This was later generalised to include a more realistic field by Pontius (1997), who concluded that the

field model was not a significant factor in the system for the equatorial plasma angular velocity. In neither paper were the currents specifically computed, however. Cowley and Bunce (2001b) calculated the currents using an empirically-based ‘current sheet’ field model and an empirical model of the equatorial plasma angular velocity, and concluded that the field model was indeed a factor, as the field-aligned currents were an order of magnitude larger for the current sheet model than for the dipole. They thus suggested that the main oval aurorae originate from the field-aligned currents driven by this system. The work was extended by Cowley, Nichols and Bunce (2002), who calculated both the equatorial plasma flow and the currents from first principles using the theory of Hill and Pontius, and confirmed the result of Cowley and Bunce (2001b). However, their model lacked self-consistency in key two areas, these concerning the jovian ionospheric Pedersen conductivity and field-aligned auroral voltages. The work described in this thesis examines the effect of self-consistently including these parameters in the model.

## ***7.2. Dependence on the Pedersen conductivity and the mass outflow rate***

The above cited papers all make key assumptions concerning two of the model input parameters, specifically the ionospheric Pedersen conductivity and the iogenic plasma mass outflow rate. They all use ‘reasonable’ spot values of both, of order a few tenths of a mho for the Pedersen current and of order a thousand  $\text{kg s}^{-1}$  for the mass outflow rate. However, the values of these parameters are not accurately known at present. This uncertainty prompted the study presented in Chapter 4, which looked at the behaviour of the system over wide ranges of the two parameters, and compared the results for both the dipole and current sheet models. We showed that the results of the previous studies, for example that the field-aligned current is much larger for the current sheet field model than the dipole, are generally valid over these ranges. The knowledge of how the system behaves with respect to these parameters, particularly the Pedersen conductivity, proved a useful background with which to pursue the more complex studies of later chapters.

### ***7.3. Effect of precipitation-induced enhancements of the Pedersen conductivity***

A major limitation of previous work on the magnetosphere-ionosphere coupling current system is the lack of any self-consistent treatment of the ionospheric Pedersen conductivity, which had just been treated as a constant parameter in the model. However, the existence of significant field-aligned currents, as predicted by the theory, is expected to enhance the Pedersen conductivity by anything up to an order of magnitude in the region of current flow. In the work presented in Chapter 5 of this thesis we have, for the first time, taken into account the enhancement of the Pedersen conductivity in regions of field-aligned current flow. We used Knight's (1973) theory to estimate the properties of the electron precipitation due to the field-aligned current, and combined this with the modelling results of Millward (2002) to develop a dependence of the Pedersen conductivity on the field-aligned current. We then incorporated this into the model for the magnetosphere-ionosphere coupling current system. The results help reconcile the theoretical predictions with three separate aspects of observational evidence. For twenty-five years it has not been understood why the plasma angular velocity in the equatorial plane does not decrease as fast as predicted by Hill's (1979) theory. Indeed, this was a motivation behind Pontius' (1997) generalisation of the theory to include a more realistic field model than the dipole, a study which found the angular velocity to be insensitive to the field model. We have shown that the effect of including precipitation-induced enhancements of the Pedersen conductivity is just such to maintain the plasma near to rigid corotation out to much further distances than predicted by a constant conductivity model. The equatorial radial current profile shows a rapid increase in the inner region and plateaus off thereafter, in accordance with Galileo observations of the equatorial magnetic field. The field-aligned current, meanwhile, is concentrated in a peak in the inner region at  $\sim 20\text{-}30 R_J$ , which is the region to which the observed main oval has traditionally been mapped.

#### ***7.4. Effect of magnetosphere-ionosphere decoupling by field-aligned auroral voltages***

The second aspect of the model which lacked any self-consistent treatment concerned the field-aligned voltages required to drive the computed field-aligned currents. In calculating the currents flowing in the system, the electric field and plasma flow were mapped between the ionosphere and the equatorial plane along equipotential field lines, and the field-aligned voltages were subsequently computed using Knight's (1973) theory. In general, however, it is expected that field-aligned voltages will decouple the ionospheric and equatorial electric fields, such that the plasma velocities in these two regions will be different. However, Cowley and Bunce (2001b) noted that the calculated field-aligned voltages are much smaller than the field-perpendicular voltages associated with plasma corotation and they suggested that the effect would be small. In the work presented in Chapter 6 we have self-consistently incorporated the potential drops in calculating the plasma flows and currents. We developed a third order differential equation for the ionospheric plasma angular velocity which was solved as a power series under 'typical' jovian conditions. The zeroth order solution in the power series was just the case presented previously, with the field-aligned voltage taken to be zero. Higher orders then introduced the effect of field-aligned potential drops. In Chapter 6 we presented results to second order. We showed that the effect of the inclusion of field-aligned voltages is small, such that the typical difference between the zeroth order profiles and those taken to second order was two orders of magnitude below the zeroth order values. The main conclusion was that the assumption made in previous works that the calculated field-aligned voltages have only a small effect on the solution is generally valid, such that their results obtained are reasonable approximations.

#### ***7.5. Future work***

A number of issues arise following the work presented in this thesis. First, the empirical model of the Pedersen conductivity greatly improved the 'fit' of the theoretical radial current profiles with the observed profile obtained from Galileo data. However, we saw

that even with the empirical model, the innermost data points had values much higher than the theoretical profile in this region, unless the mass outflow rate was raised significantly higher than observational evidence suggests it is. The conjecture was, therefore, that the values of the north-south equatorial magnetic field model are too high in this region, and may need to be revised. Therefore, a study of the validity of the model with respect to observed  $B_{ze}$  profiles is warranted.

Another result of the use of an empirical model for the conductivity was the concentration of the field-aligned current profile into a peak in the inner region of the middle magnetosphere. Previous work, which had resulted in a field-aligned current peak that was spread over the entire middle magnetosphere, led to suggestions that the brightness of the main oval would be anti-correlated with the strength of the solar wind at Jupiter (Cowley and Bunce, 2003b). The reasoning behind this is that if the strength of the solar wind decreases, for example, the magnetosphere then expands, such that the ionosphere needs to work harder to maintain the corotation of equatorial plasma out to these further distances. Hence, the currents required to enforce this corotation, and the consequential auroral brightness, would increase. However, no such variations in the brightness of the main oval have been observed. In light of the results presented in Chapter 5, however, a potential resolution of this problem becomes apparent. If the field-aligned currents responsible for the main oval flow much deeper within the magnetosphere than previously thought, then they may be much less susceptible to changes in the solar wind and outer regions of the magnetosphere than originally predicted. Therefore a study along the lines of Cowley and Bunce (2003b), but with the incorporation of the empirical model for the conductivity, is warranted to discover whether this is indeed the case.

A third potential development lies in the fact that the models presented in this thesis are all one dimensional. That is, they contain no information about the azimuthal dependence of, say, the plasma mass outflow rate, the non-dipolar terms in the ionospheric field, or the day-night asymmetry due to dayside pressure from the solar wind. A brief look at the jovian aurora, such as in the image shown in Fig. 2.8, indicates that the main oval is not, strictly, an oval. Rather, it is more like a kidney-bean in shape. The kidney-bean is observed to corotate with the dipole, such that it seems that the most important factor is the non-axisymmetric planetary field. Therefore, a substantial improvement in our

understanding of the observations would be made if azimuthal effects were incorporated into the model.

Looking more widely, another timely topic at present concerns the kronian magnetosphere, as within the last few months Cassini arrived at Saturn. Relatively little is known about Saturn's magnetosphere, although this will hopefully change as Cassini sends back data over the coming years. The kronian magnetosphere is very different again from that of Jupiter. The strength of the planetary field is less than Jupiter's, and there does not exist one substantial internal plasma source comparable to Io, although it is thought that the rings and the moons Dione and Rhea do contribute significantly. It has been suggested by Cowley and Bunce (2003b) that, although the same current system exists at Saturn, it is not strong enough to generate aurorae. They suggested, therefore, that Saturn's auroral oval is not driven by the same mechanism that energises Jupiter's, but may be more like the Earth's in nature and driven by external processes. With the new *in situ* data, it will be possible to investigate the plasma flows, currents and magnetic fields in detail to determine the processes occurring in Saturn's magnetosphere. In any case, there is much more to be discovered about the magnetospheres of both these and other worlds.

**References**

Achilleos, N., Miller, S., Tennyson, J., Aylward, A.D., Mueller-Wodarg, I., and Rees, D.: JIM: A time-dependent, three-dimensional model of Jupiter's thermosphere and ionosphere, *J. Geophys. Res.*, 103, 20089, 1998.

Alfvén, H.: *Cosmic plasmas*, Riedel, Dordrecht, 1981.

Bagenal, F.: Empirical model of the Io plasma torus, *J. Geophys. Res.*, 99, 11043, 1994.

Bagenal, F.: The ionization source near Io from Galileo wake data, *Geophys. Res. Lett.*, 24, 2111, 1997.

Bagenal, F., Crary, F.J., Stewart, A.I.F., Schneider, N.M., Gurnett, D.A., Kurth, W.S., Frank, L.A., Paterson, W.R.: Galileo measurements of plasma density in the Io torus, *Geophys. Res. Lett.* 24, 2119, 1997.

Ballester, G.E., et al.: Time-resolved observations of Jupiter's far-ultraviolet aurora, *Science* 274, 409-413, 1996.

Balogh, A., Beek, T.J., Forsyth, R.J., Hedgecock, P.C., Marquedant, R.J., Smith, E.J., Southwood, D.J., Tsurutani, B.T.: The magnetic field investigation on the Ulysses mission: instrumentation and preliminary scientific results, *Astron. Astrophys. Suppl. Ser.* 92, 221, 1992a.

Balogh, A., Dougherty, M.K., Forsyth, R.J., Southwood, D.J., , Smith, E.J., Tsurutani, B.T., Murphy, N., Burton, M.E.: Magnetic field observations during the Ulysses flyby of Jupiter, *Science* 257, 1515, 1992b.

Bame, S.J., Barraclough, B.L., Feldman, W.C., Gisler, G.R., Gosling, J.T., McComas, D.J., Phillips, J.L., Thomsen, M.F., Goldstein, B.E., Neugebauer, M.: Jupiter's magnetosphere: plasma description from the Ulysses flyby, *Science* 257, 1539, 1992.

## *References*

---

- Barbosa, D.D., Scarf, F.L., Kurth, W.L., and Gurnett, D.A.: Broadband electrostatic noise and field-aligned currents in Jupiter's middle magnetosphere, *J. Geophys. Res.*, 86, 8357, 1981.
- Belcher, J.W.: The low-energy plasma in the jovian magnetosphere, in *Physics of the Jovian Magnetosphere*, edited by A.J. Dessler, p.68, Cambridge Univ. Press, Cambridge, U.K., 1983.
- Berge, G. L.: An interferometric study of Jupiter at 10 and 21 cm, *Radio Sci.* 69D, 1552, 1965.
- Berge, G. L.: An interferometric study of Jupiter's decametric radio emission, *Astrophys. J.* 146, 767, 1966.
- Biermann, L.: Kometenschwerfe und solare korpuskularstrahlung, *Z. Astrophys.* 29,274, 1951.
- Bigg, E.K.: Influence of the satellite Io on Jupiter's decametric emission, *Nature*, 203, 1008, 1964.
- Brice, N.M. and Ioannidis, G.A.: The magnetospheres of Jupiter and Earth, *Icarus* 13, 173 1970.
- Broadfoot, A. L., Belton, M.J.S., Takacs, P.Z., Sandel, B.R., Shemansky, D.E., Holberg, J.B., Ajello, J.M., Atreya, S.K., Donahue, T.M., Moos, H.W., Bertaux, J.L., Blamont, J.E., Strobel, D.F., McConnell, J.C., Dalgarno, A., Goody, R., and McElroy, M.B.: Extreme ultraviolet observations from Voyager 1 encounter with Jupiter, *Science* 204, 979, 1979.
- Broadfoot, A.L., Sandel, B.R., Shemansky, D.E., McConnell, J.C., Smith, G.R., Holberg, J.B., Atreya, S.K., Donahue, T.M., Strobel, D.F., and Bertaux, J.L., Overview of the Voyager ultraviolet spectrometry results through Jupiter encounter, *J. Geophys. Res.*, 86, 8259, 1981.

## *References*

---

- Brown, R. A.: Optical line emission from Io, In: *Exploration of the Planetary System*, A. Woszczyk and C Iwaniszewska (Eds.), Reidel, Dordrecht, p. 527, 1974.
- Brown, M.E.: Observations of mass loading in the Io torus, *Geophys. Res. Lett.*, 21, 10, 847, 1994.
- Burke, B.F. and Franklin, K.L.: Observations of a variable radio source associated with the planet Jupiter, *J. Geophys. Res.*, 60, 213, 1955.
- Bunce, E.J. and Cowley S.W.H.: Divergence of the equatorial current in the dawn sector of Jupiter's magnetosphere: analysis of Pioneer and Voyager magnetic field data, *Planet. Space Sci.*, 49, 1089, 2001.
- Bunce, E.J., Hanlon, P.G., and Cowley, S.W.H.: A simple empirical model of the equatorial radial field in Jupiter's middle magnetosphere, based on spacecraft fly-by and Galileo orbiter data, *Planet. Space Sci.*, 50, 789-806, 2002.
- Carr, T.D., Desch, M.D., Alexander, J.K.: Phenomenology of magnetospheric radio emissions, In: *Physics of the Jovian Magnetosphere*, A. J. Dessler (Ed.), Cambridge University Press, p. 7, 1983.
- Caudal, G.: A self-consistent model of Jupiter's magnetodisc including the effects of centrifugal force and pressure, *J. Geophys. Res.*, 91, 4201, 1986.
- Chamberlain, J.W., and Hunten, D.M.: *Theory of planetary atmospheres: an introduction to their physics and chemistry*, Academic Press, New York, 1987.
- Clarke, J.T., Moos, H.W., Atreya, S.K., and Lane, A.L.: Observation from Earth orbit and variability of the polar aurora on Jupiter, *ApJ* 241, L179-L182, 1980.
- Clarke, J.T., Ballester, G., Trauger, J., Ajello, J., Pryor, W., Tobiska, K., Connerney, J.E.P., Gladstone, G.R., Waite, J.H., Jr, Ben Jaffel, L., and Gérard, J.-C.: Hubble Space Telescope imaging of Jupiter's UV aurora during the Galileo orbiter mission, *J. Geophys. Res.*, 103, 20217, 1998.

## *References*

---

- Clarke, J.T., Grodent, D., Cowley, S.W.H., Bunce, E.J., Zarka, P., Connerney, J.E.P., and Satoh, T., Jupiter's auroras, in *Jupiter*, Cambridge Univ. Press, Cambridge, U.K., in press, 2004.
- Connerney, J.E.P., Acuña, M.H., and Ness, N.F.: Modeling the Jovian current sheet and inner magnetosphere, *J. Geophys. Res.*, 86, 8370, 1981.
- Connerney, J.E.P., Acuña, M.H., Ness, N.F., and Satoh, T.: New models of Jupiter's magnetic field constrained by the Io flux tube footprint, *J. Geophys. Res.*, 103, 11929, 1998.
- Cowley, S.W.H.: *Magnetic Reconnection in Space and Laboratory Plasmas* (ed. Homes, E.W.) *Geophysics Monograph 30*, Washington DC: American Geophysical Union, 1984, 375378.
- Cowley, S.W.H. and Bunce E.J.: Jupiter: Magnetosphere, In: *Encyclopaedia of Astronomy and Astrophysics*, Institute of Physics Publ., Bristol, Vol2, pg 1341, 2001a.
- Cowley, S.W.H. and Bunce E.J.: Origin of the main auroral oval in Jupiter's coupled magnetosphere-ionosphere system, *Planet. Space Sci.*, 49, 1067, 2001b.
- Cowley, S.W.H. and Bunce, E.J.: Modulation of jovian middle magnetosphere currents and auroral precipitation by solar wind-induced compressions and expansions of the magnetosphere: Initial conditions and steady state, *Planet. Space Sci.*, 51, 31, 2003a.
- Cowley, S.W.H. and Bunce, E.J.: Corotation-driven magnetosphere-ionosphere coupling currents in Saturn's magnetosphere and their relation to the auroras, *Ann. Geophysicae*, 21, 1691-1707, 2003b.
- Cowley, S.W.H, Balogh, A., Dougherty, M.K., Dunlop, M.W., Edwards, T.M., Forsyth, R.J., Laxton, N.F., and Stanies, K.: Plasma flow in the jovian magnetosphere and related magnetic effects: Ulysses observations, *J. Geophys. Res.*, 101, 15,197, 1996.

## *References*

---

- Cowley, S.W.H., Nichols, J.D., and Bunce E.J.: Steady-state distributions of flow, current, and auroral precipitation in Jupiter's middle magnetosphere: Solutions for current sheet and dipole magnetic field models, *Planet. Space Sci.*, 50, 717, 2002.
- Cowley, S.W.H., Bunce, E.J., and Nichols, J.D.: Origins of Jupiter's main oval auroral emissions, *J. Geophys. Res.*, 108 (A4), 8002, doi:10.1029/2002JA009329, 2003a.
- Cowley, S.W.H., Bunce, E.J., Stallard, T.S., and Miller, S.: Jupiter's polar ionospheric flows: theoretical interpretation, *Geophys. Res. Lett.*, 30, 5, 1220, doi:10.1029/2002GL016030, 2003b.
- Delamere, P.A. and Bagenal, F.: Modeling variability of plasma conditions in the Io torus, *J. Geophys. Res.*, 108(A7), 1276, doi: 10.1029/2002JA009706, 2003.
- Delamere, P.A., Bagenal, F., Ergun, R.E., and Su, Y-J.: Momentum transfer between the Io plasma wake and Jupiter's ionosphere. *J. Geophys. Res.* 108(A6), 1241, doi:10.1029/2002JA009530, 2003.
- Dougherty, M.K, Balogh, A., Southwood, DJ., Smith, E.J.: Field-aligned currents in the jovian magnetosphere during the Ulysses flyby, *Planet. Space Sci.*, 41, 291, 1993.
- Dungey, J.W.: Interplanetary magnetic field and the auroral zones, *Phys. Res. Lett.* 6, 47, 1961.
- Dungey, J.W.: The length of the magnetospheric tail, *J. Geophys. Res.*, 69, 3913, 1965
- Edwards, T.M., Bunce, E.J., and Cowley, S.W.H.: A note on the vector potential of Connerney et al.'s model of the equatorial current sheet in Jupiter's magnetosphere, *Planet. Space Sci.*, 49, 1115, 2001.
- Eviatar, A., and Siscoe, G.L.: Limit on rotational energy available to excite the jovian aurora, *Geophys. Res. Lett.*, 7, 1085, 1980.

## *References*

---

- Fillius, W.: The trapped radiation belts of Jupiter, In: *Jupiter: Studies of the interior, atmosphere, magnetosphere and satellites*, T. Gehrels (Ed.), The University of Arizona Press, p. 896, 1976.
- Gazis, P.R.: A large scale survey of corotating interaction regions and their successors in the outer heliosphere, *J. Geophys. Res.*, 105, 19, 2000.
- Gérard, J.C., Dols, V., Prangé, R., and Paresce, F.: The morphology of the north jovian ultraviolet aurora observed with the Hubble Space Telescope, *Planet. Space Sci.*, 42, 905, 1994.
- Goertz, C.K.: Jupiter's magnetosphere: Particles and fields, In: *Jupiter: Studies of the interior, atmosphere, magnetosphere and satellites*, T. Gehrels (Ed.), The University of Arizona Press, p. 32, 1976.
- Goertz, C.K. and Ip, W.-H.: A dawn-to-dusk electric field in the jovian magnetosphere, *Planet. Space Sci.*, 32, 179, 1984.
- Goldreich, P., and Lynden-Bell, D., Io, a jovian uni-polar inductor, *ApJ*, 156, 59-78, 1969.
- Grodent, D., Clarke, J.T., Kim, J., Waite, J.H., Jr., and Cowley, S.W.H.: Jupiter's main oval observed with HST-STIS, *J. Geophys. Res.*, in press, 2003.
- Gurnett, D.A., and Scarf, F.L.: Plasma waves in the jovian magnetosphere, In: *Physics of the Jovian Magnetosphere*, A. J. Dessler (Ed.), Cambridge University Press, p. 285, 1983.
- Hamilton, D.C., Gloeckler, G., Krimigis, S.M., Bostrom, C.O., Armstrong, T.P.: Detection of energetic hydrogen molecules in Jupiter's magnetosphere by Voyager-2: Evidence for an ionospheric plasma source, *Geophys. Res. Lett.* 7, 813, 1980.
- Hill, T.W.: Inertial limit on corotation, *J. Geophys. Res.*, 84, 6554, 1979.

## *References*

---

- Hill, T.W.: Corotation lag in Jupiter's magnetosphere: Comparison of observation and theory, *Science*, 207, 301, 1980.
- Hill, T.W.: The jovian auroral oval, *J. Geophys. Res.*, 106, 8101, 2001.
- Hill, T.W., Dessler, A.J., and Goertz, C.K.: Magnetospheric models, in *Physics of the Jovian Magnetosphere*, edited by A.J. Dessler, p.353, Cambridge Univ. Press, Cambridge, U.K., 1983.
- Hill, T.W., and Vasyliunas, V.M.: Jovian auroral signature of Io's corotational wake, *J. Geophys. Res.*, 107(A12), 1464, doi:10.1029/2000JA009514, 2002.
- Hoffmeister, C.: Physikalische untersuchungen an kometen. I. die beziehungen des primären schweifstrahls zum radiusvektor. Mit 2 abbildungen, *Z. Astrophys.*, 22, 265, 1943.
- Huang, T.S. and Hill, T.W.: Corotation lag of the jovian atmosphere, ionosphere and magnetosphere, *J. Geophys. Res.*, 94, 3761, 1989.
- Huddleston, D.E., Russell, C.T., Kivelson, M.G., Khurana, K.K., Bennett, L.: Location and shape of the jovian magnetopause and bow shock, *J. Geophys. Res.*, 103, 20075, 1998.
- Ingersoll, A.P., Vasavada, A.R., Little, B., Anger, C.D., Bolton, S.J., Alexander, C., Klaasen, K.P., Tobiska, W.K., and the Galileo SSI Team: Imaging Jupiter's aurora at visible wavelengths, *Icarus* 135, 251-264, 1998.
- Ip, W.-H., Williams, D.J., McEntire, R.W., Mauk, B.H.: Ion sputtering and surface erosion at Europa, *Geophys. Res. Lett.* 25, 829, 1998.
- Isbell, J.A., Dessler, A.J., and Hunter, J.H., Jr.: Magnetospheric energisation by interaction between planetary spin and the solar wind, *J. Geophys. Res.*, 89, 10,716, 1984.

## *References*

---

- Kane, M., Mauk, B.H., Keath, E.P., and Krimigis, S.M.: Hot ions in the jovian magnetodisc: A model for Voyager 2 low-energy charged particle measurements, *J. Geophys. Res.*, 100, 19473, 1995.
- Kennel, C.F., and Coroniti, F.V.: Is Jupiter's magnetosphere like a pulsar's or Earth's?, in *The magnetospheres of Earth and Jupiter*, edited by V. Formisano, p. 451, D. Reidel, Norwell, Mass., 1975.
- Khurana, K.K.: Influence of solar wind on Jupiter's magnetosphere deduced from currents in the equatorial plane, *J. Geophys. Res.*, 106, 25999, 2001.
- Khurana, K.K. and Kivelson, M.G.: Inference of the angular velocity of plasma in the jovian magnetosphere from the sweepback of magnetic field, *J. Geophys. Res.*, 98, 67, 1993.
- Kivelson, M.G. and Russell, C.T. (editors): *Introduction to space physics*, Cambridge University Press, 1995
- Kivelson, M.G., Khurana, K.K., Russell, C.T., Walker, R.J.: Intermittent short-duration magnetic field anomalies in the Io torus: Evidence for plasma interchange?, *Geophys. Res. Lett* 24, 2127, 1997.
- Knight, S.: Parallel electric fields, *Planet. Space Sci.*, 21, 741, 1973.
- Krimigis, S.M., Carbary, J.F., Keath, E.P., Bostrom, C.O., Axford, W.I., Gloeckler, G., Lanzerotti, L.J., Armstrong, T.P.: Characteristics of hot plasma in the jovian magnetosphere: Results from the Voyager spacecraft, *J. Geophys. Res.*, 86, 8227, 1981.
- Krimigis, S.M., Roelof, E.C.: Low-energy particle population, In: *Physics of the Jovian Magnetosphere*, A. J. Dessler (Ed.), Cambridge University Press, p. 106, 1983.
- Krupp, N., Lagg, A., Livi, S., Wilken, B., Woch, J., Roelof, E.C., and Williams, D.J.: Global flows of energetic ions in Jupiter's equatorial plane: First-order approximation, *J. Geophys. Res.*, 106, 26017, 2001.

## *References*

---

- Kunow, H.: Solar Wind: Corotating interaction regions, In: *Encyclopaedia of Astronomy and Astrophysics*, Institute of Physics Publ., Bristol, Vol. 4, p2825, 2001.
- Lang, K.R.: *Cambridge encyclopaedia of the sun*, Cambridge University Press, 2001.
- Laxton, N.F., Balogh, A., Cowley, S.W.H., Dunlop, M.W., Forsyth, R.J., Hynds, R.J., Staines, K.: Origins of the first-order anisotropy of  $\sim 1$  MeV protons in the jovian magnetosphere during Ulysses flyby: flux gradients and plasma flows, *Planet. Space Sci.*, 45, 1143, 1997.
- Leamon, R.J., Dougherty, M.K., Southwood, D.J., Haynes, P.L.: Magnetic nulls in the outer magnetosphere of Jupiter, *J. Geophys. Res.* 100, 1829, 1995.
- Lepping, R.P., Desch, M.D., Klein, L.W., Sittler, E.C., Jr., Sullivan, J.D., Kurth, W.S., Behannon, K.W.: Structure and other properties of Jupiter's distant magnetotail, *J. Geophys. Res.* 88, 8801, 1983.
- Lundin, R. and Sandahl, I.: Some characteristics of the parallel electric field acceleration of electrons over discrete auroral arcs as observed from two rocket flights. *Symposium on European Rocket Research*, ESA SP-135, p. 125, 1978.
- Mauk, B.H., Gary, S.A., Kane, M., Keath, E.P., Krimigis, S.M.: Hot plasma parameters of Jupiter's inner magnetosphere, *J. Geophys. Res.* 101, 7685, 1996.
- Mauk, B.H., Williams, D.J., McEntire, R.W., Khurana, K.K., Roederer, J.G.: Storm-like dynamics of Jupiter's inner and middle magnetosphere, *J. Geophys. Res.* 104, 22759, 1999.
- Millward, G.H., Miller, S., Stallard, T., Aylward, A.D., and Achilleos, N.: On the dynamics of the jovian ionosphere and thermosphere III. The modelling of auroral conductivity, *Icarus*, 160, 95, 2002.

## *References*

---

- Millward G.H., Miller, S., Stallard, T., Achilleos, N., and Aylward, A.D.: On the dynamics of the jovian ionosphere and thermosphere IV: ion-neutral coupling. *Icarus*, in press, 2004.
- Ness, N.F., Acuña, M.H., Lepping, R.P., Burlaga, L.F., Behannon, K.W., Neubauer, F.M.: Magnetic field studies at Jupiter by Voyager 1: Preliminary results, *Science* 204, 982, 1979a.
- Ness, N.F., Acuña, M.H., Lepping, R.P., Burlaga, L.F., Behannon, K.W., Neubauer, F.M.: Magnetic field studies at Jupiter by Voyager 2: Preliminary results, *Science* 206, 966, 1979b.
- Ness, N.F., Acuña, M.H., Lepping, R.P., Burlaga, L.F., Behannon, K.W., Neubauer, F.M.: Jupiter's magnetic tail, *Science* 280, 799, 1979c.
- Pallier, L. and Prangé, R.: More about the structure of the high latitude jovian aurorae, *Planet. Space Sci.*, 49, 1159, 2001.
- Parker, E.N.: Dynamics of the interplanetary magnetic field, *Astrophys. J.*, 128, 664, 1958.
- Paschmann, G., Haaland, S. and Treumann, R. (editors): *Auroral plasma physics*, Kluwer Publ., Dordrecht, 2002.
- Phillips, J.L., Bame, S.J., Barraclough, B.L., McComas, D.J., Forsyth, R.J., Canu, P., Kellogg, P.J.: Ulysses plasma electron observations in the jovian magnetosphere, *Planet. Space Sci.*, 41, 877, 1993.
- Pontius, D.H., Jr.: Radial mass transport and rotational dynamics, *J. Geophys. Res.*, 102, 7137, 1997.
- Pontius, D.H., Jr. and Hill, T.W.: Departure from corotation of the Io plasma torus: Local plasma production, *Geophys. Res. Lett.*, 9, 12, 1321, 1982.

## *References*

---

- Prangé, R., Rego, D., Pallier, L., Connerney, J.E.P., Zarka, P., and Queinnec, J.: Detailed study of FUV jovian auroral features with the post-COSTAR HST faint object camera, *J. Geophys. Res.*, 103, 20195, 1998.
- Sands, M.R., and McNutt, R.L.: Plasma bulk flow in Jupiter's dayside middle magnetosphere, *J. Geophys. Res.*, 93, 8502, 1988.
- Satoh, T., Connerney, J.E.P., and Baron, R.L.: Emission source model of Jupiter's  $H_3^+$  aurorae: A generalized inverse analysis of images, *Icarus*, 122, 1, 1996.
- Scarf, F.L.: Possible traversals of Jupiter's distant magnetic tail by Voyager and by Saturn, *J. Geophys. Res.*, 84, 4422, 1979.
- Schreier, R., Eviatar, A., Vasyliunas, V.M.: A two-dimensional model of plasma transport and chemistry in the jovian magnetosphere, *J. Geophys. Res.* 103, 19,901, 1998.
- Scudder, J.D., Sittler Jr., E.C., Bridge, H.S.: A survey of the plasma electron environment of Jupiter: a view from Voyager, *J. Geophys. Res.*, 86, 8157, 1981.
- Siscoe, G.L. and Summers, D.: Centrifugally-driven diffusion of iogenic plasma, *J. Geophys. Res.*, 86, 8471, 1981.
- Sloanaker, R. M.: Apparent temperature of Jupiter at a wavelength of 10 cm, *Aston. J.* 64, 346, 1959.
- Slutz, R.J. and Winkelman, J.R.: Shape of the magnetospheric boundary under solar wind pressure, *J. Geophys. Res.*, 69, 4933-4948, 1964.
- Smith, E.J., Davis, L., Jr., Jones, D.E., Coleman, P.J., Jr., Colburn, D.S., Dyal, P., Sonett, C.P., Frandsen, A.M.A.: The planetary magnetic field and magnetosphere of Jupiter: Pioneer 10, *J. Geophys. Res.*, 79, 3501, 1974.

## *References*

---

- Smith, E.J., Davis, L., Jr., Jones, D.E., Coleman, P.J., Jr., Colburn, D.S., Dyal, P., Sonett, C.P.: Jupiter's magnetic field, magnetosphere and interaction with the solar wind: Pioneer 11, *Science* 188, 451, 1975a.
- Smith, E.J., Connor, B.V., Foster, G.T., Jr.: Measuring the magnetic fields of Jupiter and the outer solar system, *IEEE Trans. on magnetics* MAG-11, 962, 1975b.
- Smith, E.J., Davis, L., Jr., Jones, D.E.: Jupiter's magnetic field and magnetosphere, In: Gehrels, T., (Ed.), *Jupiter*. University of Arizona Press, Tucson, p. 788, 1976.
- Smith, E.J., Tsurutani, B., Rosenberg, R.L.: Observations of the interplanetary sector structure up to heliographic latitudes of 16°: Pioneer 11, *J. Geophys. Res.*, 83, 717, 1978.
- Southwood, D.J., Dougherty, M.K., Canu, P., Balogh, A., Kellogg, P.J.: Correlations between magnetic-field and electron density observations during the inbound Ulysses Jupiter fly-by, 41, 919, 1993.
- Southwood, D.J., Dougherty, M.K., Leamon, R.J., Haynes, P.J.: Origin and dynamics of field nulls detected in the jovian magnetosphere, *Adv. Space Res.* 16, 177, 1995.
- Southwood, D.J. and Kivelson, M.G.: A new perspective concerning the influence of the solar wind on Jupiter, *J. Geophys. Res.*, 106, 6123, 2001.
- Strobel, D.F. and Atreya, S.K.: Ionosphere, in *Physics of the Jovian Magnetosphere*, edited by A.J. Dessler, p. 51, Cambridge Univ. Press, Cambridge, U.K., 1983.
- Thorne, R.M.: Microscopic plasma processes in the jovian magnetosphere, in *Physics of the Jovian Magnetosphere*, edited by A.J. Dessler, p. 454, Cambridge Univ. Press, Cambridge, U.K., 1983.
- Thorne, R.M., Armstrong, T.P., Stone, S., Williams, D.J., McEntire, R.W., Bolton, S.J., Gurnett, D.A., Kivelson, M.G.: Galileo evidence for rapid interchange transport in the Io torus, *Geophys. Res. Lett.* 24, 2131, 1997.

## *References*

---

- Tsurutain, B.T., et al.: Plasma wave characteristics of the jovian magnetopause boundary layer: Relationship to the jovian aurora?, *J. Geophys. Res.*, 102, 4751, 1997.
- Vasavada, A.R., Bouchez, A.H., Ingersoll, A.P., Little, B., and Anger, C.D.: Jupiter's visible aurora and Io footprint, *J. Geophys. Res.*, 104, 27133, 1999.
- Vasyliunas, V.M.: Plasma distribution and flow, in *Physics of the Jovian Magnetosphere*, edited by A.J. Dessler, p. 395, Cambridge Univ. Press, Cambridge, U.K., 1983.
- Woch, J.N., Krupp, N., Lagg, A.: Particle burst in the jovian magnetosphere: Evidence for a near-Jupiter neutral line, *Geophys. Res. Lett.*, 29, 42-1, 2002.